Ocean-atmosphere interaction : improvement of wind stress for coastal physical modelling

Lucia Pineau-Guillou

UNIVERSITE SCIENCES BRETAGNE DE LA MER LOIRE ET DU LITTORAL

UBO Université de Bretagne Occidentale

THESE DE DOCTORAT DE

L'UNIVERSITE
DE BRETAGNE OCCIDENTALE
COMUE UNIVERSITE BRETAGNE LOIRE

ECOLE DOCTORALE N° 598
Sciences de la Mer et du littoral
Spécialité : Océanographie Physique et Environnement

Par

Lucia PINEAU-GUILLOU

Interaction Océan-Atmosphère : Amélioration de la tension de vent en modélisation physique côtière

Thèse présentée et soutenue à Plouzané, le 16 novembre 2018
Unité de recherche : Laboratoire d'Océanographie Physique et Spatiale

Rapporteurs avant soutenance :

Michel BENOIT	Professeur des Universités Centrale Marseille & IRPHE
Xavier BERTIN	Directeur de recherche CNRS LIENSs, Université de La Rochelle

Composition du Jury :

Michel BENOIT	Professeur des Universités Centrale Marseille & IRPHE
Xavier BERTIN	Directeur de recherche CNRS LIENSs, Université de La Rochelle
Président Xavier CARTON	Professeur des Universités LOPS, UBO, Brest
Vladimir KUDRYAVTSEV	Chercheur SOLab, St-Pétersbourg
Directeur de thèse Fabrice ARDHUIN	Directeur de recherche CNRS LOPS, Brest
Co-directrice de thèse Marie-Noëlle BOUIN	Chercheure Météo-France CNRM (et LOPS), Brest

Invités

Jean-Luc REDELSPERGER	Directeur de Recherche CNRS LOPS, Brest
Pierre GARREAU	Chercheur IFREMER LOPS, Brest

Version du 26 novembre 2018

Remerciements

Je remercie tous ceux qui ont permis que ce projet aboutisse.

Je remercie en particulier mes directeurs de thèse, Fabrice Ardhuin, Marie-Noëlle Bouin, mes coauteurs, Jean-Luc Redelsperger, Bertrand Chapron, Jean Bidlot, Yves Quilfen, Florent Lyard, ainsi que les membres du jury Michel Benoit, Xavier Bertin, Xavier Carton, Vladimir Kudryavtsev et Pierre Garreau.

Je remercie enfin mon employeur, l'IFREMER, qui en acceptant ce projet, m'a donné la chance de pouvoir pendant trois ans suivre cette formation.

Résumé/Abstract

Interaction Océan-Atmosphère : amélioration de la tension de vent en modélisation physique côtière

Mots clés : interaction air-mer, tension de vent, vents, surcotes, état de mer.

Les surcotes de tempête sont souvent sous-estimées dans les modèles hydrodynamiques, ainsi que les grandes vagues dans les modèles de vagues. Les causes possibles sont une sous-estimation des vents dans les modèles atmosphériques et/ou une formulation incorrecte de la tension de vent. Les objectifs de cette thèse sont (1) d'estimer les biais par vents forts dans les modèles atmosphériques (2) de développer une nouvelle paramétrisation du coefficient de traînée permettant de réduire ce biais (3) d'étudier l'impact des vagues sur la tension de vent. La méthode consiste à étudier la réponse de l'atmosphère et de l'océan à la tension de vent. Dans une première partie, nous utilisons le modèle couplé vagues-atmosphère d'ECMWF. Nous montrons que les vents forts sont sous-estimés, avec un biais de l'ordre de -7 m/s à 30 m/s. Des écarts significatifs existent aussi entre les observations, les bouées et les vents issus de ASCAT-KNMI étant généralement inférieurs à ceux des plateformes et des autres données satellites utilisées dans cette étude (AMSR2, ASCAT-RSS, WindSat, SMOS et JASON-2). La nouvelle paramétrisation développée permet d'obtenir des vents plus forts qu'avec celle d'ECMWF par défaut. Dans une deuxième partie (réponse de l'océan), nous utilisons le modèle global océanique TUGO du LEGOS forcé par le modèle couplé vagues-atmosphère d'ECMWF. Nous montrons qu'une paramétrisation de la tension de vent dépendant des vagues plutôt que du vent est plus appropriée quand l'état de mer est jeune. Elle conduit à des surcotes plus proches des observations (marégraphes et traces altimétriques de JASON-2). L'impact des vagues sur la surcote est significatif, et peut atteindre 20 cm.

Ocean-Atmosphere interaction : improvement of wind stress for coastal physical modelling

Keywords : air-sea interaction, wind stress, winds, surges, sea state.

Storm surges may be underestimated in hydrodynamic models, as well as large wave heights in wave models. This could come from an underestimation of strong winds in atmospheric models and/or an inappropriate wind stress formulation. The objectives of the present work are (1) to estimate how strong are the biases for high winds in atmospheric models (2) to develop a new drag parameterization that could reduce this bias (3) to investigate the impact of the waves on the wind stress. The method consists of studying the response of the atmosphere and the ocean to the wind stress. In a first part, we use the coupled wave-atmosphere model from ECMWF. We show that strong winds may be underestimated, as much as -7 m/s at 30 m/s. Significant differences also exist between observations, with buoys and ASCAT-KNMI generally showing lower wind speeds than the platforms and other remote-sensing data used in this study (AMSR2, ASCAT-RSS, WindSat, SMOS and JASON-2). The newly empirically adjusted Charnock parameterization leads to higher winds compared to the default ECMWF parame-

terization. In a second part, we use the global ocean model TUGO from LEGOS forced with ECMWF coupled wave-atmopshere model. We show that a wave-dependent rather than wind-dependent stress formulation is more appropriate, when the sea state is young and the sea rougher. It yields to simulated surges closer to observations (i.e. tide gauges and JASON-2 altimeter tracks). The wave impact on the surges is significant, and may reach 20 cm.

Résumé étendu

Résumé du Chapitre 1 : Introduction

Dans ce chapitre, le sujet est présenté. Différentes études suggèrent que les vents forts pourraient être sous-estimés dans les modèles atmosphériques, entraînant une sous-estimation des surcotes et des vagues dans les modèles océaniques (Rascle and Ardhuin, 2013; Hanafin et al., 2012; Stopa and Cheung, 2014). La possible sous-estimation des vents forts n'est probablement pas la seule explication. La formulation de la tension de vent pourrait également être une autre raison. En effet, pour un vent donné, un coefficient de traînée plus faible pourrait mener à une vitesse de friction plus faible, et donc à des vents plus forts.

L'objectif est d'étudier l'impact de l'état de mer sur la tension de vent, en particulier pour les vents forts (> 20 m/s). L'impact de l'état de mer sur la tension de vent a été démontré très tôt dans les années 50 (Van Dorn, 1953). L'expérience est la suivante : l'ajout de détergent dans l'eau élimine les petites vagues (de longueur d'onde inférieure à 20 cm), entraînant une dimininution de la tension de vent puis une augmentation du vent, dans ce système couplé. Ces petites vagues, en partie responsables de la tension de vent, sont les capillaires et les ondes de gravité courtes. Leur longueur d'onde varie de 1 cm (pour les capillaires) à quelques dizaines de cm (pour les ondes de gravité courtes). Elles sont à l'origine de la rugosité de la mer. Quand elles disparaissent, le vent ne peut plus agripper la surface, et la tension de vent diminue.

La tension de vent est généralement paramétrisée à partir de formules bulk. Elle est alors fonction du vent et d'un coefficient de traînée. La plupart des formulations du coefficient de traînée dépendent uniquement du vent, alors que d'autres prennent en compte l'effet des vagues, via une longueur de rugosité variable pour un vent donné (par exemple, Janssen (1991) à ECMWF). Les paramétrisations sont généralement mises en place de manière empirique, à partir de campagnes en mer. Bien que l'impact des vagues ait été démontré assez tôt, Edson et al. (2013) montre que les formulations ne dépendant que du vent sont en accord avec les observations, sans prendre en compte une quelconque information sur les vagues.

Ces résultats contradictoires soulèvent la complexité du problème. De nombreux freins empêchent de répondre simplement à la question suivante : quel est l'impact des vagues sur la tension de vent, et existe-t-il vraiment un impact ? Les difficultés sont liées au manque de mesures par vent fort, à leurs fortes incertitudes, au fait que la longueur de rugosité - un paramètre clé - ne se mesure pas et reste difficile à interpréter physiquement, au fait que les variables utilisées ne sont pas indépendantes entre elles (ce qui introduit de l'autocorrélation), et enfin, à un évident problème d'échelle (on parle de vagues de quelques cm à quelques dizaines de cm quand la résolution des modèles est de l'ordre de quelques centaines de mètres à quelques kilomètres).

Le manuscrit est organisé comme suit : le deuxième chapitre concerne la théorie, le troisième l'impact sur l'atmosphère, le quatrième l'impact sur l'océan, le cinquième présente les conclusions et le sixième

les perspectives.

Résumé du Chapitre 2 : Représentation de la tension de vent

Ce chapitre correspond à un état de l'art sur la tension de vent. Il introduit la couche limite atmosphérique qui comprend la couche visqueuse (quelques mm à quelques cm), la couche de surface (jusqu'à 20 à 200 m) et la couche d'Ekman (jusqu'à 200 à 2000 m). Dans la couche de surface, les flux sont considérés comme constants, c'est à dire indépendants de la hauteur. Les flux air-mer sont introduits, ainsi que le profil de vent en conditions neutres et non neutres. Les formulations de la tension de vent, du coefficient de traînée et de la longueur de rugosité sont décrites. Les principales formulations bulk sont résumées : de la formulation de Charnock, aux formulations en fonction du vent, ou celles fonction de l'âge des vagues, ou encore fonction de la tension induite par les vagues. Enfin, d'autres approches sont évoquées, par exemple en fonction du déferlement des vagues.

Résumé du Chapitre 3 : Impact sur l'atmosphère

Ce chapitre a pour objectif d'évaluer le biais entre les vents forts d'ECMWF et les observations, et de tester d'autres paramétrisations pouvant potentiellement réduire ce biais. Pendant les tempêtes Kaat et Lilli (23-27 Janvier 2014), nous comparons les vents issus du modèle couplé vague-atmosphère d'ECMWF avec les observations disponibles en Atlantique Nord-Est. Une nouvelle paramétrisation du coefficient de traînée est développée. Les résultats obtenus sont les suivants.

(1) Les vents modérés (5-20 m/s) sont en accord avec les mesures in-situ et satellite, alors que les vents forts ($>$ 20 m/s) sont en général sous-estimés par rapport aux observations. Le biais peut atteindre -7 m/s à 30 m/s (Figure 1).

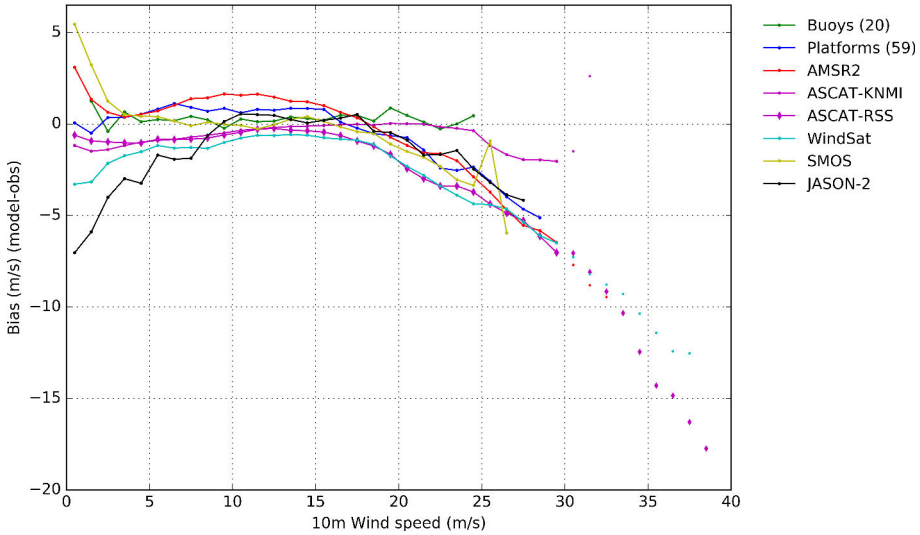

FIGURE 1 – Biais sur le vent entre le modèle ECMWF (CY41R1) et les observations (bouées, plateformes et satellites), calculés entre le 23 et le 27 Janvier 2014 en Atlantique Nord-Est. Au-delà de 30 m/s, les valeurs sont représentées sous forme de points, à cause des larges incertitudes sur les observations.

(2) Des biais existent entre les observations. Nous avons identifié deux groupes de données. Le premier, composé des bouées et des vents ASCAT-KNMI, donne des vents forts plus faibles que le second

groupe, composé des autres données satellite exploitées dans cette étude (AMSR2, ASCAT-RSS, WindSat, SMOS et JASON-2). Il est difficile de définir quelle est la référence, mais il est probable que les bouées et les vents ASCAT-KNMI soient sous-estimés.

(3) La paramétrisation développée, basée sur un coefficient de Charnock empiriquement ajusté, permet d'obtenir des vents plus forts que celle d'ECMWF par défaut. Par contre, la paramétrisation dépendante de l'âge des vagues donne des coefficients de traînée bien trop forts - et des vents trop faibles - et n'est pas appropriée pour le couplage.

Cette étude a été reproduite pour trois autres tempêtes en Atlantique Nord-Est : Alexandra (8 décembre 2014), Erich (10 mars 2015) et Uwe (7 décembre 2015). Les résultats sont similaires et confirment ces conclusions.

Concernant le biais significatif constaté entre les bouées et les plateformes (environ 3 m/s à 25 m/s), malgré des investigations supplémentaires, nous n'avons pas été en mesure de l'expliquer.

Résumé du Chapitre 4 : Impact sur l'océan

Ce chapitre a pour objectif d'étudier l'impact des vagues sur la tension de vent, via les surcotes (réponse de l'océan). Pendant les tempêtes ex-Gonzalo et Friedhelm, caractérisées par un état de mer jeune et vieux, nous comparons les surcotes avec une paramétrisation de la tension de vent dépendant du vent (Hellerman and Rosenstein, 1983) et dépendant des vagues (Janssen, 1991). Nous comparons les résultats avec les marégraphes et les traces altimétriques JASON-2. Les résultats sont les suivants.

(1) Le modèle global prédit les surcotes avec une précision satisfaisante, même dans les zones côtières (RMSE de 12 cm). Ceci est dû en partie à la grille éléments finis, qui permet d'augmenter la résolution dans les zones de petits fonds. La cohérence entre le modèle, l'altimètre et les marégraphes confirme également la capacité des altimètres à mesurer les surcotes avec une précision satisfaisante (RMSE de 8 cm le long de la trace au sol, Figure 2).

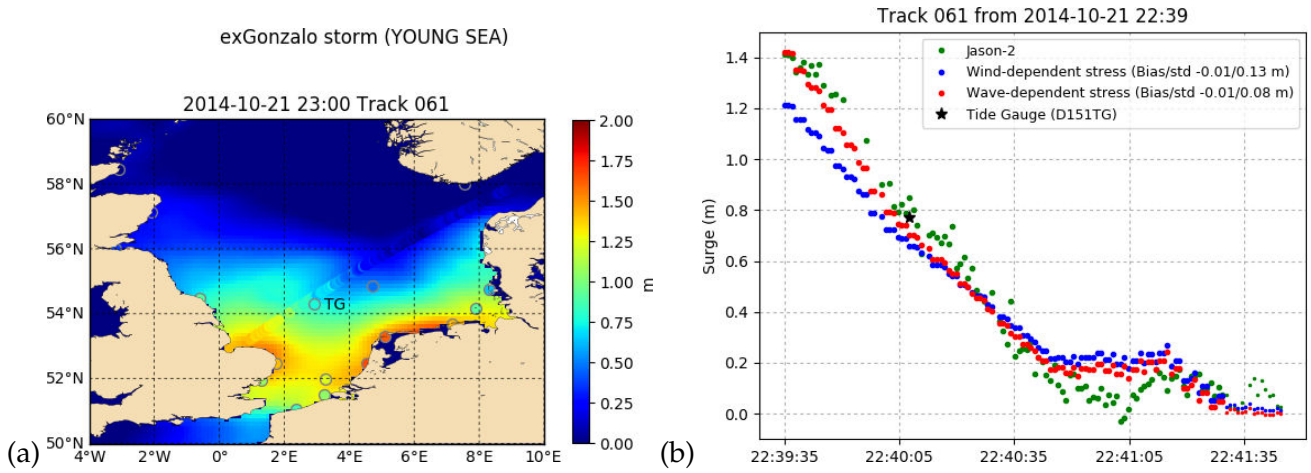

FIGURE 2 – Surcotes issues du modèle TUGO, des traces altimétriques JASON-2 et des marégraphes pendant la tempête ex-Gonzalo. Sur le graphe b), la taille du point est plus petite quand la bathymétrie est supérieure 100 m.

(2) La formule classique de la tension de vent dépendant du vent, Hellerman and Rosenstein (1983),

est satisfaisante quand la mer est vieille. Par contre, quand la mer est jeune, la présence de vagues courtes augmente la tension de vent, et la formulation dépendant des vagues devient plus adéquate. Elle réduit l'Erreur Pic de manière significative (de 0.21 m à 0.09 m). L'impact des vagues sur la surcote peut atteindre 20 à 25 cm. Ce résultat est cohérent avec de précédentes études (Mastenbroek et al., 1993; Nicolle et al., 2009; Bertin et al., 2015). Cependant le nombre de cas d'études doit être augmenté pour confirmer ces conclusions. En effet, une des difficultés est le risque de compensation d'erreurs. Ainsi, Moon et al. (2009) ont montré que Mastenbroek et al. (1993) obtenaient de bonnes surcotes malgré des coefficients de traînée surestimés, en compensant des erreurs dues à une grille de résolution spatiale trop grossière.

(3) Le biais sur les vents forts n'est pas toujours la raison principale de sous-estimation des surcotes. Augmenter les vents forts peut avoir un effet négligeable comparé à la prise en compte des vagues (par exemple augmenter les vents permet d'augmenter la surcote de 5 cm, contre 23 cm en prenant en compte l'effet des vagues).

Nous avons formulé le "paradoxe du forçage", qui conduit à obtenir des résultats divergents selon la manière dont le modèle océanique est forcé. La paramétrisation développée dans le chapitre précédent a permis d'augmenter les vents forts, par rapport à la paramétrisation d'ECMWF par défaut. Quand le modèle océanique est forcé par les vents, la surcote va augmenter, alors qu'elle va diminuer s'il est forcé par la tension de vent de la même simulation atmosphérique. Ce dernier scénario n'est pas satisfaisant, car la surcote est déjà sous-estimée par rapport aux observations.

Finalement, la comparaison des surcotes s'est avérée meilleure avec les altimètres qu'avec les marégraphes, probablement parce que les marégraphes peuvent être contaminés par des processus côtiers comme la surcote due au déferlement des vagues (wave setup).

Résumé du Chapitre 5 : Conclusions

Ce chapitre présente les conclusions de l'étude.

Dans cette étude, nous avons cherché à avoir une approche cohérente, en regardant en même temps la réponse de l'atmosphère et celle de l'océan. Cela a abouti au "paradoxe du forçage". Finalement, la paramétrisation développée dans la première partie a permis d'améliorer les vents (la réponse de l'atmosphère), mais pas les surcotes (la réponse de l'océan), quand le modèle d'océan est forcé par la tension de vent. Ce paradoxe suscite diverses interrogations, présentées dans ce chapitre.

Nous avons également cherché à confronter le maximum de données possibles, qu'elles proviennent de modèles, de mesures in-situ ou de satellites. Exploiter différents types d'observations peut se révéler complexe, car les instruments ne sont pas toujours cohérents entre eux. En particulier, nous avons trouvé un biais significatif entre les bouées et les plateformes. Malgré diverses investigations, nous n'avons pas été en mesure de l'expliquer.

Résumé du Chapitre 6 : Perspectives

Ce chapitre présente les perspectives de cette étude.

Pour les modèles d'atmosphère, cette étude a suscité plusieurs modifications du modèle couplé vagues-atmosphère d'ECMWF, de manière à obtenir des vents plus forts. L'une a été effective fin 2016, la prochaine sera effective en juin 2019. Cette étude a également suscité le développement d'une nouvelle paramétrisation du coefficient de traînée à Météo-France. Pour les modèles de vagues, la queue du

spectre est mal représentée dans les modèles, et une meilleure représentation des vagues courtes permettrait d'améliorer la tension de vent. Pour les modèles d'océan, une recommandation est de forcer les modèles par la tension qui part dans l'océan plutôt que celle qui vient de l'atmosphère. Un nouveau schéma de couplage, plus cohérent, est proposé (Figure 3).

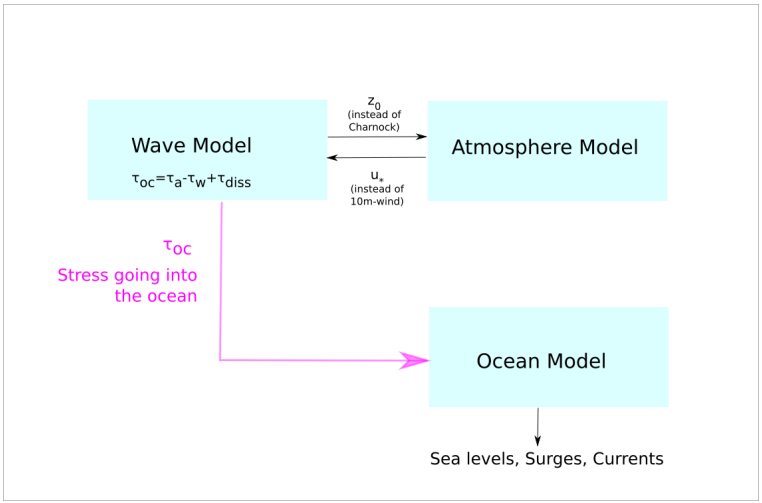

FIGURE 3 – Une manière plus cohérente de forcer le modèle d'océan

Concernant les observations, on manque clairement de mesures par vents forts. Pourtant, elles sont nécessaires pour développer les paramétrisations, valider les modèles et calibrer les instruments embarqués sur satellites.

La méthodologie développée dans cette étude permet de qualifier les vents forts, et d'estimer les biais entre les instruments, le modèle servant ici de référence commune. Cette méthode pourrait être utilisée pour qualifier les futures données satellite. A noter la prochaine mission CFOSAT (China-France Oceanography SATellite) qui devrait être lancée fin octobre 2018 pour mesurer conjointement les vagues et les vents.

Suite à ce travail, l'une des recommandations est de forcer le modèle d'océan par la tension de vent issue d'un modèle couplé vague-atmosphère (qui a vu les vagues). Ceci devrait permettre d'améliorer la SLA (Sea Level Anomaly) des produits altimétriques, en enlevant un signal atmosphérique résiduel dû aux vagues. Ces résultats ont été présentés au dernier colloque de l'OSTST (Ocean Surface Topography Science Team) en octobre 2018. Cette recommandation pourrait être suivie pour la prochaine version du produit DAC (Dynamic Atmospheric Corrections), développé par le LEGOS et CLS.

Enfin, dans ces travaux, nous avons étudié l'impact des vagues sur la tension de vent, en regardant la réponse de l'océan, via les surcotes. Une étude similaire pourrait être menée via les courants de surface plutôt que les surcotes. Ces travaux pourraient s'appuyer sur la campagne DRIFT4SKIM, planifiée en novembre 2018 en mer d'Iroise, et qui vise à démontrer la faisabilité de la mesure des courants de surface par satellite.

Contents

List of Tables

List of Figures

Chapter 1

Introduction

The exchanges between the atmosphere and the ocean are a key component of the Earth climate system. Air-sea fluxes are responsible of the exchange of momentum and heat between the ocean and the atmosphere. Obtaining reliable fluxes is crucial for ocean and atmosphere modelling. It encompasses a very broad field of time-scales and phenomena, from the instantaneous forecast of fine-scale events (nowcast) to global climate runs over several decades (Shimura et al., 2017).

Several studies suggest that strong winds may be systematically underestimated by atmospheric models, with a consequent underestimation in surge and wave models (Rascle and Ardhuin, 2013; Hanafin et al., 2012; Stopa and Cheung, 2014). So far, it is not clear whether the strong negative bias obtained in wave simulations is caused by underestimated wind speed, inaccurate stress formulation or imprecise wave growth and dissipation parameterization at high wind speeds. The possible underestimation of high winds in atmospheric models is probably not the only explanation for wave underestimation. Parameterization of wind stress could also be another reason. Indeed, for a given wind field at the surface, lower drag coefficient C_d could result in lower friction velocity and, as a feedback, could yield to higher surface wind.

The objective is to investigate the impact of the sea state on the wind stress, particularly for strong winds (i.e. greater than 20 m/s). Over the last century, numerous measurements were carried out in order to understand the momentum flux variability. Many authors developped parameterizations in order to be able to predict the momentum flux (e.g. Charnock, 1955; Smith and Banke, 1975; Wu, 1982; Janssen, 1991; Oost et al., 2002; Moon et al., 2007; Edson et al., 2013). However, despite years of research, there is still no consensus on the interpretation of these data. What Amorocho and DeVries (1980) reported almost 40 years ago is still appropriate: "For the past 100 years or so, numerous investigators have carried out measurements of wind shear over water surfaces, both in the laboratory and at sea. A large volume of data has been collected, but no consensus has been reached yet on its interpretation." This subject is still an active research area.

The impact of the sea state on the wind stress has been demonstrated as early as the 50's (Van Dorn, 1953). The experiment is the following: adding some surfactant (e.g. soap, oil, detergent) to the water eliminates the small waves (shorter than 20 cm), the wind stress decreases, and then the wind increases, in this coupled ocean-atmosphere system. These small waves with shortest period are the capillary and the short gravity waves (Figure 1.1). Their wave length is around 1 cm for the capillaries and up to a few tens of cm for the short gravity waves, and their period varies between 0.1 s and a few seconds. A large part of these short waves are responsible of the roughness of the sea, and support the stress. When they disappear, the wind can not grip anymore the surface, and the wind stress decreases.

The wind stress is usually parametrized using bulk formulae, that express it as a function of the

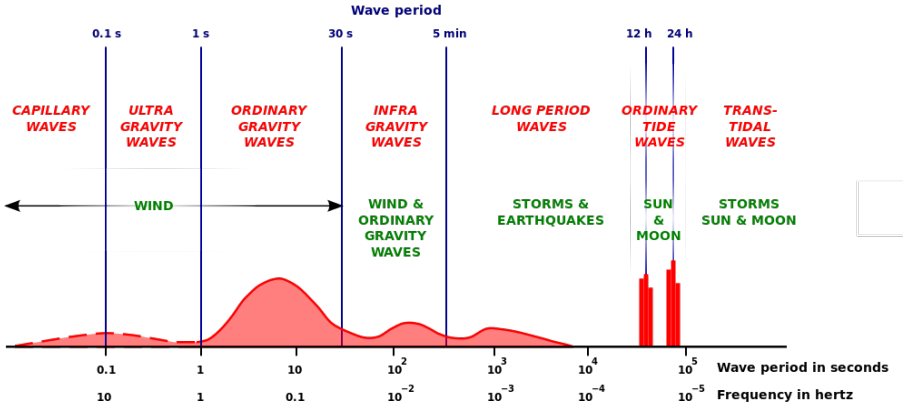

Figure 1.1 – Tentative classification of ocean waves according to wave period. The forces responsible for various portions of the spectrum are shown. The relative amplitude is indicated by the curve. From (Munk, 1950)

wind speed and of a drag coefficient. Most formulations of the drag depend only on the wind speed, whereas others take into account the wave effect using a variable roughness length for a given wind-speed - e.g. Janssen (1991) in ECMWF (European Centre for Medium-Range Weather Forecasts) coupled wave-atmosphere model. Parameterizations are generally built from experiments. Despite the fact that the impact of the waves was demonstrated early, Edson et al. (2013) showed that wind-speed formulation of the drag matches well with observations without any wave information.

These contrasted results can be explained by the complexity of the problem. They are major issues that prevent from answering simply to the simple question: what is the wave impact on the wind stress, if any? (1) First of all, wind stress measurements - and then drag estimations - are difficult to conduct, particularly at high winds. Strong uncertainties in observations could explain the variability of the drag at a given wind speed. Estimations from several recent field experiments based on direct in situ measurements (e.g. Black et al., 2007; Edson et al., 2013) or indirect ones (Powell et al., 2003; Holthuijsen et al., 2012), as well as laboratory tank measurements (e.g (Donelan et al., 2004) (Jarosz et al., 2007) (Takagaki et al., 2012) show differences on the drag up to a factor 2 at 30 m/s (Figure 3.4). It is not known if these differences are due to measurements uncertainties or various environmental conditions (fetch, sea state, bathymetry...). (2) The second point is that wind stress measurements are scarce. They generally come from short dedicated campaigns, with moderate winds, often lower than 20 m/s (see Table A.1). There is clearly a lack of observations at very high winds, even if dedicated efforts were undertaken (e.g. Powell et al., 2003). (3) The third point is that the roughness length which is a key parameter (see Eq. 2.2) can not be measured and has no physical meaning, i.e. values of 0.1 mm or 1 cm does not correspond to any height of geometric elements (for example, height of the surface ripples). (4) The fourth point is that all the variables used to explain wind stress variability are interdependent. As a consequence, good correlations between the drag and variable as wave age may be mainly due to self-correlation (Andreas, 2009). This contributes to a lack of confidence in these relationships from a part of the scientific community. (5) The last point is an obvious problem of scale. We are dealing with 1-20 cm short gravity waves, whereas the ocean model resolution is of few km.

The manuscript is organised as follows. The second chapter describes the wind stress representation. The third chapter analyses the atmosphere response (i.e. the wind at 10 m) through a coupled wave-atmosphere model. Different experiments will help to answer to these questions: are the strong winds underestimated in atmospheric models? Does an alternative parameterization help to reduce the bias? The fourth chapter analyses the ocean response, through an ocean model forced with the coupled wave-

atmosphere model. Different experiments should help to answer to this question: what is the wave impact on the wind stress? Finally, the fifth and sixth chapters present the conclusions and the perspectives.

Here, we are going to focus on waves and atmospheric surges. However, the processes are numerous and complex in the upper part of the ocean (Figure 1.2), as well as at the air sea interface (spray, foam, bubbles...). All these processes interact with each other, and the response of the ocean is the result of all these interactions. The sea level includes the signature of atmospheric surge, but also internal waves, eddies, density fronts...which are not considered in this study.

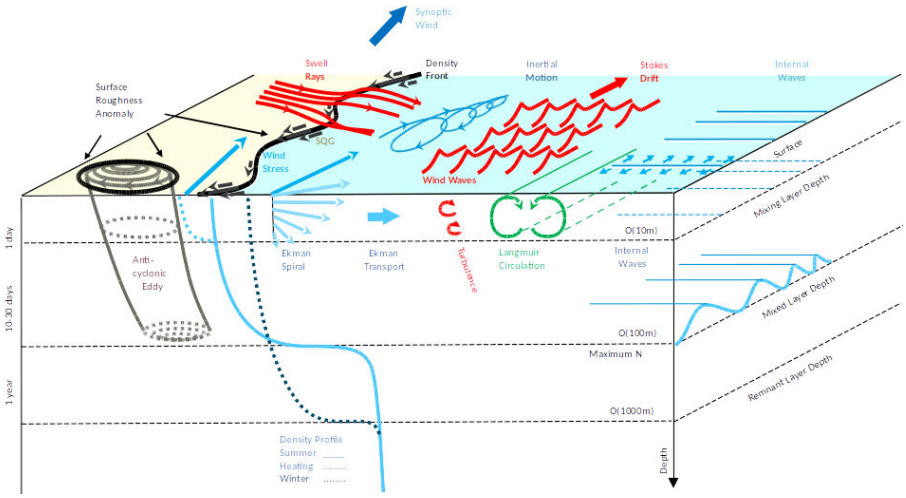

Figure 1.2 – Processes that influence the upper ocean layer. From GlobCurrent project (Chapron, 2017).

Chapter 2

Wind stress representation

2.1 Boundary layer

The Atmospheric Boundary Layer (ABL) - also called Planetary Boundary Layer (PBL) - is the bottom layer of the atmosphere which is in contact with the surface of the earth. The ABL is directly influenced by the terrestrial and maritime surface, and reacts very rapidly to changes (from few hours up to one day). The ABL depth is variable in time and space, but it ranges approximatively from 200 to 2 000 m over the oceans.

The ABL can be separated into three layers (Figure 2.1):
— The viscous layer is the really thin layer right next to the surface. Its depth reaches only a few centimeters. In this layer, viscous forces dominate.
— The surface layer is the low portion of the ABL (10% of ABL depth). It ranges from 20 to 200 m. In this layer, wind gradients are strong, as the wind decreases until zero at the surface. However, wind stress is quite constant (independent from the height).
— The Ekman layer is the main part of the ABL. The winds change gradually with height, to reach geostrophic winds in the free atmosphere.

In the Atmospheric Boundary Layer, neutral conditions correspond to an homogeneous stratification. In case of non-neutral conditions, the stratification can be stable (positive buoyancy) or unstable (negative buoyancy).

The present work takes place in the surface layer, from a few centimeters up to a hundred meters above the surface.

2.2 Air-sea fluxes

At the air-sea interface, the fluxes are radiative and turbulent fluxes. The turbulent fluxes of sensible and latent heat typically transfer heat from the sea to the air. The sensible heat flux is caused by the difference of temperature between the sea and the air, whereas the latent heat flux is caused by the evaporation of the water. The momentum flux is the downward transfer of horizontal momentum caused by the drag of the sea surface on the wind (Taylor, 2002). This transfer causes the waves (and the wave growth), as well as the wind-driven currents.

In the present work, we focus only on the momentum flux, i.e. the wind stress. The wind stress represents the turbulence in the surface layer, and is then also called turbulent stress. It is considered as

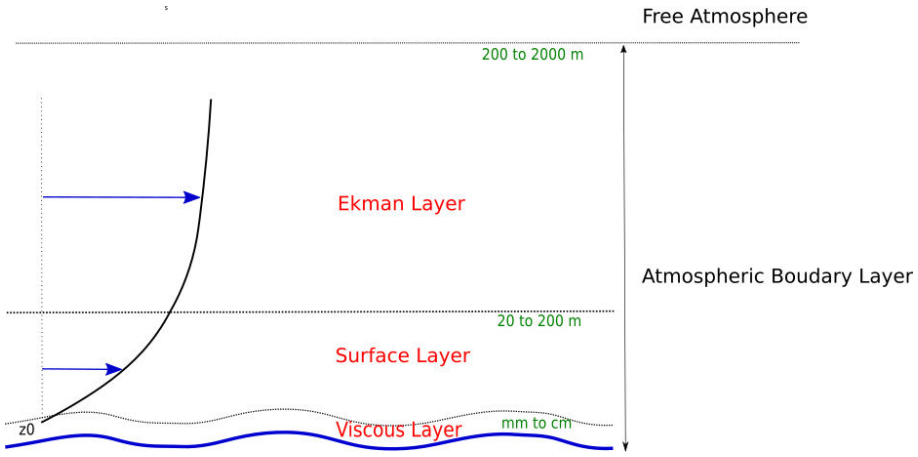

Figure 2.1 – Schematic representation of the Atmospheric Boundary Layer (ABL)

independent of height in the surface boundary layer. The wind stress τ is proportional to the square of the friction velocity u_* , which corresponds to the average of the wind fluctuations

$$\tau = -\rho_a \overline{u'w'} = \rho_a u_*^2 \tag{2.1}$$

where ρ_a is the air density, u', w' are the horizontal and vertical wind turbulent fluctuations.

2.3 Wind profile

2.3.1 In neutral conditions

In the case of homogeneous stratification (i.e. neutral conditions), wind measurements at different heights follow a logarithmic law. The wind at z height is expressed as

$$u(z) = \frac{u_*}{\kappa} log\left(\frac{z}{z_0}\right) \tag{2.2}$$

where u_* is the friction velocity, κ is the von Kármán's constant and z_0 the roughness length.

z_0 is a key parameter. It represents the surface roughness, and influences directly the wind profile. When the surface becomes rougher, the winds slow down. z_0 represents theoretically the distance from the "wall" (here, the height above the ocean) where the wind becomes zero. Note that this essential parameter in the surface layer theory is difficult to apprehend for different reasons: (1) z_0 is not a measurable parameter (but it can be estimated from wind measurements at at least two heights, with Eq. 2.2), (2) z_0 has a typical value of a few millimeters, which does not correspond to any height of geometric elements (for example, height of the surface ripples).

2.3.2 Non neutral conditions

In the case of inhomogeneous stratification, the wind profile differs from the logarithmic law. Monin and Obukhov (1954) introduced the effect of the thermal stratification on the wind profile through a stability correction function ψ_m, which depends of only one parameter $\xi = z/L$, where L the Obukhov length. This last parameter L was introduced by Obukhov (1946), in a paper he finished in fact in 1943 (when he was 25), but which was not published before 1946 because of World War II (Businger and

Yaglom, 1971). The Obukhov length L (often also called abusively Monin-Obukhov length) is expressed as

$$L = \frac{-u_*^3 T_v}{\kappa g Q_{v0}} \tag{2.3}$$

where T_v is a reference virtual temperature, g the mean gravitational acceleration and Q_{v0} a kinematic virtual temperature flux at the surface.

The Obukhov dimensionless stability parameter $\xi = z/L$ expresses the stability of the atmosphere: it is positive for stable stratification, negative for unstable stratification, and close to zero for neutral stratification. Following Obukhov (1946) and Monin and Obukhov (1954), the wind at z height is expressed as

$$u(z) = \frac{u_*}{\kappa}\left[log\left(\frac{z}{z_0}\right) - \psi_m\left(\frac{z}{L}\right)\right]. \tag{2.4}$$

Stability correction functions ψ_m are determined empirically from field measurements. From 1968 Kansas field experiment, Businger et al. (1971) suggested the following relationships

$$\psi_m = \begin{cases} 1 + 4.7\xi & \text{if stable} & \xi > 0, \\ 1 + 3\xi + 10.2\xi^2 & \text{near neutral stability} & \xi = 0, \\ (1 - 15\xi)^{-1/4} & \text{if unstable} & \xi < 0. \end{cases} \tag{2.5}$$

Other experiments yielded different expressions, as for example Dyer (1974)

$$\psi_m = \begin{cases} 1 + 5\xi & \text{if stable} & \xi > 0, \\ (1 - 16\xi)^{-1/4} & \text{if unstable} & \xi < 0. \end{cases} \tag{2.6}$$

There are many other published stability functions, e.g. Benoit (1977), Holtslag et al. (1990) or Beljaars (1995). Note that this last reference is the one of COARE 3.0 bulk flux algorithm (Fairall et al., 2003), widely used in the scientific community, and considered as a reference.

For strong winds, stability effect can be significant (around 10%, see Figure 2.2). However, this effect is not always taken into account. For example, the winds estimated from remote-sensing data are neutral winds, whereas the ones from the buoys are real winds (i.e. taking into account stratification information).

2.4 Parameterizations

2.4.1 Bulk formulae

The turbulent fluxes are represented by bulk formulae, as the space and time resolution of the atmospheric models do not allow an explicit representation of the turbulent fluctuations. These formulae assume that the stress and the wind are aligned and relate the stress and the mean wind speed at a given height, generally 10 m above sea surface, through a drag coefficient C_d

$$\tau = \rho_a C_d U_{10}^2 \tag{2.7}$$

where C_d and U_{10} are the drag coefficient and the wind speed at 10 m above the surface, respectively. In neutral conditions, the drag coefficient can be expressed as

$$C_d = \frac{\kappa^2}{\left[log\left(\frac{10}{z_0}\right)\right]^2} \tag{2.8}$$

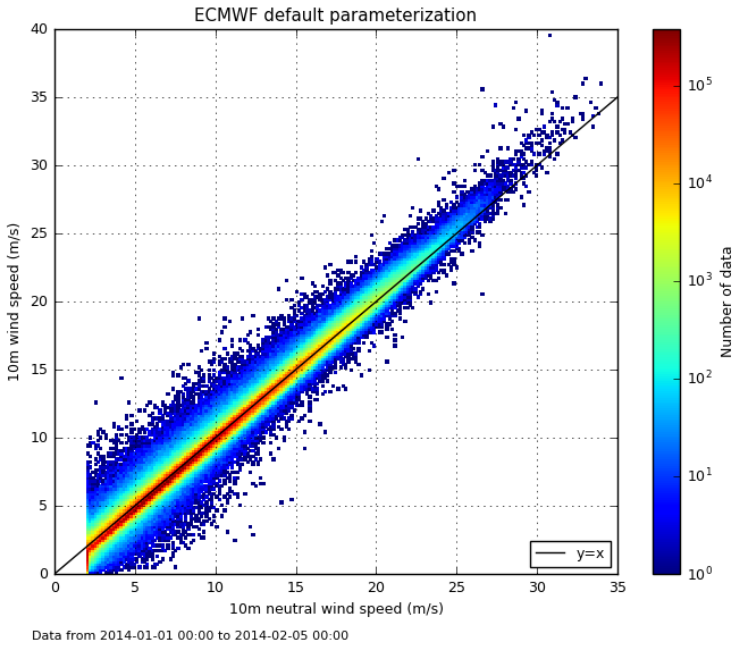

Figure 2.2 – Correlation between 10 m wind speed and 10 m neutral wind speed. Data come from a month of simulation of ECMWF model (CY41R1 cycle with default ECMWF parameterization).

where z_0 is the roughness length, and κ is von Kármán's constant (0.4). Eqs (2.7) and (2.8) link the roughness length to the wind stress and to the wind profile. The roughness length is the sum of two contributions

$$z_0 = z_{0visc} + z_{0wave}. \tag{2.9}$$

At very light winds, the roughness z_{0visc} is known to depend on the viscous properties of the flow

$$z_{0visc} = \frac{0.11\nu}{u_*} \tag{2.10}$$

where ν is the kinematic viscosity. At stronger winds, the roughness z_{0wave} is associated to an overall form drag of the wave field.

2.4.2 Wave effect

Wave effect on wind stress was demonstrated very early in the 50's. Van Dorn (1953) computed the wind stress over an artificial pond, through the measurement of its surface slope (which is proportional to the surface stress). The pond was 240 m long, 60 m large, and 2 m depth. Van Dorn (1953) measured the slope before and after the application of a detergent, which eliminates all the waves (see Figure 2.3, this effect of detergent on waves was discovered by Keulegan (1951)). The results show that above a certain value of wind U_c, the presence of waves increases significantly the stress (Figure 2.4). The stress is the combination of two effects: the "friction" drag and the "form" drag due to the waves, which occurs when the sea surface becomes rougher. Empirical adjustement led to the following stress formulation

$$\tau = \begin{cases} \rho\alpha^2 U_{10}^2 & \text{with a smooth surface} \quad U_{10} < U_c, \\ \rho\alpha^2 U_{10}^2 + \rho\beta^2 (U_{10} - U_c)^2 & \text{with a rough surface} \quad U_{10} > U_c. \end{cases} \tag{2.11}$$

The main interest of this (old) paper is to show clearly the wave influence on the wind stress and to give a first formulation of its effect. Waves tend to increase the turbulence in the surface layer, then the

wind stress increases, and as a consequence, the wind decreases. Note that this wind-only dependent formula takes into account the waves effect through the second term in U_{10}^2, even if no wave parameter appears explicitely.

Even if the wave effect on wind stress was demonstrated very early in the 50's, the question of how to take it into account is still in debate in the scientific community. Next section presents different parameterizations, with different ways to represent the sea state.

2.4.3 Position of the problem

Parameterizations are necessary because temporal and spatial resolution of models does not allow the direct computation of the wind fluctuations. Formulations for the roughness length or the drag coefficient are sufficient, as they are linked to the wind stress through Eqs (2.7) and (2.8).

The basic idea is to compute relationships between the drag (or roughness length) and the parameters that are usually known (e.g. 10 m wind speed). Empirical relationships are generally computed from observations, and rarely deduced from a physical approach. Many experiments have been devoted to measurements of air-sea fluxes. Edson et al. (2013) collected momentum fluxes from four of them. Data show that the drag increases with the wind speed, but also that for a given wind, data are scattered with a large variability (e.g. from 1 to 3 at 15 m/s, see Figure 2.5). The challenge is to find the parameter(s) that may explain these discrepancies. Despite more than 60 years of research, there is still no consensus among the scientific community on what should be this (these) parameter(s). Different approaches coexist with various parameters to represent the sea state, for instance: wave age (e.g. Oost et al., 2002; Drennan et al., 2003), wave slope (e.g. Kraus and Businger, 1994; Edson et al., 2013), wave-induced stress (e.g. Janssen, 1991; Ardhuin et al., 2010) or wave breaking (e.g. Amorocho and DeVries, 1980; Kudryavtsev et al., 2014).

Here, we focus on the waves, which appear to be a first order parameter. However, other physical processes (than the wind and the waves) may explain this variability as precipitations, surface currents, spray or foam at strong winds (Soloviev et al., 2014; Andreas and Emanuel, 2001), but also surface films, which reduce the wind stress by supressing the waves (Wei and Wu, 1992). These processes (and probably others that are missing) are not taken into account in the following parameterizations. Lastly, uncertainties in observations may probably also explain a part of the data variability.

Concerning the relative wind speed, note that Eq. 2.7 should be written as

$$\tau = \rho_a C_d (U_{10} - U_S)^2 \tag{2.12}$$

where U_S is the ocean surface current. This current is generally considered as negligible with respect to the wind speed U_{10}. However, it should be taken into account in areas where it is significant (e.g. strong tide range areas). Different studies show that in a coupled ocean-atmosphere model, as the atmosphere adjusts with the surface current, the effect of the surface current is too strong when formulated following Eq. 2.12. Some authors suggest to introduce a reduction factor of the surface currents r, leading to the following formula

$$\tau = \rho_a C_d (U_{10} - rU_S)^2. \tag{2.13}$$

In ECMWF atmosphere model, this coefficient equals 0.5.

2.4.4 Charnock's formulation

In the 50's, Charnock (1955) measured the vertical distribution of the horizontal mean wind in the lowest 8 m over a reservoir (1.6kmx1km). Profiles are close to logarithmic (see Eq. 2.2). Plotting their

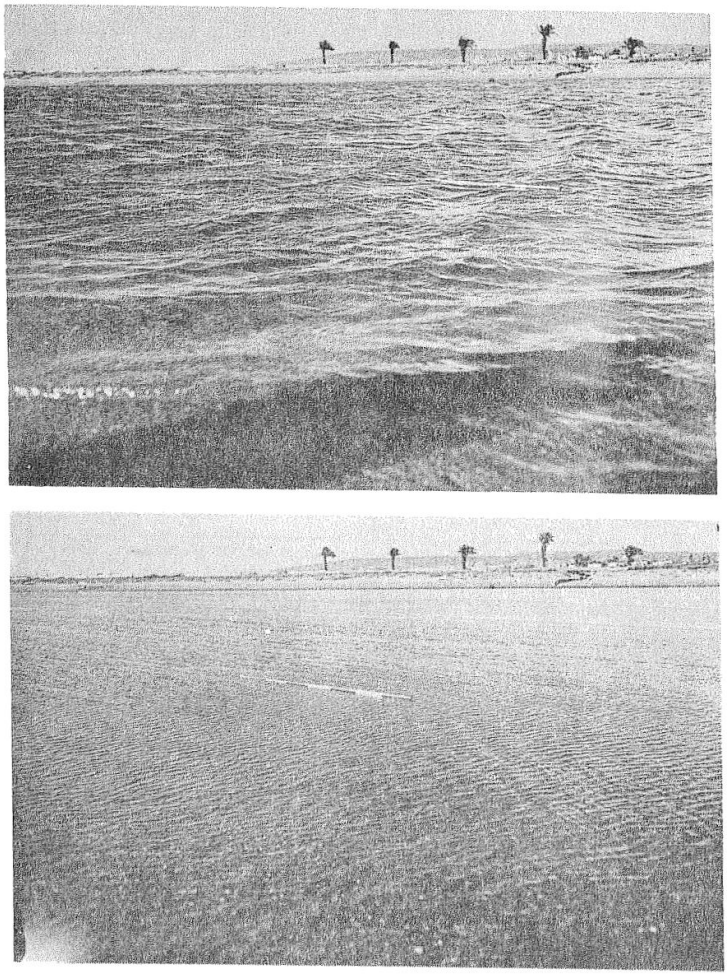

Figure 2.3 – The artificial pond before (top) and after (bottom) the addition of a detergent to the surface, wind speed is 17 m/s. From Van Dorn (1953).

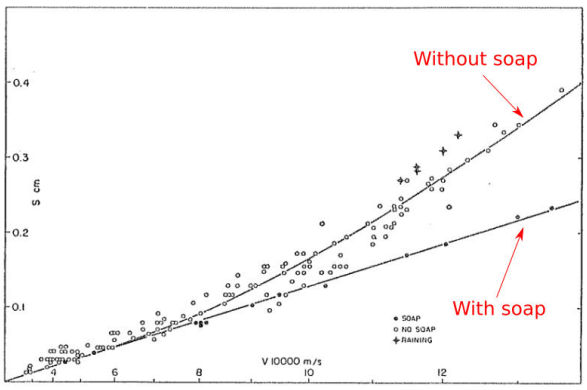

Figure 2.4 – Setup measurements (proportional to wind stress) in function of wind speed, without soap (circles, upper curve) or with soap (dots, lower curve). From Van Dorn (1953).

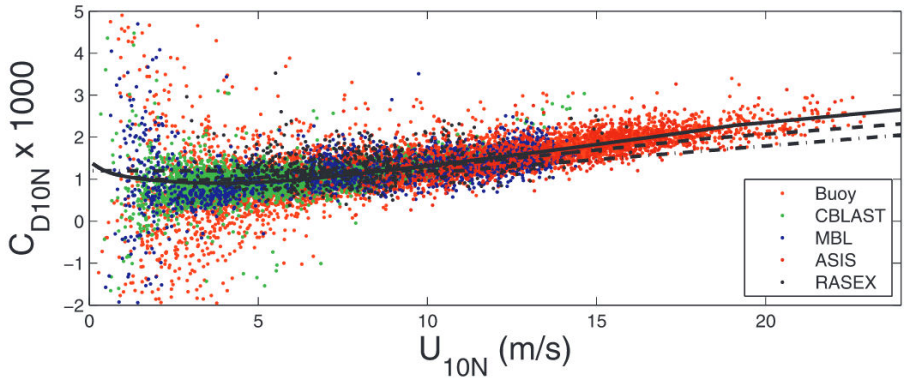

Figure 2.5 – Direct estimates of the surface stress vs relative wind speed adjusted to 10 m and neutral stability from four field programs. The dashed line represents the original COARE 3.0 bulk algorithm and the solid black line is the modified COARE 3.5 algorithm. From Edson et al. (2013)

slope u_*/κ in relation to their interceipt z_0, Charnock found the following relationship

$$z_{0wave} = \alpha \frac{u_*^2}{g} \tag{2.14}$$

where α is known as the Charnock's parameter. This parameter corresponds to an adimensional roughness length. It increases when the sea is rougher. However, in models, α can be considered as constant, or related explicitly to the wind-speed (e.g. Edson et al., 2013) or the wave parameters, as for example the wave age (e.g. Oost et al., 2002; Drennan et al., 2003). When considered as constant, the standard value is of 0.0185 (Wu, 1982), but it can vary from 0.011 (Fairall et al., 1996) to 0.032 for rougher sea (Mastenbroek et al., 1993). Measurements lead to different values depending on environmental conditions, e.g. 0.012 in the North Sea in Peña and Gryning (2008), 0.028 for wind speed ranging from 20 to 25 m/s in Edson et al. (2013).

Note that other parameterizations similar to Charnock's - with roughness length depending on friction velocity - were developped. For example, Garfinkel et al. (2011) expresses roughness length as

$$z_0 = \frac{A_1}{u_*} + A_2 + A_3 u_* + A_4 u_*^2 + A_5 u_*^3 \tag{2.15}$$

where the first term corresponds to z_{0visc} (see Eq. 2.10) and A_i are tunable parameters used to match the air-sea roughness scheme to observations. In Garfinkel et al. (2011), these parameters are tuned between an old and new version, in order to better match with recent observations of air-sea exchange. Finally, comparisons show that the old parameters are very close to a Charnock's formulation with $\alpha = 0.011$, whereas the new ones are close to a Charnock's formulation with $\alpha = 0.032$ (Figure 2.6).

2.4.5 Various formulations

The relationships are formulations of:

1. the drag coefficient C_d; in this case, the wind stress is deduced from 2.7;
2. the roughness length z_0; in this case, the drag coefficient is deduced from 2.8 and the wind stress from 2.7;
3. the Charnock parameter α; in this case, the roughness length is deduced from 2.14, 2.10, 2.9, and the drag coefficient and wind stress respectively from 2.8 and 2.7.

Formulations are mainly empirically determined from ocean field experiments.

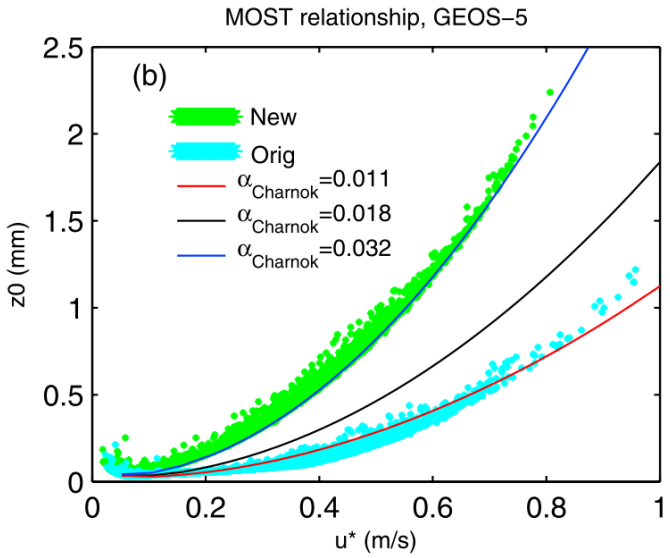

Figure 2.6 – Relationship between friction velocity (u_*) and roughness length (z_0) over all ocean grid points averaged over one day of GEOS5 model output. Isolines of $z_0 = \alpha u_*^2/g$ (Charnock, 1955) but with different values of the Charnok parameter α are included for comparison. From Garfinkel et al. (2011).

Wind speed-dependent formulations

Many drag formulations depend only on the wind speed. Table A.1 and Figure A.1 in Appendix A give some examples. Some of them are still in use in ocean models, as Hellerman and Rosenstein (1983) for ocean model TUGO (Lyard et al., 2006). Note that only Hellerman and Rosenstein (1983) parameterization takes into account the stability effect through the ΔT parameter (air temperature minus sea temperature). Relationships were also suggested between roughness length or Charnock parameter and the wind speed. Moon et al. (2007) proposed a parameterization of the roughness length based on a coupled wave-wind model simulations. Edson et al. (2013) proposed a linear dependence of the Charnock parameter to the wind speed, up to 19 m/s. Above this value and up to 25 m/s, the Charnock parameter deduced from the observations seems to level off at a constant value around 0.028.

However, Figure 2.5 shows that for a given wind speed, drag values are scattered. This suggests that drag coefficient is probably not only wind-speed dependent. We may expect a dependency on the development of the sea.

Wave age-dependent formulation

Many authors investigated the dependence to the wave age (Kitaigorodskii, 1973; Donelan, 1982; Geernaert et al., 1986; Nordeng, 1991; Komen et al., 1998; Oost et al., 2002; Drennan et al., 2003). Table A.2 in Appendix A give some examples. The wave age is expressed as

$$\xi = \frac{C_p}{u_*} \tag{2.16}$$

where C_p is the phase velocity at the peak of the wave spectrum. Depending on authors, it is sometimes expressed as a function of the wind speed at 10 m

$$\xi_{10} = \frac{C_p}{U_{10}}. \tag{2.17}$$

The wave age represents the degree of developement of the sea. Low wave age corresponds to waves moving more slowly than the wind, i.e. young sea with steep waves. Higher wave age corresponds to old sea with smoother waves, moving faster than the wind.

Considerations based on dimensional analysis led the authors to propose expressions of the form $\alpha = a\xi^b$, where a and b are determined from in situ measurements. The parameterization by Oost et al. (2002) (used in this study, see Table 3.2) is based on data from a research platform in the North Sea, with wind speed ranging from 6 to 18 m/s

$$\alpha = 50\xi^{-2.5}. \tag{2.18}$$

Drennan et al. (2003) suggested another expression, based on data from field campaigns in the Mediterranean Sea, with winds also lower than 20 m/s:

$$\alpha = 1.7\xi^{-1.7}. \tag{2.19}$$

The differences between these two expressions underline the possible influence of the dataset in each parameterization. Moreover, there are still discussions - and no consensus - on these results, as the strong correlations obtained in the observations could be mainly due to self-correlation, u_* being part of the two parameters α and ξ (Andreas, 2009).

Wave-induced stress-dependent formulation

Other authors consider that the roughness length depends on the fraction of the stress carried by the waves. Janssen (1991) parametrized the quasi-linear wave growth effect as an effective larger roughness length z_{0wave}, expressed as a function of the wave-induced stress τ_w

$$z_{0wave} = \frac{z_1}{\sqrt{1 - \frac{\tau_w}{\tau}}}. \tag{2.20}$$

The reference roughness length z_1 follows the Charnock's relation

$$z_1 = \alpha_1 \frac{u_*^2}{g} \tag{2.21}$$

with $\alpha_1 = 0.006$. This value of α_1 has been fixed, so that for old sea, the associated roughness z_{0wave} (Eq. 2.20) corresponds to the standard value of Charnock parameter 0.0185 (Wu, 1982). The wave-induced stress τ_w is the momentum flux transferred from the atmosphere to the waves. It can be related to the wind-wave growth parameter β and the directional wave spectrum $E(f,\theta)$

$$\tau_w = g \int_0^\infty k \int_0^{2\pi} \beta(f,\theta) E(f,\theta)/(2\pi f) df d\theta \tag{2.22}$$

where k is the wave number, θ the direction and f the relative wave frequency (Janssen, 2004). The wave-growth parameter is expressed as $\beta = (\beta_m/\kappa^2)\mu ln^4(\mu), \mu \leqslant 1$, where β_m is a constant (1.2), and μ the dimensionless critical height (ECMWF, 2015b).

The stress τ_w , and thus the roughness z_{0wave}, is highly sensitive to the high-frequency content of the wave spectrum, which is in itself highly sensitive to the choice of wave generation and dissipation parameterizations (e.g. Rascle and Ardhuin, 2013). In ECWAM, the wave spectrum $E(f,\theta)$ high-frequency tail is diagnostically forced to $E(f,\theta)(f_t/f)^5$ for $f > f_t$ with $f_t = 2.5 f_{windsea}$ and $f_{windsea}$ the mean frequency of the modelled wind sea (part of the full spectrum corresponding to the wind sea only, and

defined where the input source term S in is positive).

Ardhuin et al. (2010) parameterization is close to Janssen's. It also uses Eqs (2.20) (2.21) (2.22) but with β given by Ardhuin et al. (2010) and $E(f,\theta)$ influenced by a different dissipation term.

The impact of Janssen's parameterization on surges was studied by Mastenbroek et al. (1993). A coupled wave and storm surge model was tested for three storm periods. The authors showed that a wind-only dependent stress (Smith and Banke, 1975) underestimated the surges by 20%, whereas the wave-dependent stress (Janssen, 1991) reproduced the surges within a few percent. The main result of the paper is that Janssen's theory is consistent with the storm surges elevation. This improvement can also be reproduced with Charnock's formulation increasing the constant Charnock parameter up to $\alpha = 0.032$. However, the Charnock parameter is not universal, and would have to be tuned depending on the sites and the conditions.

Nevertheless, these good results must be clarified. Moon et al. (2009) showed that Mastenbroek et al. (1993) obtained good simulated surges with overestimated drag, by compensating surge error due to a too coarse grid.

Other formulations

Some authors expressed the drag as dependent on the wave slope (Kraus and Businger, 1994). Other authors expressed it in function of the wave breaking. Amorocho and DeVries (1980) showed that three regions exist in the development of the wind stress:

1. a lower region ($U_{10} < 7$ m/s), where waves are not yet breaking; in this area, C_d is approximatively constant (0.00104);
2. an intermediate region ($7 < U_{10} < 20$ m/s), from the onset of breakers until full breaker saturation; in this area, C_d increases nonlinearly with the wind speed;
3. a limiting region ($U_{10} > 20$ m/s), where full breaker saturation prevails; in this area, C_d tends again to a constant value (0.00254).

Amorocho and DeVries (1980) tried to introduce more physics in the parameterization, taking into account the effect of breaking waves. However, Smith (1980a) commented that the corresponding drag values were too high compared to recent observations, suggesting the revision of the empirical funtion proposed by Amorocho and DeVries (1980). More recently, Kudryavtsev et al. (2014) discussed the contribution of the breaking waves to the drag.

Chapter 3

Impact on the atmosphere

3.1 Introduction

This section presents the impact of the wind stress on the atmosphere. This work was published in Pineau-Guillou et al. (2018) (see section 3.8). Here, we present the scientific questions, the method to investigate these questions, the summary of the main results, and further investigations on the wind bias between the buoys and the platforms.

3.2 Scientific questions

Several studies suggest that large wave heights could be underestimated in the wave models (Rascle and Ardhuin, 2013; Hanafin et al., 2012; Stopa and Cheung, 2014) , as well as storm surges in the ocean models (Mastenbroek et al., 1993; Muller et al., 2014). This may come from (1) a possible underestimation of strong winds in some (or most) atmospheric models (2) an inappropriate parameterization of the wind stress, leading for strong winds to drag values significantly higher than estimations from in-situ measurements (Black et al., 2007; Edson et al., 2013; Powell et al., 2003; Holthuijsen et al., 2012) as well as laboratory tank measurements (Donelan et al., 2004; Jarosz et al., 2007; Takagaki et al., 2012). Note that (1) and (2) are probably not independent, as the underestimation of strong winds may come from an inappropriate parameterization of the wind stress.

The scientific questions we will investigate are:
— How strong are the biases for high wind speeds in atmospheric models?
— Can they be corrected by changing the C_d parameterization?
— What other physical processus - we have missed - could have a significant impact on the C_d?

3.3 Method

To answer to the first question (How strong are the biases for high wind speeds in atmospheric models?), we used the coupled wave-atmosphere model Integrated Forecasting System (IFS) from ECMWF. IFS is unique in coupling its atmospheric model and the wave model ECWAM operationally, thus providing a dynamic prediction of the drag coefficient as a function of the sea state. Thanks to a 3-year "Special Project" between the LOPS laboratory and ECMWF, we had the great opportunity to access to ECMWF's computing and archive facilities. We could acces directly to IFS sources, create branches, modify it, and run all the simulations on the Cray supercomputer, with a research priority queue.

To evaluate the biases for high wind speeds in atmospheric models, we simulated the case study of the two extratropical storms Kaat and Lilli which crossed the North Atlantic in January 2014. We

compared the simulated winds with observations from buoys, platforms and satellites (Figure 3.1). In-situ winds came from ECMWF (Figure 3.2). We selected data on the North East Atlantic area. We carried out a brief visual quality control on all the observations. This led to the invalidation of 7 platforms. We adjusted the wind data from measurement height (usually from 2 to 4 m for the buoys) to 10 m, based on a logarithmic law. The platforms were generally yet reduced to 10 m. We averaged multiple wind speed data coming from platforms, when they were located in the same grid cell of the IFS model. This leads to one averaged measurement per model grid cell, which is more consistent for comparison. Finally, 20 buoys and 59 platforms were available. Remote sensing winds came from different satellites. They are summarised in Table 3.1.

(a)  (b)  (c) 

Figure 3.1 – Wind observations come from (a) platforms, (b) buoys and (c) satellites

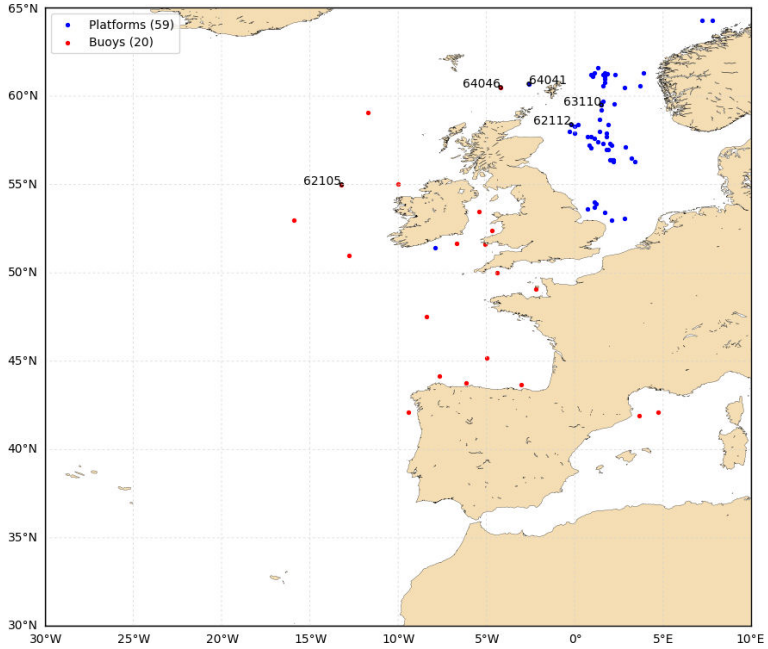

Figure 3.2 – In-situ data used in this study

To answer to the second question (Can the biases be corrected by changing the C_d parameterizations?), we tested five alternative wind stress parameterizations, including a newly developped one (Table 3.2). The objective is to attempt to reduce the discrepancies between the modelled and observed high winds.

Type of instrument	Instrument	Satellite	Data provider	**Name** (in this study)	Swath width (km)	Wind product sampling (km)
Scatterometer	ASCAT	MetOp-A/B	KNMI	**ASCAT-KNMI**	2*512.5	12.5
Scatterometer	ASCAT	MetOp-A	RSS	**ASCAT-RSS**	2*512.5	27
Radiometer	AMSR2	GCOM-W1	SOLab	**AMSR2**	1450	10
Radiometer	WindSat	Coriolis	RSS	**WindSat**	1000	25
Radiometer	MIRAS	SMOS	Ifremer	**SMOS**	600	15
Altimeter	Poséidon-3	JASON-2	NASA	**JASON-2**	-	6

Table 3.1 – Remote sensing wind products used in this study

Parameterization	References
[1] Coupled ECWAM/IFS with default ECMWF parameterization	Janssen (1991)
[2] Coupled ECWAM/IFS with WW3 physics (i.e. different wave dissipation and growth parameterizations)	Ardhuin et al. (2010) as implemented in ECWAM.
[3] Coupled ECWAM/IFS with wave age dependent parameterization	Oost et al. (2002)
[4] Coupled ECWAM/IFS with empirically-adjusted Charnock parameterization	This study
[5] Constant Charnock 0.018	

Table 3.2 – Wind stress parameterizations tested in this study.

3.4 Summary of the main results

Strong winds are biased in the atmospheric model

The first result is that moderate simulated winds (5-20 m/s) agree well with both in situ and satellite observations, whereas strong winds (above 20 m/s) are generally underestimated compared with observations; the negative bias can reach -7 m/s at 30 m/s (Figure 3.3).

Biases exist between observations

The second result is that biases exist between observations. We identified two groups of data. The first one, composed of buoys and ASCAT-KNMI, gives lower strong winds than the second one, which is composed of platforms and other remote-sensing data used in this study (AMSR2, ASCAT-RSS, WindSat, SMOS and JASON-2).

For the first group, ECMWF, ASCAT-KNMI and buoy winds all agree well, as indeed each of the three data source are mutually interdependent. ASCAT-KNMI retrievals strongly rely on ECMWF winds for calibration (Verspeek et al., 2012). Moreover, buoys are used to calibrate empirical scatterometer Geophysical Model Functions at KNMI (Zeng and Brown, 1998). Buoys are also considered as a reference for ECMWF model validation.

For the second group, AMSR2, WindSat and SMOS products are all consistent, because of shared sensitivities of the foam-induced brightness temperature to wind speed for these passive microwave wind sensors, but also of dedicated efforts to calibrate and align high wind speeds. Strong correlations between platforms and AMSR2 have already been reported (Zabolotskikh et al., 2014). While there is still no full consensus on calibration between data providers, the overall agreement between these remote-sensing datasets is encouraging.

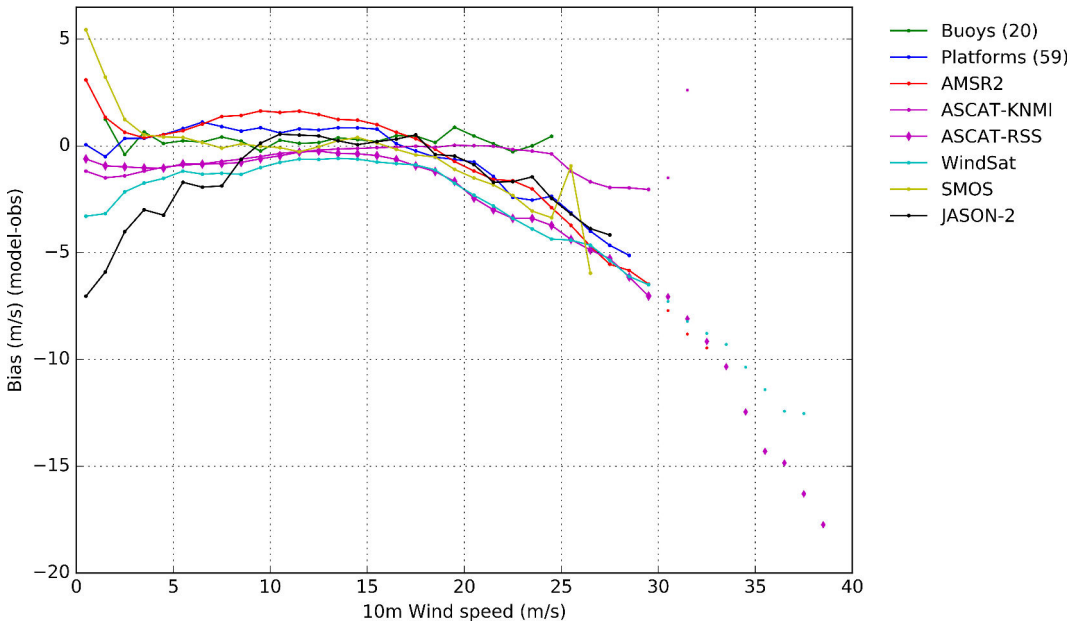

Figure 3.3 – Wind biases between ECMWF (CY41R1) model and observations (buoys, platforms, and satellite data), computed from 23 to 27 January 2014 on the northeast Atlantic. Beyond 30 m/s, values are plotted as points, due to large uncertainties in observations.

Finally, it is difficult to conclude which dataset should be used as a reference, but buoys and ASCAT-KNMI winds are likely to be underestimated. Note, the role of the wind datasets in building the Geophysical Model Functions (GMF) is essential and different datasets lead to different GMFs. As a consequence, ASCAT-KNMI strong winds show a systematic negative bias with respect to ASCAT-RSS ones.

New parameterization reduces the bias

Lastly, the third result is that a newly empirically adjusted Charnock parameterization would lead to higher winds than the default ECMWF ones. Yet, common wave-age-dependent parameterization gives larger drag coefficients than measurements and lower winds and is not appropriate for coupling.

But the bias is still significant...

The new parameterization reduces the bias between the model and the observations, because the drag was reduced by construction, in order to be closer to the observations (Figure 3.4). Note that the model improvement is not due to a better understanding of the physics. Drag values are too high with the default parameterization probably because there is too much energy in the tail of the wave spectrum. The next step is to better model the high frequency of the wave spectrum, as well as the wave growth parameter.

Even with drag values closer to the observations, the simulated winds are still quite far from observed ones. The new parameterization reduces the bias around 2 m/s at 30 m/s, but there is still a bias around 5 m/s. This raises the question of possible other physical processes we have missed (see section 3.6).

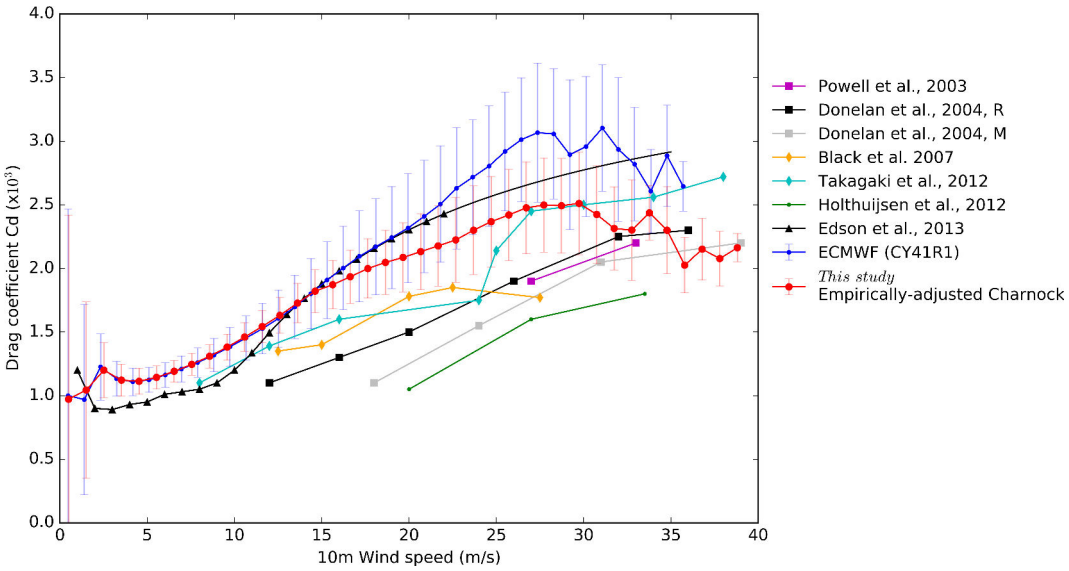

Figure 3.4 – Comparison of drag coefficient for ECMWF (CY41R1) parameterization, empirically adjusted Charnock parameterization and observations (Donelan et al., 2004). 'R' or 'M' corresponds to different measurement techniques, 'Reynolds' or 'Momentum Budget'. Error bars correspond to one standard deviation.

3.5 Further investigations on the bias between buoys and platforms

Figure 3.3 shows that platform strong winds are higher than buoys, around 3 m/s at 25 m/s. This bias could be due to (1) underestimation of buoy winds or/and (2) uncertainties introduced reducing winds from 60-150 m to 10 m for platform winds. Concerning the first point (1), different authors mention a possible underestimation of high winds measured by buoys (Zeng and Brown, 1998; Taylor et al., 1999; Zabolotskikh et al., 2014). This could be due to the sea state, the buoy motion and the wave sheltering effects. Zabolotskikh et al. (2014) mention that buoy reports generally do not contain wind speed exceeding storm-force (25 m/s) even for the areas and seasons of frequent hurricane and extratropical cyclone passing (National Data Buoy Center network). Concerning the second point (2), buoys measure winds at 2-4 m in height, whereas the height of the sensors on platforms is typically 60-150 m. Uncertainties are probably introduced when reducing platforms winds from around 100 m to 10 m.

3.5.1 Analysis of the 20-year wind database

We analysed the 20-year database obtained from ECMWF through the Global Telecommunication System (GTS). These data cover the period 1994-2015, and include 20 buoys and 59 platforms over the North East Atlantic (Figure 3.2). Winds were reduced to 10 m using a logarithmic law (see 3.5.3).

Comparison of buoy and platform maximum from the 20-year database

The maximum winds for the buoys and platforms are generally between 25 m/s and 35 m/s (Figure 3.5). There is no visual evidence of differences between buoys and platforms maxima. Winds higher than 35 m/s occured at buoy 62105 and platforms 62112 and 63110 (see Figure 3.2 for location).

Buoy 62105, also called K4 buoy, is located at the west of Northern Ireland, far from the coast (Figure 3.2), and maintained by the UK Met Office. The height of the sensor is 3 m. Data winds at this buoy cover the period 1994-2015. The maximum reached 38.1 m/s the 11^{th} of January 2005 (Figure 3.6 (a)). This corresponds to the severe Atlantic windstorm Gero, which swept across Northern Ireland and Northwest

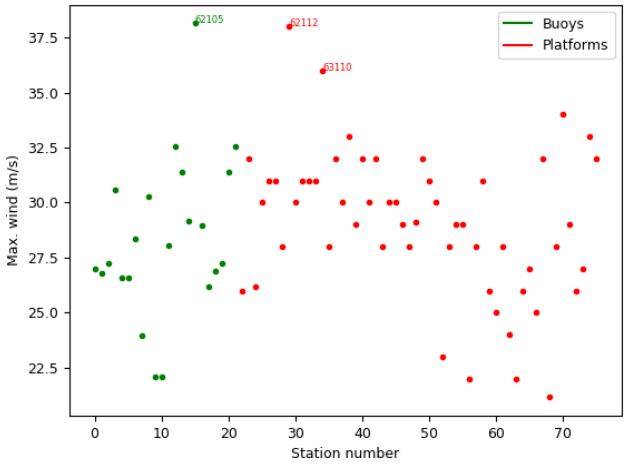

Figure 3.5 – Maximum winds at buoys and platforms from the 20-year database

Scotland on the evening of the 11^{th} and early morning of the 12^{th}. Wind speeds of 60 m/s (equivalent to a weak Category 4 hurricane) were recorded on North Rona Island, in the North of Scotland. We compared buoy winds with ECMWF operational analyses and forecasts. For comparison, we choosed the nearest point on the 0.5 degree model grid. Figure 3.6 (a) shows that the buoy and simulated winds are consistent up to 30 m/s, suggesting the capability of buoys to measure high winds up to 30-40 m/s. The wind peak is underestimated by the model, with a negative bias around 8 m/s at 38 m/s, consistent (but smaller) with the bias we found between the model and the radiometers. This is probably partly due to model temporal resolution, which is only 3 hours, whereas buoy temporal resolution is 1 hour. Moreover, model spatial resolution is only of 0.5 degree in 2005.

Oil platforms 62112 (Claymore AWS) and 63110 (Beryl A AWS) are located in the North Sea (see Figure 3.2), and operated by private companies. The winds were yet reduced to 10 m. Data are respectively available over the period 1994-2015, and 2006-2015. Winds reached 38.0 m/s the 2^{nd} and the 6^{th} of January 2000 at platform 62112 (Figures 3.6 (b) and (c)), and 36 m/s the 14^{th} of February 2011 at platform 63110 (3.6 (d)). No severe storms were found to correspond to these dates. Comparison between platform and ECMWF winds shows clearly that a bias exist between the platform and ECMWF winds, and platform winds seem to be overestimated. This could be due to structure effect, that could locally accelerate the winds. However, the problem of flow distorsion on platforms is complex. Stoffelen (2018) mention that measuring representative winds on a platform is quite challenging due to wind flow distortions by the platform, whereas Hasager et al. (2013) found that at 100 m height wind observations by the lidars deployed mainly on offshore platforms in the North Sea were not significantly influenced by flow distortion. Platform 63110 is integrated in National Buoy Data Center (NDBC) network, but with the mention that data from this station are not quality controlled by NDBC. Platform 62112 is not integrated in NDBC network. These results suggest that platform data are probably not as well quality controlled as buoys, and these data should be considered with care.

Comparison of buoy and platform PDF from the 20-year database

We computed the PDF (Probability Density Function) of all the buoys and platforms over the North Atlantic during the commun period 1994-2015 (Figure 3.7 (a)). The PDF function is higher for platforms than buoys, at strong winds. This seems to confirm a possible underestimation of buoy high winds. However, the geographical repartition of instruments is not uniform: Figure 3.2 shows that the platforms are mainly located in the North Sea, whereas the buoys are mainly located in the North East Atlantic. Figure

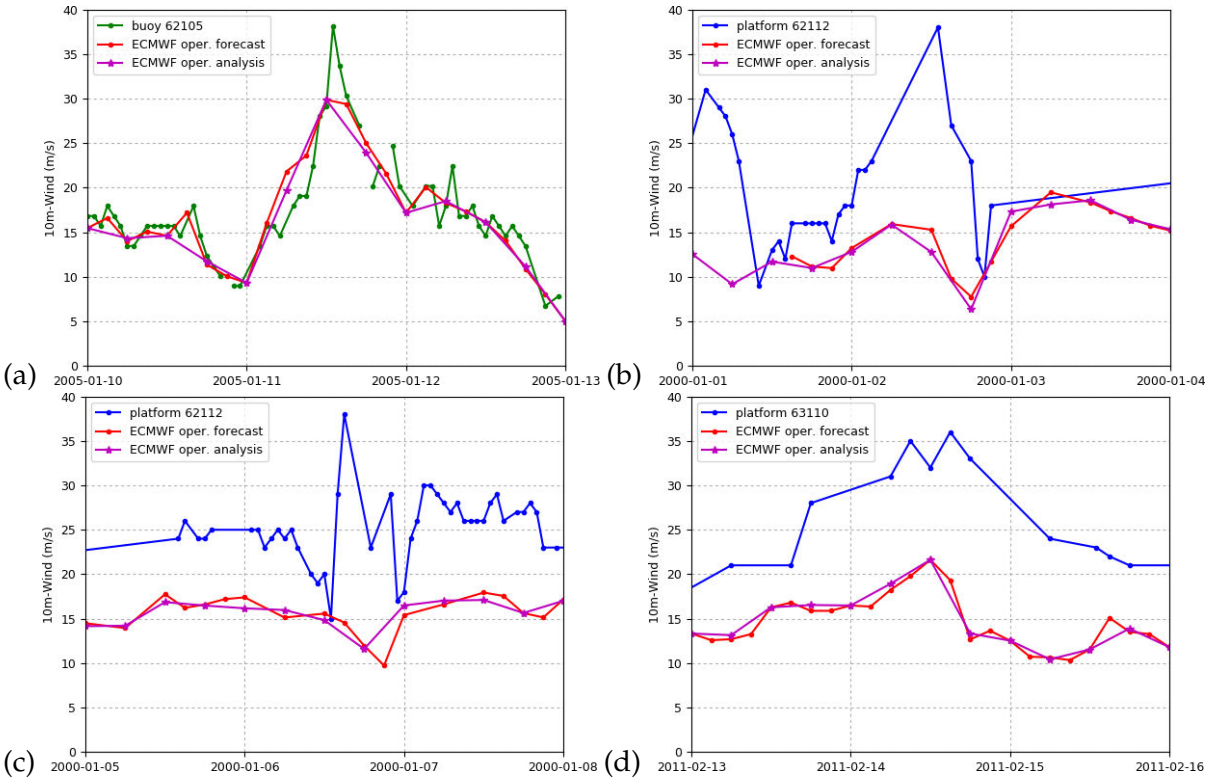

Figure 3.6 – Winds at buoy 62105 from 10th to 12th January 2005 (a) at platform 62112 from 1st to 3rd January 2014 (b) and from 5th to 7th January 2014 (c) and at platform 63110 from 13th to 15th February 2011 (d)

3.8 shows that the probability to have wind higher than 20 m/s varies a lot depending on the location, and is probably not the same for the buoys and the platforms. As a consequence, it is difficult to conclude from Figure 3.7 (a), that buoy winds are underestimated.

To avoid the influence of the location, we compared the PDF of the closest platform and buoy (see Figure 3.2, buoy 64046 and platform 64041 at the North of Scotland). Buoy data were from 1999 to 2015 whereas platform data from 2011 to 2015. We computed the PDF over the common period 2011-2015. Figure 3.7 (b) shows that the two PDF are very similar, and we can not conclude on a possible underestimation of buoy winds compared to platform winds.

3.5.2 Comparison of platform and model winds at the height of the sensor

The height of the sensors on platforms is typically 60-150 m, instead of 2-4 m for the buoys. The winds are reduced to standard 10 meters height, with a reduction law. To see if the bias between the buoys and the platform at 10 m may come from the reduction law, we compared the model and the platform winds directly at the height of the sensor. Wind data at 7 platforms were provided by Norwegian Met Office (data obtained thanks to O. Breivik, see Figure 3.9 (a) for the location).

The reduction law is a power law (Eq. 3.1) with $\alpha = 0.13$. We had not the height of the sensor, but from the wind data (at the height of the sensor and at 10 m) and Eq. 3.1, we could deduce it (see Table 3.3). It varies from 69 m for Ekofisk, up to 136 m for Sleipner.

At the height of the sensor, we made comparisons between platform winds and ECMWF winds

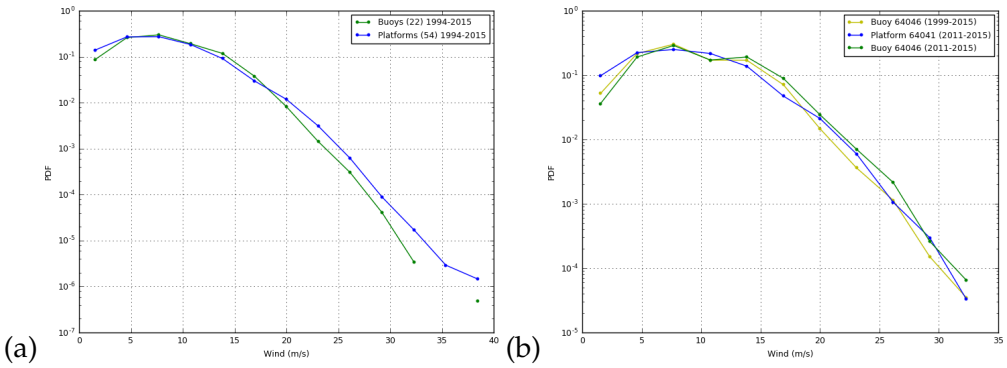

Figure 3.7 – Wind Probability Density Function (PDF) for (a) all the buoys and platforms over the North Atlantic (b) only the buoy 64046 and platform 64041

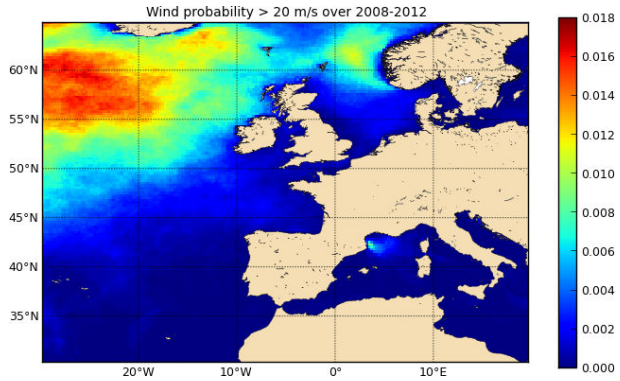

Figure 3.8 – Probability of occurence of wind greater than 20 m/s over 2008-2012 period (computed from ECMWF operational winds)

from our simulations with the default parameterization. Correlation shows clearly that ECMWF winds are underestimated at platform height (Figure 3.10). Biases were computed, with the same method as described in the paper (see section 3.8). Figure 3.11 shows that the 7 platforms are representative of all the platforms. Indeed, the bias at 10 m for these 7 platforms (blue curve), is very close to the one obtained for the 59 platforms (blue curve with dots). At the height of the platform, moderate simulated winds ($<$ 20 m/s) are underestimated around 1 m/s compared with platform winds. Strong simulated winds are also underestimated, with a bias around 4 m/s at 30 m/s. To conclude, the comparison at the height of the sensor leads also to negative biases, showing an underestimation comparable (but smaller) to 10 m winds.

3.5.3 Impact of the reduction law at FINO1 research platform

Here, we investigate the impact of different reduction laws. In the ECMWF in-situ database, data from platforms were generally yet reduced to 10 m by producers. The method depends on providers and it is quite difficult to have the information. For Norwegian Met Office, wind speed U_z at height z is reduced to 10 m using a wind power law, expressed as

$$U_{10} = U_z \left(\frac{10}{z} \right)^{\alpha} \tag{3.1}$$

where α=0.13 is an empirical determined coefficient. A coefficient $\alpha = 0.06$ is suggested in Furevik and Haakenstad (2012) in case of neutral stability. When the data in ECMWF database were at the height of the sensors (i.e. mainly for the buoys), we reduced at 10 m using a logarithmic law (2.2), expressed as

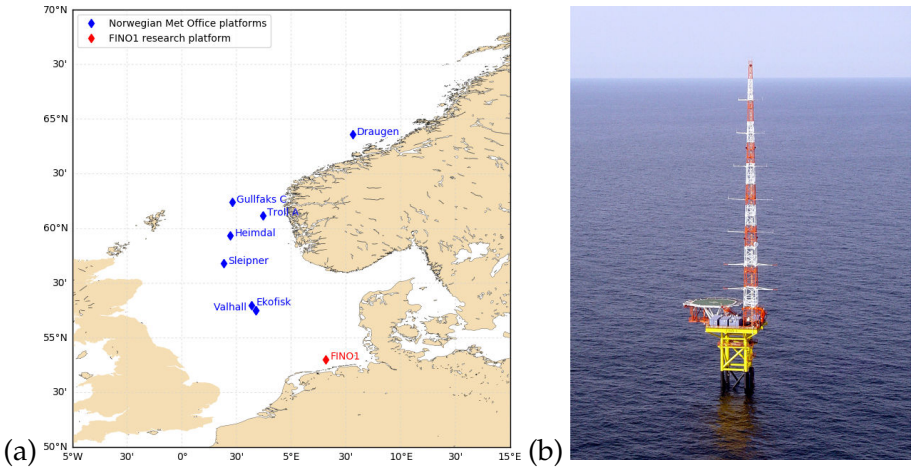

Figure 3.9 – (a) Location of platforms from Norwegian Met Office and FINO1 research platform (b) FINO1 research platform

Station name	Longitude	Latitude	Altitude
Draugen	7.800	64.300	78 m
Ekofisk	3.200	56.500	69 m
Gullfaks C	2.300	61.200	101 m
Heimdal	2.223	59.674	71 m
Sleipner	1.900	58.400	136 m
Troll A	3.700	60.600	94 m
Valhall	3.395	56.278	114 m

Table 3.3 – Heights of the sensor for the Norwegian Met Office platforms

$$U_{10} = U_z \frac{\log(\frac{10}{z_0})}{\log(\frac{z}{z_0})} \tag{3.2}$$

where U_z is the wind at the height z of the sensor, and z_0=0.152 mm. In this formulation, the effect of stability is not taken into account, as we did not have enough information to compute it.

We investigated the impact of these reduction laws (Eqs 3.1 and 3.2) from FINO1 platform data (Figure 3.9 (b)). FINO1 is one of the three research platforms of BSH (Federal Maritime and Hydrographic Agency of Germany) operated in the framework of FINO project, mainly dedicated to offshore wind turbines research. FINO1 measures winds at 33 m, and then every 10 meters from 40 to 100 m. We reduced winds observed at 100 m to 33 m using four different reduction laws: power law with α=0.06 and α=0.13 (Eq. 3.1), and logarithmic law with $z0$=0.152 mm (the value we used for the reduction) and $z0$=1 cm (Eq. 3.2). The typical roughness length over the ocean is around 0.1 mm, but when the sea becomes rougher it increases and can reach 1 or 2 cm (results from ECMWF simulations).

Correlations between observed and reduced winds at 33m, for the power law with α=0.13 (the one used by Norwegian Met Office) show a small underestimation of strong reduced winds (Figure 3.12). Biases for each law are shown on Figure 3.13. The bias increases with wind speed. The first result is that at 30 m/s, it varies between -1 to 2 m/s, depending of the reduction law. The second result is that the power law with α=0.13 tends to underestimate reduced wind speed, whereas the one with α=0.06 tends to overestimate it. 10 m platforms winds are then probably underestimated in our study, which can not explain the differences with buoys. However, it is very difficult to conclude, as we do not know exactly

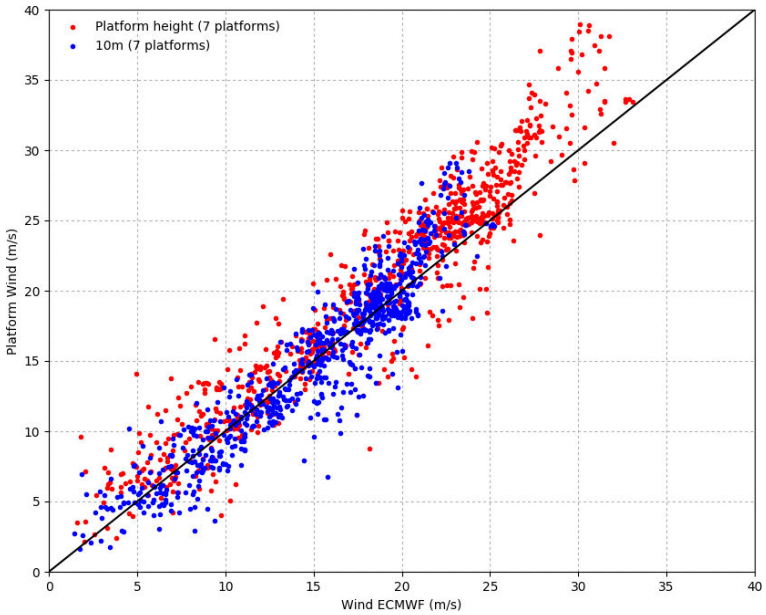

Figure 3.10 – Correlations between Norwegian Met Office platform winds and ECMWF simulated winds at 10 m (blue) and at platform height (red)

which reduction law is effectively used by the producers.

3.6 Other physical processes influencing drag

From a physical point of view, the drag is expected to combine various processes including air flow separation over breaking waves (Reul et al., 1999, 2008; Kudryavtsev et al., 2014), which is not represented in the quasi-linear model of Fabrikant (1976) and Janssen (1986) on which the ECMWF parameterization is based. Also, Janssen's parameterization (Eq. (2.20)) produces a ratio τ_w/τ that is often very close to 1 for young seas and is very sensitive to the high-frequency spectrum tail, a part of the spectrum that is very crudely represented in wave models today (Kudryavtsev et al., 2014; Peureux and Ardhuin, 2016).

At very high winds, other processes as spray and sea drops could influence the drag (Andreas, 2004; Makin, 2004; Kudryavtsev, 2006; Kudryavtsev and Makin, 2006; Soloviev et al., 2014). These processes were not taken into account in the present work.

3.7 Conclusions

We started this work because different atmospheric models had different biases on the wind speed in storm conditions, possibly due to different surface drag parameterizations. The objectives were (i) to evaluate ECMWF strong winds against observations, and (ii) to test how an alternative wind stress parameterization could lead to a more accurate model. During Kaat and Lilli storms (23-27 January 2014), we compared simulated winds from the ECMWF coupled wave-atmosphere model with in situ and satellite observations available in the North Atlantic. We then developed an empirically adjusted Charnock parameterization, to obtain winds closer to observations.

The first result is that moderate simulated winds (5-20 m/s) agree well with both in situ and satellite observations, whereas strong winds (above 20 m/s) are generally underestimated compared with ob-

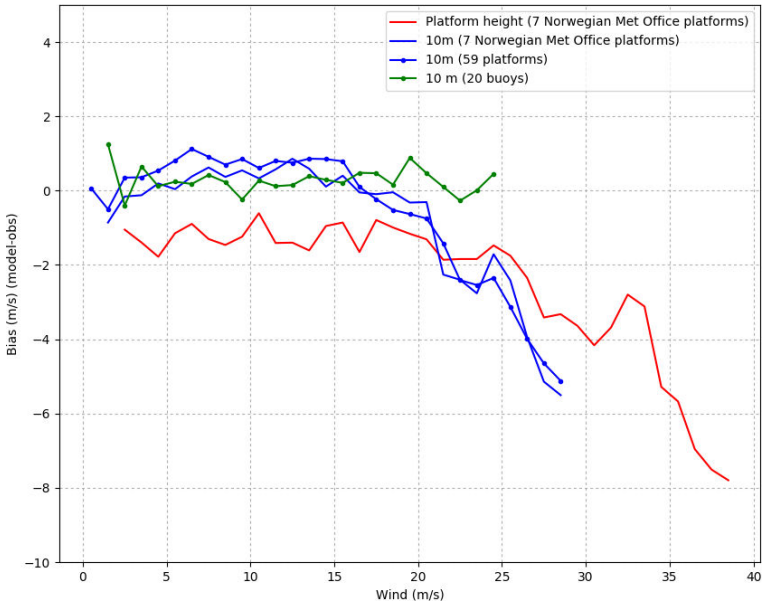

Figure 3.11 – Wind bias between ECMWF model and all the platforms, all the buoys, the 9 Norwegian Met Office platforms at 10m ant at platform height.

servations; the negative bias can reach -7 m/s at 30 m/s .

The second result is that biases exist between observations. We identified two groups of data. The first one, composed of buoys and ASCAT-KNMI, gives lower strong winds than the second one, which is composed of platforms and other remote-sensing data used in this study (AMSR2, ASCAT-RSS, WindSat, SMOS and JASON-2). It is difficult to conclude which dataset should be used as a reference, but buoys and ASCAT-KNMI winds are likely to be underestimated.

Lastly, the third result is that a newly empirically adjusted Charnock parameterization would lead to higher winds than the default ECMWF ones. Yet, common wave-age-dependent parameterization gives larger drag coefficients than measurements - and lower winds - and is not appropriate for coupling.

This study was then reproduced for three other storms in the northeast Atlantic: Alexandra (8 December 2014), Erich (10 March 2015) and Uwe (7 December 2015); results are similar and confirm these conclusions. Moreover, NASA/SMAP data were also exploited for Uwe, showing similar biases with the model consistent with WindSat and SMOS (Meissner et al., 2017).

The significant bias between buoy and platform strong winds suggests that in situ measurements should be handled with particular care. Despite more investigation, we were not able to explain the bias we found between the buoys and the plaforms. Finally, it is not clear what the ”surface wind reference” should be, and where the ”truth” lies.

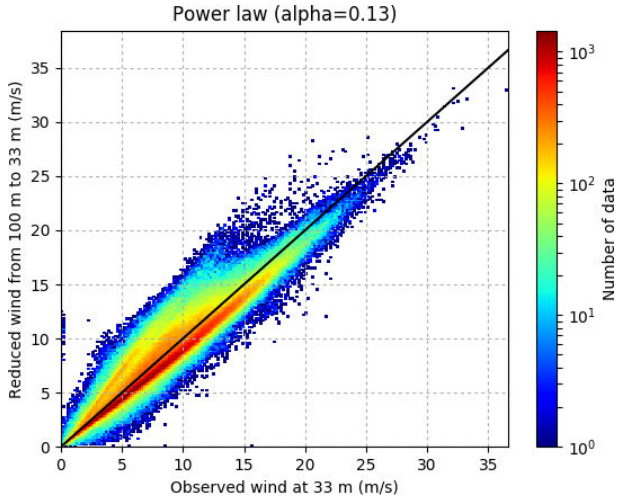

Figure 3.12 – Correlation between reduced and observed wind at 33 m at FINO1 for the power law of 0.13

(b)

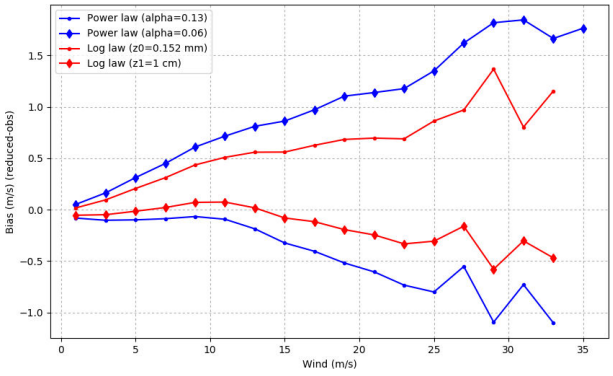

Figure 3.13 – Bias between reduced and observed wind at 33 m depending on the reduction law

3.8 Article in QJRMS

Quarterly Journal of the Royal Meteorological Society *Q. J. R. Meteorol. Soc.* 144: 317–332, January 2018 B DOI:10.1002/qj.3205

Strong winds in a coupled wave–atmosphere model during a North Atlantic storm event: evaluation against observations

Lucia Pineau-Guillou,[a]* Fabrice Ardhuin,[a] Marie-Noëlle Bouin,[a,b] Jean-Luc Redelsperger,[a] Bertrand Chapron,[a] Jean-Raymond Bidlot[c] and Yves Quilfen[a]

[a]*Ifremer, CNRS, IRD, UBO / Laboratoire d'Océanographie Physique et Spatiale (LOPS), UMR 6523, IUEM, Plouzané, France*
[b]*CNRM, UMR 3589, Météo-France et CNRS, Toulouse, France*
[c]*European Centre for Medium-range Weather Forecasts, Reading, UK*

*Correspondence to: L. Pineau-Guillou, Ifremer, Technopôle Brest Iroise, 29280 Plouzané, France. E-mail: lucia.pineau.guillou@ifremer.fr

Strong winds may be biased in atmospheric models. Here the European Centre for Medium-range Weather Forecasts (ECMWF) coupled wave–atmosphere model is used (i) to evaluate strong winds against observations, and (ii) to test how alternative wind stress parametrizations could lead to a more accurate model. For the period of storms *Kaat* and *Lilli* (23–27 January 2014), we compared simulated winds with *in situ* – moored buoys and platforms – and satellite observations available from the North Atlantic. Five wind stress parametrizations were evaluated. The first result is that moderate simulated winds (5–20 m s^{-1}) match with all observations. However, for strong winds (above 20 m s^{-1}), mean differences appear, as much as −7 m s^{-1} at 30 m s^{-1}. Significant differences also exist between observations, with buoys and Advanced Scatterometer ASCAT-KNMI generally showing lower wind speeds than the platforms and other remote-sensing data used in this study (AMSR2, ASCAT-RSS, WindSat, SMOS and JASON-2). Buoy and ASCAT-KNMI winds are likely to underestimate the real wind speed. It is difficult to conclude which dataset should be used as a reference. The second result is that common wave-age dependent parametrizations produce unrealistic drags and are not appropriate for coupling, whereas a newly empirically adjusted Charnock parametrization leads to higher winds compared to the default ECMWF parametrization. This proposed new parametrization may lead to more accurate results in an operational context.

Key Words: air–sea exchanges; northeast Atlantic; winds; IFS; sea state; roughness length; drag coefficient; wind stress

Received 2 June 2017; Revised 2 October 2017; Accepted 6 November 2017; Published online in Wiley Online Library 9 January 2018

1. Introduction

Winds over the ocean generate waves and storm surges, and are a dominant source in driving the ocean circulation, including western boundary currents, upwellings and coastal circulations. They are also a major contributor to surface air–sea turbulent fluxes (heat, moisture and momentum). In ocean and wave modelling, winds are generally taken as a forcing field provided by an atmospheric model (e.g. operational analyses or reanalysis). Several studies suggest that strong winds may be systematically underestimated by atmospheric models, with a consequent underestimation in storm surges and wave models. Rascle and Ardhuin (2013) observed a bias between the wave model WAVEWATCH III® and observations depending on the wind fields, 5% for the Climate Forecast System Reanalysis (CFSR) (Saha *et al.*, 2010) and 15% for the European Centre for Medium-range Weather Forecasts (ECMWF) operational analyses. Hanafin *et al.* (2012) and Stopa and Cheung (2014) showed that large wave heights were underestimated when forcing the simulations with ECMWF operational analyses or ERA-Interim reanalysis (Dee *et al.*, 2011). So far, it is not clear whether the strong negative bias obtained in wave simulations is caused by underestimated wind speed, inaccurate stress formulation or imprecise wave growth and dissipation parametrization at high wind speeds. The possible underestimation of high winds in atmospheric models is probably not the only explanation for wave underestimation. Parametrization of wind stress could also be another reason. Indeed, for a given wind field aloft, lower drag coefficient C_d will result in lower friction velocity and, as a feedback, will yield higher surface wind.

For atmospheric modelling, obtaining reliable atmosphere-to-ocean momentum fluxes is crucial. It encompasses a very broad field of time-scales and atmospheric phenomena, from the instantaneous forecast of fine-scale events (nowcast) to global climate runs over several decades (Shimura *et al.*, 2017). In atmospheric models, various parametrizations for the magnitude

Table 1. Maximum of wind, wind gust, minimum of mean-sea-level (MSL) pressure, maximum significant wave height (Hs), and precipitation over 24 h for the ten more energetic events, based on ERA-Interim analysis during the period 2005–2015 over the northeast Atlantic. In bold, the storm event of this study.

Date yyyy-mm-dd	Rank	Name	Wind ($m\,s^{-1}$)	Wind Gust ($m\,s^{-1}$)	MSL Pressure (hPa)	Hs (m)	Precip. (mm per 24 h)
2005-09-26	10	*Zeljko*	35.9	46.3	967	8.2	27
2006-12-09	7	*Xynthia*	37.6	50.4	951	9.0	29
2007-12-10	3	No name	39.0	54.0	963	7.5	30
2009-01-23	1	*Hans/Klaus*	41.8	37.8	944	9.4	44
2013-12-15	9	*Zaki*	36.9	48.0	957	9.7	27
2014-01-25	**5**	***Kaat/Lilli***	**38.1**	**56.3**	**953**	**11.7**	**31**
2014-12-08	2	*Alexandra*	39.6	45.5	964	7.8	25
2015-01-19	8	*Jan*	37.0	51.7	974	9.9	26
2015-03-10	4	*Erich*	38.2	52.6	966	7.8	28
2015-12-07	6	*Uwe*	37.9	57.9	959	6.8	38

of drag coefficient C_d produce wind speeds above $10\,m\,s^{-1}$ with 10% or more relative discrepancies between datasets (Rascle and Ardhuin, 2013). In ocean models, various C_d parametrizations can modify storm surges amplitude by up to 20% (Mastenbroek *et al.,* 1993; Muller *et al.*, 2014).

The ECMWF Integrated Forecasting System (IFS) is unique in using a coupled system between its atmospheric model and the wave model ECWAM operationally, thus providing a dynamic prediction of the drag coefficient as a function of the sea state. This C_d representation was developed by Janssen (1991) to reproduce the behaviour of the coupled wave–atmospheric boundary-layer model of Janssen (1986). This parametrization was generally found to provide more accurate weather forecasts (Janssen, 2004). Nevertheless, there are few reliable observations at strong wind speeds for comparisons. Several recent field experiments produced estimations of C_d, based on direct *in situ* measurements (Black *et al.*, 2007; Edson *et al.*, 2013) or indirect ones (e.g. Powell *et al.*, 2003; Holthuijsen *et al.*, 2012), as well as laboratory tank measurements (e.g. Donelan *et al.*, 2004; Jarosz *et al.*, 2007; Takagaki *et al.*, 2012). At wind speeds above $20\,m\,s^{-1}$, reported C_d observations are significantly lower than those given by the ECMWF parametrization.

The present work started from the possible link between a probable underestimation of strong winds in some (or most) atmospheric models and high values of C_d used in their boundary-layer parametrizations. The objective of the present article, based on a numerical simulation of the case-study of the two extratropical storms *Kaat* and *Lilli* which crossed the North Atlantic in January 2014, is twofold: how strong are the biases for high wind speeds in atmospheric models, and can they be corrected by changing C_d parametrizations? For this we first evaluated the strong surface wind speeds obtained using the default parametrization used operationally in the IFS by comparing them with observations. We then tested several alternative parametrizations (including a newly developed parametrization) to attempt to reduce the discrepancies between the modelled and observed strong winds. The first part of this article describes the *Kaat* and *Lilli* storm events. In the following part, we describe the coupled wave–atmosphere model, as well as the different sources of wind observations: satellite data, buoys and platforms. Then, we focus on the comparisons between simulated winds and observations. Finally, we analyse the impact of several parametrizations – including a newly developed one – on the atmosphere.

2. Case-study: storm description

In the following paragraphs, we describe the selection criteria for the case-study, the synoptic situation and the storm tracks.

2.1. Event selection

The events that are the subject of the present study were selected from ERA-Interim (Dee *et al.*, 2011), a global atmospheric reanalysis produced by ECMWF, covering the years 1979 to the present time. The horizontal resolution is about 80 km, forecast outputs are every 3 h, and analyses every 6 h. To take advantage of recent satellite wind data, we restricted our selection from 2005 to 2015 and to the northeast Atlantic only (30°W to 10°E and 30°N to 65°N, see geographical extension, Figure 3). The ten most energetic events were selected taking into account two criteria: maximum 10 m wind speed higher than $32\,m\,s^{-1}$ and minimum mean-sea-level (MSL) pressure lower than 975 hPa (Table 1). Wind, MSL pressure and significant wave height (Hs hereafter) come from ERA-Interim analyses, whereas wind gust and precipitation come from ERA-Interim forecasts. The storm names were taken from Germany's National Meteorological Service (DWD) nomenclature. No name is attributed when the storm is too far from Europe, and two names are mentioned when a primary system is followed by a secondary one.

Among these ten events, a particular case was selected. We chose the event with the strongest winds, where satellite remote-sensing data were available (e.g. AMSR2 radiometer data have been available only since 2012). The storms *Kaat* and *Lilli* of 25 January 2014, classified 5th, were the best candidates. The next part presents an overview of these storms.

2.2. Synoptic situation

Synoptic charts from DWD show the evolution of the situation (Figure 1). From 23 to 26 January, *Kaat* crossed the North Atlantic, moving from the east coast of Canada to Iceland, whereas *Lilli* was generated from a secondary cyclogenesis on 25 January. It started in the middle of the North Atlantic and moved on a more southerly path towards northern Europe, and reached Scotland on 26 January.

2.3. Storm tracks

Hoskins and Hodges (2002) analysed the winter storm track organization and behaviour in the Northern Hemisphere, from a climatological point of view. The storm tracks in the North Atlantic lower troposphere were classified along two main common paths (cf. the black dotted lines in Figure 2). The first path starts from the east coast of North America, then crosses the North Atlantic, moving in a northeasterly direction, reaching Iceland and continuing along the east coast of Greenland to finally dissipate near Svalbard. The second path is located further south; it starts from the middle of the North Atlantic, and moves in a northeasterly direction, towards the northern part of Europe ending up south of Finland.

Kaat and *Lilli* storm tracks (cf. the red/blue lines in Figure 2) were computed from the ERA-Interim database, following the method elaborated by Hoskins and Hodges (2002). These tracks follow the typical trajectories described above.

Kaat lasted 9 days from 19 to 27 January 2014, including 4 days over the Atlantic which is a typical crossing time. The system appeared on 19 January inland in north Canada, and

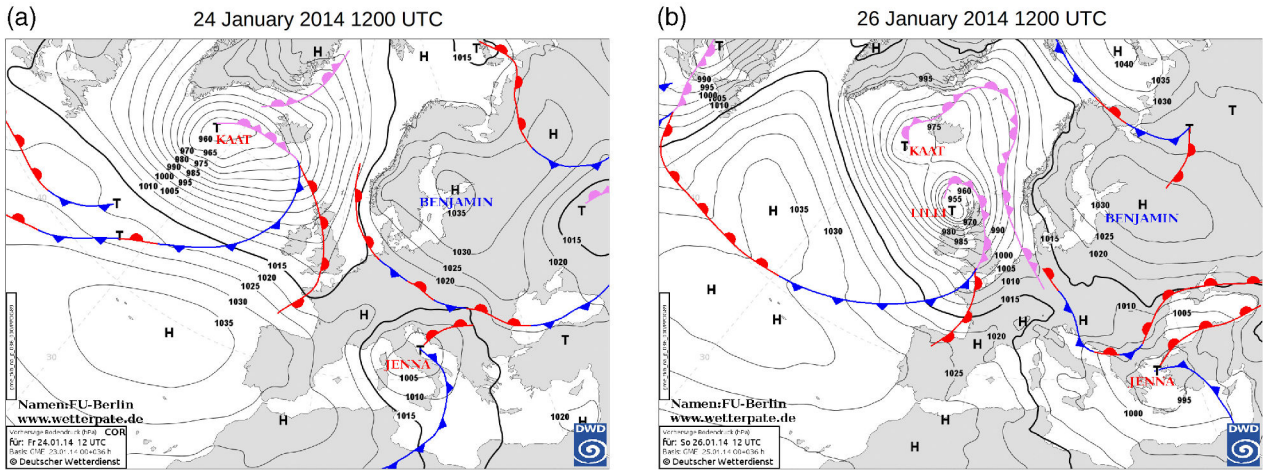

Figure 1. DWD synoptic charts on (a) 24 and (b) 26 January 2014, 1200 UTC. [Colour figure can be viewed at wileyonlinelibrary.com].

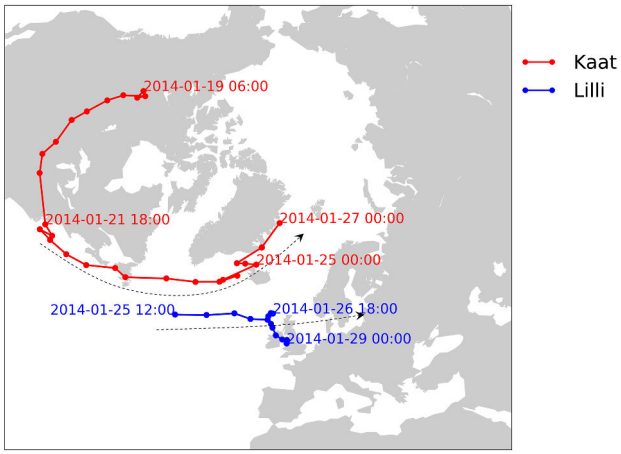

Figure 2. *Kaat* and *Lilli* storm tracks on January 2014 (data every 6 h). In black dotted line are shown the principal tracks from Hoskins and Hodges (2002). [Colour figure can be viewed at wileyonlinelibrary.com].

was probably caused by mountain cyclogenesis. It then moved southeastwards to reach the Atlantic on 21 January 2014. Crossing the ocean along a northeasterly path, it passed Iceland on the 25th, and finally dissipated along the Greenland coast on 27 January.

Lilli followed on *Kaat*, as a secondary system generated on 25 January, in the middle of the North Atlantic. This system moved in a northeasterly direction, reaching an area to the north of Ireland on 26 January. Then *Lilli* changed direction, moving southeastwards, reaching Ireland on the 28th and finally dissipating over Great Britain on 29 January. According to ERA-Interim, this secondary system was more intense than *Kaat*, with maximum winds speeds reaching 34.1 m s^{-1}, instead of 27.7 m s^{-1}.

3. Model and observations

In the following paragraphs, we describe the coupled wave–atmosphere model and the observations used in this study.

3.1. Coupled wave–atmosphere model

3.1.1. Configuration description

We used the Integrated Forecasting System (IFS) CY41R1 cycle (ECMWF, 2015a), with a TL1279 Gaussian grid corresponding to a spatial resolution around 16 km, and 137 vertical levels. The IFS includes the spectral wave model ECWAM (ECMWF WAve Model: ECMWF, 2015b), which has been coupled within IFS since 1998. To explicitly take into account the wave impact on the atmosphere boundary layer, the Charnock parameter, which defines the roughness length $z_{0\mathrm{wave}}$ (see Eqs (5) and (6)) is exchanged each time step from ECWAM to IFS, whereas IFS produces neutral wind speeds at 10 m height that are used to force the wave model. The ECWAM uses a coarser horizontal resolution than IFS at around 28 km, with 36 directions and 36 frequencies logarithmically spaced, with starting frequency 0.035 Hz and an increment of 1.1.

Hourly output fields include the Charnock parameter, drag coefficient, wind stress and wind speed, and are extracted on a 0.125° resolution grid over the northeast Atlantic. Five days were simulated from 23 January 0000 UTC to 28 January 0000 UTC. In order to keep a similar representation of the atmosphere throughout the whole simulation period, the simulation was restarted from the operational analysis each day at midnight. The simulations presented here do not assimilate data (forecast mode experiment). Initial conditions come from the ECMWF operational analysis, obtained with data assimilation.

The strong correlation between our 24 h simulations and the corresponding operational analyses for wind (coefficient r of 0.94) and the 500 hPa geopotential (coefficient r of 0.99) show that the storm is well simulated by the model. To prevent a possible influence of the analysis on the adjustment period over the first few hours of every 24 h simulation, only the time range between 3 and 26 h after each run start was kept for this study.

3.1.2. Wind stress representation

The wind stress τ is proportional to the square of the friction velocity u_* in the surface layer, which corresponds to the average of the wind fluctuations:

$$\tau = -\rho_{\mathrm{air}}\overline{u'w'} = \rho_{\mathrm{air}}u_*^2, \qquad (1)$$

where ρ_{air} is the air density, u', w' are the horizontal and vertical wind turbulent fluctuations. Turbulent stress – and wind friction velocity – can be considered as independent of height in the surface boundary layer. Because the space and time resolution of the atmospheric models do not allow an explicit representation of the turbulent fluctuations, the turbulent fluxes, including the wind stress, are represented by bulk formulae. These formulae assume that the stress and the wind are aligned and relate the stress and the mean wind speed at a given height, generally 10 m above sea surface, through a drag coefficient C_{d}:

$$\tau = \rho_{\mathrm{air}}C_{\mathrm{d}}U_{10}^2, \qquad (2)$$

where C_{d} and U_{10} are the drag coefficient and the wind speed at 10 m above the surface, respectively. In neutral conditions, the

Table 2. Main characteristics of satellite wind products on 26 January 2014 over the northeast Atlantic, and number of points for collocation.

Instrument	Satellite	Data provider	Swath width (km)	Wind product sampling (km)	Max. wind ($m\,s^{-1}$)	No. of points for collocation
ASCAT	MetOp-A/B	KNMI	2*512.5	12.5	36.2	367 032
ASCAT	MetOp-A	RSS	2*512.5	27	34.1	43 469
AMSR2	GCOM-W1	SOLab	1450	10	31.9	166 803
WindSat	Coriolis	RSS	1000	25	37.4	35 974
MIRAS	SMOS	Ifremer	600	15	39.8	31 622
Poséidon-3	JASON-2	NASA	/	6	27.6	4868
Buoys	–	–	–	–	–	2389
Platforms	–	–	–	–	–	6587

drag coefficient can be expressed as:

$$C_{\mathrm{d}} = \frac{\kappa^2}{\left\{\log\left(\frac{10}{z_0}\right)\right\}^2}, \tag{3}$$

where z_0 is the roughness length, and κ is von Kármán's constant (0.4). Eqs (2) and (3) link the roughness length to the wind stress and to the wind profile. At very light winds, the roughness $z_{0\mathrm{visc}}$ is known to depend on the viscous properties of the flow, whereas at stronger winds, the roughness $z_{0\mathrm{wave}}$ is associated to an overall form drag of the wave field. A common parametrization of the roughness $z_{0\mathrm{wave}}$ was given by Charnock (1955), and depends on the surface waves through the friction velocity u_*. This leads to total roughness:

$$z_0 = z_{0\mathrm{visc}} + z_{0\mathrm{wave}} = \frac{0.11\upsilon}{u_*} + \alpha\frac{u_*^2}{g}, \tag{4}$$

where υ is the kinematic viscosity, g is the mean gravitational acceleration and α is known as Charnock's parameter. α can be constant or related explicitly to the wave parameters, in particular the wave age, using different parametrizations (e.g Oost *et al.*, 2002; Drennan *et al.*, 2003).

Janssen (1991) parametrized the quasi-linear wave growth effect as a modification of the wind profile giving way to an effective larger roughness length $z_{0\mathrm{wave}}$, expressed as a function of the wave-induced stress τ_{w},

$$z_{0\mathrm{wave}} = \frac{z_1}{\sqrt{1-\frac{\tau_{\mathrm{w}}}{\tau}}}, \tag{5}$$

The reference roughness length z_1 is:

$$z_1 = \alpha_1\frac{u_*^2}{g}, \tag{6}$$

with $\alpha_1 = 0.006$. This value of α_1 has been fixed, so that for old sea, the associated roughness $z_{0\mathrm{wave}}$ (Eq. (5)) corresponds to the standard value of Charnock parameter 0.0185 (Wu, 1982). The wave-induced stress τ_{w} is the momentum flux transferred from the atmosphere to the waves. It can be related to the wind-wave growth parameter β and the directional wave spectrum $E(f,\theta)$:

$$\tau_{\mathrm{w}} = g\int_0^{\infty}\mathbf{k}\int_0^{2\pi}\beta(f,\theta)E(f,\theta)/(2\pi f)\mathrm{d}f\,\mathrm{d}\theta \tag{7}$$

where k is the wave number, θ the direction and f the relative wave frequency (Janssen, 2004). The wave-growth parameter is expressed as $\beta = (\beta_{\mathrm{m}}/\kappa^2)\mu\ln^4(\mu), \mu \leqslant 1$, where κ is the von Kármán's constant, β_{m} a constant (1.2), and μ the dimensionless critical height (ECMWF, 2015b).

The stress τ_{w}, and thus the roughness $z_{0\mathrm{wave}}$, is highly sensitive to the high-frequency content of the wave spectrum, which is in itself highly sensitive to the choice of wave generation and dissipation parametrizations (e.g. Rascle and Ardhuin, 2013). In ECWAM, the wave spectrum $E(f,\theta)$ high-frequency tail is diagnostically forced to $E(f,\theta)(f_{\mathrm{t}}/f)^5$ for $f > f_{\mathrm{t}}$ with $f_{\mathrm{t}} = 2.5f_{\mathrm{windsea}}$ and f_{windsea} the mean frequency of the modelled wind sea (part of the full spectrum corresponding to the wind sea only, and defined where the input source term S_{in} is positive).

3.2. Wind measurements

In this part, we describe the wind observations used to assess the simulated wind speed in our case-study.

3.2.1. General description

We took advantage of winds both from *in situ* measurements – buoys and platforms – and remote-sensing measurements – scatterometers (ASCAT), passive microwave radiometers (AMSR2, SMOS), passive polarimetric radiometers (WindSat) and altimeters (JASON-2). Some of these data are assimilated in the ECMWF operational system, but not assimilated in our simulations. In spite of this, they influence results because initial conditions are taken from operational analyses. The main characteristics of satellite data used in this study are presented in Table 2.

In situ wind measurements are the most direct measurements of wind speed and are available at high temporal resolution, but restricted to few locations. They represent a smaller surface (defined as a footprint) compared to the model grid cell. The buoy footprint is difficult to evaluate, but it can probably represent around 1 km, depending on the wind speed and on the stratification, whereas the platform footprint is usually larger, depending on the height of the measurement.

Conversely, remote sensing provides wind speeds over a large swath but at sparse temporal resolution, with larger footprints (10–30 km) than *in situ*. In recent years, the capability of ocean remote-sensing data to characterize high wind speeds, with higher resolution (typically 10 km in the recent period), has rapidly improved (Quilfen *et al.*, 2007; Chapron *et al.*, 2010; Reul *et al.*, 2017). Their accuracy is theoretically homogeneous and of about $2\,m\,s^{-1}$, but Chou *et al.* (2013) reported that ASCAT strong winds (higher than $18\,m\,s^{-1}$) were negative biased about $7\,m\,s^{-1}$ versus observations. Remote-sensing measurements are always indirect and rely on the characteristics of the sea surface: amplitude of short gravity waves, radiometric signature of foam and increased ocean surface with waves, to name a few. Geophysical Model Functions (GMFs) are used to transform the measured parameters (radar cross-section and brightness temperature) into wind speeds. They are empirical relationships, generally globally adjusted to *in situ* datasets, other satellites products, or atmospheric numerical model output. As a result, different training datasets can produce different GMFs. Especially high wind speed regime estimates can then vary between different processing algorithms that start from the same raw satellite data.

All the wind observations used in this study are corrected to correspond to a height of 10 m above the sea surface. Data from satellites are generally conventionally referred to as neutral winds, whereas data from models and *in situ* are non-neutral. In this study atmosphere stability effects are not taken into account, as they are considered to be second order for strong wind situations. Wind speeds on 26 January 2014 obtained from the different satellites and *in situ* datasets are listed below and presented in Figures 3(a)–(f).

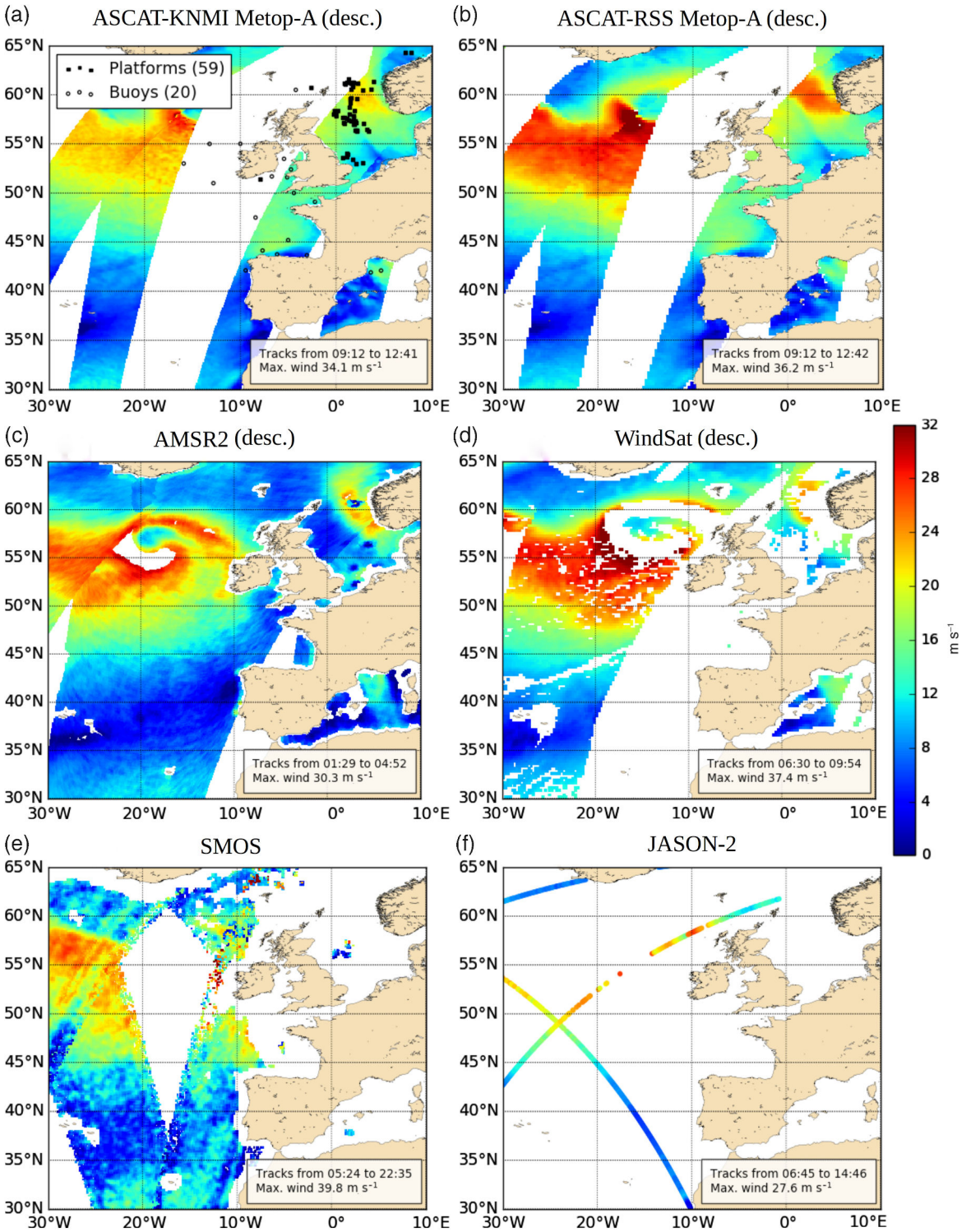

Figure 3. Wind field on 26 January 2014 estimated from (a) ASCAT-KNMI MetOp-A, (b) ASCAT-RSS MetOp-A, (c) AMSR2, (d) WindSat for descending passes, and for (e) SMOS and (f) JASON-2. Platforms and buoys are plotted on (a). [Colour figure can be viewed at wileyonlinelibrary.com].

3.2.2. *ASCAT scatterometer*

The Advanced SCATterometer (ASCAT) is a real aperture radar, to enable the estimation of wind speed and direction from backscatter coefficients. It is carried on board the Meteorological Operational (MetOp) polar satellites, launched by the European Space Agency (ESA) and operated by EUMETSAT (EUropean organisation for the exploitation of METeorological SATellites). MetOp-A was launched in 2006, MetOp-B in 2012.

ASCAT wind products used in this study are provided by KNMI (Royal Netherlands Meteorological Institute) and RSS (Remote Sensing Systems). The ASCAT-KNMI is a Level 2 swath product, with a 12.5 km spatial resolution, using MetOp-A and MetOp-B data. The ASCAT-RSS version 2.1 is a gridded product, with 0.25° spatial resolution, based on MetOp-A data only. For these two datasets, rain-contaminated data are discarded depending on the rain flags.

The comparisons between winds from ASCAT-KNMI and ASCAT-RSS on 26 January 2014 for MetOp-A (Figures 3(a) and (b)) show that RSS high winds are stronger than KNMI, clearly related to different retrieval algorithms. The GMF used by RSS is calibrated using previous passive microwave satellite

measurements and other wind analysis, whereas KNMI GMF is calibrated on buoys and ECMWF winds (Verspeek *et al.*, 2012).

Scatterometers have a decreased sensitivity at high winds, leading to difficulties in calibrating the GMF at strong winds and to a possible underestimation of high winds (Quilfen *et al.*, 1999; Bentamy *et al.*, 2008; Sapp *et al.*, 2016).

Note that KNMI ASCAT winds and ECMWF operational winds are not independent: ASCAT wind retrievals rely on ECMWF winds through their 'ocean calibration process' (Verspeek *et al.*, 2012) and ASCAT winds are assimilated in the ECMWF operational analysis (De Chiara *et al.*, 2016). For the assimilation operations, ECMWF re-computes ASCAT winds from the backscatter coefficients, using a procedure very similar to KNMI. The wind speeds obtained are then systematically corrected to avoid a global bias between ASCAT and the model, prior to data assimilation.

3.2.3. AMSR2 radiometer

The Advanced Microwave Sounding Radiometer 2 (AMSR2) is a passive microwave radiometer, enabling estimation of wind speeds from brightness temperature of the oceans. It has operated on board the Global Change Observation Mission–Water 1 (GCOM-W1) satellite since 2012.

AMSR2 winds are provided by SOLab (Satellite Oceanography Laboratory, Russian State Hydrometeorological University). The wind product used in this study is Level 2, ungridded, with a spatial resolution of 10 km. Low microwave frequency winds were preferred, as a high microwave frequency AMSR2 algorithm can significantly underestimate high winds and is more likely contaminated by atmospheric liquid water content. Comparisons (Zabolotskikh *et al.*, 2014) show that the AMSR2 wind products obtained using the low-frequency based algorithm exhibit very strong correlation with platform winds for high wind speeds. The data we used were filtered for outliers and interpolated on a regular grid of $0.1^\circ \times 0.1^\circ$ (Figure 3(c)). Areas without data near the centre of the storm are due to rain masking. These areas are reduced to a minimum thanks to efficient processing of rain effects on brightness temperature measurements (Zabolotskikh *et al.*, 2013, 2014).

AMSR2 winds are not assimilated in the ECMWF numerical weather prediction system. However, the radiances are directly assimilated (Kazumori *et al.*, 2016).

3.2.4. WindSat radiometer

WindSat is a multi-frequency polarimetric microwave radiometer (Gaiser *et al.*, 2004). It provides estimates of the ocean surface wind vector from brightness temperatures. It has operated since 2003 on board the Coriolis satellite.

WindSat data are processed and distributed by RSS. Data are inter-calibrated with the other microwave radiometers. As for AMSR2, low microwave frequency 10 m winds were preferred to high-frequency winds. Even if their effective resolution is lower (25×38 km instead of 16×27 km), they are less affected by the atmosphere and rain (Meissner and Wentz, 2009). The dataset consists of a daily product v7.0.1 on a 0.25° grid (Figure 3(d)).

WindSat data are not assimilated in the ECMWF numerical weather prediction system; these data and simulated winds are thus totally independent from each other.

3.2.5. SMOS radiometer

Microwave Imaging Radiometer by Aperture Synthesis (MIRAS) is an L-band radiometer, whose primary goal was to estimate soil moisture and ocean surface salinity, in the framework of ESA's Soil Moisture Ocean Salinity (SMOS) mission. However, in addition, the observed sensitivity of the excess emissivity at L-band can be interpreted in terms of high wind speed (Reul *et al.*, 2012, 2016). This instrument is only marginally affected by rain and clouds, and can provide complementary information about storm structures and intensity. SMOS wind data are produced and archived at Centre ERS (Earth and Space Research) d'Archivage et de Traitement at Institut Français de Recherche pour l'Exploitation de la Mer (CERSAT, Ifremer). The Level 2 (gridded) 15 km wind data product was used here. SMOS winds are not assimilated in the ECMWF numerical weather prediction system.

3.2.6. JASON-2 altimeter

The JASON-2 altimeter operates at two frequencies (13.6 GHz in the Ku band, 5.3 GHz in the C band) to determine ionospheric electron content, which affects the radar signal path delay. This dual-frequency capability can be used to mitigate contamination of the normalized radar cross-section measurements (NRCS), by rain (Quilfen *et al.*, 2006). The NRCS data from the Geophysical Data Records (GDR) are processed at the Aviso centre in Toulouse under the responsibility of the Centre National d'Etudes Spatiales (CNES) and the National Aeronautics and Space Administration (NASA). The NRCS measurements do not show systematic saturation at high wind speed up and above hurricane force (Quilfen *et al.*, 2006; Hanafin *et al.*, 2012). This sensitivity enables derivation of altimeter high wind speed estimates (Figure 3(e)) using a GMF tailored with radiometer measurements (Quilfen *et al.*, 2011). JASON-2 winds are not assimilated in the ECMWF numerical weather prediction system.

3.2.7. Buoys

Buoy networks (Figure 3(a)) are mainly deployed by meteorological offices. In the northeast Atlantic, data providers are the UK Met Office, Irish Marine Institute, Météo-France and Puertos del Estado. Buoy data come from the Wave Forecast Verification Project managed by ECMWF for the Joint Technical Commission for Oceanography and Marine Meteorology (JCOMM). A brief quality control was carried out on wind observations, based on a visual check. We kept all the buoys, and we adjusted the wind data from measurement height (usually from 2 to 4 m) to 10 m, based on a logarithmic law. A total of 20 buoys is available.

Buoy wind measurements are likely affected by sea state and buoy motion, and so could potentially underestimate high wind speeds (Zeng and Brown, 1998; Zabolotskikh *et al.*, 2014). The wind speed could further be reduced because of sheltering effects by waves (Skey *et al.*, 1995).

Buoy winds are assimilated in the ECMWF forecasting system.

3.2.8. Platforms

Platforms are all located in the North Sea (Figure 3(a)), and are deployed mainly by oil and gas private companies. Data come from the Global Telecommunication System (GTS) and Norwegian Meteorological Institute. Data were selected using the same method as buoys. The brief quality control led to the invalidation of 7 platforms among 67. Platforms' wind data are generally reduced to 10 m, with methods depending on data providers and about which precise information is difficult to obtain. For Met Norway, wind speed U at height z is reduced to 10 m using a wind power law expressed as:

$$U_{10} = U\left(\frac{10}{z}\right)^{0.13}. \tag{8}$$

This formulation, with the exponent empirically determined, is often used when no information about stability or surface roughness is available (Furevik and Haakenstad, 2012).

Multiple wind speed data coming from platforms located in the same grid cell of the IFS model were averaged to obtain one

Table 3. Correlation coefficients (r) between ECMWF simulated winds and observations from 23 to 27 January 2014, over the northeast Atlantic.

Instrument	Satellite	Data provider	Correlation coefficient (r)
ASCAT	MetOp-A/B	KNMI	0.95
ASCAT	MetOp-A	RSS	0.94
AMSR2	GCOM-W1	SOLab	0.90
WindSat	Coriolis	RSS	0.94
MIRAS	SMOS	Ifremer	0.79
Poséidon-3	JASON-2	NASA	0.92
Buoys	–	–	0.91
Platforms	–	–	0.91

value per model grid cell, to enable a more coherent comparison. Finally, 59 averaged stations were available.

Wind sensors on platforms are usually located higher than on buoys (e.g. more than 100 m for some platforms in the North Sea). While Zabolotskikh *et al.* (2014) consider that platform measurements are more accurate than buoy measurements for high winds, transforming wind measurements at more than 100 m to 10 m wind speed using empirical formulae like Eq. (8) is an additional source of uncertainty.

GTS platform winds are presented to the ECMWF data assimilation system.

4. Comparison between simulated winds and observations

In this part, we assess the wind speeds obtained in the *Kaat–Lilli* simulation using the default ECMWF parametrization by comparing them with observations. Collocations were made with all available observations as described in section 3 during the 5 days of simulation (23–27 January 2014) on the northeast Atlantic (30°N–65°N, 30°W–10°E, see geographical extension, Figure 3). For *in situ* observations (buoys and platforms), temporal resolution is the same as the model (1 h) and all the data are used for comparison. For remote sensing, data are considered collocated and used for the comparison if the time difference between model and observations is less than 15 min. The model, whose default resolution is 16 km, was extracted on a 0.125° grid, so the maximum distance between observations and model (depending on the grid resolution of the observations, see Table 2) is around 6 km. The number of correlated points between simulated and observed winds depends on each instrument: it ranges from 2389 points for buoys up to 367 032 for ASCAT-KNMI (Table 2). The correlation coefficients (r), for the wind speed range 0–40 m s^{-1}, range from 0.95 for ASCAT-KNMI to 0.79 for SMOS (Table 3). This lower value for SMOS is due to a noisier signal (Figure 4(e)). At high wind speeds, simulated winds are consistent throughout the whole range with ASCAT-KNMI winds (Figure 4(a)) and buoy winds (Figure 4(g)). In contrast, simulated winds show a negative bias with respect to all other data

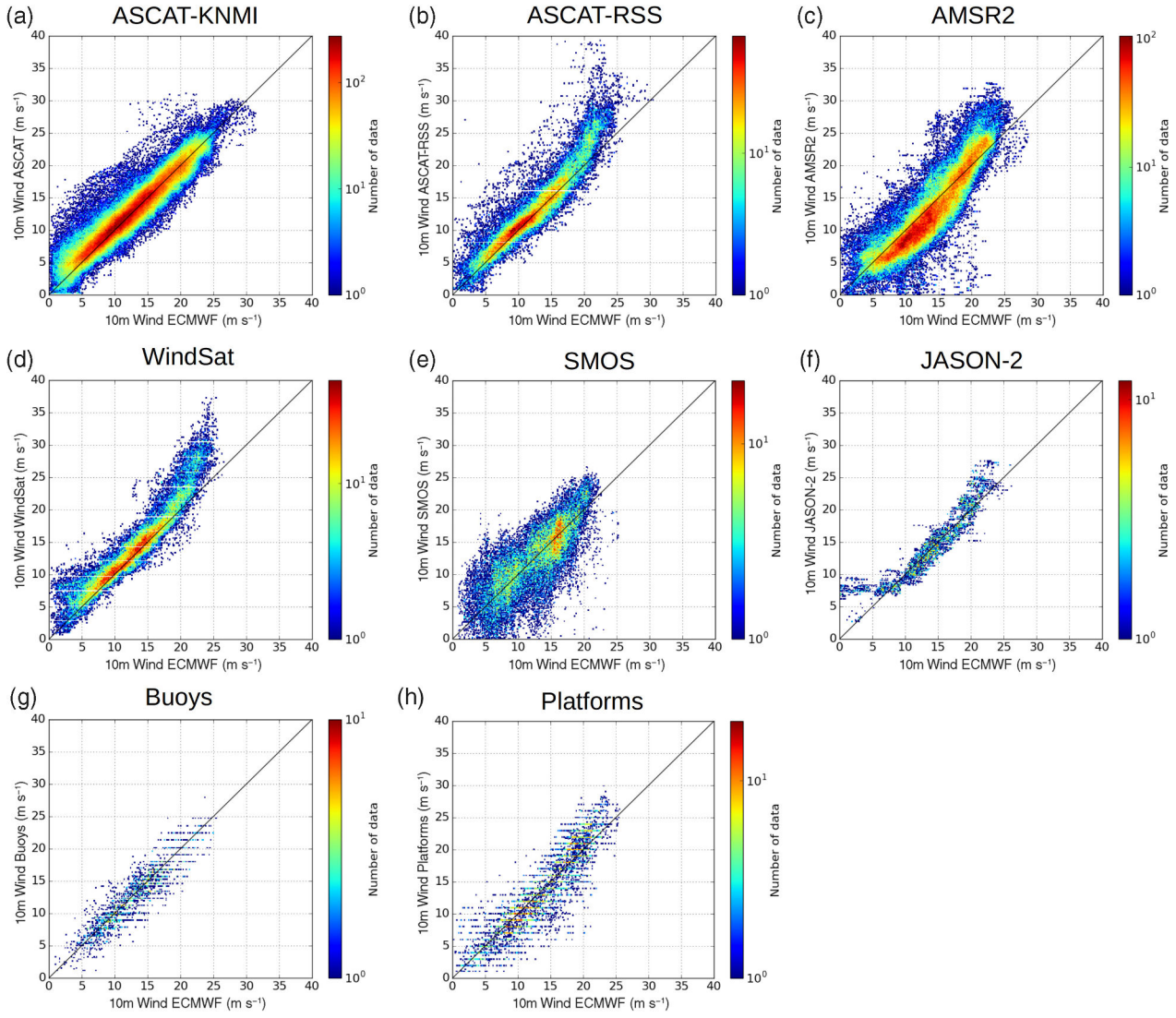

Figure 4. Wind correlations from 23 to 27 of January 2014 between default ECMWF parametrization (CY41R1) and (a) ASCAT-KNMI, (b) ASCAT-RSS, (c) AMSR2, (d) WindSat, (e) SMOS, (f) JASON-2, (g) buoys and (h) platforms. [Colour figure can be viewed at wileyonlinelibrary.com].

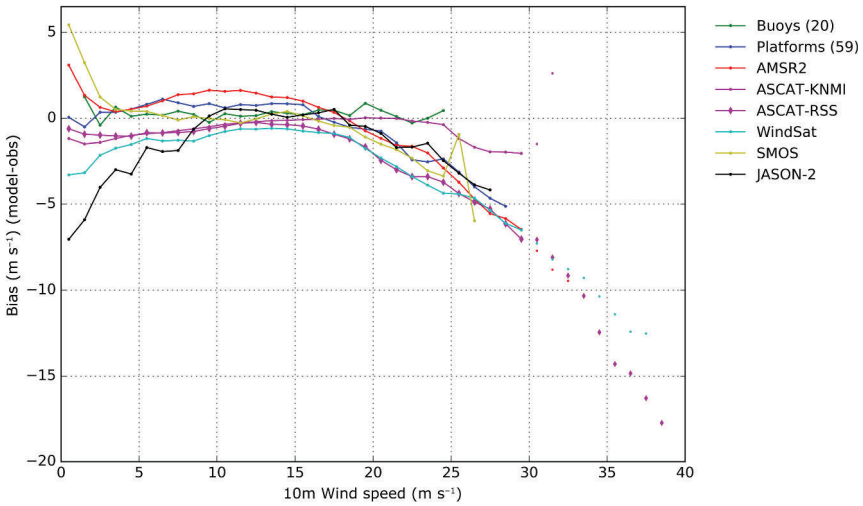

Figure 5. Wind biases between ECMWF (CY41R1) model and observations (buoys, platforms, and satellite data), computed from 23 to 27 January 2014 on the northeast Atlantic. Beyond 30 m s^{-1}, values are plotted as points, due to large uncertainties in observations. [Colour figure can be viewed at wileyonlinelibrary.com].

(Figures 4(b–f) and (h)). ASCAT-RSS and WindSat correlations are similar, because they were processed by the same data provider (RSS), using WindSat products as a reference for calibrating ASCAT winds. Note that strong winds from platforms are higher than ECMWF ones, which is not the case for buoy winds. To analyse in greater depth the differences between datasets, we computed biases between ECMWF simulations and observations.

4.1. *Biases*

Wind biases were computed between ECMWF simulations and observations (Figure 5). We averaged differences between model and observations along the *x*-axis as well as along the *y*-axis, every bin of 1 m s^{-1}. Note that the curves end at different wind speeds depending on observations. This is partly due to different spatial coverage according to the instruments used (e.g. a buoy or a satellite do not see the same event spatially) and to biases between datasets (e.g. ASCAT-RSS strong winds are higher than KNMI ones, then the RSS curve ends after the KNMI one). Error bars are not displayed in the figure in order to improve readability, but standard deviations and root-mean-square errors are given in appendix B. For very high winds (>30 m s^{-1}), biases are statistically less relevant, as they are computed with only a few points. Moreover, for this range of wind speed, uncertainties of observations increase dramatically, as there is a lack of high-quality measurements. For these reasons, values for this wind speed range are only plotted as points on figures of biases (Figures 5, 6 and 11).

The first result is that for moderate winds (5–20 m s^{-1}), the biases are slight (±1 to 2 m s^{-1}) for all observations. This shows that the model agree well with all observations.

The second result is that for winds stronger than 20 m s^{-1}, biases are generally negative or close to zero, showing that simulated winds are generally lower than observations. Observations can be divided into two groups: one with small biases, the other one with large. The first group with small biases is composed of ASCAT-KNMI and buoys. The bias between model and buoys is close to zero. This result is not surprising, as buoys are used as one part of the reference data used to calibrate the ECMWF model. The bias between ECMWF and ASCAT-KNMI is also close to zero up to 25 m s^{-1}. It then slowly increases with wind speed to reach about −2 m s^{-1} at 30 m s^{-1}. Note that the last binned value with a positive bias must be carefully interpreted, because it represents only a few points with large standard deviations (Figure B1). This slight negative bias with ASCAT-KNMI is not at all surprising as ASCAT-KNMI retrievals strongly rely on ECMWF winds for calibration (Verspeek *et al.*, 2012) (see section 3.2.2). Moreover, buoys are used to calibrate empirical scatterometer GMFs (Zeng and Brown, 1998) at KNMI. In conclusion for the first group, ECMWF, ASCAT-KNMI and buoy winds all agree well, as indeed each of the three data source are mutually interdependent.

The second group with stronger biases is composed of all the other satellite or *in situ* wind products considered in this study (scatterometer from RSS, radiometers, altimeter and platforms). ECMWF high winds are systematically lower than these observations with a significant bias increasing with wind speed. Bias is of about −4 m s^{-1} at 25 m s^{-1}, and reaches −7 m s^{-1} at 30 m s^{-1}. AMSR2, WindSat and SMOS products are all consistent, because of shared sensitivities of the foam-induced brightness temperature to wind speed for these passive microwave wind sensors, but also of dedicated efforts to calibrate and align high wind speeds. Note that AMSR2 and WindSat are also consistent due to the combination of (i) similar retrieval algorithms between AMSR2 and Stepped-Frequency Microwave Radiometer on board aircraft (SFMR), and (ii) SFMR data being used as a reference for WindSat GMFs calibration. Strong correlations between platforms and AMSR2 have already been reported (Zabolotskikh *et al.*, 2014). While there is still no full consensus on calibration between data providers, the overall agreement between these remote-sensing datasets is encouraging.

4.2. *Discussion*

The estimates of correlations and biases between ECMWF simulations and observations show that there are systematic biases between ECMWF and most datasets derived from observations at high wind speeds. Moreover, biases exist between various datasets.

These results suggest a possible underestimation of ASCAT-KNMI high winds, as already mentioned in previous studies (Chou *et al.*, 2013). It can be associated with a decrease of sensitivity of scatterometry instruments at high winds, which make calibration more complicated in this wind range, whereas radiometers show a better sensitivity and no saturation issues at high wind speeds (Quilfen *et al.*, 2007; Reul *et al.*, 2017). ASCAT-RSS high winds are estimated using a different GMF, and are stronger than KNMI ones because wind products are tailored to the radiometer winds. Apparently, this method mitigates the reduced sensitivity of scatterometer measurements.

There is also a significant bias between buoys and platforms at high wind speeds. Buoy winds are lower than platform winds, by about 3 m s^{-1} at 25 m s^{-1}. Earlier works mentioned that buoys could underestimate high wind speeds (Zeng and Brown, 1998), because of sea state, buoy motion and sheltering effects. All these differences raise questions on the relevancy of measuring wind at such heights and on the methods used to reduce values to

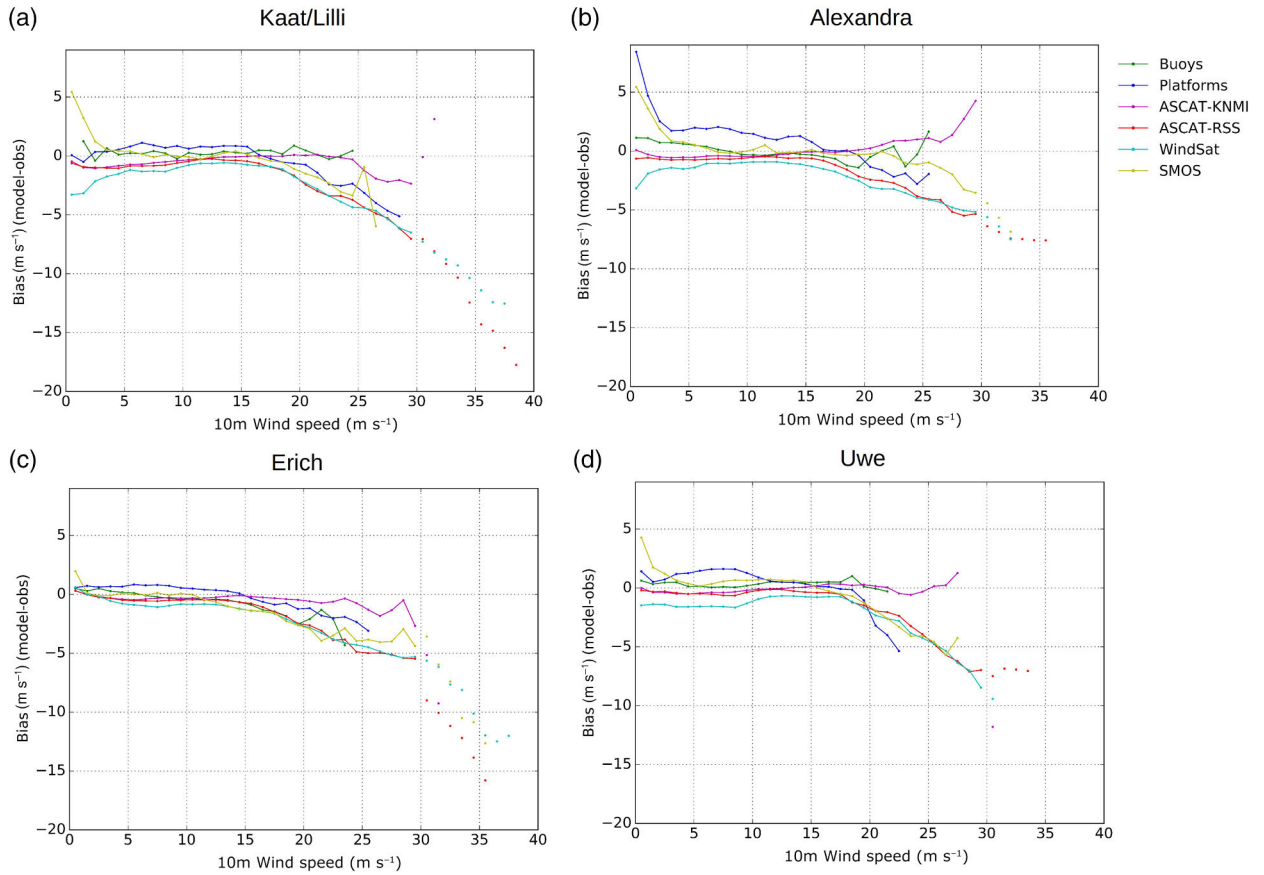

Figure 6. Wind biases between ECMWF (CY41R1) model and observations (buoys, platforms and satellite data), computed on the northeast Atlantic for storms (a) *Kaat/Lilli,* (b) *Alexandra,* (c) *Erich*, (d) *Uwe*. Beyond 30 m s^{-1}, values are plotted as points, due to large uncertainties in observations. [Colour figure can be viewed at wileyonlinelibrary.com].

10 m. Buoys used in this study measure at 2–4 m in height, in a reference frame moving with waves, whereas the height of the sensors on platforms is typically 60–150 m. We made similar comparisons between ECMWF-simulated winds and platform winds at the height of the sensor (not shown), leading to similar biases showing an underestimation comparable to 10 m winds. Further work is needed to analyse if wind on platforms is representative of wind around the platform, and if structure effects could generate differences.

In conclusion for strong winds, we found biases between the two groups of data: on one hand ECMWF, buoys and ASCAT-KNMI winds match well, and on the other hand, platforms and other satellite winds also match well but are higher, with biases reaching −7 m s^{-1} at 30 m s^{-1}. Defining the reference for observed winds between these two groups is certainly not evident. There are many assumptions and approximations in models, experiments and data processing. Note that in the first group, the common link is buoys, and is used as a reference for ECMWF model validation and ASCAT-KNMI calibration. Several studies mentioned a possible underestimation of buoy winds (Zeng and Brown, 1998). This could cause the first group of data to be biased low.

4.3. *Application to other storms*

In order to have more robust statistics, we applied this method to three other storms. We selected them among the ten more energetic events over period 2005–2015 in the northeast Atlantic (Table 1). We chose the events with the strongest winds, where remote-sensing data were available. The storms *Alexandra*, *Erich* and *Uwe* were the best candidates. Simulations were conducted during 5 days, and wind biases were computed between model and buoys, platforms, ASCAT-KNMI, WindSat and SMOS data. The method was exactly as described previously, except that we use L3 instead of L2 products for ASCAT-KNMI winds. Results on Figure 6 are comparable to the ones obtained for *Kaat* and *Lilli* storms, showing the same order of magnitude for the underestimation of high winds. We find the same bias between buoys and platforms, except for *Erich* storm where buoy and platform winds are coherent.

Table 4. Wind stress parametrizations tested in this study.

Parametrization	References
[1] Coupled ECWAM/IFS with default ECMWF parametrization.	Janssen (1991)
[2] Coupled ECWAM/IFS with WW3 physics (i.e. different wave dissipation and growth parametrizations).	Ardhuin *et al.* (2010) as implemented in ECWAM.
[3] Coupled ECWAM/IFS with wave-age-dependent parametrization.	Oost *et al.* (2002)
[4] Coupled ECWAM/IFS with empirically adjusted Charnock parametrization.	This study
[5] Constant Charnock 0.018	

5. Sensitivity to wind stress parametrization

In this part, we examine five alternative wind stress parametrizations (Table 4), including a newly developed one. The objective is to evaluate how high winds could deviate from those derived from ECMWF default parametrization.

5.1. *Alternative wind stress parametrizations*

In the coupled wave–atmosphere model, the effects of waves on the stress are represented by a modification of the Charnock

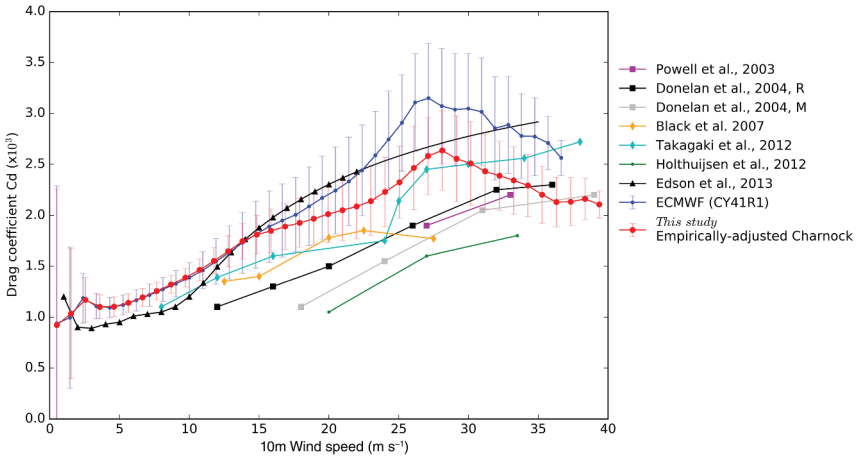

Figure 7. Comparison of drag coefficient for ECMWF (CY41R1) parametrization, empirically adjusted Charnock parametrization and observations (Donelan *et al.*, 2004). 'R' or 'M' corresponds to different measurement techniques, 'Reynolds' or 'Momentum Budget'. Error bars correspond to one standard deviation. [Colour figure can be viewed at wileyonlinelibrary.com].

parameter α. The operational ECMWF parametrization is used as a reference ([1] in Table 4).

The second parametrization ([2]) uses an adjustment to the Janssen parametrization described as 'ST4-TEST471' in WW3DG (2016) and also implemented in ECWAM. It uses Eq. (7), as in default ECMWF, but with β given by Ardhuin *et al.* (2010) and $E(f,\theta)$ influenced by a different dissipation term. The main difference consists in the parametrization for the dissipation of waves, based on swell dissipation measurements (Ardhuin *et al.*, 2009) and the saturation-based dissipation of Phillips (1985), that gives excellent results in terms of wave heights and spectral parameters, including a spectral tail that is significantly different from the one produced by the Janssen (1994) parametrizations. Parametrizations in Ardhuin *et al.* (2010) had spurious jumps in the swell dissipation rate that were corrected in Rascle and Ardhuin (2013), but show very little variability of C_d as a function of wave age (Rascle and Ardhuin, 2013). This reduced variability of C_d comes from a sheltering coefficient s_u, set to 1 in Ardhuin *et al.* (2010), that reduces the wave growth at high frequency. It was introduced to balance the dissipation rate. Using $s_u = 0.3$ restores some of the C_d variability. This setting is described as 'TEST471' (WW3DG, 2016). The parameters tested in ECWAM are similar with $\alpha_1 = 0.006$ instead of 0.0095 and $s_u = 0.4$ instead of 0.3. Note also that WAVEWATCH III® TEST471 imposes a high-frequency tail as discussed in section 3.1.

The third parametrization ([3]) uses a Charnock parameter defined from the wave age. Several studies based on observations of sea state and wind stress, devised to demonstrate a possible sea-state influence on the wind stress, suggested than the Charnock parameter may indeed be expressed as a function of the wave age (Donelan, 1982; Komen *et al.*, 1998; Oost *et al.*, 2002; Drennan *et al.*, 2003). Considerations based on dimensional analysis led these authors to propose expressions of the form $\alpha = a\xi^b$, where a and b are determined from *in situ* measurements and ξ is the wave age, $\xi = C_p/u_*$ where C_p is the phase velocity at the peak of the wave spectrum. The parametrization by Oost *et al.* (2002) used in this study is based on data from a research platform in the North Sea, with wind speed ranging from 6 to 18 m s^{-1},

$$\alpha = 50\xi^{-2.5}. \tag{9}$$

Drennan *et al.* (2003) suggested another expression, based on data from field campaigns in the Mediterranean Sea, with winds also lower than 20 m s^{-1},

$$\alpha = 1.7\xi^{-1.7}. \tag{10}$$

The differences between these two references underline the possible influence of the dataset in each parametrization. Moreover, there are still discussions – and no consensus – on these results, as the strong correlations obtained in the observations could be mainly due to self-correlation, u_* being part of the two parameters α and ξ (Andreas, 2009).

The fourth parametrization ([4]) is our empirically adjusted Charnock parametrization. It keeps the Janssen (1991) parametrization in the wave model, but modifies the value of α passed to the atmospheric model. This modification keeps the wave-induced variability but reduces the values of α at high wind speeds to obtain values of the drag coefficient closer to those obtained *in situ* (Powell *et al.*, 2003; Black *et al.*, 2007; Holthuijsen *et al.*, 2012; Edson *et al.*, 2013). These studies give drag coefficients that potentially saturate for winds above 30 m s^{-1}. This is still a matter of debate, due to uncertainties in wind and stress measurement at very high winds. We adjusted our parametrization to obtain a maximum C_d of 2.5×10^{-3} for wind speed around 30 m s^{-1} (Figure 7), and to keep a lower variability with the sea state. We thus relaxed the Charnock coefficient obtained from default ECMWF towards lower values. This adjusted Charnock is only used for the atmospheric model roughness, but the wave model integration is unchanged. For this, we first tabulated the mean Charnock (α, see appendix A) given by default ECMWF every 1 m s^{-1} bin, from the full year 2014 of global IFS simulations. Below 15 m s^{-1} we use:

$$\alpha_i = \overline{\alpha}_{ib} + \beta(\alpha_i - \overline{\alpha}_{ib}) \tag{11}$$

in which we keep the mean Charnock α_{ib}, but we reduce the variability through the β coefficient, ranging from 0 (no variability) to 1 (keeping all variability). Above 15 m s^{-1}, we use:

$$\alpha_i = \alpha_0 + \beta(\alpha_i - \overline{\alpha}_{ib}) \tag{12}$$

in which the mean Charnock reduced to the constant α_0. We further adjusted parameters to have drag values more consistent with *in situ* measurements (Figure 7), leading to a threshold of 15 m s^{-1}, $\alpha_0 = 0.02$ and $\beta = 0.5$. These parameters could be optimized in future studies.

With this parametrization [4], the Charnock variability decreases by a factor two, and the average values of the Charnock parameter are lowered for winds greater than 15 m s^{-1} (Figures 8(a) and (b)). This leads to maximum Charnock values of about 0.06 instead of 0.12, and an average value of about 0.02 instead of 0.04 at 25 m s^{-1}. As a consequence, this parametrization reduces the drag coefficient, the average value decreasing from 0.003 to 0.0025 at 30 m s^{-1} (Figures 8(c) and (d)). For low wind speeds, high drag values correspond to the viscous laminar flow (Eq. (4)). In comparison with high winds observations, the parametrization [4] gives lower drag values than default ECMWF.

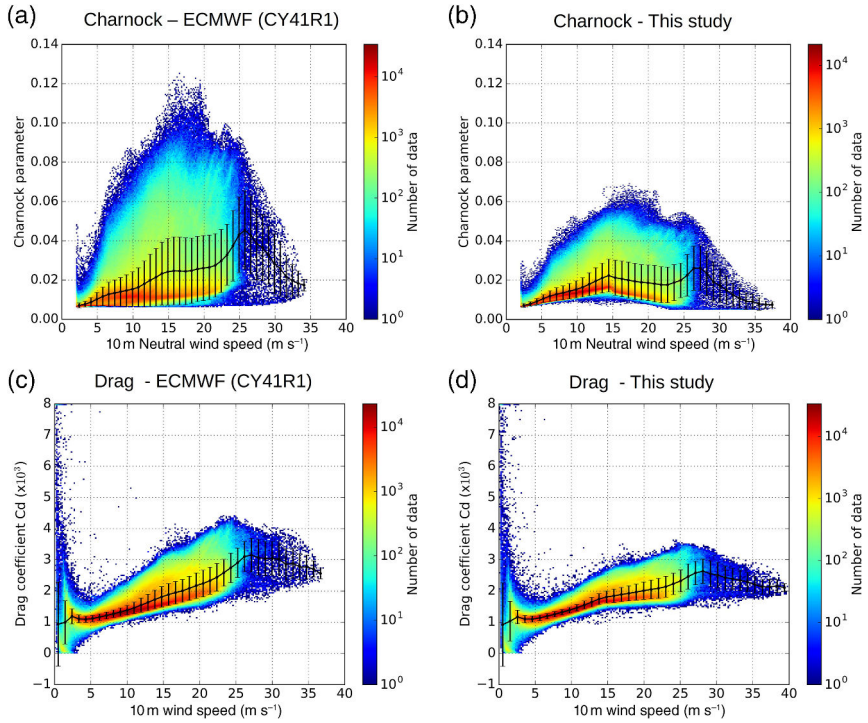

Figure 8. (a, b) Charnock parameter and (c, d) drag coefficient, during *Kaat* and *Lilli* storms from 23 to 27 January 2014, with (a, c) ECMWF (CY41R1) parametrization and (b, d) empirically adjusted Charnock parametrization. Error bars correspond to one standard deviation. [Colour figure can be viewed at wileyonlinelibrary.com].

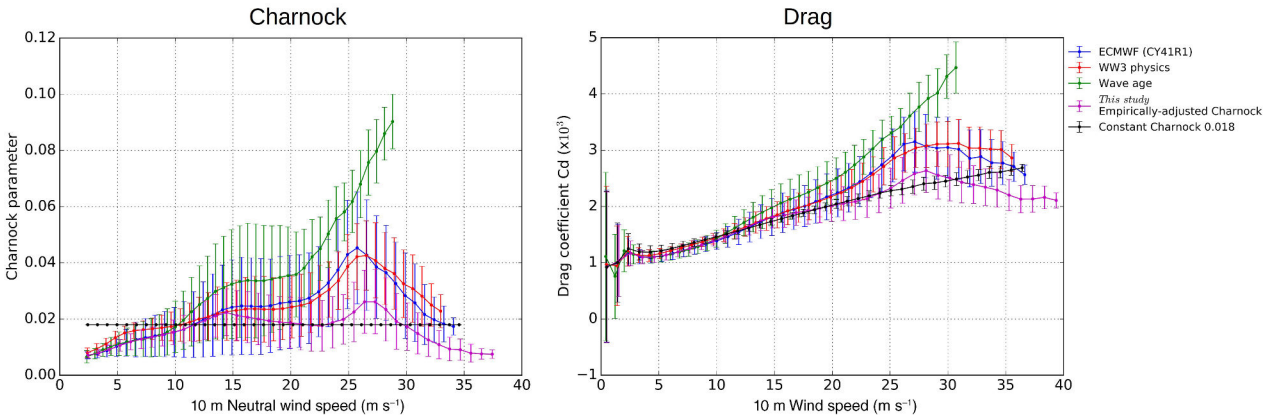

Figure 9. (a) Charnock parameter and (b) drag coefficient, during *Kaat* and *Lilli* storms (from 23 to 27 January 2014), for the five tested parametrizations. Error bars correspond to one standard deviation. [Colour figure can be viewed at wileyonlinelibrary.com].

Finally, the fifth parametrization ([5]) is without wave feedback, using a constant Charnock parameter of 0.018 in IFS.

We simulated *Kaat* and *Lilli* storms from 23 to 27 January 2014, with the five parametrizations described above. The resulting Charnock parameters and drag coefficients were extracted on a 0.125° grid over the northeast Atlantic (Figure 9). The parametrization [3] gives the strongest values of Charnock, leading to high values of drag, above 0.003 for wind speeds above 25 m s^{-1}. These drag values are unrealistic compared with observations (Figure 7). The wave-age-dependent parametrization [3] is based on an experiment with winds ranging from 6 to 18 m s^{-1}; when extrapolating this relation to higher winds, unrealistically high drag coefficients are produced. The WW3 physics parametrization [2] is close to the default ECMWF parametrization, but with less variability of C_d as a function of wave age. This could be adjusted with fine-tuning parameters, particularly by decreasing the sheltering coefficient. The empirically adjusted Charnock parametrization [4] helps reducing the Charnock parameter and drag coefficient compared with ECMWF parametrization, leading to the lowest drag values, even lower than the constant Charnock parameter: C_d reaches 0.002 at 36 m s^{-1}, instead of 0.0027 for a constant Charnock.

5.2. *Results*

Considering alternative parametrizations, we expect to have stronger winds, compared to those obtained with the default ECMWF parametrization. Simulations were carried out from 23 to 27 January 2014. ECWAM computes (i) wave-induced stress following Eq. (7), (ii) total stress from tabulated solution of Eqs (1), (2) and (5) depending on 10 m wind speed (coming from the atmospheric model) and wave-induced stress, (iii) roughness length following Eqs (5) and (6), and finally (iv) the Charnock parameter following the second part of Eq. (4) which passes into the atmosphere. Then, IFS computes (i) u_* and z_0 following Eq. (4), (ii) the drag following Eq. (3), and then (iii) U_{10} following Eq. (2), which is sent on to ECWAM.

For midlatitude storms such as *Kaat* and *Lilli*, a larger Charnock parameter generally leads to a larger roughness length (not shown), a higher drag coefficient, higher wind stress, and lower wind speed (Figure 10). Conversely, a lower Charnock parameter

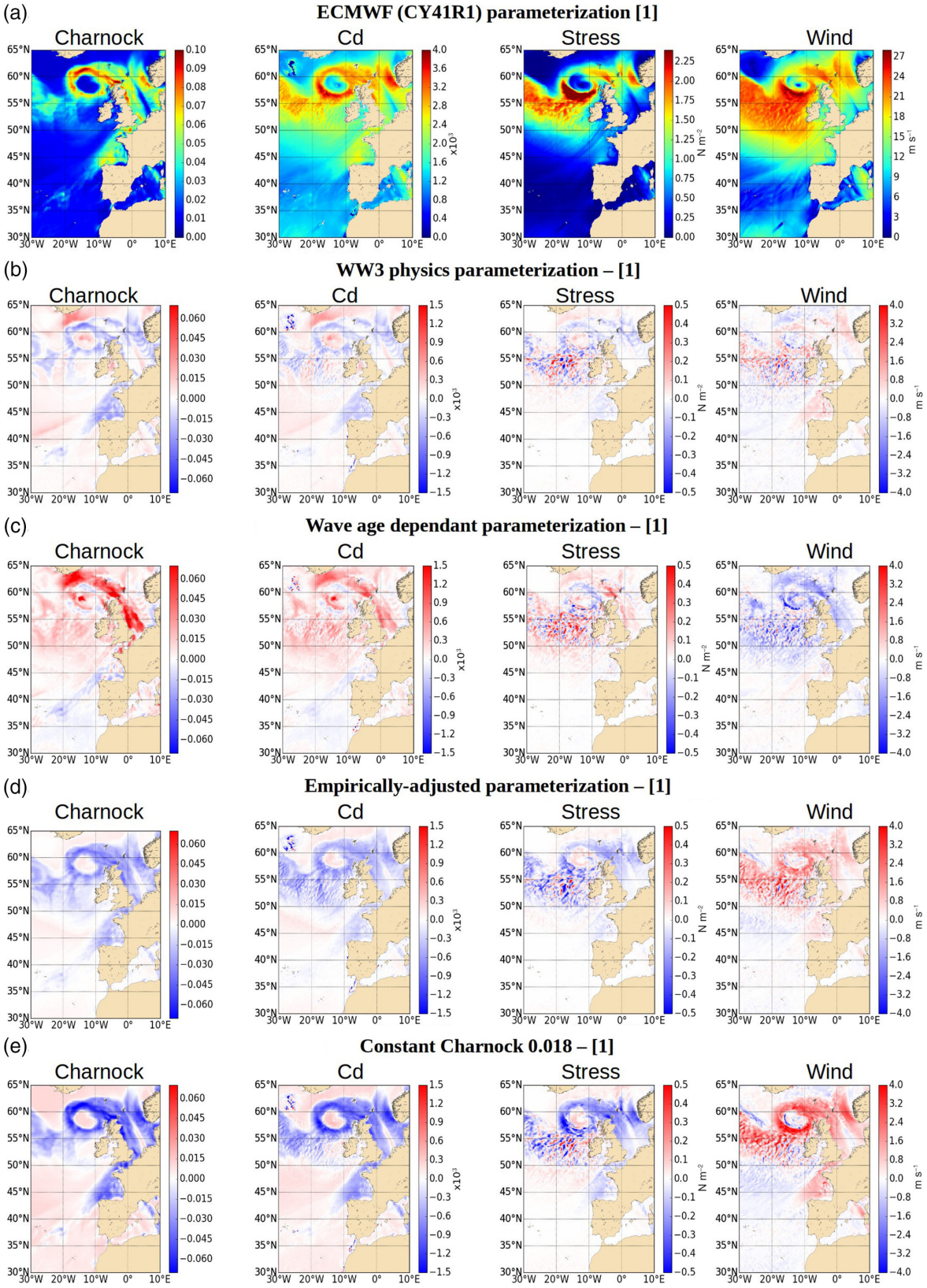

Figure 10. (a–e) Impact of different parametrizations on Charnock, drag coefficient, wind stress and wind on 26 January 2014 at 1200 UTC. [Colour figure can be viewed at wileyonlinelibrary.com].

leads to higher wind speed and lower central surface pressure in the storm. The wave-age dependency of the Charnock parameter is based on the fact that young – compared to old – waves are steeper and lead to a higher roughness length (expressed as Eq. (5) in Janssen (1991)). However, the roughness length is still physically difficult to interpret. It is not a direct measurable parameter over the ocean, but generally deduced from other measurements (for example wind measurements at different heights, and application of a logarithmic formula to infer the roughness length). When roughness increases, friction also increases and slows the wind down. As the wind decreases, the feedback effect results in a smoother sea state, possibly leading in

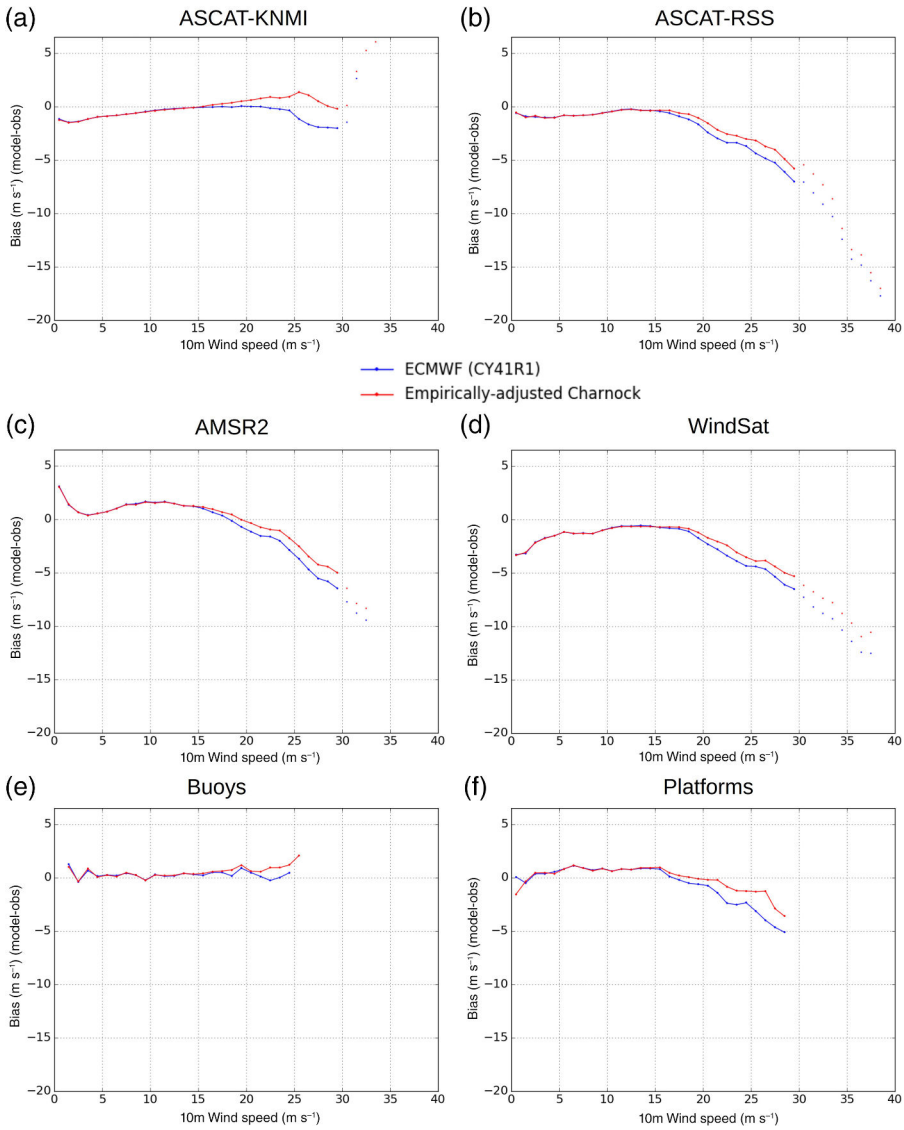

Figure 11. Ten-metre wind speed biases, over the period 23–27 of January 2014 on the northeast Atlantic, between (a) ASCAT-KNMI, (b) ASCAT-RSS, (c) AMSR2, (d) WindSat, (e) buoys, (f) platforms, and model for the default ECMWF CY41R1 (blue) and empirically adjusted (red) parametrizations. Beyond 30 m s^{-1}, values are plotted as points, due to large uncertainties in observations. [Colour figure can be viewed at wileyonlinelibrary.com].

turn to a reduced friction velocity and consequently to increased wind speed.

The use of the WW3-physics-based parametrization [2] instead of the ECMWF default parametrization [1] (Figure 10(b)) leads to slightly lower Charnock values, and consequently marginally higher wind speeds. The wave-age-dependent parametrization [3] (Figure 10(c)) gives higher Charnock values and lower winds. This is due to unrealistic extrapolation to high winds of a relation based on winds ranging from 6 to 18 m s^{-1} (Oost *et al.*, 2002). Finally, an empirically adjusted Charnock parametrization [4] (Figure 10(d)) leads to lower Charnock parameters and stronger high winds than with the ECMWF parametrization. Winds become close to but lower than those with the constant Charnock parametrization (Figure 10(e)). For winds above 30 m s^{-1}, the parametrization [4] gives higher winds than with the constant Charnock parametrization [5], as the adjusted Charnock parameter is lower than 0.018 (Figure 9(a)).

To estimate the impact of the new wind stress parametrization [4], we computed biases between winds from the model and the observations for the default ECMWF and the empirically adjusted Charnock parametrizations. The new parametrization efficiently reduces the bias by about 2 m s^{-1} at 30 m s^{-1} for ASCAT-KNMI, ASCAT-RSS, AMSR2 and WindSat (Figures 11(a–d) and (f)). This demonstrates that adjusting the parametrization is one way of obtaining winds closer to satellite estimates, in particular radiometer estimates.

The bias (Figure 11(e)) between the wind speeds obtained with the default ECMWF and buoy observations is close to zero, and the new parametrization leads to a positive bias, i.e. simulated winds higher than buoy winds.

Although this new parametrization certainly improves high winds, there is still a negative bias with the majority of observations. The effective ECWMF model resolution (about 6–8 times the 16 km spatial resolution for the TL1279 Gaussian grid) might be too coarse to represent accurately high winds as in the case of satellite products, which have a resolution of 0.125°. Moreover, initial conditions come from the ECMWF operational analysis, and the data assimilation process used in the operational system may prevent high winds from ASCAT from being integrated adequately: (i) ASCAT data are systematically corrected from a possible bias with the model, and (ii) some strong ASCAT winds can be rejected prior to assimilation, partially because of the thinning applied (only one observation out of four is assimilated) and quality control (De Chiara *et al.*, 2016); an alternative method to the current quality control is under testing at ECMWF. On the top of that (see the discussion in section 4.3) observations can also be biased at high wind speed.

6. Conclusions

We started this work because different atmospheric models had different biases on the wind speed in storm conditions, possibly due to different surface drag parametrizations. The objectives were (i) to evaluate ECMWF strong winds against observations, and (ii) to test how an alternative wind stress parametrization could lead to a more accurate model. During *Kaat* and *Lilli* storms (23–27 January 2014), we compared simulated winds from the ECMWF coupled wave–atmosphere model with *in situ* and satellite observations available in the North Atlantic. We then developed an empirically adjusted Charnock parametrization, to obtain winds closer to observations.

The first result is that moderate simulated winds ($5–20\,m\,s^{-1}$) agree well with both *in situ* and satellite observations, whereas strong winds (above $20\,m\,s^{-1}$) are generally underestimated compared with observations; the negative bias can reach $-7\,m\,s^{-1}$ at $30\,m\,s^{-1}$.

The second result is that biases exist between observations. We identified two groups of data. The first one, composed of buoys and ASCAT-KNMI, gives lower strong winds than the second one, which is composed of platforms and other remote-sensing data used in this study (AMSR2, ASCAT-RSS, WindSat, SMOS and JASON-2). It is difficult to conclude which dataset should be used as a reference, but buoys and ASCAT-KNMI winds are likely to be underestimated.

Lastly, the third result is that a newly empirically adjusted Charnock parametrization would lead to higher winds than the default ECMWF ones. Yet, common wave-age-dependent parametrization gives larger drag coefficients than measurements – and lower winds – and is not appropriate for coupling.

This study was then reproduced for three other storms in the northeast Atlantic: *Alexandra* (8 December 2014), *Erich* (10 March 2015) and *Uwe* (7 December 2015); results are similar and confirm these conclusions. Moreover, NASA/SMAP data were also exploited for *Uwe*, showing similar biases with the model consistent with WindSat and SMOS (Meissner *et al.*, 2017).

While this sensitivity study shows the impact of drag parametrizations on winds, a next step is needed to study how the atmosphere evolves and adjusts, particularly the 500 hPa geopotential. Similar work should be further undertaken to study the impact of the drag on the ocean circulation.

The significant bias between buoy and platform strong winds suggests that *in situ* measurements should be handled with particular care. Despite investigation, it is finally not clear what the 'surface wind reference' should be, and where the 'truth' lies. More dedicated investigations are necessary to document the respective quality of *in situ* wind measurements for high winds better. More datasets representing extreme conditions are needed, in order to validate models and to calibrate remote-sensing instruments.

Indeed, the role of the wind datasets in building the GMFs is essential and different datasets lead to different GMFs. As a consequence, ASCAT-KNMI strong winds show a systematic negative bias with respect to ASCAT-RSS ones.

Not surprisingly, the sensitivity of the atmosphere to drag parametrizations shows that stronger winds can be obtained. Our limited simulations do not show a big impact on the overall atmospheric circulation but more tests will have to be performed before our alternative parametrization is considered for operational applications.

From a physical point of view, the drag is expected to combine various processes including air flow separation over breaking waves (e.g. Reul *et al.*, 1999, 2008; Kudryavtsev *et al.*, 2014), which is not represented in the quasi-linear model of Fabrikant (1976) and Janssen (1986) on which the ECMWF parametrization is based. Also, Janssen's parametrization (Eq. (5)) produces a ratio τ_w/τ that is often very close to 1 for young seas and is very sensitive to the high-frequency spectrum tail, a part of the spectrum that is very crudely represented in wave models today (Kudryavtsev *et al.*, 2014; Peureux and Ardhuin, 2016).

Finally, high-quality strong winds from *in situ* and remote sensing are essential, as these data are assimilated in numerical weather prediction models. In the near future, MetOp-Second Generation (MetOp-SG) will be launched after 2020 and will include on board a C-band scatterometer with co-polarization (VV, similar to ASCAT), but also cross-polarization (VH). The addition of VH-polarization will significantly improve strong winds retrieval (e.g. Zhang and Perrie, 2012; Mouche *et al.*, 2017).

Acknowledgements

This work was performed as part of an ECMWF 'special project', which provided access to ECMWF computing and archive facilities in this research. We thank all ECMWF staff for the warm welcome and excellent support provided to LPG, FA and MNB. KNMI (Royal Netherlands Meteorological Institute), SOLab (Satellite Oceanography Laboratory, Russian State Hydrometeorological University), Remote Sensing Systems (RSS), NASA PODAAC and CNES Aviso provided remote-sensing data, and Germany's National Meteorological Service provided synoptic charts. We also thank O. Breivik and Norwegian Meteorological Institute for providing wind measurements from Norwegian platforms. We warmly thank Glyn Orpwood for his great help in improving the written English. Finally, the authors would like to thank reviewers for their careful reading and their constructive comments, which allowed this article to be improved.

Appendix A: Mean Charnock for empirically-adjusted parametrization

The Table A1 gives the values of the mean Charnock provided by default ECMWF parametrization. Values are computed every $1\,m\,s^{-1}$ bin, from the full year 2014 of global IFS simulations. This table A1 is used for empirically adjusted Charnock parameterization (see section 5.1).

Appendix B: Standard deviations and root-mean-square errors between ECMWF simulated winds and observations

The Figures B1 and B2 show standard deviation and root-mean-square (RMS) errors between ECMWF model (CY41R1) and observations (buoys, platforms, and satellite data), computed

Table A1. Mean Charnock tables for empirically adjusted Charnock parametrization, based on 2014 year analysis.

Wind ($m\,s^{-1}$)	Mean Charnock	Wind ($m\,s^{-1}$)	Mean Charnock
1	0.0066	23	0.0397
2	0.0069	24	0.0413
3	0.0079	25	0.0422
4	0.0094	26	0.0431
5	0.0109	27	0.0443
6	0.0120	28	0.0463
7	0.0129	29	0.0487
8	0.0139	30	0.0491
9	0.0150	31	0.0494
10	0.0164	32	0.0537
11	0.0178	33	0.0543
12	0.0192	34	0.0586
13	0.0205	35	0.0582
14	0.0219	36	0.0515
15	0.0234	37	0.0518
16	0.0249	38	0.0463
17	0.0264	39	0.0492
18	0.0281	40	0.0490
19	0.0300	41	0.0508
20	0.0322	42	0.0362
21	0.0348	43	0.0338
22	0.0374	–	–

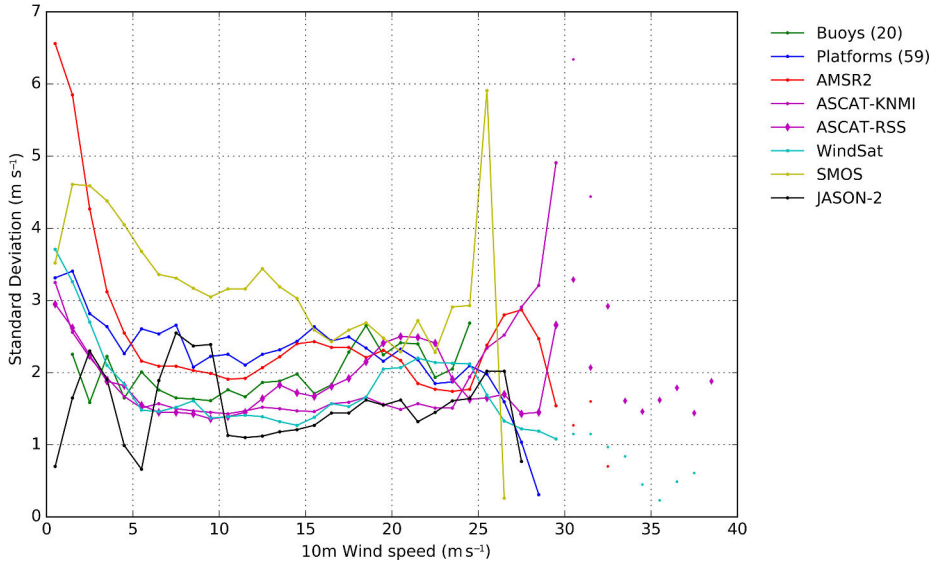

Figure B1. Standard deviation between ECMWF model (CY41R1) and observations (buoys, platforms and satellite data), computed from 23 to 27 January 2014 on the northeast Atlantic. [Colour figure can be viewed at wileyonlinelibrary.com].

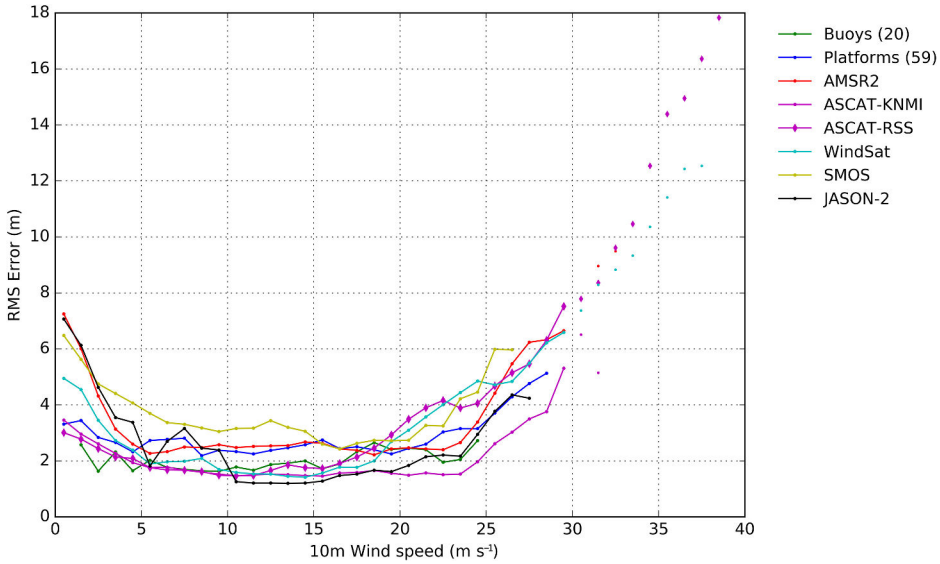

Figure B2. Root-mean-square (RMS) errors between ECMWF model (CY41R1) and observations (buoys, platforms and satellite data), computed from 23 to 27 January 2014 on the northeast Atlantic. [Colour figure can be viewed at wileyonlinelibrary.com].

from 23 to 27 January 2014 on the northeast Atlantic. The last binned values have large standard deviations because they represent only a few points.

References

Andreas EL. 2009. Relating the drag coefficient and the roughness length over the sea to the wavelength of the peak waves. *J. Phys. Oceanogr.* **39**: 3011–3020.

Ardhuin F, Chapron B, Collard F. 2009. Observation of swell dissipation across oceans. *Geophys. Res. Lett.* **36**: L06607. https://doi.org/10.1029/2008GL037030.

Ardhuin F, Rogers E, Babanin AV, Filipot J, Magne R, Roland A, Westhuysen A van der, Queffeulou P, Lefevre J, Aouf L, Collard F. 2010. Semi empirical dissipation source functions for ocean waves. Part I: Definition, calibration, and validation. *J. Phys. Oceanogr.* **40**: 1917–1941.

Bentamy A, Croize-Fillon D, Perigaud C. 2008. Characterization of ASCAT measurements based on buoy and QuikSCAT wind vector observations. *Ocean Sci.* **4**: 265–274. https://doi.org/10.5194/os-4-265-2008..

Black PG, D'Asaro EA, Drennan WM, French JR, Niller PP, Sanford TB, Terrill EJ, Walsh EJ, Zhang JA. 2007. Air–sea exchange in hurricanes: Synthesis of observations from the coupled boundary layer air–sea transfer experiment. *Bull. Am. Meteorol. Soc.* **88**: 359–374.

Chapron B, Bingham A, Collard F, Donlon C, Johannessen JA, Piolle JF, Reul N. 2010. 'Ocean remote sensing data integration – Examples and outlook'. *OceanObs' OceanObs '09: Sustained Ocean Observations and Information for Society*, Vol. 1, 21–25 September 2009. Venice, Italy.

Charnock H. 1955. Wind stress on a water surface. *Q. J. R. Meteorol. Soc.* **81**: 639–640.

Chou KH, Wu CC, Lin SZ. 2013. Assessment of the ASCAT wind error characteristics by global dropwindsonde observations. *J. Geophys. Res. Atmos.* **118**: 9011–9021. https://doi.org/10.1002/jgrd.50724.

De Chiara G, English S, Janssen P, Bidlot JR. 2016. '*ASCAT ocean surface wind assessment*'. ECMWF Technical Memorandum 776.

Dee DP, Uppala SM, Simmons AJ, Berrisford P, Poli P, Kobayashi S, Andrae U, Balmaseda MA, Balsamo G, Bauer P, Bechtold P, Beljaars ACM, van de Berg L, Bidlot JR, Bormann N, Delsol C, Dragani R, Fuentes M, Geer AJ, Haimberger L, Healy SB, Hersbach H, Hólm EV, Isaksen L, Kållberg P, Köhler M, Matricardi M, McNally AP, Monge-Sanz BM, Morcrette JJ, Park BK, Peubey C, de Rosnay P, Tavolato C, Thépaut JN, Vitart F. 2011. The ERA-Interim reanalysis: Configuration and performance of the data assimilation system. *Q. J. R. Meteorol. Soc.* **137**: 553–597. https://doi.org/10.1002/qj.828.

Donelan MA. 1982. 'The dependence of the aerodynamic drag coefficient on wave parameters'. Paper presented at *1st International Conference on Meteorology and Air–Sea Interaction of the Coastal Zone*, The Hague, Netherlands, 10–14 May 1982. American Meteorological Society: Boston, pp. 381–387.

Donelan MA, Haus BK, Reul N, Plant WJ, Stiassnie M, Graber HC, Brown OB, Saltzman ES. 2004. On the limiting aerodynamic roughness of the ocean in

very strong winds. *Geophys. Res. Lett.* **31**: L18306. https://doi.org/10.1029/2004GL019460.

Drennan WB, Graber HC, Hauser D, Quentin C. 2003. On the wave age dependence of wind stress over pure wind seas. *J. Geophys. Res.* **108**: 8062. https://doi.org/10.1029/2000JC000715.

ECMWF. 2015a. *IFS Documentation CY41R1*. ECMWF Book.

ECMWF. 2015b. *IFS Documentation CY41R1. Part VII: ECMWF Wave Model*. ECMWF Book Chapter.

Edson JB, Jampana V, Weller RA, Bigorre SP, Plueddemann AJ, Fairall CW, Miller SD, Mahrt L, Vickers D, Hersbach H. 2013. On the exchange of momentum over the open ocean. *J. Phys. Oceanogr.* **43**: 1589–1610. https://doi.org/10.1175/JPO-D-12-0173.1.

Fabrikant AL. 1976. Quasilinear theory of wind-wave generation. *Izv. Atmos. Ocean. Phys.* **12**: 524–526.

Furevik BR, Haakenstad H. 2012. Near-surface marine wind profiles from rawinsonde and NORA10 hindcast. *J. Geophys. Res.* **117**: D23106. https://doi.org/10.1029/2012JD018523.

Gaiser PW, St. Germain KM, Twarog EM, Poe GA, Purdy W, Richardson D, Grossman W, Jones LW, Spencer D, Golba G, Cleveland J, Choy L, Bevilacqua RM, Chang PS. 2004. TheWindSat spaceborne polarimetric microwave radiometer: Sensor description and early orbit performance. *IEEE Trans. Geosci. Remote Sens.* **42**: 2347–2361.

Hanafin J, Quilfen Y, Ardhuin F, Sienkiewicz J, Queffeulou P, Obrebski M, Chapron B, Reul N, Collard F, Corman D, De Azevedo EB, Vandemark D, Stutzmann E. 2012. Phenomenal sea states and swell from a North Atlantic storm in February 2011: A comprehensive analysis. *Bull. Am. Meteorol. Soc.* **93**: 1825–1832. https://doi.org/10.1175/BAMS-D-11-00128.1.

Holthuijsen LH, Powell MD, Pietrzak JD. 2012. Wind and waves in extreme hurricanes. *J. Geophys. Res.* **117**: C09003. https://doi.org/10.1029/2012JC007983.

Hoskins BJ, Hodges KI. 2002. New perspectives on the Northern Hemisphere winter storm tracks. *J. Atmos. Sci.* **59**: 1041–1061.

Janssen PAEM. 1986. '*On the effect of gustiness on wave growth*'. KNMI Afdeling Oceanografisch Onderzoek memo 00-86-18, De Bilt, The Netherlands.

Janssen PAEM. 1991. Quasi-linear theory of wind-wave generation applied to wave forecasting. *J. Phys. Oceanogr.* **21**: 1631–1642.

Janssen PAEM. 1994. '*Results with a coupled wind wave model*'. ECMWF Technical Report 71. ECMWF: Reading, UK.

Janssen PAEM. 2004. *The Interaction of Ocean Waves and Wind*. Cambridge University Press: Cambridge, UK.

Jarosz ED, Mitchell A, Wang DW, Teague WJ. 2007. Bottom-up determination of air–sea momentum exchange under a major tropical cyclone. *Science* **315**: 1707–1709. https://doi.org/10.1126/science.1136466.

Kazumori M, Geer AJ, English SJ. 2016. Effects of all-sky assimilation of *GCOM-W*/AMSR2 radiances in the ECMWF numerical weather prediction system. *Q. J. R. Meteorol. Soc.* **142**: 721–737. https://doi.org/10.1002/qj.2669.

Komen G, Janssen PAEM, Makin V, Oost W. 1998. On the sea state dependence of the Charnock parameter. *Global Atmos. Ocean. Syst.* **5**: 367–388.

Kudryavtsev V, Chapron B, Makin V. 2014. Impact of wind waves on the air–sea fluxes: A coupled model. *J. Geophys. Res. Oceans* **119**: 1217–1236. https://doi.org/10.1002/2013JC009412.

Mastenbroek C, Burgers G, Janssen PAEM. 1993. The dynamical coupling of a wave model and a storm surge model through the atmospheric boundary layer. *J. Phys. Oceanogr.* **23**: 1856–1866.

Meissner T, Wentz FJ. 2009. Wind-vector retrievals under rain with passive satellite microwave radiometers. *IEEE Trans. Geosci. Remote Sens* **47**: 3065–3083.

Meissner T, Ricciardulli L, Wentz FJ. 2017. Capability of the SMAP mission to measure ocean surface winds in storms. *Bull. Am. Meteorol. Soc.* **98**: 1660–1677. https://doi.org/10.1175/BAMS-D-16-0052.1.

Mouche AA, Chapron B, Zhang B, Husson R. 2017. Combined co- and cross-polarized SAR measurements under extreme wind conditions. *IEEE Trans. Geosci. Remote Sens.* **PP**: 1–10. https://doi.org/10.1109/TGRS.2017.2732508.

Muller H, Pineau-Guillou L, Idier D, Ardhuin F. 2014. Atmospheric storm surge modeling methodology along the French (Atlantic and English Channel) coast. *Ocean Dyn.* **64**: 1671–1692. https://doi.org/10.1007/s10236-014-0771-0.

Oost WA, Komen GJ, Jacobs CMJ, van Oort C. 2002. New evidence for a relation between wind stress and wave age from measurements during ASGAMAGE. *Boundary-Layer Meteorol.* **103**: 409–438.

Peureux C, Ardhuin F. 2016. Ocean bottom pressure records from the Cascadia array and short surface gravity waves. *J. Geophys. Res. Oceans* **121**: 2862–2873. http://dx.doi.org/10.1002/2015JC011580

Phillips OM. 1985. Spectral and statistical properties of the equilibrium range in wind-generated gravity waves. *J. Fluid Mech.* **156**: 505–531.

Powell MD, Vickery PJ, Reinhold TA. 2003. Reduced drag coefficient for high wind speeds in tropical cyclones. *Nature* **422**: 279–283.

Quilfen Y, Chapron B, Bentamy A, Gourrion J, Elfouhaily T, Vandemark D. 1999. Global ERS 1 and 2 and NSCAT observations: Upwind crosswind and upwind downwind measurements. *J. Geophys. Res.* **104**: 11459–11469. https://doi.org/10.1029/1998JC900113.

Quilfen Y, Tournadre J, Chapron B. 2006. Altimeter dual-frequency observations of surface winds, waves, and rain rate in tropical cyclone *Isabel*. *J. Geophys. Res.* **111**: C01004. https://doi.org/10.1029/2005JC003068.

Quilfen Y, Prigent C, Chapron B, Mouche AA, Houti N. 2007. The potential of QuikSCAT and WindSat observations for the estimation of sea surface wind vector under severe weather conditions. *J. Geophys. Res.* **112**: C09023. https://doi.org/10.1029/2007JC004163.

Quilfen Y, Vandemark D, Chapron B, Feng H, Sienkiewicz J. 2011. Estimating gale to hurricane force winds using the satellite altimeter. *J. Atmos. Oceanic Technol.* **28**: 453–458. https://doi.org/10.1175/JTECH-D-10-05000.1.

Rascle N, Ardhuin F. 2013. A global wave parameter database for geophysical applications. Part 2: Model validation with improved source term parameterization. *Ocean Modell.* **70**: 174–188.

Reul N, Branger H, Giovanangeli JP. 1999. Air flow separation over unsteady breaking waves. *Phys. Fluids* **11**: 1959–1961. https://doi.org/10.1063/1.870058.

Reul N, Branger H, Giovanangeli JP. 2008. Air flow structure over short-gravity breaking water waves. *Boundary-Layer Meteorol.* **126**: 477–505. https://doi.org/10.1007/s10546-007-9240-3.

Reul N, Tenerelli J, Chapron B, Vandemark D, Quilfen Y, Kerr Y. 2012. SMOS satellite L-band radiometer: A new capability for ocean surface remote sensing in hurricanes. *J. Geophys. Res.* **117**: C02006. https://doi.org/10.1029/2011JC007474.

Reul N, Chapron B, Zabolotskikh E, Donlon C, Quilfen Y, Guimbard S, Piolle JF. 2016. A revised L-band radio-brightness sensitivity to extreme winds under tropical cyclones: The 5 year SMOS-Storm database. *Remote Sens. Environ.* **180**: 274–291.

Reul N, Chapron B, Zabolotskikh E, Donion C, Mouche AA, Tenerelli J, Collard F, Piolle JF, Fore A, Yueh S, Cotton J, Francis P, Quilfen Y, Kudryavtsev V. 2017. A new generation of tropical cyclone size measurements from space. *Bull. Am. Meteorol. Soc.* **98**: 2367–2385, https://doi.org/10.1175/BAMS-D-15-00291.1.

Saha S, Moorthi S, Pan HL, Wu X, Wang J, Nadiga S, Tripp P, Kistler R, Woollen J, Behringer D, Liu H, Stokes D, Grumbine R, Gayno G, Wang J, Hou YT, Chuang HY, Juang HMH, Iredell M, Treadon R, Kleist D, Delst PV, Keyser D, Derber J, Ek M, Meng J, Wei H, Yang R, Lord S, van den Dool H, Kumar A, Wang W, Long C, Chelliah M, Xue Y, Huang B, Schemm JK, Ebisuzaki W, Lin R, Xie P, Chen M, Zhou S, Higgins W, Zou CZ, Liu Q, Chen Y, Han Y, Cucurull L, Reynolds RW, Rutledge G, Goldberg M. 2010. The NCEP climate forecast system reanalysis. *Bull. Am. Meteorol. Soc.* **90**: 1015–1057.

Sapp JW, Alsweiss SO, Jelenak Z, Chang PS, Frasier SJ, Carswell J. 2016. Airborne co-polarization and cross-polarization observations of the ocean-surface NRCS at C-band. *IEEE Trans. Geosci. Remote Sens.* **54**: 5975–5992.

Stopa J, Cheung KF. 2014. Intercomparison of wind and wave data from the ECMWF Reanalysis Interim and the NCEP Climate Forecast System Reanalysis. *Ocean Model* **75**: 65–83. https://doi.org/10.1016/j.ocemod.2013.12.006

Shimura T, Mori N, Takemi T, Mizuta R. 2017. Long-term impacts of ocean wave-dependent roughness on global climate systems. *J. Geophys. Res. Oceans* **122**: 1995–2011. https://doi.org/10.1002/2016JC012621.

Skey SGP, Berger-North K, Swail VR. 1995. 'Detailed measurements of winds and waves in high sea states from a moored NOMAD water buoy'. In *Proceeding of the Fourth International Workshop on Wave Hindcasting and Forecasting*, Banff, Canada, pp. 213–223.

Takagaki N, Komori S, Suzuki N, Iwano K, Kuramoto T, Shimada S, Kurose R, Takahashi K. 2012. Strong correlation between the drag coefficient and the shape of the wind sea spectrum over a broad range of wind speeds. *Geophys. Res. Lett.* **39**: L23604. https://doi.org/10.1029/2012GL053988.

The WAVEWATCH III® Development Group (WW3DG). 2016. '*User manual and system documentation of WAVEWATCH III® version 5.16*', Technical Note 329. NOAA/NWS/NCEP/MMAB: College Park, MD.

Verspeek J, Stoffelen A, Verhoef A, Portabella M. 2012. Improved ASCAT wind retrieval using NWP ocean calibration. *IEEE Trans. Geosci. Remote Sens.* **50**: 2488–2494.

Wu J. 1982. Wind-stress coefficients over sea surface from breeze to hurricane. *J. Geophys. Res.* **87**: 9704–9706.

Zabolotskikh EV, Mitnik LM, Chapron B. 2013. New approach for severe marine weather study using satellite passive microwave sensing. *Geophys. Res. Lett.* **40**: 3347–3350. https://doi.org/10.1002/grl.50664.

Zabolotskikh E, Mitnik L, Chapron B. 2014. GCOM-W1 AMSR2 and MetOp-A ASCAT wind speeds for the extratropical cyclones over the North Atlantic. *Remote Sens. Environ.* **147**: 89–98.

Zeng L, Brown RA. 1998. Scatterometer observations at high wind speeds. *J. Appl. Meteorol.* **37**: 1412–1420.

Zhang B, Perrie W. 2012. Cross-polarized synthetic aperture radar: A new potential technique for hurricanes. *Bull. Am. Meteorol. Soc.* **93**: 531–541. https://doi.org/10.117 5/BAMS-D-11-00001.1.

Chapter 4

Impact on the ocean

4.1 Introduction

This section presents the impact of the wind stress on the ocean. In coastal areas, the wind stress generates surges, due to water pileup along the coast, as well as resonant effects (Moon et al., 2009; Bertin et al., 2012). The amplitude of the surges depends at least from the path of the storm, the intensity and direction of the wind forcing, the bathymetry, and the geometry of the coastline. In some geographical configurations, such as bays, the surge can be the superosition of two contributions: a term due to the local wind, and another one due to incoming wave, generated by remote wind effect (Shen and Gong, 2009). Different authors showed that increasing the surface stress enhances the surges (Mastenbroek et al., 1993; Moon et al., 2009; Bertin et al., 2012).

The wind stress effect is stronger in shallow waters, as its contribution in the momentum equation is divided by the water height (Eq. 4.5). For this reason, we focused on the North Sea, where the bathymetry is lower than 50 m in the southern part (Figure 4.1).

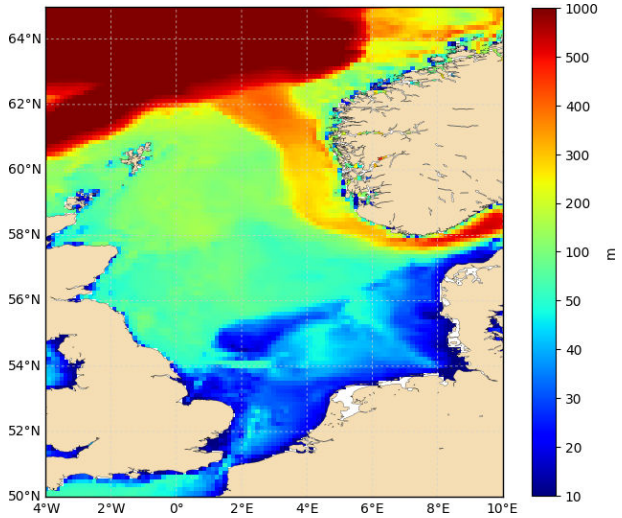

Figure 4.1 – Bathymetry in the North Sea (from TUGO model)

In the North Sea, the tide is semi-diurnal. Its amplitude is quite small, particularly because of the presence of two amphidromic points (Figure 4.2). Amplitude of M_2 tidal wave is smaller than 1.5 m in the North Sea, whereas it is larger than 4 m in some part of the English Channel.

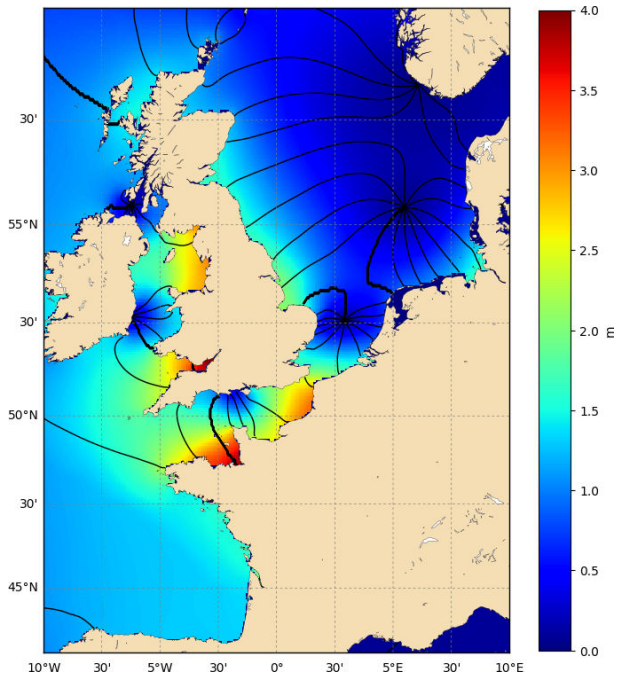

Figure 4.2 – M_2 amplitude and phase (from FES2012 tidal model)

4.2 Generalities on surge observations

4.2.1 Definition

The surges are the differences between the observed and predicted sea level (Simon, 2007). It corresponds to the non determinist part of the sea level signal, whereas the prediction is the determinist part of it. The prediction includes the astronomical tide, but also the radiational tide, i.e. the predictible part of the water levels of meteorological (and not astronomical) origine. As the surge is estimated by substracting the prediction to the observation, it also includes the prediction uncertainty. Note that the surge has no vertical reference, whereas the sea level has one (Chart Datum, Ellipsoid, Mean Sea Level...).

4.2.2 Processes contributing to the surges

The surges are due to many different processes. Generally, the dominant one is atmospheric forcing (Mean Sea Level Pressure and winds), that generates the atmospheric surge. This contribution is commonly of the order of 50 cm, but can reach more than 1 m in case of storms, e.g. for Xynthia in February 2010 at La Rochelle (Pineau-Guillou et al., 2012; Bertin et al., 2012). In case of progression in very shallow waters, as for example in the South of the North Sea, the surges can reach up to 2 or 3 m.

Another important contribution to the total surge is the wave setup, i.e. surge due to wave breaking, in the nearshore areas (Brown et al., 2010; Idier et al., 2012b; Bertin et al., 2015). Its contribution to the total surge can be significant and reach several tens of centimetres, and even more ($>$ 1 m). For instance, values of 0.5 to 1.5 m were reported in Liverpool Bay (Brown et al., 2010), more than 0.5 m in the south part of the Bay of Biscay, i.e. 50% or more of the total surge (Idier et al., 2012b), and 10 to 20 cm in the central part of the Bay of Biscay (Bertin et al., 2015). In very coastal areas, it can contribute up to 80% of the total storm surge (Pedreros et al., 2018).

Another contribution to the surges is tide-surge interaction, which can locally reach more than 70 cm in the English Channel (Idier et al., 2012a).

Other contributions are the waves whose signature may be significant at the surface when propagating in coastal areas, e.g. meteo-tsunami (Haigh et al., 2016), infragravity waves - only few cm in deep ocean (Aucan and Ardhuin, 2013) but can reach more than 1 m in coastal areas (Sheremet et al., 2014)), internal solitary waves (can reach 20 cm in coastal areas) as well as internal waves, rogue waves, tsunamis - surge due to an earthquake, landslide or volcanic eruption.

Finally, seiches - resonnance phenomena in closed or semi-closed basins - are also contributing to the surges. Their amplitude can be significant in harbours, and reach sometimes several tens of centimeters.

Process	Location	Computed in hydrodynamic models
Atmospheric surge due to wind and atm. pressure	Everywhere	Yes, if there is atmospheric forcing
Wave setup, i.e. surge due to wave breaking	In nearshore areas	Yes, if there is radiation stress
Tide surge interaction	Significant in very shallow waters	Yes, if meteorological and tide forcing
Meteo-tsunami		Yes, if space resolution is fine enough
Infragravity waves		No, in wave models only
Internal waves	Everywhere	Yes, in a baroclinic model
Rogue waves		No
Tsunamis i.e. surge due to an earthquake, landslide or volcanic eruption		No
Seiches i.e. resonnance phenomena in closed or semi-closed basins	Mainly in harbours or bays	Yes, if spatial resolution is sufficient. This is rarely the case in global models.

Table 4.1 – Various processes contributing to the surge

Here, we focus only on the atmospheric surge, caused by the wind and the Mean Sea Level Pressure. This is the only processus represented in the ocean model used in this study. However, it is essential to keep in mind all these processes, as the observations will include them (or not, e.g. wave setup will be in tide gauge only if wave breaking took place offshore the harbour).

4.2.3 Observations at tide gauges

Tide gauges record sea level related to a reference level (e.g. Chart Datum, Mean Sea Level). To compute the surges, we subtract the prediction to the observations. We used the Tidal ToolBox developped by LEGOS (Allain, 2013). The method is the following:

1. A harmonic analysis is performed on the sea level observations to estimate the harmonic constants (amplitude and phase) of the tidal constituents. The constituent list we used is the "COASTAL" default one in the Tidal ToolBox, which includes 75 constituents. The duration of the observations (generally several years) allows a good precision of the harmonic analysis. However, when the duration is not long enough to separate two constituents, the Tidal Toolbox uses automatically the admittance method (Simon, 2007; Allain, 2013).

2. From the harmonic constants, a prediction is computed over the same period than the observations.
3. The difference between the observed and predicted sea levels corresponds to the surges. In fact, this residual also includes the error associated with the prediction.

4.2.4 Observations from altimetry

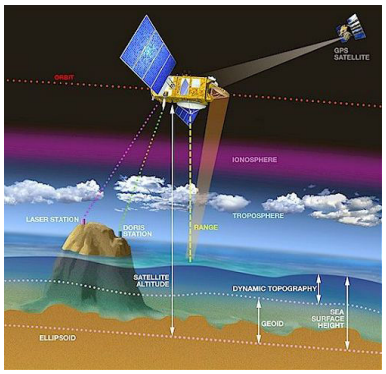

Figure 4.3 – Basic principle of altimetry measurement

For 25 years, different altimetry missions have been measuring the sea level. Radar altimeters send a signal to the Earth and receive an echo from the sea surface, after its reflection. The time for the signal to go and return allows the estimation of the distance between the satellite and the sea level surface, also called the range R, estimated with a precision of 2 cm. The satellite altitude above the ellipsoid is available with a precision of 3 cm. The Sea Surface Height (SSH) is the difference between the satellite altitude referred to the ellipsoid S and the range R

$$SSH = S - R. \tag{4.1}$$

The Mean Sea Surface (MSS) related to the ellipsoid corresponds to the mean of several years of SSH, eventually using several satellites. The Sea Level Anomaly (SLA) is the difference between the instantaneous SSH and the MSS. However, many geophysical and environmental corrections are made to estimate SLA, leading to the following formula (Antony et al., 2014):

$$SLA = SSH - (iono - dry\_topo - wet\_tropo - solid\_earth\_tide - pole\_tide - loading\_tide - SSB - tide - DAC) - MSS \tag{4.2}$$

where corrections are the ionospheric, dry tropospheric and wet tropospheric corrections, the solid earth tide, pole tide and loading tide, the Sea State Bias (SSB), the tide and the Dynamic Atmospheric Corrections (DAC). The DAC corresponds to the ocean response to atmospheric forcing (atmospheric pressure and winds). This correction is necessary, because of the aliasing of wind and atmospheric pressure effects in the altimeter measurements (Gaspar and Ponte, 1997; Stammer et al., 2000). The DAC generally comes from an ocean model elevations for high frequency part (e.g. MOG2D/TUGO 2D, Carrère and Lyard (2003)), and inverted barometer law for low-frequency part (e.g. using ECMWF atmospheric pressure products).

Altimetry data were often considered as unreliable in coastal areas, partly because of the interaction between radar signal and land topography. However, recently developped processing methods enhanced the precision of the products in nearshore areas (Passaro et al., 2014; Birol et al., 2016). We first

analysed ALES (Adaptive Leading Edge Subwaveform) 20 Hz JASON-2 coastal product (Passaro et al., 2014). In this product, JASON-2 data were retracked to be more precise in coastal areas. However, the Sea Level Anomaly signal is very noisy at 20Hz, and we had to filter it at 1Hz. Moreover, near the coasts, they are many outliers, even taking into account the flags and excluding data corresponding to $err_{ALES} > 0.5$. It was suggested to also exclude the data closer than 3 km to the coasts (personal communication from M. Passaro). As we had not the distance to the coast in the data, we had to download a global coastline and compute this flag. Processing the data was time-consuming and moreover, we did not benefit from the high resolution of this product (20 Hz), as we had to filter it to 1Hz. Finally, we preferred to investigate the JASON-2 1Hz X-track coastal product (Birol et al., 2016), developped by Center of Topography of the Ocean and Hydrosphere (CTOH/LEGOS, Toulouse). X-TRACK is a post-processing software which increases the sea surface height information derived from satellite altimetry in the coastal ocean areas. Tracks are going closer to land, up to 5 km, against 10 km with the standard AVISO product.

To be consistent with the model and the tide gauges, we added to the SLA the DAC correction, to obtain the surge (Figure 4.4)

$$Surge_{alti} = SLA + DAC. \tag{4.3}$$

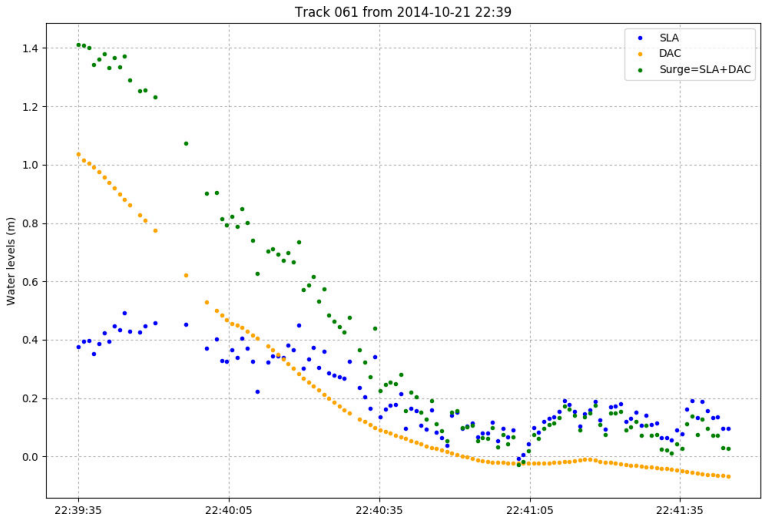

Figure 4.4 – JASON-2 data along the track 61 on the 21 October 2014, during ex-Gonzalo storm

4.3 Generalities on surge modelling

4.3.1 Hydrodynamic equations

The ocean model in barotropic mode resolves the classical Saint-Venant shallow water continuity and momentum equations, formulated similarly as in Bertin et al. (2012)

$$\frac{\partial \eta}{\partial t} + \vec{\nabla}. \int_{-h}^{\eta} \vec{u} dz = 0, \tag{4.4}$$

$$\frac{D\vec{u}}{Dt} = -f\vec{k} \times \vec{u} + \alpha g \vec{\nabla}\hat{\psi} - \frac{\vec{\nabla} P_a}{\rho} - g\vec{\nabla}\eta + \frac{\vec{\tau}_s - \vec{\tau}_b}{\rho(\eta + h)}. \tag{4.5}$$

where η is the surface elevation, $\vec{u}$ the horizontal velocity, h the bathymetry, f the Coriolis parameter, α the earth-elasticity factor, g the mean gravitational acceleration, $\hat{\psi}$ the earth tidal potential, P_a the sea-

level atmospheric pressure, ρ the water density, τ_s the surface stress and τ_b the bottom stress.

We investigated the contribution of wind stress and atmospheric pressure in the shallow water equations. These terms correspond respectively to $\vec{\tau_s}/\rho(\eta+h)$ and $\nabla\vec{P_a}/\rho$ in Equation 4.5. Figure 4.5 from (a) to (d) shows the evolution of these terms, as well as the wind and the surge, during the storm ex-Gonzalo (Table 4.5) . The wind stress term is stronger in the shallow waters, when the bathymetry is lower than 50 m. Comparison of the two terms shows that the wind stress term is largely dominant in the North Sea (note that the scales are not the same for the wind stress ($10^{-4}m/s^2$) and the pressure term ($10^{-6}m/s^2$). The wind stress term contributes to more than 90% of the sum of the two terms (Figure 4.6). This suggests that the currents are mainly driven by the wind. The effect of the atmospheric pressure is negligible.

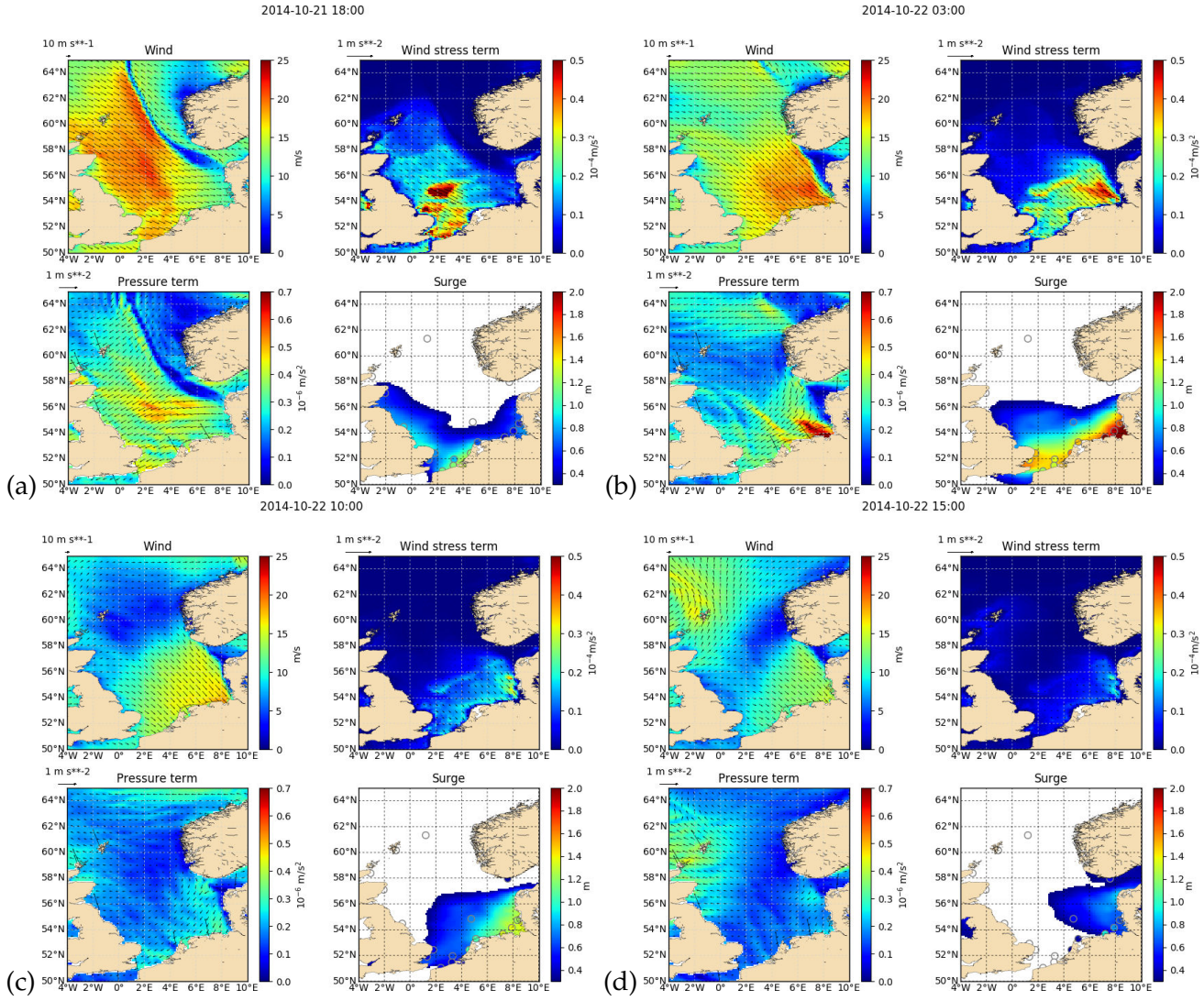

Figure 4.5 – Wind, wind stress and pressure gradient terms in Eq. 4.5, and surge during ex-Gonzalo storm on the 2014-10-21 18:00 (a) 2014-10-22 03:00 (b) 10:00 (c) and 15:00 (d)

4.3.2 Processus that are not modelled

To model the wave setup, the radiation stress has to be introduced. This is possible when the grid resolution is very high (around 10 m). As a consequence, due to a too coarse grid, the wave setup is

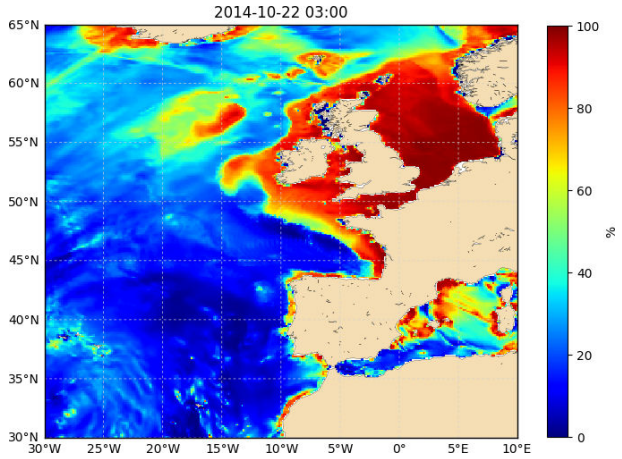

Figure 4.6 – Contribution of the wind stress term to the total wind and pressure terms in Eq. 4.5, on the 2014-10-22 03:00, during ex-Gonzalo storm

generally not modelled in global and regional models. Note also that wave-current interactions are not modelled at the scale of regional and global models.

4.3.3 Different ways to estimate the surges

They are two ways to conduct the simulations in order to estimate the surges (Figure 4.7):

— method A: run of two simulations (1) with tide and atmospheric forcing and (2) with tide only; the surges are the difference between simulation (1) and (2); in this case, the surges include tide-surge interaction;

— method B: run of a simulation with atmospheric forcing only; in this case, the surge corresponds to atmospheric surge only, without tide-surge interaction.

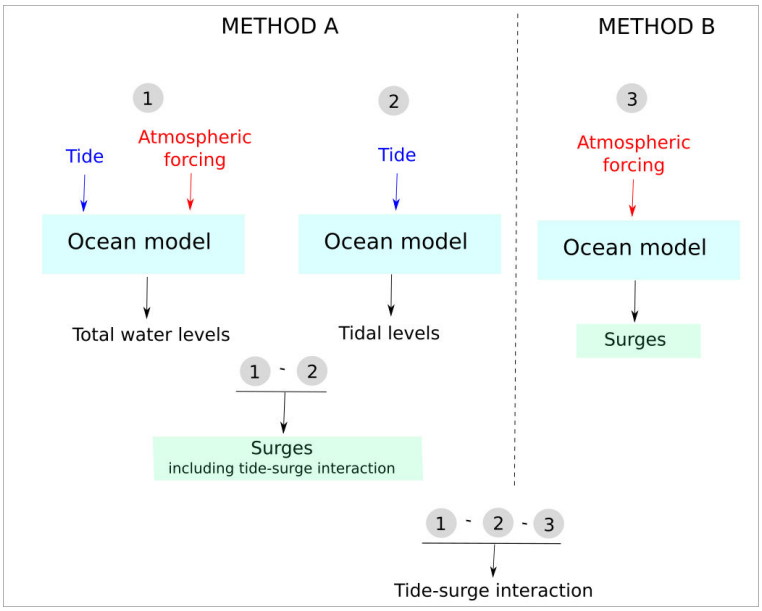

Figure 4.7 – Schematic representation of the two methods to compute the surges

The choice of the method to compute the surge has a quite significative impact on the surge (Figure

4.8, right pannel). The figures for the 23 tide gauges are shown in Appendix D. On average between the two methods, the RMS error is of 10 cm, the absolute bias of 5 cm and the absolute Peak Error (difference between the two maximum surges) of 5 cm. The Peak Error is always smaller than 10 cm, except in Harwich, where it reaches 19 cm.

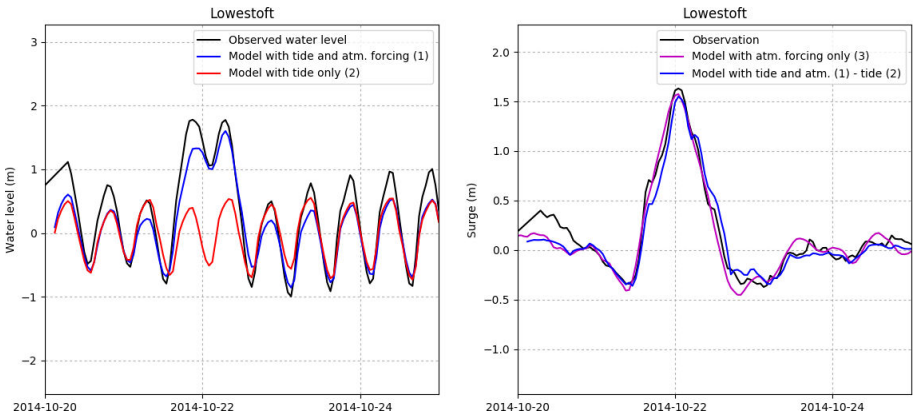

Figure 4.8 – Impact of the method to compute the surge

The drawback of the method B is that we miss the tide-surge interactions. Tide-surge intercation can be expressed as the differences between method A and B, i.e. differences between the simulations: 1-2-3 (Figure 4.7). Figure 4.9 shows the maximum of tide-surge interaction during the 5-day simulation of ex-Gonzalo storm (Table 4.5). It is significant in shallow waters and can reach 50 cm along the South coast of the North Sea. However, figures in Appendix D show that very often, these differences are not due to differences in the peak surge, but are due to semi-diurnal oscillations that are stronger with method A than with B (e.g. at DunkerqueTG or Harwich on Figure D.1). It is not clear if these oscillations could be due to radiational tide or not (i.e. the predictible part of the water levels of meteorological - and not astronomical - origin).

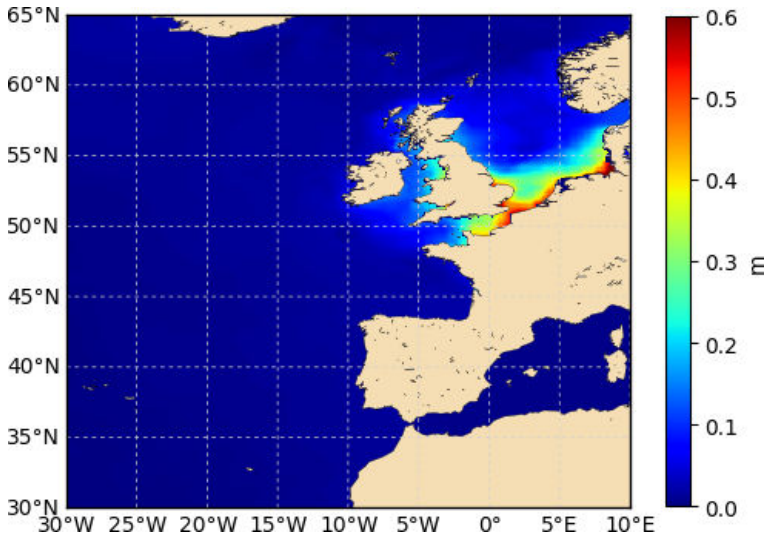

Figure 4.9 – Maximum of tide-surge interaction during ex-Gonzalo storm, from 20^{th} to 24^{th} October 2014

4.4 Storms selection

First ocean simulations were conducted for the storms selected in the first part (Kaat and Lilli storms). Results showed that the surges were not very strong in the North Sea for these events. As a consequence, it was difficult to detect a significant impact of the parameterization on the surges. For this reason, we analysed data in order to select new events with strong surges in the North Sea.

This section presents the analysis of tide gauges and altimeter data, followed by a short description of selected storms.

4.4.1 Analysis of 101 tide gauges

To select the storms, we analysed 101 tide gauges in the North Sea (Figure 4.10), obtained thanks to Copernicus Marine Environment Monitoring Service (CMEMS). Tide gauges are mainly located in the coastal areas, and rarely offshore. The sea level database covers the period January 2012-October 2017 (date of the extraction). The duration of observations depend on sites, and ranges from less than 3 years to more than 5 years (Figure 4.10 (a)). Observations from the UK National Tide Gauge Network and French National Network RONIM (Réseau d'Observation du NIveau de la Mer) generally cover the whole 6-year period, whereas observations along Belgian, Dutch, and German coasts generally cover only 3 to 4 years. The observations are related to different datum, depending on the producer (e.g. Chart Datum or Mean Sea Level). Data include a quality flag, and we kept only the data flagged as 'good'.

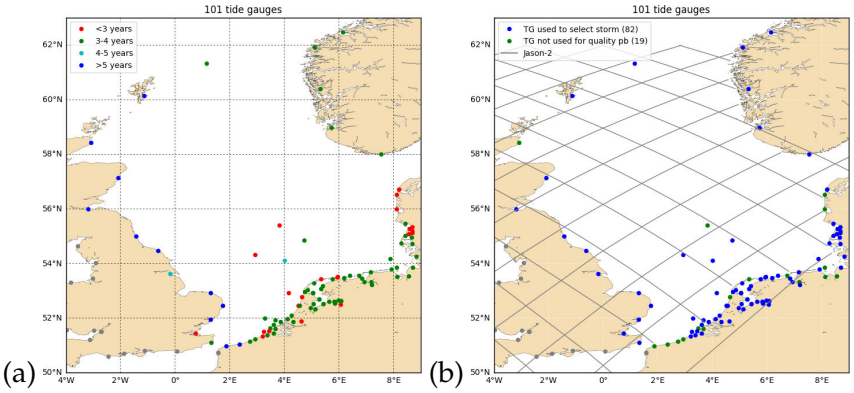

(a) (b)

Figure 4.10 – Tide gauge duration (a) and tide gauges used for storms selection (b)

We used the Tidal ToolBox (Allain, 2013) to process the data and estimate the surges (cf. section 4.2.3). We carried out a visual quality control on the 101 tide gauges. This led to invalidate 19 of them, i.e. almost 20% of the tide gauges. For example, Figure 4.11 shows surges reaching unrealistic value of 3 m at Dunkerque. This error is due to a shift in the sea levels, despite only values flagged as 'good' were processed.

Finally, the storms selection was based on the analysis of 82 valid tide gauges, over the period January 2012 - October 2017 (Figure 4.10 (b)). The 10 more energetic events were selected, based on the maximum surge (Table 4.2). For each event, maximum winds range from 20 to 30 m/s (maximum winds are computed from ECMWF 1h operational forecasts, during the day of the event, over the North East Atlantic (30°E 10°W 30°N 65°N)). The maximum surges occur generally in tide gauges located in very shallow waters or along rivers, where the surge progresses while increasing. This explains the very high values of maximum surges, exceeding 2 or 3 m (Table 4.2).

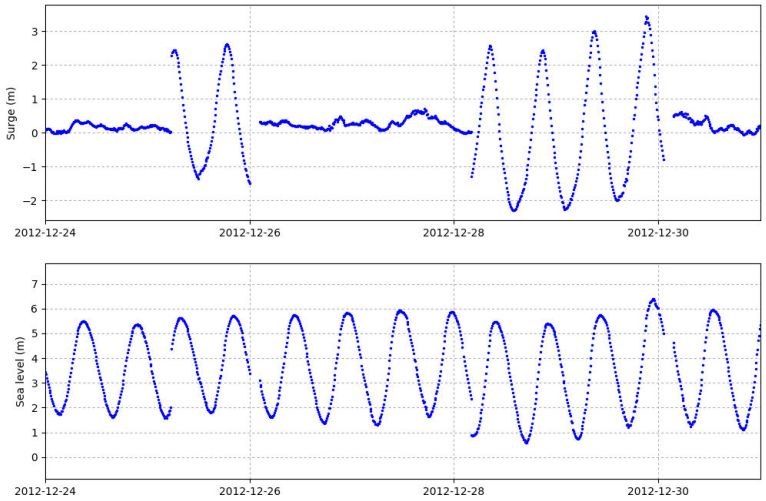

Figure 4.11 – Observed surges (top) and sea levels (bottom) at Dunkerque from 24 to 30 December 2012

Date	Name	Rank	Max. surge (m)	Corresponding Tide Gauge	Max. wind (m/s)
2014-10-22	ex-Gonzalo	1	3.18	NieuweStatenzijlTG	22.7 m/s
2015-01-11	Felix	5	2.88	NorderneyTG	25.4 m/s
2015-03-31	Niklas	3	3.14	BremerhavenTG	25.5 m/s
2015-11-29	Nils	6	2.86	BremerhavenTG	26.6 m/s
2016-11-21		9	2.55	Sheerness	22.5 m/s
2016-12-26		8	2.62	BronsTG	29.3 m/s
2017-01-13		4	3.04	NieuweStatenzijlTG	24.1 m/s
2017-01-14		10	2.52	NieuweStatenzijlTG	20.8 m/s
2017-09-13		2	3.17	EiderSPTG	25.6 m/s
2017-10-29		7	2.82	BremerhavenTG	25.5 m/s

Table 4.2 – Storms with the maximum surges in the North Sea, over the period January 2012 - October 2017. Maximum winds are computed over the North East Atlantic (30°W 10°E 30°N 65 °N), from ECMWF operational forecasts.

For technical reasons, we could not easily simulate events after March 2016. Indeed, at this date, IFS moved from its original reduced gaussian grid to a new octahedral one (this allowed an enhancement of the spatial resolution from 16 to 9 km without changing the truncature T1279). As a consequence, it was not possible to initiate the simulations built previously (based on the traditional reduced grid, see Chapter 3) with operational analysis (archived on the new octahedral grid). Taking into account this technical restriction, four storms were selected: ex-Gonzalo, Felix, Niklas and Nils, respectively ranked 1, 5, 3 and 6 (Table 4.2). We then analysed altimeter data in order to select events combining tide gauge observations and remote sensing data.

4.4.2 Analysis of JASON-2 altimeter data

We analysed 8 years (2008-2015) of JASON-2 data along tracks in the North Sea (Figure 4.10 (b)), from the CTOH 1Hz SLA product in the North East Atlantic.

The objectives of the altimeter data analysis were 1) to select storms with remote sensing data among these coming from tide gauge analysis (Table 4.2) 2) to select storms with different sea state (young and

old), in order to investigate the effect of the waves. It is not evident which parameter should be relevant to characterize the sea state. A common way is to consider the wave age, following the expression $\xi_{10} = C_p/U_{10}$, where C_p is the phase velocity at the peak of the wave spectrum. When the wind has just started blowing, the waves are short-period, steep and sharpened. At this stage, the wind speed is higher that the wave phase velocity, and waves are growing. It is commonly considered that the value of 1.2 separates the young and the old sea. We computed the wave age from WAVEWATCH III North East Atlantic hindcast (Rascle and Ardhuin, 2013), from the relation

$$\xi_{10} = \frac{g}{2\pi f_p U_{10}} \tag{4.6}$$

where f_p is the peak frequency. Note that there is no partition in WAVEWATCH III separating the wind sea and the swell. As a consequence, the peak frequency may be contaminated by the swell. In this case, the interpretation of the wave age is difficult.

The 50 first storms were ranked following the criteria of maximum surge (see Figures B.1, B.2 and B.3 in Appendix B). The surge is computed following Equation 4.3, the wind comes from ECMWF 1h forecasts, and the wave age is computed from WAVEWATCH III following Equation 4.6. Note that the storm ranked 1^{st} (Figure B.1 (a) first line) is not meaningful, as there are fery few data. Figures in Appendix B show that the wave age is generally around 0.8 in the North Sea. There is no storm with wave age around 0.4-0.5 (i.e. very young sea state), but there are storms with wave age larger than 1.2. Note that in what follows, sea state is considered as "young" when the wave age is close to 0.8, and "old" when the wave age is greater than 1.2 (swell). In order to have different sea state, as well as the maximum of observations (tide gauges and remote sensing), we finally selected the following storms (Table 4.3):

1. ex-Gonzalo storm, ranked 2^{nd} (Figure B.1 (a) second line), and previously ranked 1^{st} in tide gauge analysis (Table 4.2). The wave age is around 0.9, the sea state can then be considered as young.
2. Friedhelm storm, ranked 5^{nd} (Figure B.1 (a) last line). This storm was not ranked in tide gauge analysis, because it occured in 2011, whereas as the tide gauge database starts in 2012. The wave age is larger than 1.2, the sea state can then be considered as old.
3. Felix storm, ranked 6^{th} (Figure B.1 (b) first line), and previously ranked 5^{th} in tide gauge analysis. The wave age is around 0.8, the sea state can then be considered as young.
4. Gunter storm, ranked 20^{th} (Figure B.2 (b) last line) occured just after Felix storm, ranked 5^{th} in tide gauge analysis. The wave age is generally larger than 1.2 along the track, the sea state can then be considered as old.

Name	Date	Track number	Type of sea state	Rank from JASON-2 analysis	Rank from TGs analysis	Max. wind (m/s)	Corresponding date
Friedhelm	2011-12-10	170	old sea	5	/	29.9	2011-12-08 21:00
ex-Gonzalo	2014-10-21	061	young sea	2	1	22.9	2014-10-21 13:00
Felix	2015-01-10	94	young sea	6	5	29.2	2015-01-10 11:00
Gunter	2015-01-13	170	old sea	20	/	30.4	2015-01-12 10:00

Table 4.3 – Storms selected for this study. Maximum winds are computed over the North Sea (4°E 10°W 50°N 65°N) from ECMWF simulations.

Figure 4.12 shows the wave age along the tracks for each selected storm. The data corresponding to bathymetry deeper than 100 m appear in grey. These along track data confirm that wave age is larger than 1.2 for Friedhelm and Gunter (old sea), and lower than 1.2 for ex-Gonzalo and Felix (young sea).

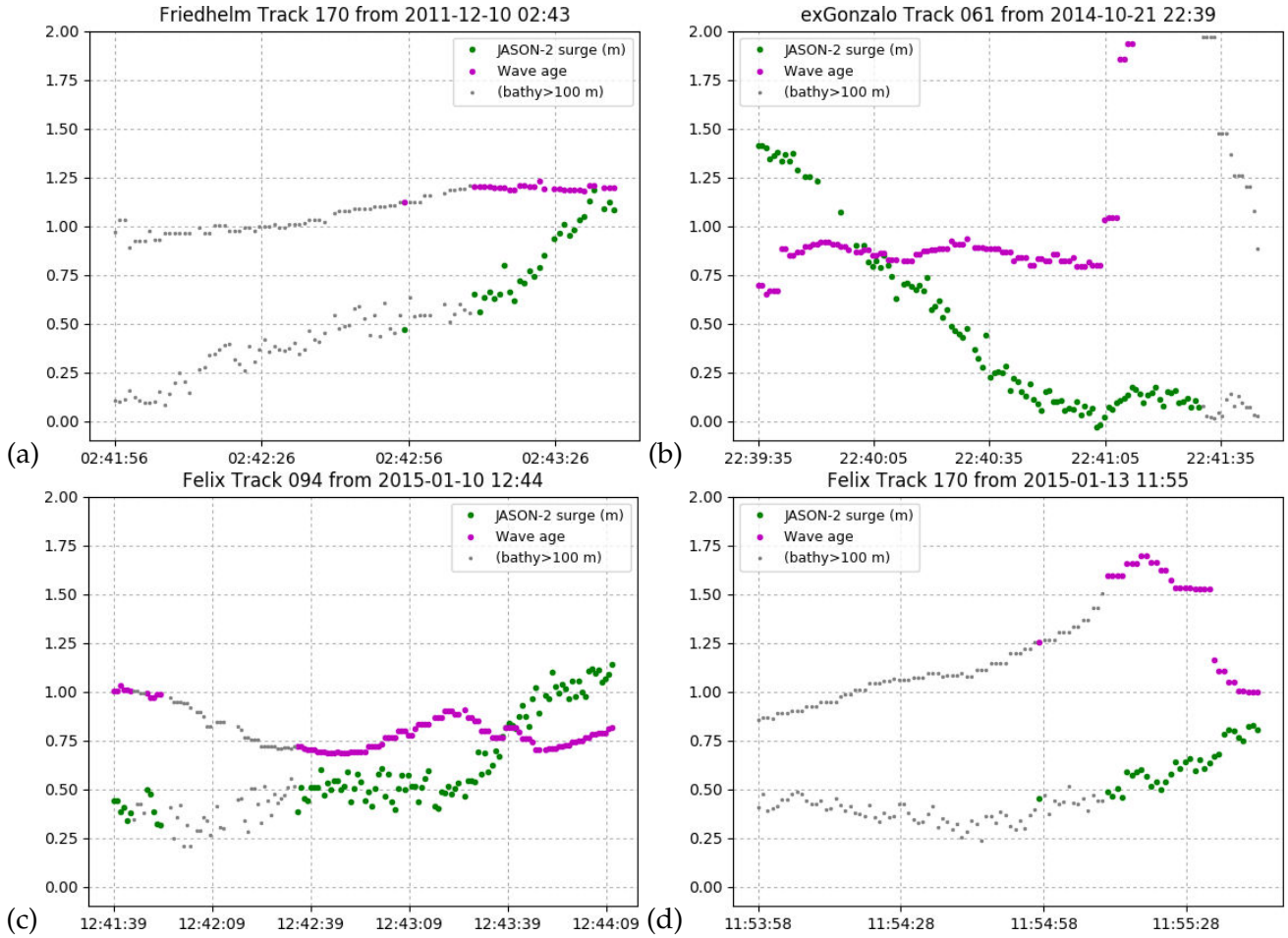

Figure 4.12 – Wave age and JASON-2 surges during Friedhelm (a), ex-Gonzalo (b), Felix (c) and Gunter (d)

4.4.3 Storms description

The minimum of Mean Sea Level (MSL) Pressure was computed from ECMWF simulations, with default parameterization, over the North East Atlantic (30°W 10°E 30°N 65°N) (Figure 4.13). Winds for each storm, at the instant highlighted by an asterisk on Figure 4.13, are plotted Figure 4.14.

In December 2011, Friedhelm storm crossed the North East Atlantic. Its track is the northernmost one (Figure 4.13). In the North sea, the winds were very strong (up to 30 m/s), and the sea state old (Figure B.1 (a) fifth line, third column), with wave age larger than 1.2.

In October 2014, ex-Gonzalo storm reached the North of the British Islands. This storm corresponds to the remnants of Category 4 Atlantic Hurricane Gonzalo. It is the strongest storm in terms of surges, but not in term of winds. One of the characteristics of this storm is that the strong winds moved from the west to the east as a quite North-South front around 1 000 km long (Figure 4.14 (b)). This explains the discontinuity in the MSL Pressure observed in ex-Gonzalo track over the North Sea (red curve on Figure 4.13), as the minimum moves along this front. In the North Sea, the winds are not so strong (only 23 m/s), and the sea state is young with wave age for this storm around 0.8 (Figure B.1 (a) second line, third column).

In January 2015, Felix and Gunter storms crossed the North Atlantic. In fact, three storms succeeded:

first Elon, then Felix which crossed the North Sea the 10^{th} of January, and finally Gunter the 12^{th} of January 2015. The winds were strong and reached 30 m/s (Table 4.3). For Felix, the sea state was young with wave age close to 0.8 (Figure B.1 (b) first line, third column), whereas for Gunter it was old with wave age larger than 1.2 (Figure B.2 (b) fifth line, third column). The old sea for Gunter can be easily explained by the succession of three storms in a very short period (few days). Gunter track is northern than Felix one, which probably explains that the storm has less impact in term of surges in the North Sea.

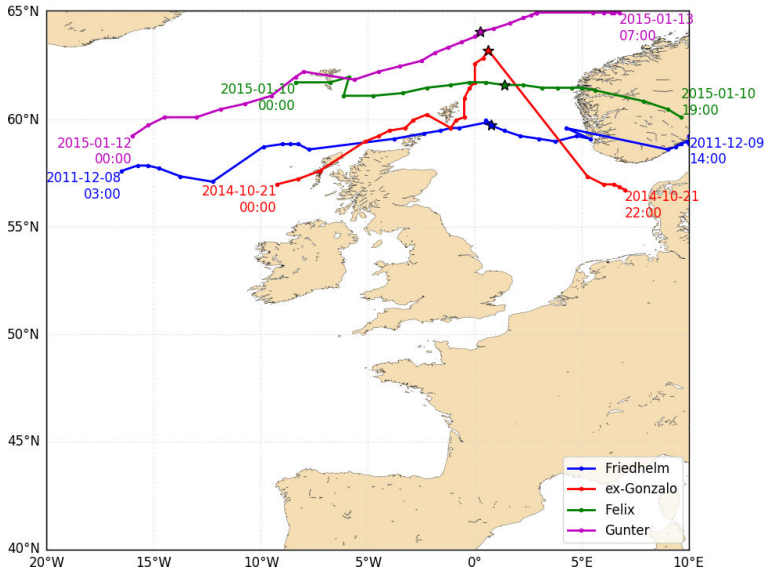

Figure 4.13 – Tracks of the minimum of the Mean Sea Level Pressure for the selected storms (from ECMWF simulations). The asterisk on the figure corresponds to the time for wind plot (Figure 4.14)

4.5 Observations

This section describes the observations used in this study: tide gauges and altimeter data.

4.5.1 Tide gauges

Among the 101 tide gauges (see section 4.4.1), 23 tide gauges were selected for comparison with the model (Figure 4.15). The criteria were 1) to have data available during the storms 2) to have tide gauges open up to the ocean, rather than at the end of a bay 3) to have a maximum of tide gauges offshore (where processes are different than in harbours, see the discussion below) 4) to have a maximum of tide gauges located along the JASON-2 tracks. Finally, we had 4 tide gauges offshore (EuroplatformTG, D151TG, F3platformTG, NorthCormorantTG).

To compute the surges at tide gauges, data were processed as described in 4.4.1 (data downloaded from CMEMS, harmonic analysis over the whole period and detiding). Note that observed surges may include many other processes than atmospheric surges (cf. section 4.2.2, wave setup, seiches, internal waves...). Many of these processes take place in harbours and not offshore. Their contribution will then be larger in tide gauges along the shore, than in tide gauges offshore or along JASON-2 tracks.

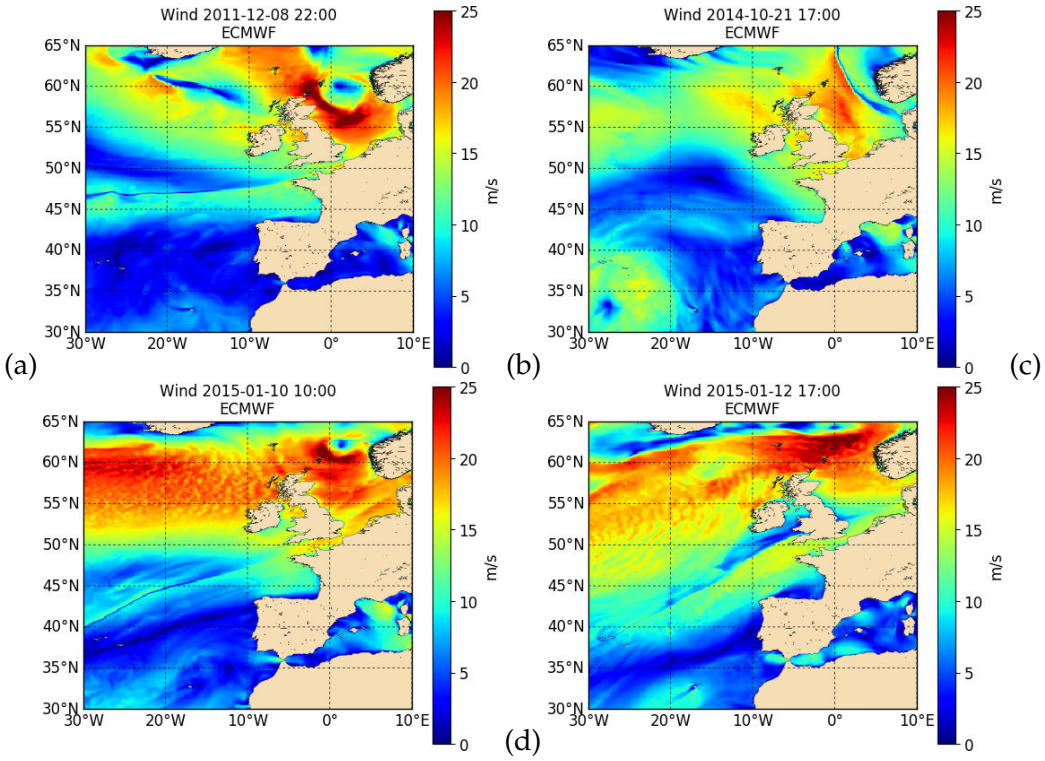

Figure 4.14 – Winds during the storms (a) Friedhelm 8 December 2011 22:00 (b) ex-Gonzalo 21 October 2014 17:00 (c) Felix 10 January 2015 10:00 (d) Gunter 12 January 2015 17:00 (from ECMWF simulations)

4.5.2 JASON-2 altimeter

To compute the surges, JASON-2 data were processed as described in section 4.4.2 (1Hz SLA product downloaded from CTOH, surges correspond to SLA plus DAC). The tracks with the maximum surges are tracks 170 for Friedhelm, 61 for ex-Gonzalo, 94 for Felix, and 170 for Gunter (Table 4.3). Surges along these tracks are shown on Figure 4.16.

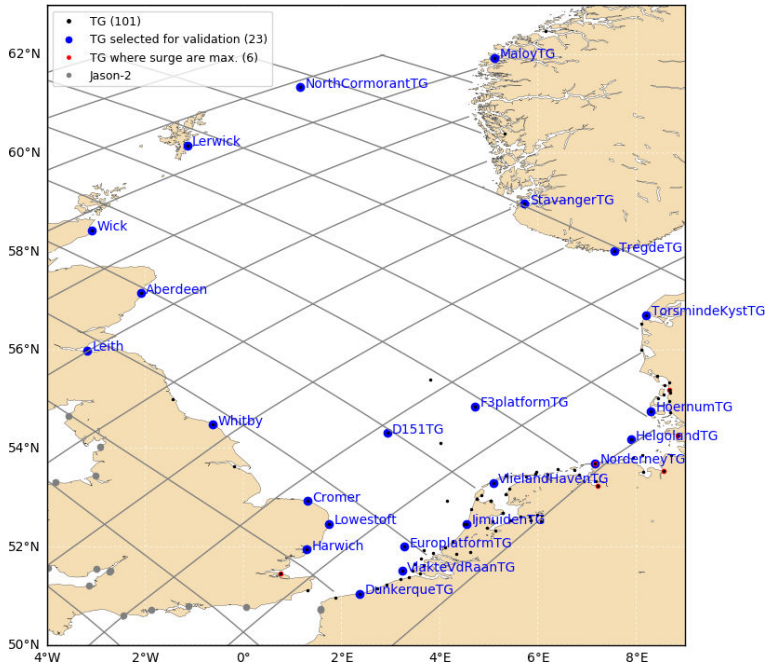

Figure 4.15 – Tide gauges selected and JASON-2 tracks for model validation

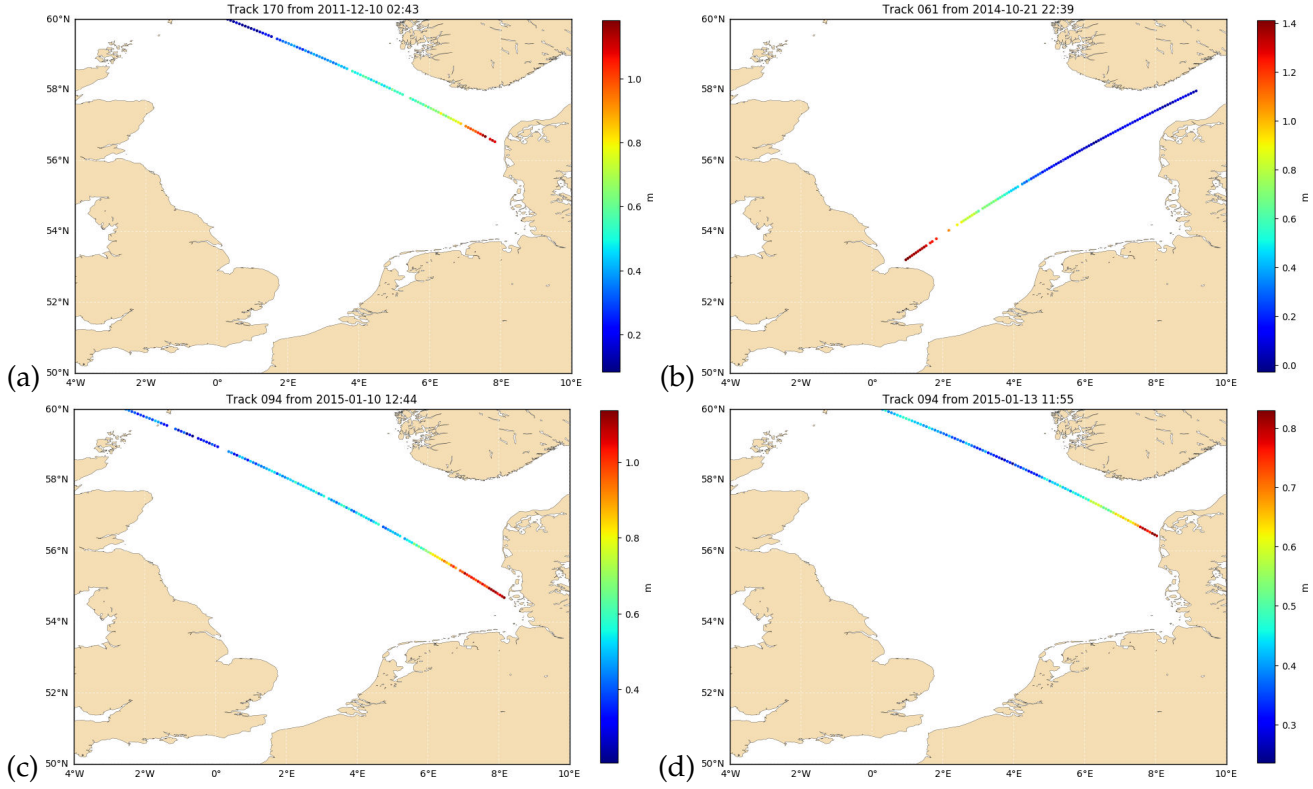

Figure 4.16 – Surges computed from JASON-2 data during the storms (a) Friedhelm 8 December 2011 (b) ex-Gonzalo 21 October 2014 (c) Felix 10 January 2015 (d) Gunter 13 January 2015

4.6 The numerical atmosphere model

We used the ECMWF coupled wave-atmosphere model to generate atmospheric forcing (Figure 4.17). The IFS (Integrated Forecasting System) CY41R1 cycle (ECMWF, 2015a) has a spatial resolution around 16 km, and 137 vertical levels. It has been coupled with the spectral wave model ECWAM (ECMWF Wave Model, ECMWF (2015b)) since 1998. The ECWAM uses a coarser horizontal resolution than IFS at around 28 km, with 36 directions and 36 frequencies logarithmically spaced, with starting frequency 0.035 Hz and an increment of 1.1. Figures 4.13 and 4.14 show tracks and winds for each of the selected storm (Friedhelm, ex-Gonzalo, Felix and Gunter), with ECMWF default wind stress parameterization. In the North Sea, the maximum winds range from 23 m/s for ex-Gonzalo to 30 m/s for Gunter (Table 4.3).

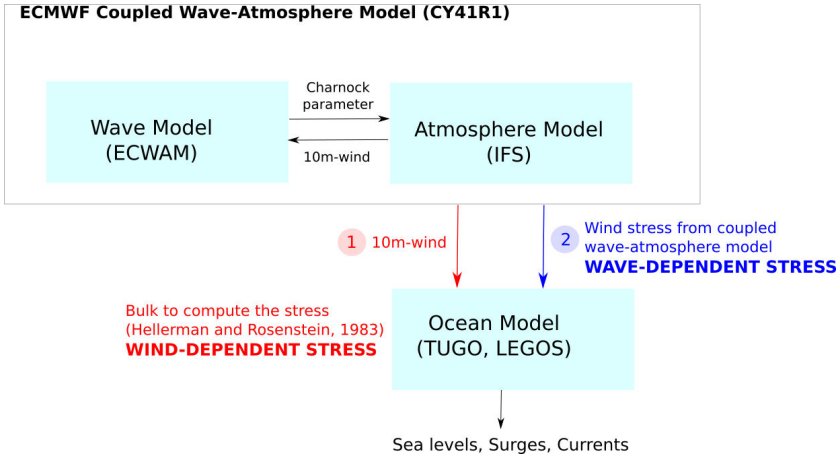

Figure 4.17 – Wave, atmosphere and ocean model coupling

They are two ways to force the ocean model from the atmosphere (1) with 10-m wind or (2) with wind stress (Figure 4.17). The first method is largely used in the scientific community, and most of the operational models are forced this way. In this case, the wind stress is computed from the ocean model bulk formula, which raises the problem of the consistency of the drag between air and water in meteorological, hydrodynamic and wave models (van Nieuwkoop et al., 2015).

4.7 The numerical ocean model

4.7.1 Configuration

We used TUGO shallow water global ocean model, developped by LEGOS (Lyard et al., 2006). This model in barotropic mode resolves the classical shallow water continuity and momentum equations (Eqs 4.4 and 4.5). The model was installed on Ifremer supercomputer Datarmor. We used the default configuration, which has been extensively validated with tide gauges for tide and surges. This model allowed the development of the tidal model FES2014 (Carrère et al., 2015), a worlwide reference model for tides, widely used in the scientific community. It also produces Dynamic Atmospheric Corrections to correct altimeter data from atmospheric effects (Carrère and Lyard, 2003). This correction is officially used by CNES and NASA for altimeter data processing (see AVISO portal).

Note that due to a coarse grid (3 to 15 km in the North Sea), the wave setup is not modelled (see section 4.3). This is a strong limitation for comparison with tide gauges, but not with altimeter, as wave setup is close to zero far from the coasts.

4.7.2 Finite element mesh

The main originality of TUGO is the finite element space discretisation, which allows increasing the resolution in shallow waters, as well as along strong topographic gradient areas (Figure 4.18). In the North East Atlantic, the resolution is around 50 km in the deep ocean, 15 km on the continental shelves, 4 km along the continental slope, and up to around 3 km along the coasts (Figure 4.18 (a)). In the North Sea, the resolution varies from 10-15 km offshore to 4 km along the French and English coasts, and 2 km along the north of the Norwegian coasts (Figure 4.18 (b)). Note that the resolution is not refined in the southeast of the North Sea, due to a lack of bathymetry in this area (not enough available data).

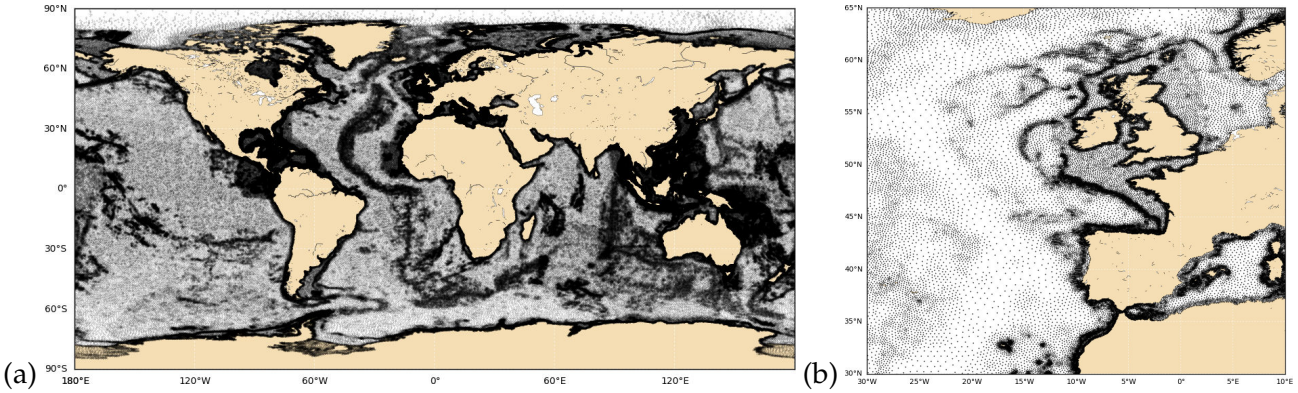

Figure 4.18 – Global FES2014 grid (a) and zoom over the North East Atlantic (b)

4.7.3 Parameterizations

The bottom stress is expressed as

$$\tau = \frac{C}{H}||\vec{u}||\vec{u} \tag{4.7}$$

where H is the mean local depth and C a dimensionless friction coefficient usually taken as 2.5 10^{-3} (Lyard et al., 2006). This coefficient has been optimized so that the simulated tidal levels match with the tide gauges. Note that the wave effect on bottom stress is here not taken into account, as it is significant only in very shallow waters (<10 m). When the bathymetry increases rapidly to 10-20 m, it reaches only 5 cm in tide gauges (Bertin et al., 2015).

The wind stress is represented by classical bulk formulae (Eq. 2.7). The drag coefficient is expressed following Hellerman and Rosenstein (1983), which is a wind-only dependent formulation

$$10^3 C_d = 0.934 + 0.788 \times 10^{-1} U_{10} + 0.868 \times 10^{-1} \Delta T - 0.616 \times 10^{-3} U_{10}^2 - 0.12 \times 10^{-2} \Delta T^2 - 0.214 \times 10^{-2} U_{10}(\Delta T) \tag{4.8}$$

where U_{10} is the wind at 10 m, ΔT the air-sea temperature difference to take into account the stability effect. Figure 4.19 shows this TUGO drag for a $\Delta T = 0$. For winds between 20 and 23 m/s, TUGO drag is quite similar to ECMWF default parameterization, but with no variability. For winds between 23 and 33 m/s, TUGO drag is lower than ECMWF default, and for winds stronger than 33 m/s, TUGO drag is higher than ECMWF default parameterization. These values for very strong winds are unrealistically high, and are not consistent with recent observations suggesting that the drag coefficient could potentially saturate for winds above 30 m/s, and even decrease after 40 m/s (Powell et al., 2003; Jarosz et al.,

2007; Holthuijsen et al., 2012). As a consequence, at very high winds, TUGO simulated surges will probably be overestimated.

Note that the bulk formula we used in this study (Hellerman and Rosenstein, 1983) is the classical one in TUGO default configuration. It is used for the development of FES2014 tidal model (Carrère et al., 2015), as well as for Dynamic Atmospheric Corrections (Carrère and Lyard, 2003). However, other bulk formulae are implemented in TUGO model, particularly the Charnock's formulation (Eq 2.14). They are not tested here.

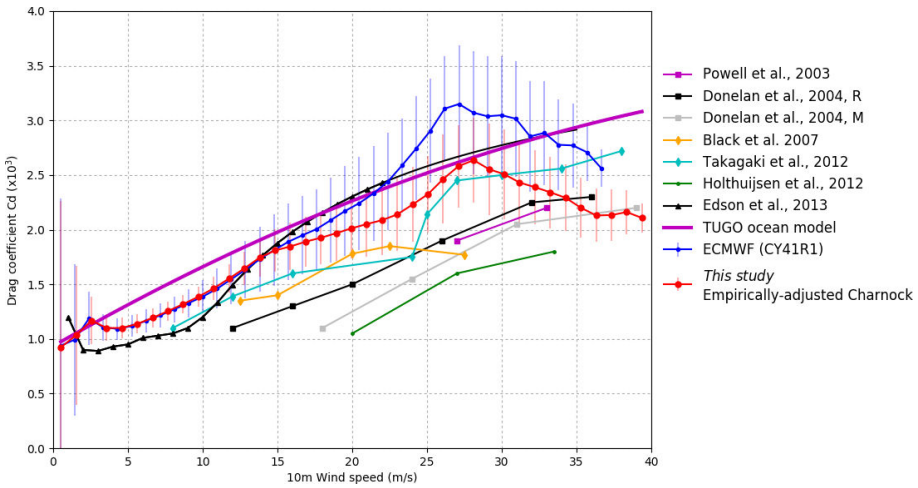

Figure 4.19 – Comparison of drag coefficient for TUGO parameterization (Hellerman and Rosenstein, 1983), ECMWF (CY41R1) parameterization, empirically adjusted Charnock parameterization and observations. For Donelan et al. (2004), R or M corresponds to different measurement techniques, Reynolds or Momentum Budget. Error bars correspond to one standard deviation.

The ocean model TUGO was modified to be forced directly by the wind stress from an external file, i.e. coming from the coupled IFS/WAM model (Figure 4.17). This led to strong instabilities on water levels, due to the presence of high wind stress values near the coasts, even with a land-sea mask. Despite modifications conducted by LEGOS (masking isolated points), some instabilities still remained. To solve this problem, we finally had to introduce a land-sea mask on the native IFS gaussian grid, before the interpolation on a regular grid.

4.7.4 Atmospheric forcing

We forced the ocean model with atmospheric forcing only (method B in Figure 4.7), as the first tidal simulations showed significant differences with observations. This choice is probably not so appropriate, as the impact of the method may be significant (see discussion in section 4.3.3). However, the sensitivity study conclusions should not be impacted.

For each storm, the model was initialised during at least 15 days, with winds and atmospheric pressure coming from ECMWF operational 1h forecasts (Figure 4.20). Once initialised, each storm simulation lasted 5 days and was forced by (1) the 10m-wind or (2) directly by the wind stress, and the atmospheric pressure, with a 1 hour temporal resolution. When forced by the 10m-wind (1), the wind stress is a wind-dependent formulation, computed by TUGO bulk formula (Hellerman and Rosenstein, 1983), whereas when forced by the wind stress (2), the stress is a wave-dependent formulation, which has seen the

waves through IFS/WAM coupling (Janssen, 1991).

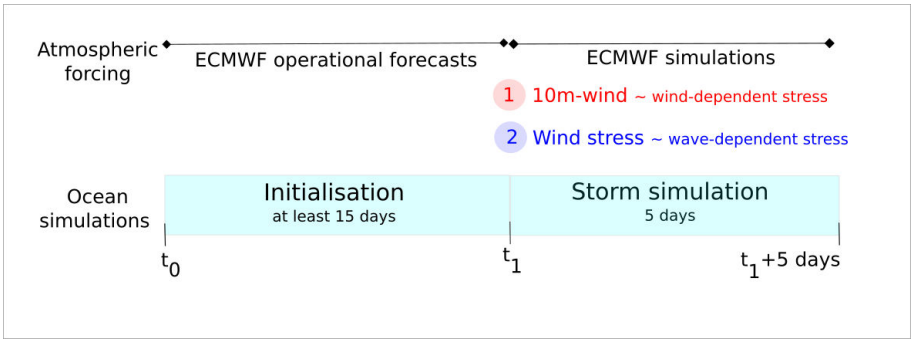

Figure 4.20 – Schematic representation of atmospheric forcing

Simulated water levels were detided from the wave S_2 to take off oscillations (blue curve on Figure 4.21), corresponding to radiational tide, i.e. the predictible part of the water levels of meteorological - and not astronomical - origin. The amplitude of these oscillations is around 10 cm at HelgolandTG (Figure 4.21), but can reach 50 cm at St-Helier, on Jersey Island, in the English Channel (not shown). At S_2 frequency (30°/h), there is a superposition of astronomical and radiational tide. We removed this signal from simulations to be consistent with observations, where radiational and astronomical tide are removed. This point must be treated very carefully, as this signal can enhance the peak of the surge (e.g. around 20 cm at St-Helier, not shown). Note that this raises the problem of forcing a regional model with tide and atmospheric forcing: the predictible part of the atmospheric signal appears twice. It is easy to remove from the forcing harmonic that are purely radiational tide as the annual component S_a, but it is more complex to remove components that are at the same frequency as astronomical tide (e.g. S_2).

Finally, note that if we had forced the model with tide and atmospheric forcing (method A in Figure 4.7), we would not have had these oscillations in the simulations.

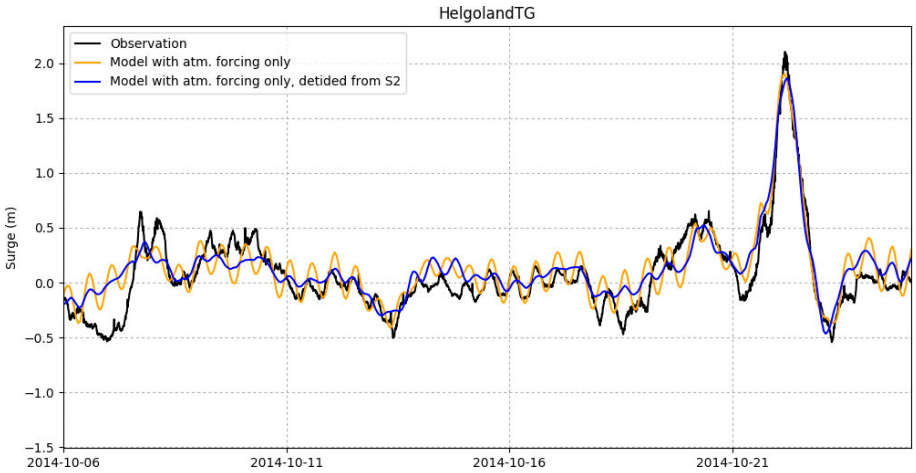

Figure 4.21 – Oscillations in the simulated water levels at HelgolandTG, due to radiational tide in the atmospheric forcing

4.7.5 Experiments

We simulated 4 storms: ex-Gonzalo, Friedhelm, Felix and Gunter (Table 4.4). Note that Felix and Gunter are in the same simulation as they follow each other.

Storm	Initialisation	Begin of simulation	End of simulation
ex-Gonzalo	2014-10-01	2014-10-20	2014-10-24
Friedhelm	2011-11-15	2011-12-08	2011-12-12
Felix/Gunter	2014-12-15	2015-01-09	2015-01-13

Table 4.4 – Date of initialisation and simulation for each storm

We conducted 11 experiments, synthetised in Table 4.5. The fourth column corresponds to TUGO wind stress type of parameterization (wind-dependent if the model is forced by ECMWF wind, wave-dependent otherwise). The fifth column corresponds to the wind stress parameterization in ECMWF atmosphere model.

Exp.	Storm	Sea State	TUGO param.	ECMWF param.
Exp. 1	**ex-Gonzalo**	Young sea	Wind-dep. stress	[1] Default
Exp. 2			Wave-dep. stress	[1] Default
Exp. 2a			Wave-dep. stress	[2] WW3 Physics
Exp. 2b			Wave-dep. stress	[3] Emp.-adjusted Charnock
Exp. 2c			Wave-dep. stress	[4] Contant Charnock 0.0018
Exp. 2d			Wind corrected-dep. stress	[1] Default
Exp. 2e			Wind-dep. stress	[5] Emp.-adjusted Charnock
Exp. 3	**Friedhelm**	Old sea	Wind-dep. stress	[1] Default
Exp. 4			Wave-dep. stress	[1] Default
Exp. 5	**Felix/Gunter**	Young then old	Wind-dep. stress	[1] Default
Exp. 6			Wave-dep. stress	[1] Default

Table 4.5 – Experiments to investigate the impact of the waves

4.8 Results

This section presents (1) the impact of the wind direction (2) the impact of the waves (3) the impact on the altimetric corrections (4) the extension of the study to other storms (5) the impact of wind increase versus wave (6) a sensitivity study to the wind stress parameterization and (7) the formulation of a paradox relative to the way of forcing the ocean model.

4.8.1 Impact of the wind direction

Analysis of tide gauge and altimeter data revealed that ex-Gonzalo was the storm with the highest surge, whereas it was the one with the weaker winds (only 23 m/s in the North Sea, against 30 m/s for Gunter, see Table 4.3). This is mainly due to the wind direction. Figure 4.22 shows wind roses in the middle of the North Sea (4°E 56°N), during the 5-day simulations of the storms. For ex-Gonzalo (Figure 4.22 (a)), strong winds were mainly from the northwest direction, pushing the waters along the southern coast of the North Sea; whereas for other storms, strong winds came mainly form the west direction.

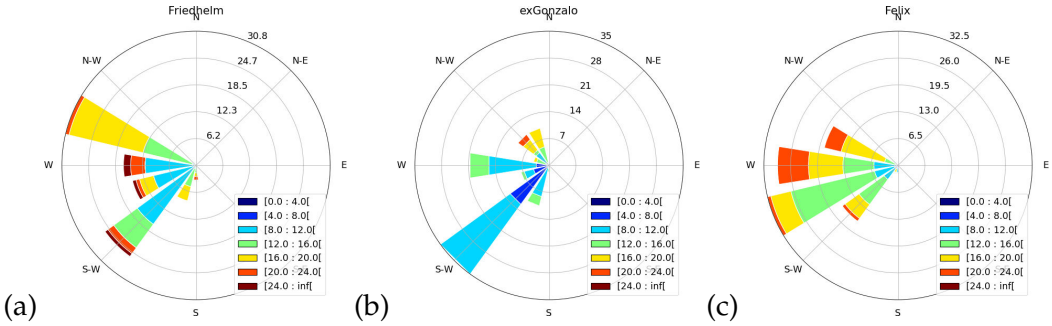

Figure 4.22 – Wind roses (m/s) in the middle of the North Sea (4°E 56°N), during the 5-day of simulations of storms Friedhelm (a) ex-Gonzalo (b) Felix/Gunter (c)

4.8.2 Impact of the waves

To investigate the impact of the waves, we compared the surges with wind-dependent (Hellerman and Rosenstein, 1983) and wave-dependent (Janssen, 1991) parameterization during two storms, one with young sea state (ex-Gonzalo, Exps 1 and 2 in Table 4.5) and one with old sea state (Friedhelm, Exps 3 and 4 in Table 4.5). We compared the simulated surges with observations, i.e. tide gauges and JASON-2 altimetric data. Figure 4.23 shows the comparison with 6 tide gauges, quite representative of the 23 ones, for ex-Gonzalo storm (Figures E.2 and E.1 in Appendix E for all tide gauges). Table 4.6 summarized the error statistics between the model and the tides gauges: bias, Root Mean Square Error (RMSE) and Peak Error (defined as the difference between the maximum observed and modelled surge). Note that there is no tide gauge comparison for 2011 storm Friedhelm, as the CMEMS tide gauge database starts only in 2012. Finally, Figures 4.24 and 4.25 show the comparison with JASON-2 altimetric data, for ex-Gonzalo and Friedhelm storms. Note that the markersize is smaller when the bathymetry is deeper than 100 m, as in this range, the effect of wind stress is lower.

The first result is that globally, the model matches very well with the observations, particularly for ex-Gonzalo storm. For the wave-dependent parameterization, in average, the bias between the model and all the tide gauges is close to zero, the RMSE is of 0.12 m, and the Peak Error is of -0.09 m (Table 4.6). The errors between the model and JASON-2 along the track are similar, and even better: the bias is close to zero, and the RMSE is of 0.08 m, whereas the surge ranges up to 1.40 m (Figure 4.24). Note the very good agreement with the tide gauge situated along the track (D151TG). Unfortunately, the tide gauge Cromer located on the northeast coast of England just at the end of the track did not recorded data just during the storm (see Figure 4.15 for the tide gauge location). For Friedhelm storm, the model matches also quite well with the altimeter, but not as well as for ex-Gonzalo. The bias and RMSE reach respectively 0.14 m and 0.07 m (Figure 4.25). The differences could be due to uncertainties in altimeter corrections, e.g. geophysic corrections as tide. Note that the agreement is very good, when bathymetry is lower than 100 m. To conclude, the errors between the model and the observations for these two storms are small enough to confirm the capability of a global model to accurately predict storm surges, even in coastal areas, when its spatial resolution is fine enough to catch the storm structure. These results confirm also the capability of altimeters to measure surges with a good precision (Antony et al., 2014).

The second result is that the wave-dependent parameterization yields higher surges, only when the sea state is young (exGonzalo storm, Figures 4.23 and 4.24). Otherwise, the surges are similar, regardless the parameterization (Friedhlem storm, Figure 4.24). Physically, this is not surprising as old sea corresponds mainly to swell. When the sea state is old, the drag coefficients from the two parameterizations are close to each other, and the surges are then similar. However, in the presence of young and steep waves, the drag increases with Janssen's parameterization (see Chapter 3), yielding to higher drag than

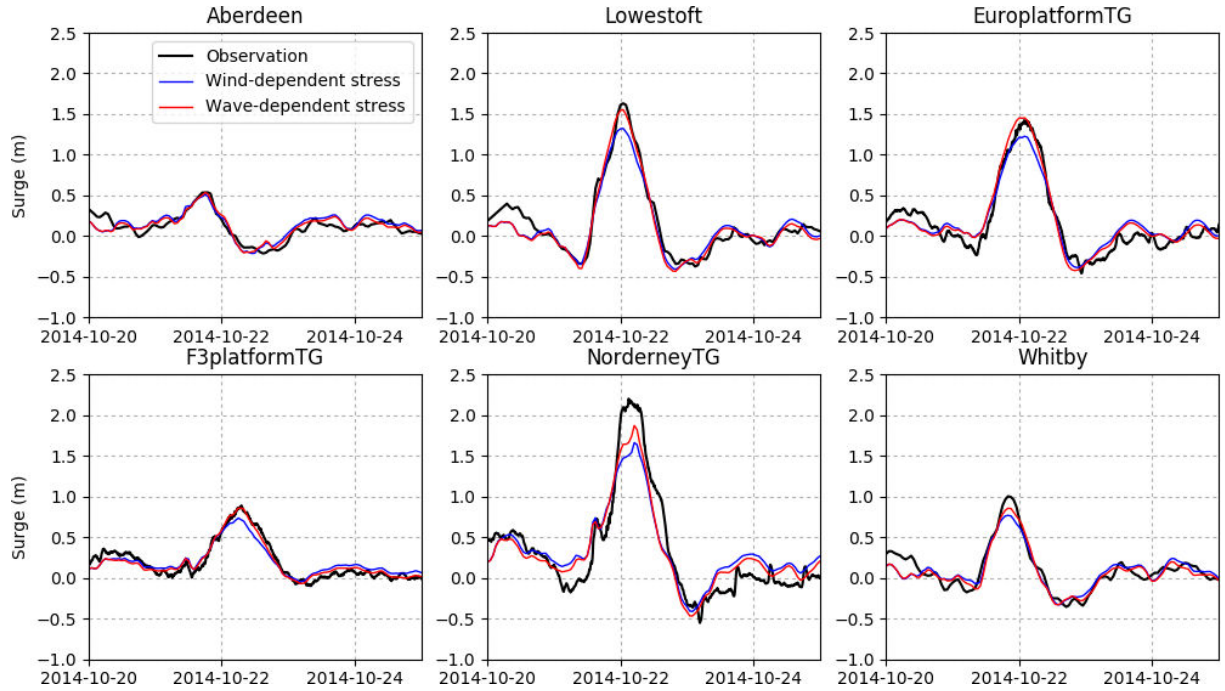

Figure 4.23 – Observed surges and modelled surges with two parameterizations (wind- and wave-dependent) at tide gauges (Aberdeen, Lowestoft, EuroplatformTG, F3platformTG, NordeneyTG, Whitby) from 20^{th} to 24^{th} of October 2014, during ex-Gonzalo storm

.

the wind-dependent one (Figure 4.19), and then higher wind stress, and higher surges. The differences between these two parameterizations corresponds to the effect of the waves on the surges. It reaches around 25 cm at Lowestoft (Figure 4.23) and around 20 cm along Jason-2 track (Figure 4.24).

The third result is that the wave-dependent parameterization is closer to the observations than the wind-dependent one. These results are consistent with those previously obtained by Mastenbroek et al. (1993), Nicolle et al. (2009) and Bertin et al. (2015). Along the JASON-2 track, the RMSE is reduced from 0.13 m to 0.08 m (Figure 4.24). In average, in the 21 tide gauges, the Peak Error is reduced from -0.21 m to -0.09 m (Table 4.6). However, in some tide gauges, the surges are still underestimated. The tides gauges can be separated into three groups:

— A first group of 8 tide gauges, where the surges with the wave-dependent stress match well with observations (i.e. peak error $<$ 0.05 m, e.g. Lowestoft, EuroplatformTG and F3platformTG on Figure 4.23). This corresponds to the 4 offshore tide gauges (F3platformTG, D151TG, EuroplatformTG, VlakteVdRaanTG) as well as 4 other tide gauges onshore (Harwich, IjmuidenTG, Leith, Lowestoft).

— A second group of 6 tide gauges, where the surges with the wave-dependent stress are still underestimated (e.g. NorderneyTG and Whitby on Figure 4.23, but also DunkerqueTG, HelgolandTG, HoernumTG and VlielandHavenTG).

— A third group of 7 tide gauges, where the surges are smaller than 0.50 m and the effect of the parameterization is not significant; this corresponds to tide gauges located in the northern part of the North Sea, e.g. Aberdeen (see Figure 4.23), but also Lerwick, MaloyTG, NorthCormorant, StavangerTG, TredgeTG and Wick. In this part, the bathymetry ranges from 50 to 200 m, and the effect of wind stress is smaller than in the southern part, with shallow waters. That may explain the non significant differences between the two paramaterizations.

In the second group, where surges are still underestimated, there is no tide gauges offshore. This

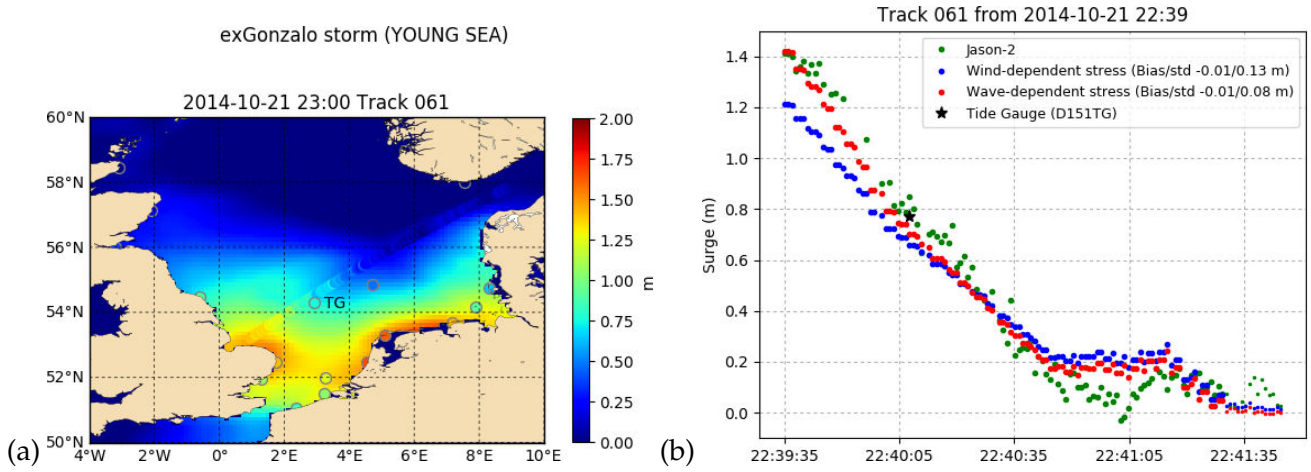

Figure 4.24 – Surges from TUGO model, JASON-2 altimeter and tide gauges during ex-Gonzalo. The markersize is smaller on (b) when the bathymetry is deeper than 100 m.

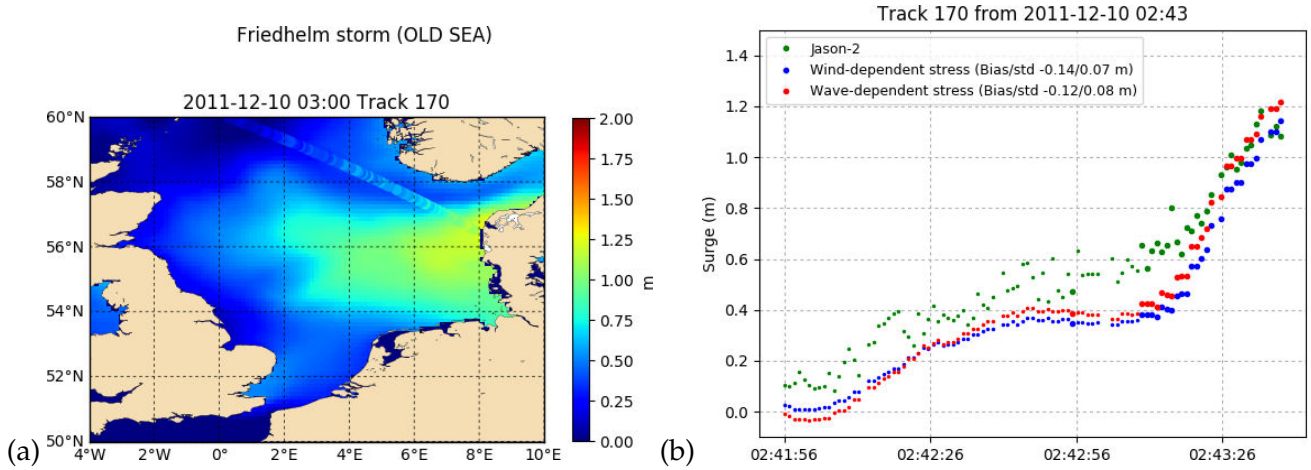

Figure 4.25 – Surges from TUGO model, JASON-2 altimeter and tide gauges during Friedhelm. The markersize is smaller on (b) when the bathymetry is lower than 100 m.

underestimation is probably partly due to processus taking place in the very nearshore, and not modelled by TUGO (e.g. wave setup, see the discussion in section 4.5.1). This could explain that comparisons with the altimeter is better, as the tracks are offshore, and not contaminated by coastal processes as wave setup (Figure 4.24).

4.8.3 Impact on the altimetric corrections

The accuracy of the simulated storm surges is essential, as it impacts directly the accuracy of SLA products through the Dynamic Atmospheric Correction (Eq.4.2). Figure 4.26 shows the differences between the default SLA from CTOH (blue curve) and the new reconstructed one (red curve) with the DAC taking into account the waves, i.e. from TUGO simulation forced with ECMWF wind stress. The new reconstructed SLA is on average closer to zero. The SLA has been improved, by removing some surge residual due to atmospheric effect. The difference between the two SLA (the native and reconstructed one) reaches 40 cm near the coast. Note that in this 40 cm, around 20 cm may be attributed to the wave impact, the other 20 cm are probably due to a better ocean model resolution and a better temporal atmospheric forcing (1h versus 6h in the DAC product from CTOH).

Tide Gauge	Bias (m) Wind-dep.	Bias (m) Wave-dep.	RMSE (m) Wind-dep.	RMSE (m) Wave-dep.	Peak Err. (m) Wind-dep.	Peak Err. (m) Wave-dep.
EX-GONZALO						
Aberdeen	0.03	0.01	0.08	0.07	-0.03	-0.00
D151TG	0.01	0.00	0.08	0.07	-0.12	-0.02
DunkerqueTG	-0.02	-0.04	0.19	0.18	-0.47	-0.32
EuroplatformTG	0.02	0.02	0.13	0.12	-0.16	0.06
F3platformTG	0.01	0.00	0.08	0.06	-0.13	-0.00
Harwich	-0.07	-0.04	0.16	0.15	-0.17	0.11
HelgolandTG	0.08	0.07	0.20	0.17	-0.43	-0.21
HoernumTG	0.10	0.07	0.23	0.18	-0.44	-0.22
IjmuidenTG	0.02	-0.00	0.19	0.16	-0.34	-0.17
Leith	-0.02	-0.01	0.12	0.11	-0.14	-0.08
Lerwick	0.01	0.02	0.04	0.04	-0.01	-0.00
Lowestoft	-0.03	-0.03	0.13	0.11	-0.31	-0.08
MaloyTG	0.03	0.01	0.06	0.05	-0.07	-0.04
NorderneyTG	0.03	-0.00	0.26	0.22	-0.54	-0.33
NorthCormorantTG	0.04	0.04	0.05	0.05	0.03	0.03
StavangerTG	0.02	-0.00	0.10	0.07	-0.10	-0.02
TregdeTG	0.01	-0.00	0.13	0.11	-0.25	-0.15
VlakteVdRaanTG	-0.01	-0.01	0.16	0.16	-0.16	0.05
VlielandHavenTG	0.01	-0.01	0.20	0.17	-0.37	-0.22
Whitby	-0.01	-0.02	0.11	0.10	-0.23	-0.15
Wick	0.03	0.00	0.08	0.07	0.01	-0.03
Mean	**0.01**	**0.00**	**0.13**	**0.12**	**-0.21**	**-0.09**
FELIX/GUNTER						
Mean	**0.01**	**0.00**	**0.20**	**0.19**	**-0.14**	**-0.10**

Table 4.6 – Bias, RMSE and Peak Error for wind- and wave-dependent parameterization during 5-days for ex-Gonzalo and Felix/Gunter storms

4.8.4 Extension to other storms

After the analysis of ex-Gonzalo (young sea) and Friedhelm (old sea), we extended the study to Felix (young sea) and Gunter (old sea) storms. Figure 4.27 shows the comparison with 6 tides gauges, quite representative of the 23 ones (Figures E.3 and E.4 in Appendix E for all tide gauges). We see clearly the succession of the three storms during 5 days: Elon, Felix and Gunter. Figures F.1 and F.2 in Appendix F show the comparison with JASON-2 tracks for Felix and Gunter. The results are partly similar to what we found previously for ex-Gonzalo and Fridhelm storms. (1) The model matches still quite well with the tide gauges (bias, RMSE and Peak Error of 0 cm, 19 cm and -10 cm for the wave-dependent parameterization, see Table 4.2). (2) The wave-dependent parameterization still yields to higher surges, when the sea state is young (Figures 4.27, F.2 and F.1). The impact of the waves on the surges reaches around 11 cm at Europlatform (Figure 4.27) and around 20 cm along Jason-2 track (Figure F.1). (3) We find also that the wave-dependent parameterization is closer to the tide gauge observations, reducing in average the Peak Error from -0.14 m to -0.10 m. However, comparison between the model and the altimeter is not as good as for ex-Gonzalo and Friedhelm, and it is difficult to conclude which parameterization is the most appropriate from Figures F.1 and F.2. This suggests that the number of case studies should be increased, to give more confidence in our conclusions.

Note the very strong high frequency signal at NorderneyTG (Figure 4.27) with an amplitude around

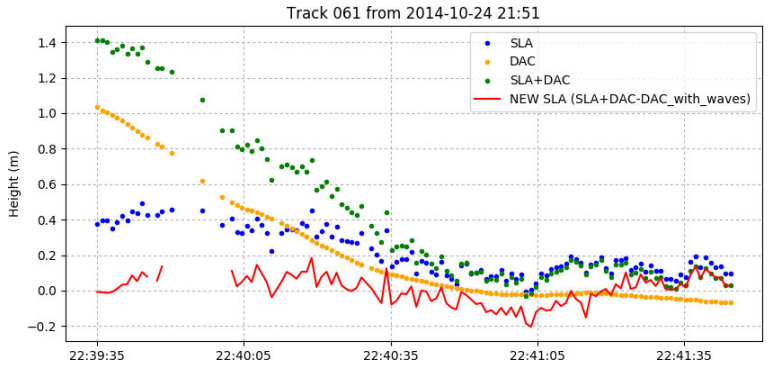

Figure 4.26 – Impact on SLA of taking into account the waves in the DAC, for track 061 during ex-Gonzalo

1 m, which is not catched by the model. If this is not a problem coming from the instrument (to be confirmed), it could be due to resonnance effect generating some oscillations or/and the signature of a wave (internal solitary wave? infragravity wave? see the discussion section 4.2.2 for the various processes contributing to the surge).

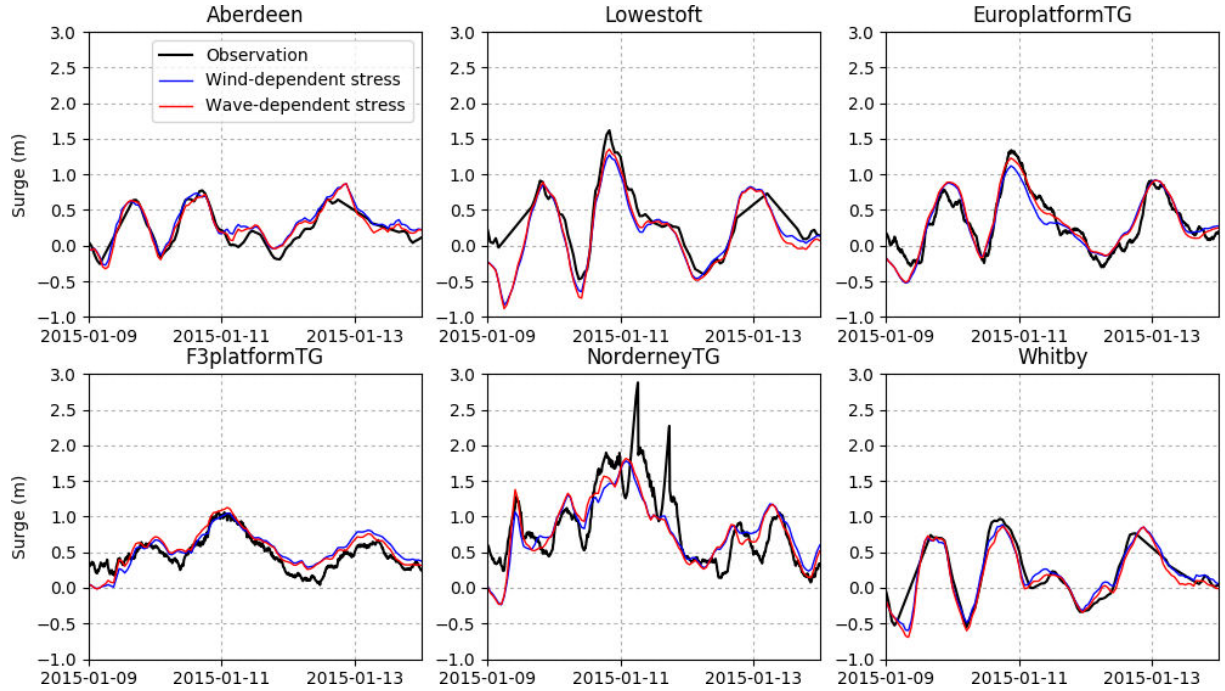

Figure 4.27 – Observed surges and modelled surges with two parameterizations (wind- and wave-dependent) at tide gauges (Aberdeen, Lowestoft, EuroplatformTG, F3platformTG, NordeneyTG, Whitby) from 9^{th} to 13^{th} of October 2014, during Elon, Felix and Gunter storms

.

4.8.5 Impact of wind increase versus wave

We showed previously that the wind speeds may be underestimated in the atmospheric model (Pineau-Guillou et al., 2018). The negative bias reaches around 7 m/s at 30 m/s (Figure 3.3). We applied the same method to compute the bias between the atmospheric model and WindSat for the selected

storms (Friedhelm, ex-Gonzalo, Felix/Gunter) as well as for two other ones (Niklas and Nils, see Table 4.2). Whatever the storm, the biases between the model and WindSat are all consistent, reaching around 7 m/s at 30 m/s (Figure 4.28). The RMS errors and standard deviations are shown in Appendix C.

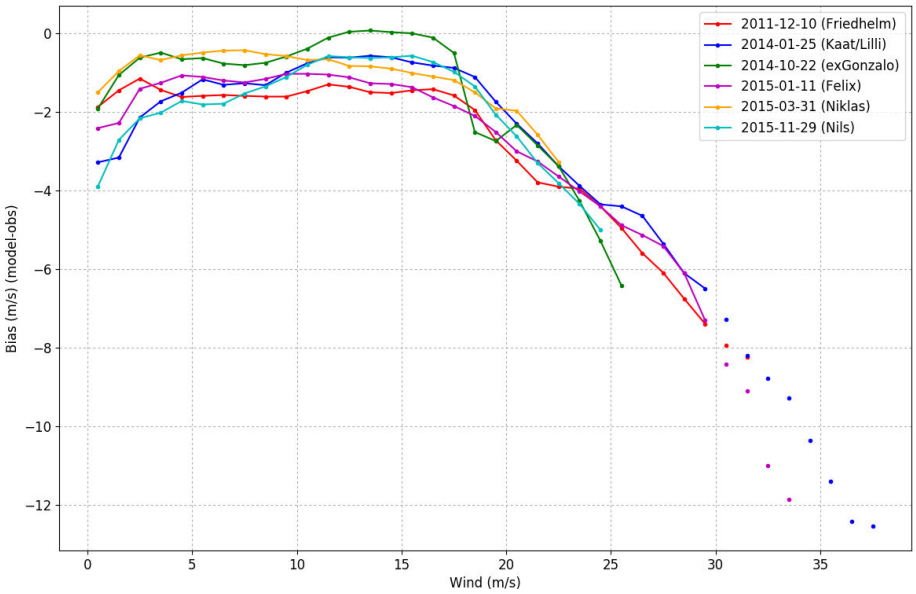

Figure 4.28 – Wind biases between ECMWF (CY41R1) model and WindSat, computed over a 5-day simulation for each storm. The date in the legend corresponds to the first of the five days. Beyond 30 m/s, values are plotted as points, due to large uncertainties in observations.

Underestimation of winds in atmospheric model is often considered as a major cause of underestimation of large wave heights or storm surges in wave and ocean models. To investigate this, we enhanced the winds to match with WindSat observations (Figure 4.28). The corrected winds were increased up to 7 m/s at 30 m/s. We then compared the simulated surges with three parameterizations: wind-dependent stress, wind corrected-dependent stress, and wave-dependent stress (Exps 1, 2d and 2 in Table 4.5). Results show that increasing the wind has a limited impact comparing to taking into account the waves (Figure 4.29). At Lowestoft, increasing the wind yields to an enhancement of the peak surge of only 5 cm, whereas taking into account the waves enhances the peak surge of 23 cm.

4.8.6 Sensitivity to wind stress parameterization

Here, we investigate the impact of the wind stress parameterization on the ocean (i.e. surges). The parameterizations are the ones previously studied in Chapter 3 (Table 3.2). However, we did not test the wave age dependent parameterization (Oost et al., 2002), as it gave unrealistic high drag and was not appropriate for coupling. The tested parameterizations are summarized in Table 4.7. The ocean model TUGO is directly forced by the wind stress from ECMWF simulations.

Figure 4.30 shows the impact of the various parameterizations for ex-Gonzalo storm. The ECMWF default parameterization [1] is taken as the reference (Figure 4.30 first line). Compared to this reference, the different parameterizations [2], [3] and [4] decrease the wind stress and, as a consequence, increase the wind. At the same time, as the wind stress decreases, the surge also decreases. This is particularly significant in the very shallow waters, in the southern part of the North Sea, where the effect of the wind stress is the strongest. At the contrary, in the northern part of the North Sea, the surge increases slightly. This is probably partly due to lower MSL Pressure (see Figure 4.30, third column).

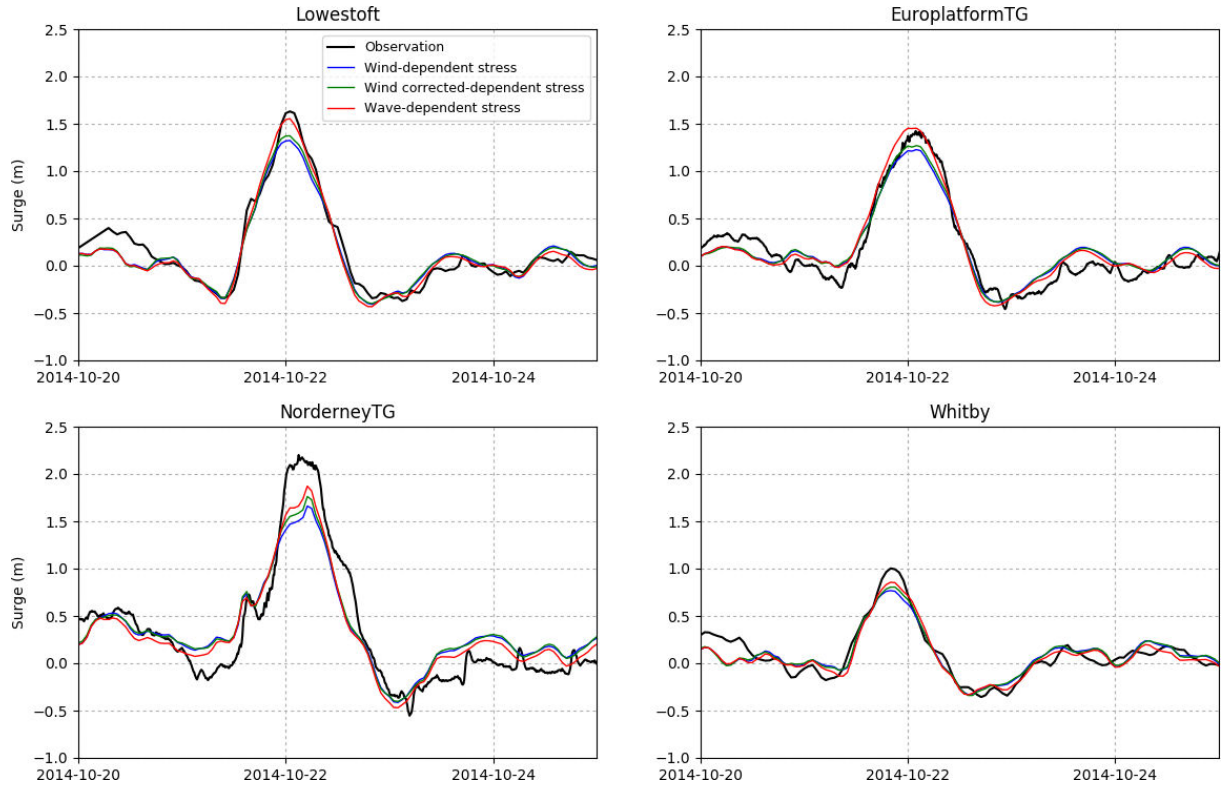

Figure 4.29 – Observed surges and modelled surges with wind-, wind corrected- and wave-dependent stress at tide gauges (Aberdeen, Lowestoft, EuroplatformTG, F3platformTG, NordeneyTG, Whitby) during ex-Gonzalo storm

.

Parameterization	References	Experiment
[1] ECMWF default (reference)	Janssen (1991)	Exp. 2
[2] WW3 physics	Ardhuin et al. (2010)	Exp. 2a
[3] Empirically-adjusted Charnock	This study	Exp. 2b
[4] Constant Charnock 0.018		Exp. 2c

Table 4.7 – Wind stress parameterizations tested. For experiment number, see the Table 4.5.

The WW3 physics parameterization [2] is quite close to ECMWF default parameterization in term of drag (see Chapter 3). As a consequence, the impact on surge is not significant (<5 cm in the southern part of the North Sea). The empirically-adjusted parameterization [3] and constant Charnock one [4] lead to larger differences, reaching respectively 10 and 20 cm.

We compared the surges with the observations at 4 tide gauges, for the different parameterizations (Figure 4.31 and Table 4.8 for the maximum surges). With ECMWF parameterization [1], the maximum surge is generally underestimated compared to the observations, except at EuroplatformTG which is offshore. The negative bias ranges from a few cm to 0.33 m (i.e. 15% of the observed surge). The main result is that all the other parameterizations increase this negative bias, i.e. the surge decreases around 2%, 4% and 8% respectively with parameterizations [2] WW3 physics, [3] Empirically-adjusted Charnock and [4] Constant Charnock of 0.018. It is finally the ECMWF default parameterization which gives surges closest to the observations.

TG	Param.	Max. surge (m)	Diff. with obs (m)	Diff. with ECMWF (m)
Lowestoft	ECMWF (CY41R1)	1.55	-0.08 (5%)	/
	WW3 physics	1.54	-0.10 (6%)	-0.02 (1%)
	Emp.-adjusted Charnock	1.48	-0.15 (10%)	-0.08 (5%)
	Constant Charnock 0.018	1.42	-0.22 (13%)	-0.14 (8%)
EuroplatformTG	ECMWF (CY41R1)	1.45	0.03 (2%)	/
	WW3 physics	1.43	0.01 (1%)	-0.02 (1%)
	Emp.-adjusted Charnock	1.39	-0.04 (3%)	-0.07 (5%)
	Constant Charnock 0.018	1.32	-0.11 (7%)	-0.14 (10%)
NorderneyTG	ECMWF (CY41R1)	1.87	-0.33 (15%)	/
	WW3 physics	1.82	-0.38 (17%)	-0.06 (3%)
	Empirically-adjusted Charnock	1.78	-0.42 (19%)	-0.09 (4%)
	Constant Charnock 0.018	1.68	-0.52 (24%)	-0.19 (9%)
Whitby	ECMWF (CY41R1)	0.85	-0.15 (15%)	/
	WW3 physics	0.84	-0.16 (16%)	-0.02 (2%)
	Empirically-adjusted Charnock	0.83	-0.18 (18%)	-0.03 (3%)
	Constant Charnock 0.018	0.78	-0.22 (22%)	-0.08 (8%)

Table 4.8 – Impact of parameterizations on the maximum surge at 4 tide gauges. The percentages are related to the maximum observed surge.

4.8.7 Paradox on ocean model forcing

These results lead to the following "forcing paradox" (see illustration Figure 4.32):

1. if the ocean model is forced by the wind stress: from [1] ECMWF default to [4] Empirically-adjusted Charnock parameterization (Exps 2 and 2b in Table 4.5), the surge will decrease, as the wind stress decreases;
2. if the ocean model is forced by the wind: from [1] ECMWF default to [4] Empirically-adjusted Charnock parameterization (Exps 1 and 2e in Table 4.5), the surge will increase, as the wind stress computed with default TUGO bulk formula (Hellerman and Rosenstein, 1983) will increase with the wind.

This paradox points out 1) possible processes misunderstood in the physics and/or 2) difficulties to compare model with measurements, when the model has previously been tuned. For example, the term of stress in the momentum equation (Eq. 4.5) corresponds to $(\vec{\tau}_s - \vec{\tau}_b)$. The bottom stress τ_b is expressed following Eq. 4.7, where C is a dimensionless quadratic friction coefficient previously tuned and usually taken as 2.5 10^{-3} (Lyard et al., 2006). Sensitivity study shows that at Lowestoft, during ex-Gonzalo storm, with default ECMWF parameterization, changing C from 0.0025 to 0.0015 increases significantly the maximum surge of 0.11 m, i.e. around 5% of the observed surge.

4.9 Conclusions

We started this work because storm surges were undestimated in hydrodynamic models, as well as large wave heights in wave models. The objective was to investigate the effect of the waves on the wind stress. During ex-Gonzalo and Friedhelm storms, characterized respectively by young and old sea state, we compared simulated surges with wind-dependent and wave-dependent stress (Hellerman and Rosenstein, 1983; Janssen, 1991). We compared the results with tide gauges and altimetric data.

We showed that the global model accurately predicts storm surges in coastal areas (RMSE of 0.12 m). This can be attributed partly to the finite element grid, which allows increasing the resolution in the shallow waters. The consistency between the model, the altimeter and the tide gauges confirm also the capability of altimeters to measure surges with a good precision (RMSE of 0.08 m along the track).

We showed that when the sea state is old, the classical wind-dependent formulation is appropriate (here, Hellerman and Rosenstein (1983)). However, when the sea becomes younger and rougher, the waves increase the wind stress, and a wave-dependent formulation is more appropriate (here, Janssen (1991)). It reduces significantly the Peak Error (e.g. from 0.21 m to 0.09 m). The wave effect on the surge can reach 20 to 25 cm. This result is consistent with previous studies (Mastenbroek et al., 1993; Nicolle et al., 2009; Bertin et al., 2015). However, the number of case studies should be increased, to confirm these conclusions. Indeed, one of the difficulties is that taking into the waves to obtain surges closer to observations, could be a way to compensate other errors, i.e. we could improve the results for wrong reasons. For example, Moon et al. (2009) concluded that Mastenbroek et al. (1993) obtained good simulated surges with overestimated drag, by compensating surge error due to a too coarse grid.

We showed that underestimated winds were not always the main reason for surge underestimation in models. Increasing the wind to obtain enhanced surges is not always sufficient, as the wave effect can be larger. For example, in one of our case study, increasing the wind to match with observations enhances the peak surge of 5 cm, whereas taking into account the waves enhances the peak surge of 23 cm.

This work underlines the lack of consistency of the drag between the wave, atmosphere and ocean models (van Nieuwkoop et al., 2015). One recommendation could be to force the ocean model with the wind stress from a coupled wave-atmosphere model, which has seen the waves (e.g. ECMWF model). This would yield to (1) more consistency between the drag from the ocean and the atmosphere models (2) improvement of the storm surges taking into account the wave effect. Finally, note that in our simulations, the ocean model is forced by the atmosphere model and there is no coupling. The surface current also impacts the wind stress (Eq. 2.12 and 2.13). This should be further investigated.

This work led to formulate the disturbing "forcing paradox", i.e. contrasted results depending on how the ocean model is forced. In the first part of this work, we developped an empirically-adjusted Charnock parameterization to increase the strong winds and reduce the bias with observations (compared to ECMWF default paramaterization, see Chapter 3). With this new parameterization, if the model is forced by the wind, the surges will increase, whereas if forced by the wind stress, the surges will decrease. This last scenario is not satisfying, as the surges are yet lower than observations. Despite investigations, we have no clear explanation for this paradox.

In this study, we compared the simulated surges with tide gauges and altimeters. We showed that the model better matches with tide gauges offshore as well as altimeter tracks. This is probably due to coastal effects in tide gauges (e.g. wave set up) that are not modelled in TUGO ocean model and that are not seen with the altimeters. This suggest that tide gauges should not always be considered as a reference, and that what we generally call "errors" between model/tide gauges or altimeter/tide gauges also includes local coastal processes. As a consequence, we should not always want the model (or altimeter) match perfectly with tide gauges.

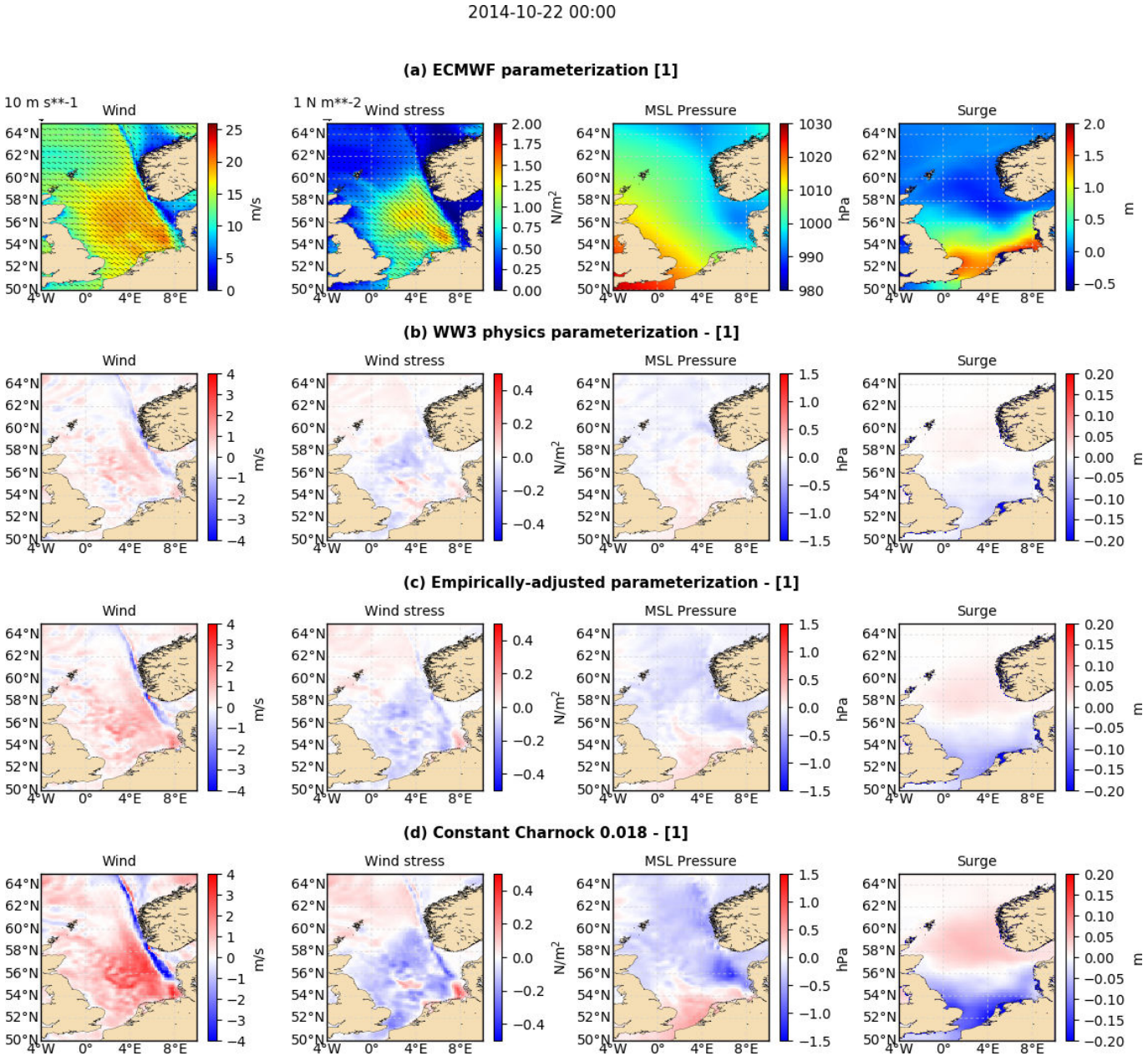

Figure 4.30 – Impact of different parameterizations on wind, wind stress, MSL Pressure and surge on the 22^{nd} of October 2014, during ex-Gonzalo storm

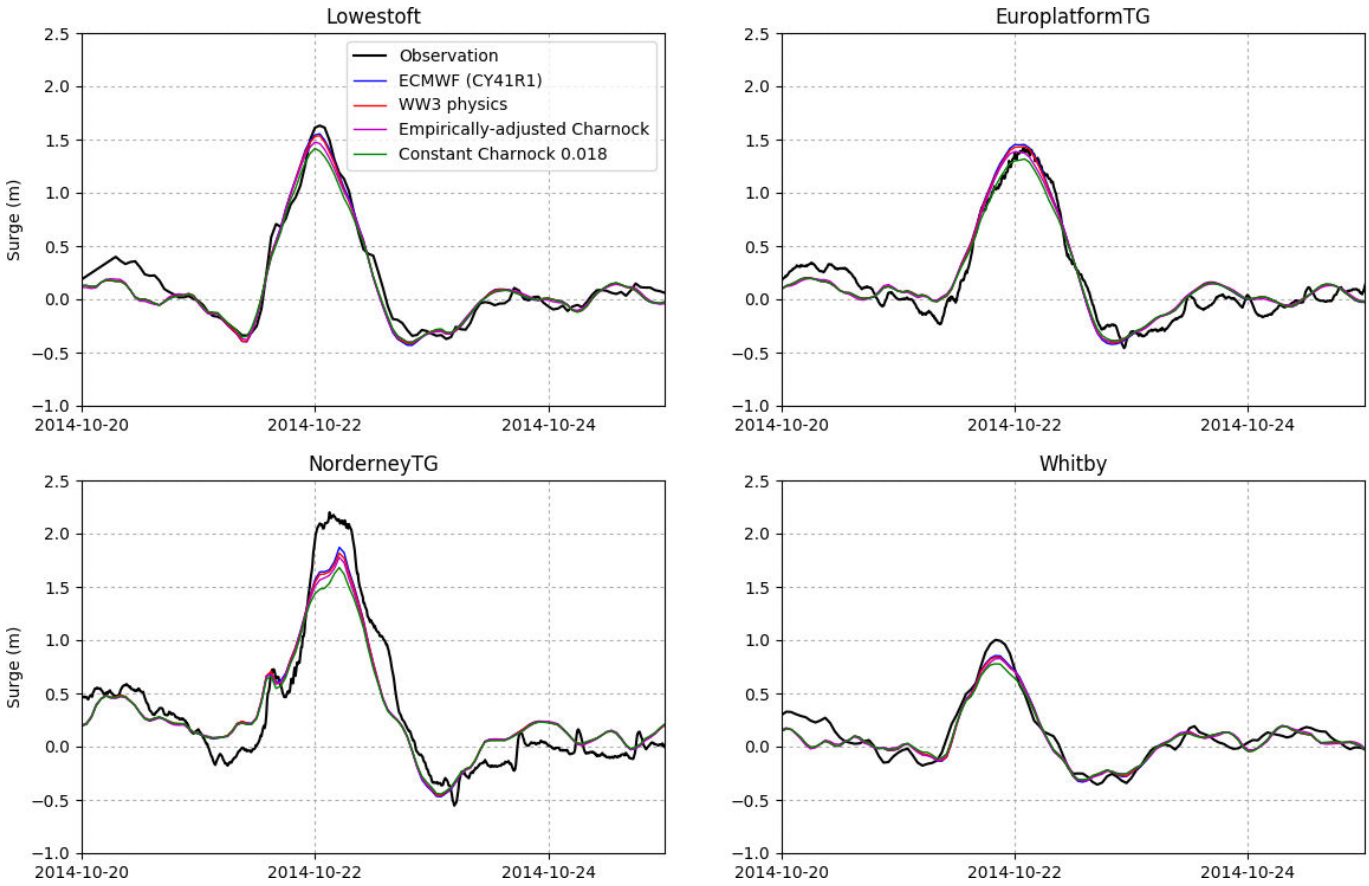

Figure 4.31 – Observed surges and modelled surges with different parameterizations at tide gauges (Aberdeen, Lowestoft, EuroplatformTG, F3platformTG, NordeneyTG, Whitby) from 20^{th} to 24^{th} of October 2014, during ex-Gonzalo storm

.

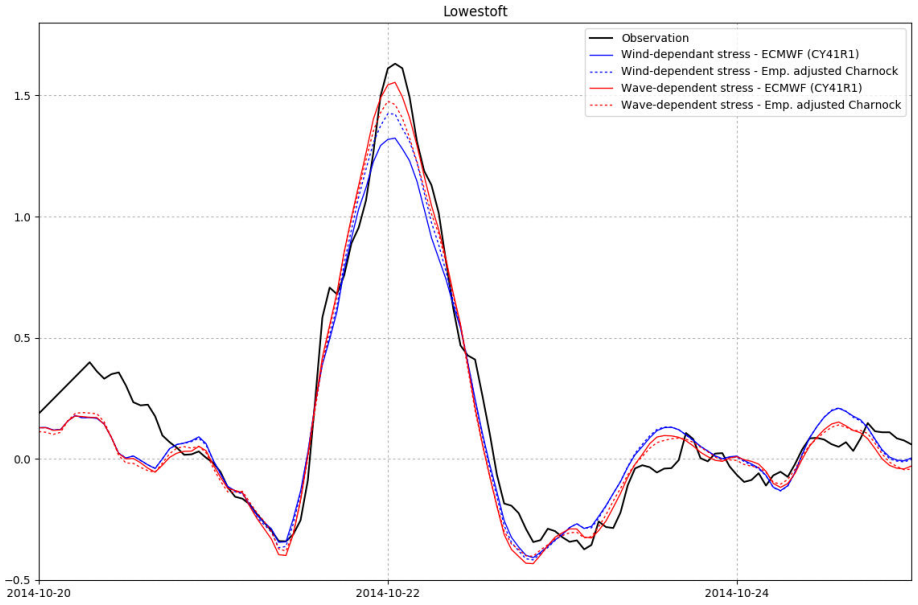

Figure 4.32 – Impact of the forcing (wave- or wind-dependent) on surges for two different parameterizations at Lowestoft from October 20^{th} to 24^{th} 2014, during ex-Gonzalo storm

.

Chapter 5

Conclusions

We started this work because storm surges were undestimated in hydrodynamic models, as well as large wave heights in wave models (Rascle and Ardhuin, 2013; Hanafin et al., 2012; Stopa and Cheung, 2014). This could come from (1) underestimation of strong winds in atmospheric models (2) inapropriate wind stress formulation. The objectives were (1) to estimate how strong are the biases for high winds in atmospheric models (2) to explore new drag parameterizations that could reduce this bias (3) to investigate the impact of the waves on the wind stress. To answer these questions, we used a consistent approach, studying the response of the atmosphere and the ocean to the wind stress. For the atmosphere response, we used the coupled wave-atmosphere model from ECMWF (ECMWF, 2015a), and for the ocean response the global finite element ocean model TUGO, forced by the same coupled wave-atmosphere model. We simulated various storms characterized by various sea states. We compared the simulated winds and surges with the maximum of observations available: winds measured from the buoys and the platforms, as well as estimated from remote sensing sensors (scatterometers, radiometers and altimeters); surges from tide gauges, as well as from altimeters.

For the first part of the study, we compared simulated winds from the ECMWF coupled wave-atmosphere model with in situ and satellite observations available in the North Atlantic during Kaat and Lilli storms (23-27 January 2014). We developed an empirically adjusted Charnock parameterization, to obtain winds closer to observations. We showed that moderate simulated winds (5-20 m/s) agree well with both in situ and satellite observations, whereas strong winds (above 20 m/s) are generally underestimated compared with observations; the negative bias can reach -7 m/s at 30 m/s . We showed that biases exist between observations. It is difficult to conclude which dataset should be used as a reference, but buoys and ASCAT-KNMI winds are likely to be underestimated. We showed that a newly empirically adjusted Charnock parameterization would lead to higher winds than the default ECMWF ones. Yet, common wave-age-dependent parameterization gives larger drag coefficients than measurements - and lower winds - and is not appropriate for coupling.

For the second part of the study, we compared simulated surges from TUGO global ocean model with tide gauges and altimeter data in the North Sea for different wind stress parameterizations and during various storms characterized by different sea states (young and old sea states). The results are the following. (1) We showed that the global model predicts accurately surges (RMSE of 0.12 cm), even in coastal areas, despite a global grid. This can be attributed partly to the finite element grid, which allows increasing the resolution in shallow waters. (2) The present work confirms the capability of altimeters to measure surges with a good precision (RMSE of 0.08 m along the track). (3) When the sea state is old, the classical wind-dependent stress formulation is appropriate (here, (Hellerman and Rosenstein, 1983)). However, when the sea becomes younger and rougher, the waves increase the wind stress, and a wave-dependent stress formulation is preferred (here, Janssen (1991)). The wave effect on the surge can reach 20 to 25 cm. (4) Underestimated winds are not always the main reason for surge underestimation

in models, the wave impact may be higher. (5) The forcing paradox (i.e. contrasted results depending on how the ocean model is forced) was one of the disturbing result of this study. Finally, the number of case studies should be increased in order to have a more statistical approach and confirm these conclusions. It is not yet clear if the improved results do not come from compensation of other errors.

In the present work, we tried to have a consistent approach, looking at the same time at the atmosphere and the ocean response. However, this led to the "forcing paradox". Finally, the newly developped parameterization allowed an improvement of the winds, but not of the surges (compared with observations), when the ocean model is forced with the wind stress. This paradox raises various questions: (1) the difficulty to compare the model with observations (observations must be carefully processed and deeply understood, which processes are in the observations, which ones are in the models?), (2) the problem of compensating errors in models (Moon et al., 2009), and (3) the lack of consistency between the wave, atmosphere and ocean models (van Nieuwkoop et al., 2015). To be more consistent, the ocean model should be forced directly by the stress from the atmosphere model.

We also tried to use the maximum of data, from models, in-situ and satellites. Investigating at the same time various type of observations is complex, as they are rarely consistent with each other. Here, we found a significant bias between the buoy and the platform winds. Despite investigations, finally it is not clear what the surface wind reference should be, and where the truth lies. The combined use of tide gauges and altimeters raised the question of the processes observed by each instrument. In validation processes, we should not systematically want the model to match with tide gauges. Similarly, for trend detection, particularly in the context of climate change, comparison between tide gauges and altimetric data should be conducted with care, as the processes are not always the same onshore and offshore.

Finally, from a physical point of view, the drag is expected to combine various processes including air flow separation over breaking waves (Reul et al., 1999, 2008; Kudryavtsev et al., 2014), which is not represented in the quasi-linear model of Janssen (1986) on which the ECMWF parameterization is based. Some approaches introducing more physics in the parameterization through the effect of breaking waves, could be further investigated (e.g. Kudryavtsev et al., 2014). Note that many other processes may influence the drag: precipitations, surface currents, spray and sea drops at strong winds (Makin, 2004; Kudryavtsev, 2006; Kudryavtsev and Makin, 2006; Soloviev et al., 2014). These processes were not taken into account in the present work.

Chapter 6

Perspectives

6.1 Modelling

6.1.1 Atmosphere models

Previous coupled modelling studies had suggested that high drag coefficients were not compatible with severe storms and hurricanes, and other studies (e.g. Doyle, 2002) identified that coupling of atmosphere and waves could lead to more intense storms, probably due to larger heat and moisture fluxes. In the present work, we have not investigated the mechanisms by which the atmosphere adjusts to the modified roughness. This is clearly an area where more work is needed to understand the complex feedback between the surface boundary conditions and the surface winds.

The present work, in close collaboration with ECMWF, led to several modifications in their system. In cycle CY43R1 (November 2016), the introduction of a limiting factor for the steepness of the waves led to a reduction of the drag for very high wind speed (Magnusson et al., 2018). In future cycle CY46R1 (June 2019), the introduction of the physics from Ardhuin et al. (2010) will lead to a slightly tighter distribution for Charnock values, and will potentially adress the problem of too low winds in storms. The next developments at ECMWF will focus on rain effects and spray impact on the drag.

Note that following this work, a new drag parameterization has also been developped at Météo-France.

6.1.2 Wave models

The wind stress is mainly supported by the capillary and short gravity waves, i.e. the tail of the spectrum, which is very crudely represented in wave models today (Kudryavtsev et al., 2014; Peureux and Ardhuin, 2016). Dedicated efforts are undergoing to improve wave breaking parameterization, in order to also improve the tail of the spectrum (Peureux et al., 2018). Note that there are also many uncertainties of the wave growth parameter β.

6.1.3 Ocean models

The wave setup may significantly contribute to the total water level. This component can reach several tens of centimetres, and even more (> 1 m) (Brown et al., 2010; Idier et al., 2010; Sheremet et al., 2014). The wave setup is modelled taking into account the radiation stress (Longuet-Higgins and Stewart, 1964). At the coastal scale (resolution of hundreds meters), the relative contribution of wave-induced hydrodynamics (i.e. wave-induced currents and large scale wave setup) to the overall hydrodynamics could be investigated using fully coupled hydrodynamic and wave model (Bertin et al., 2015; Pedreros

et al., 2018).

Ocean models should be forced by the stress going into the ocean, whereas they are generally forced by the winds or by the atmospheric stress coming from an atmosphere model. Indeed, a part of the atmospheric stress, expressed as $\tau_a = \rho_a u_*^2$, is going into the waves. The momentum flux going into the ocean τ_{oc} is the sum of two contributions (Figure 6.1): the part of the atmospheric flux which was not used to generate the waves $\tau_o = (\tau_a - \tau_w)$ and the momentum flux transferred from the waves to the ocean by dissipation τ_{diss} (ECMWF, 2015b)

$$\tau_{oc} = \tau_o + \tau_{diss} = \tau_a - \tau_w + \tau_{diss}. \tag{6.1}$$

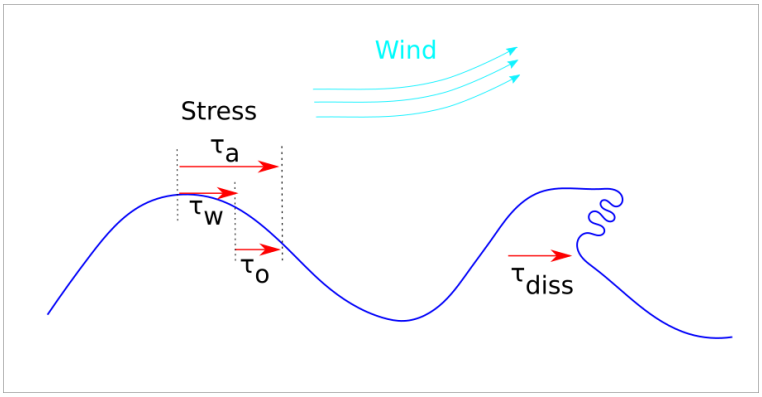

Figure 6.1 – Schematic representation of momentum fluxes at the the air-sea interface (adapted from Janssen et al. (2013)). The momentum flux going into the ocean τ_{oc} is the sum of τ_o and τ_{diss}.

The normalized stress going into the ocean corresponds to the ratio τ_{oc}/τ_a (output parameter of ECMWF operational version). It is globally close to 1, but can reach higher values as 1.5, under extreme conditions, e.g. with a passing front (Janssen, 2012). Figure 6.2 shows the normalized stress going into the ocean during ex-Gonzalo storm, the 21^{st} October 2014 at 17:00. Note that this parameter comes from ECMWF operational forecasts, as it is not available as an output parameter in the IFS research version we used in this study. The winds at the same instant are shown on Figure 4.14 (b). The normalized stress is in average close to 1. Its spatial mean over the North East Atantic is 1.001. However it can be locally greater than 2, for instance when ex-Gonzalo front is passing. The maximum value reaches 4. The strong gradients suggest a potential impact on the ocean model. Further investigations have to be conducted to test the impact of forcing the ocean model with the stress going into the ocean, rather than the atmospheric stress.

Finally, Figure 6.3 suggests a more consistent way of forcing the ocean model. The stress would come directly from the wave model (or coupled wave-atmosphere model), instead of the atmosphere model. The waves at the air-sea interface play a key role: they take the energy from the wind for growing, and redistribute it into the ocean by wave breaking.

6.2 Observations

6.2.1 Extreme winds

More datasets representing extreme conditions are needed, in order to develop parameterizations, validate models and calibrate remote-sensing instruments.

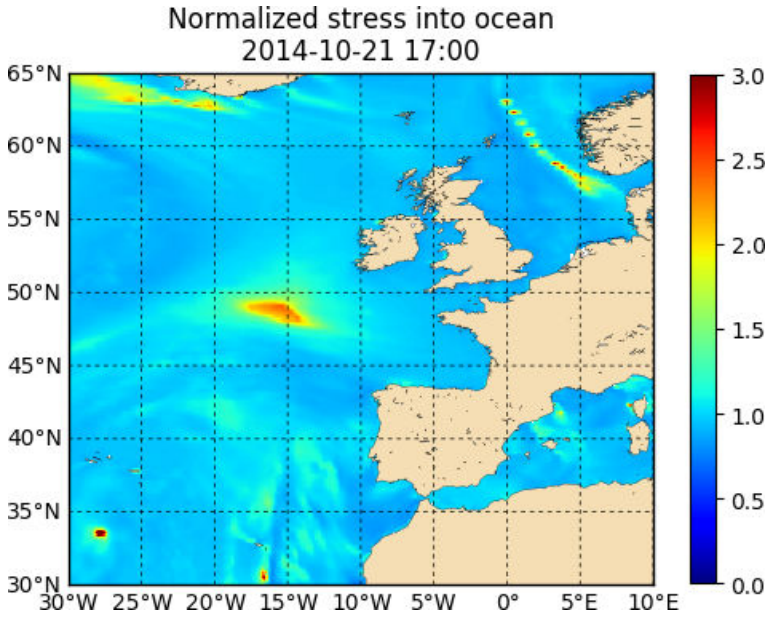

Figure 6.2 – Normalized stress into ocean the 21 October 2014 17:00. Values come from ECMWF operational forecasts.

6.2.2 Buoy and platform wind bias

We found a significant bias between buoy and platform strong winds. It reaches around 3 m/s at 25 m/s and suggests that buoy winds are lower than platform ones. Despite investigation, it is finally not clear where these differences come from. Recent studies show contrasted results. Emond and Vandemark (2018) compared wind measurements from a buoy (NDBC station 44030) and a tower platform on a island (NDBC station IOSN3), located close to each other (around 20 km). The data cover the period 2002-2017, with a temporal resolution of 10 minutes. Filtering was applied to remove samples where the wind speed is changing significantly in a 1 hour time window. Figure 6.4 shows the correlation between the buoy and the tower winds. There is no significant bias between the buoy and the tower. Further investigations should be undertaken to try to understand these contrasted results, and define what the surface wind reference should be.

6.2.3 Qualification of remote sensing winds

The methodology developped during this work allows the detection of biases between instruments, that can not be easily compared between each other, as they are not at the same location (e.g. buoys and platforms). The atmosphere model is used here as a common reference. This approach should be extended for future satellite's missions, in order to qualify the winds estimated from instruments. A the end of October 2018, CNES and the China National Space Administration (CNSA) will launch CFOSAT (China-France Oceanography SATellite). It will carry onboard two radar instruments: a wave scatterometer and a wind scatterometer. Wind estimation could be qualified with the same approach as the one described in Pineau-Guillou et al. (2018).

Note the launch in August 2018 of ESA ADM-Aeolus (Atmospheric Dynamics Mission), the first satellite mission to acquire profiles of Earth's wind on a global scale.

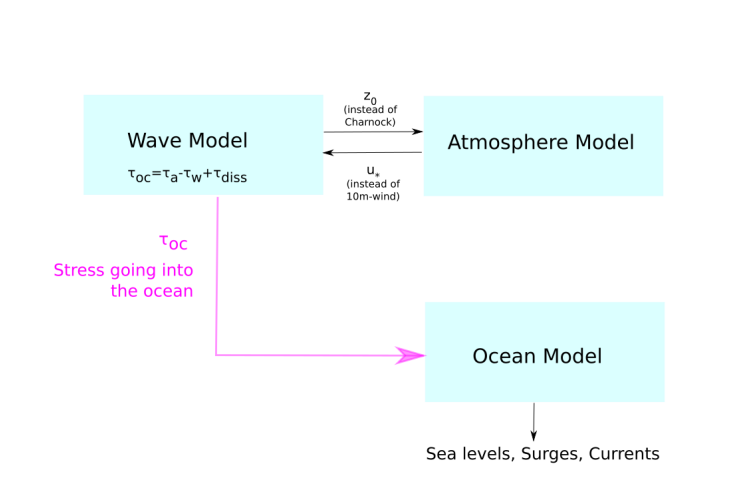

Figure 6.3 – A more consistent way of forcing the ocean model

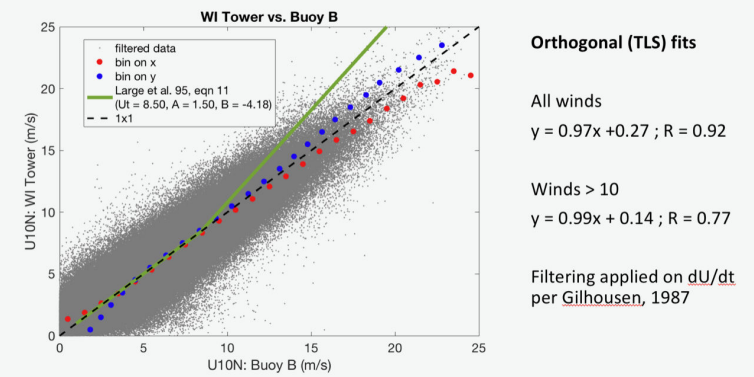

Figure 6.4 – Correlation between the buoy and the tower winds (Courtesy of D. Vandermark)

6.2.4 Surges from altimeters

We demonstrated the capability of altimeters to estimate the surges with a good precision, even in coastal areas. Whereas tide gauges give only local information near the coast, remote sensing data give useful complementary information on the spatial repartition of the wave over hundred of kilometers. Recent and coming years correspond to a "golden era" for Earth Observations, and remote sensing data should help to understand storm surge events, and probably also other events, as for example meteo-tsunami. In this work, we used only JASON-2 data, but as today, up to 6 altimeter missions are available to provide unprecedented coverage (the NASA/CNES Topex/Poseidon and Jason instruments, the European Space Agency ERS, Envisat, CryoSat-2 instruments, and more recently Sentinel 3, the French/Indian Ka-band SARAL, and Chinese HY-2A). Moreover, dedicated efforts are ongoing to improve the precision of sea level products in coastal areas (Passaro et al., 2014; Birol et al., 2016). Data are now reliable up to 3 km near the coasts, and 20 Hz high-frequency products have a spatial resolution around 350 m along the track (but note that the data has to be filtered). Note also the launch in 2021 of the NASA/CNES SWOT (Surface Water and Ocean Topography) mission, a high-resolution wide-swath altimetry mission, that should allow characterizing the ocean mesoscale and sub-mesoscale circulation (15-200 km) at spatial resolutions of 15 km and greater.

6.2.5 Improvement of altimetric corrections

Following this work, one of the recommendation is to force the ocean model with the wind stress of a coupled wave-atmosphere model (which has seen the waves), rather than with the winds from the same atmosphere model. This allows indirectly the coupling between the ocean model with the waves. These results were presented at the Ocean Surface Topography Science Team annual meeting in October 2018. This recommendation could be followed for the next version of Dynamic Atmospheric Corrections, conducted by LEGOS and CLS.

6.3 Wind stress and surface currents

In this work, we investigated the impact of the waves on the drag, through the surges. Similar work could be further undertaken to study the impact of the waves on the drag, through the ocean circulation. In this case, the use of a 3D ocean model is necessary. Simulated currents could be compared with measurements. The main difficulties for ocean current measurements is the lack of permanent observations. Whereas altimeters have been measuring the sea level for 25 years, the ocean currents have not yet been directly measured from the space. Some authors propose current products from altimeters, but this corresponds only to large scale geostrophic currents (e.g. Rio et al., 2014). Note that there is also a lack of in-situ measurements: whereas permanent tide gauges have been measuring the sea level continuously from more than 30 years in many harbours - and more than 100 years in some of them, permanent surface currents observations as Radar HF stations were implemented quite recently.

The DRIFT4SKIM campaign dedicated to surface current measurements could be an opportunity to investigate the relation between the wind stress and the surface currents. The objective of this campaign is to demonstrate that the novel instrument SKIM based on Doppler radar measurement of the ocean surface can provide surface currents (Chapron et al., 2005). The campaign is planned in the Iroise Sea, in November 2018, and will focus on two 4-km side squares located in the field-of-view of a shore-based HF radar system measuring surface current vectors (Figure 6.5). Observations will consist of airborne doppler measurements, as well as the deployment around 80 surface drifters, around 10 drifters with drogues at 15, 5, 2 and 1 m, around 10 drifting wave-measuring buoys, an eddy-correlation air/sea fluxes measurement buoy (measuring wind stress and wind) and a buoy carrying a current profiler providing eulerian current, and vertical shear (Marié and Ardhuin, 2018).

Previously, we underlined that many processes contributed to the total surge (atmospheric surge, wave setup, tide-surge interaction...see Table 4.1). Similarly, the total surface current includes many contributions: tidal current, wind driven Ekman current, wave-induced Stokes drift, Langmuir circulation, internal waves, geostrophic currents, inertial currents...As a consequence, the data has to be analysed with care, to extract (if possible) each contribution, and particularly the wind driven currents.

The simultaneous measurements of wave, wind, and wind stress thanks to eddy-correlation air/sea fluxes measurement buoy could be analysed to investigate the impact of the waves on the wind stress. This will be relevant, if the wind is strong enough during the campaign, i.e. higher than 20 m/s. However, the air/sea fluxes measurement buoy is still under development, and it is difficult to know how reliable will be the fluxes data.

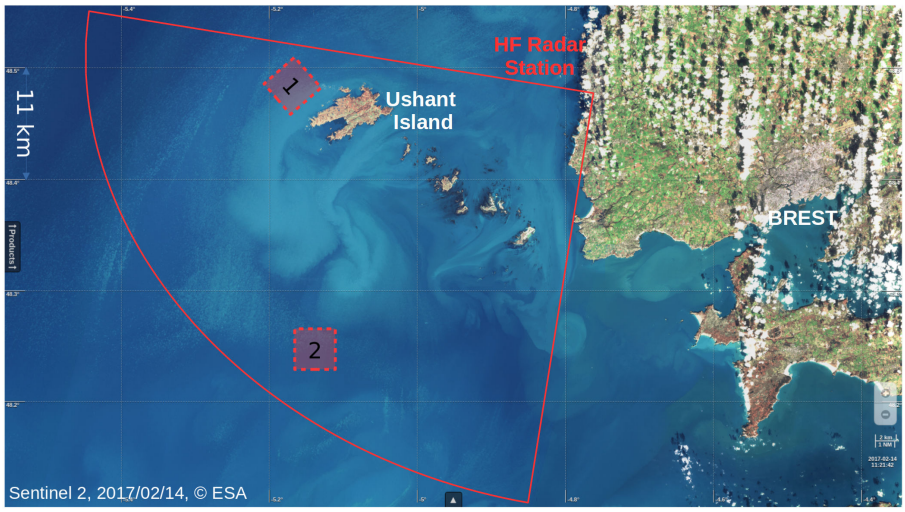

Figure 6.5 – DRIFT4SKIM campaign in the Iroise Sea, planned 19-30 November 2018. Observations will be performed in the two squares 1 and 2. (Courtesy of L. Marié)

Acknowledgment

Acknowledgement is made for the use of ECMWF's computing and archive facilities in this research. We thank all ECMWF staff for the warm welcome and excellent support provided. KNMI (Royal Netherlands Meteorological Institute), SOLab (Satellite Oceanography Laboratory, Russian State Hydrometeorological University), Remote Sensing Systems (RSS), NASA PODAAC and CNES Aviso provided remote-sensing data, and Germany's National Meteorological Service provided synoptic charts. We also thank O. Breivik and Norwegian Meteorological Institute for providing wind measurements from Norwegian platforms, BSH for providing FINO1 platform data, M. Passaro and Technical University of Munich for providing ALES 20 Hz JASON-2 coastal product, F. Léger and CTOH/LEGOS for providing JASON-2 1Hz X-track coastal product, F. Lyard and LEGOS for providing TUGO ocean model and CMEMS for providing tide gauges data.

Appendices

Appendix A

Examples of bulk formulae

Authors	Formulation	Wind speed range
Smith and Banke (1975)	$10^3 C_d = 0.63 + 0.066 U_{10}$	2.5-21 m/s
Smith (1980b)	$10^3 C_d = 0.61 + 0.063 U_{10}$	6-22 m/s
Large and Pond (1981)	$10^3 C_d = 1.2$	4-11 m/s
	$10^3 C_d = 0.49 + 0.065 U_{10}$	11-25 m/s
Wu (1982)	$10^3 C_d = 0.8 + 0.0655 U_{10}$	
Hellerman and Rosenstein (1983)	$10^3 C_d = 0.934 + 0.788 \times 10^{-1} U_{10} + 0.868 \times 10^{-1} \Delta T - 0.616 \times 10^{-3} U_{10}^2 - 0.12 \times 10^{-2} \Delta T^2 - 0.214 \times 10^{-2} U_{10} (\Delta T)$	
Geernaert et al. (1987)	$10^3 C_d = 0.577 + 0.085 U_{10}$	4 - 24 m/s
Yelland and Taylor (1996)	$10^3 C_d = 0.29 + 3.1/U_{10} + 7.7/U_{10}^2$	3 - 6 m/s
	$10^3 C_d = 0.6 + 0.07 U_{10}$	6 - 26 m/s
Peng and Li (2015)	$C_d = -0.0215 (U_{10} - 33)^2 + 2.797$	10 - 50 m/s
Moon et al. (2007)	$z_0 = \frac{0.0185}{g} (0.001 U_{10}^2 + 0.028 U_{10})^2$	$\leqslant$ 12.5 m/s
	$z_0 = (0.085 U_{10} - 0.58) 10^{-3}$	$>$ 12.5 m/s
Edson et al. (2013)	$\alpha = 0.017 U_{10N} - 0.05$	$\leqslant$ 19 m/s
	$\alpha = 0.028$	19 - 25 m/s

Table A.1 – Wind speed-dependent formulations of drag coefficient (C_d), roughness length (z_0) and Charnock parameter (α). ΔT is air temperature minus sea temperature.

Authors	Formulation	Wind speed range
Geernaert et al. (1987)	$C_{dN} = 0.012 \xi^{-2/3}$	
Smith et al. (1992)	$\alpha = 0.48 \xi^{-1}$	
Oost et al. (2002)	$\alpha = 50 \xi^{-2.5}$	6 - 18 m/s
Drennan et al. (2003)	$\alpha = 1.7 \xi^{-1.7}$	$<$ 20 m/s
Edson et al. (2013)	$\alpha = 0.114 \xi^{-0.622}$	

Table A.2 – Wave age (ξ) dependent formulations of drag coefficient (C_d), roughness length (z_0) and Charnock parameter (α).

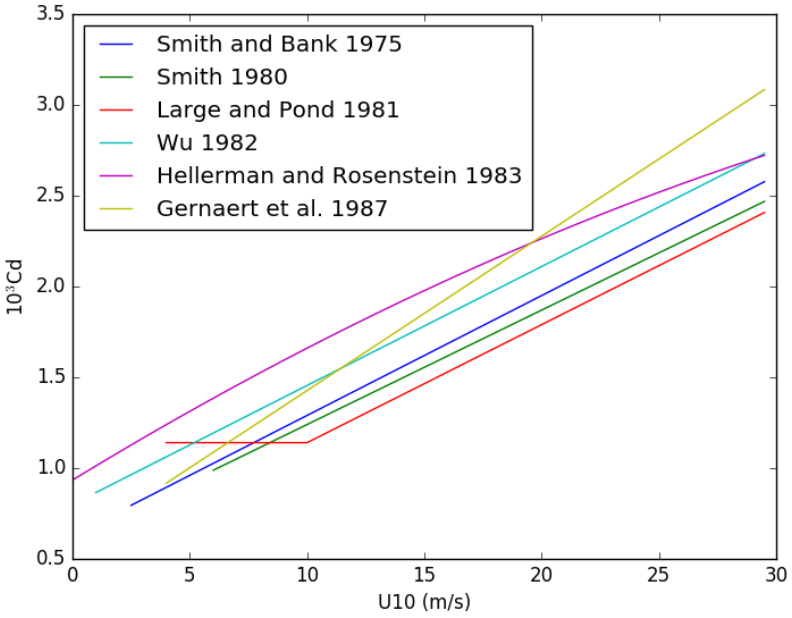

Figure A.1 – Usual wind speed-dependent formulations of drag coefficient

Appendix B

Classification of the 50 strongest storm surges from JASON-2 data analysis

JASON-2 data come from CTOH/LEGOS X-track 1Hz SLA product. The surge is computed following Equation 4.3, the wind comes from ECMWF 1h forecasts, and the wave age is computed from WaveWatchIII following Equation 4.6.

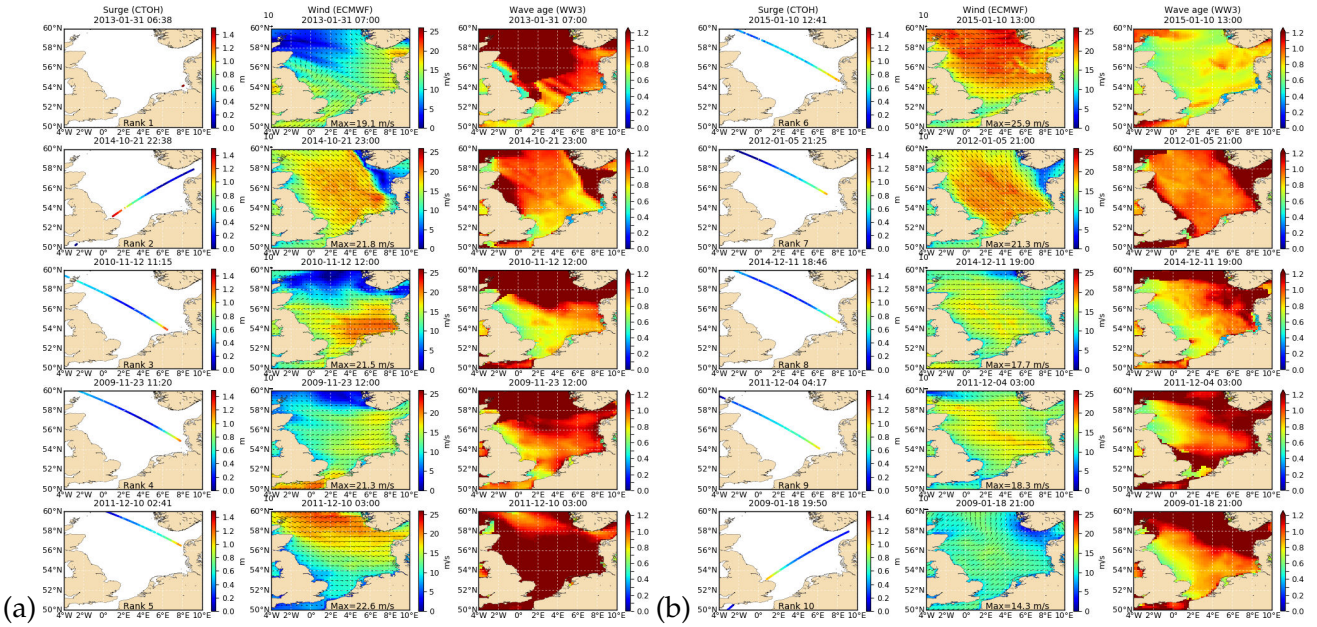

Figure B.1 – Surge from CTOH/JASON-2, wind from ECMWF and wave age from WaveWatchIII for the storms ranked 1-5 (a) 6-10 (b) over the period 2008-2015. The criteria is the maximum surge along the tracks.

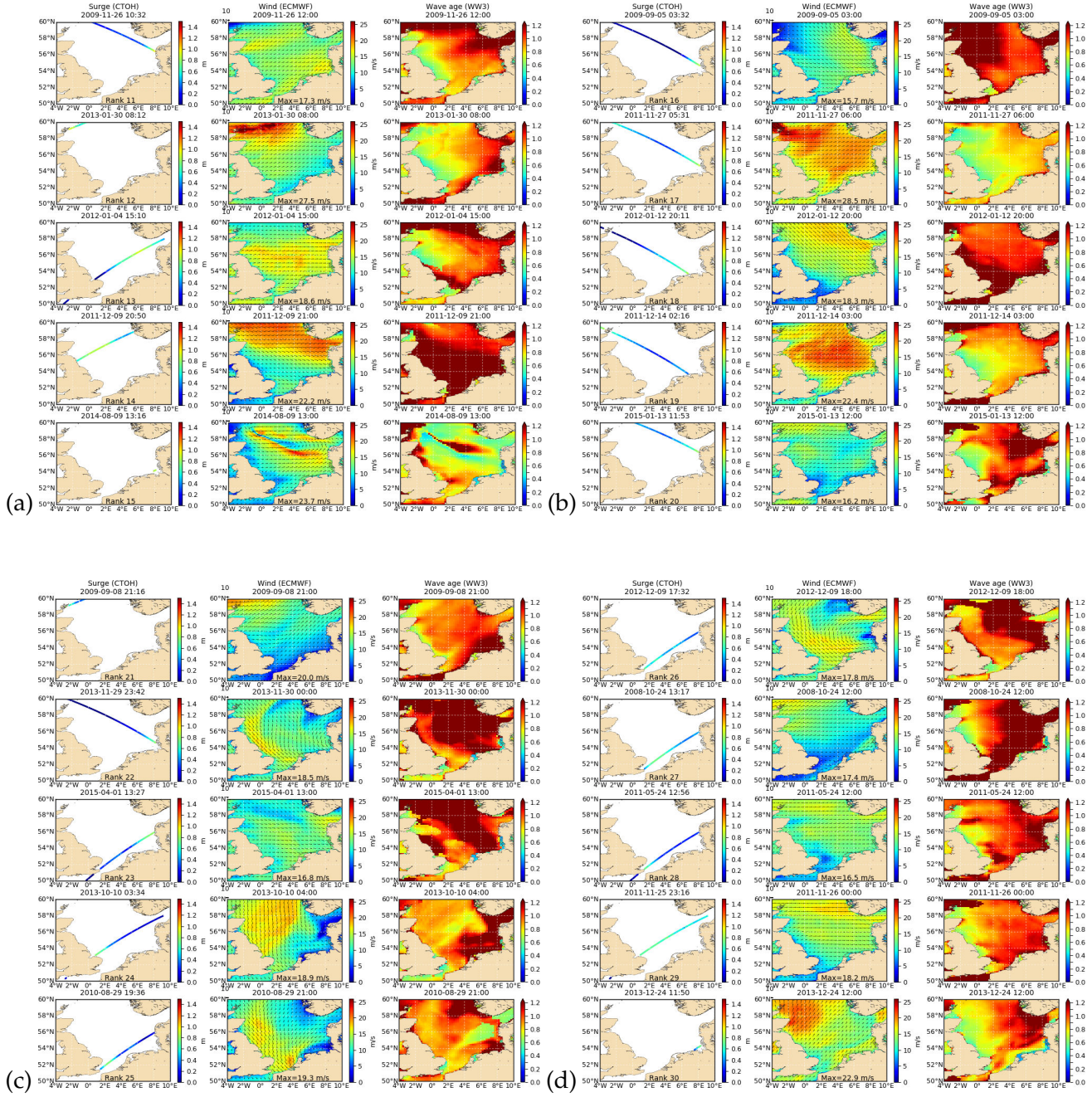

Figure B.2 – Surge from CTOH/JASON-2, wind from ECMWF and wave age from WaveWatchIII for the storms ranked 11-15 (a) 16-20 (b) 21-25 (b) 26-30 (d) over the period 2008-2015. The criteria is the maximum surge along the tracks.

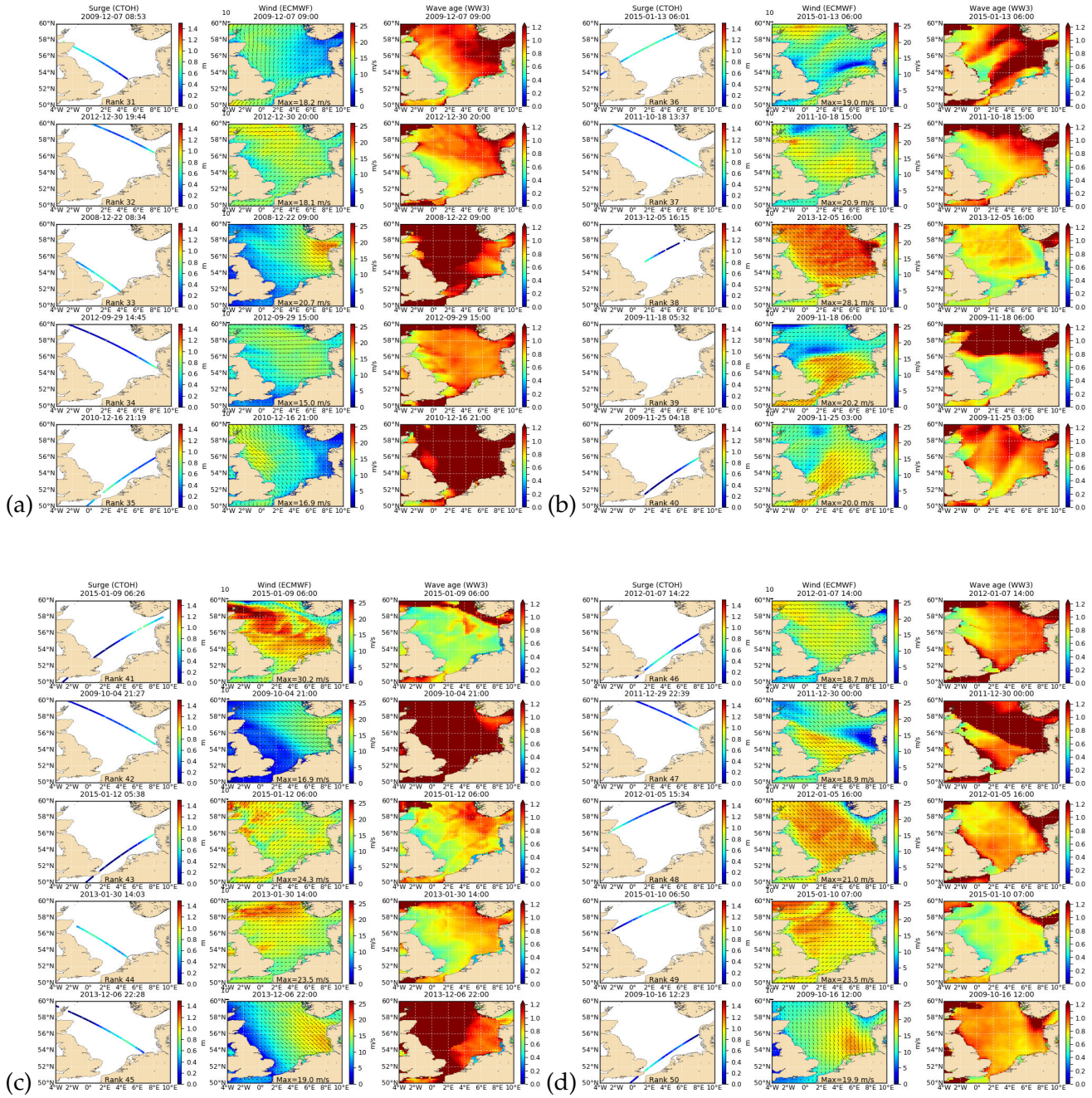

Figure B.3 – Surge from CTOH/JASON-2, wind from ECMWF and wave age from WaveWatchIII for the storms ranked 31-35 (a) 36-40 (b) 41-45 (b) 46-50 (d) over the period 2008-2015. The criteria is the maximum surge along the tracks.

Appendix C

Comparison of atmospheric model with WindSat

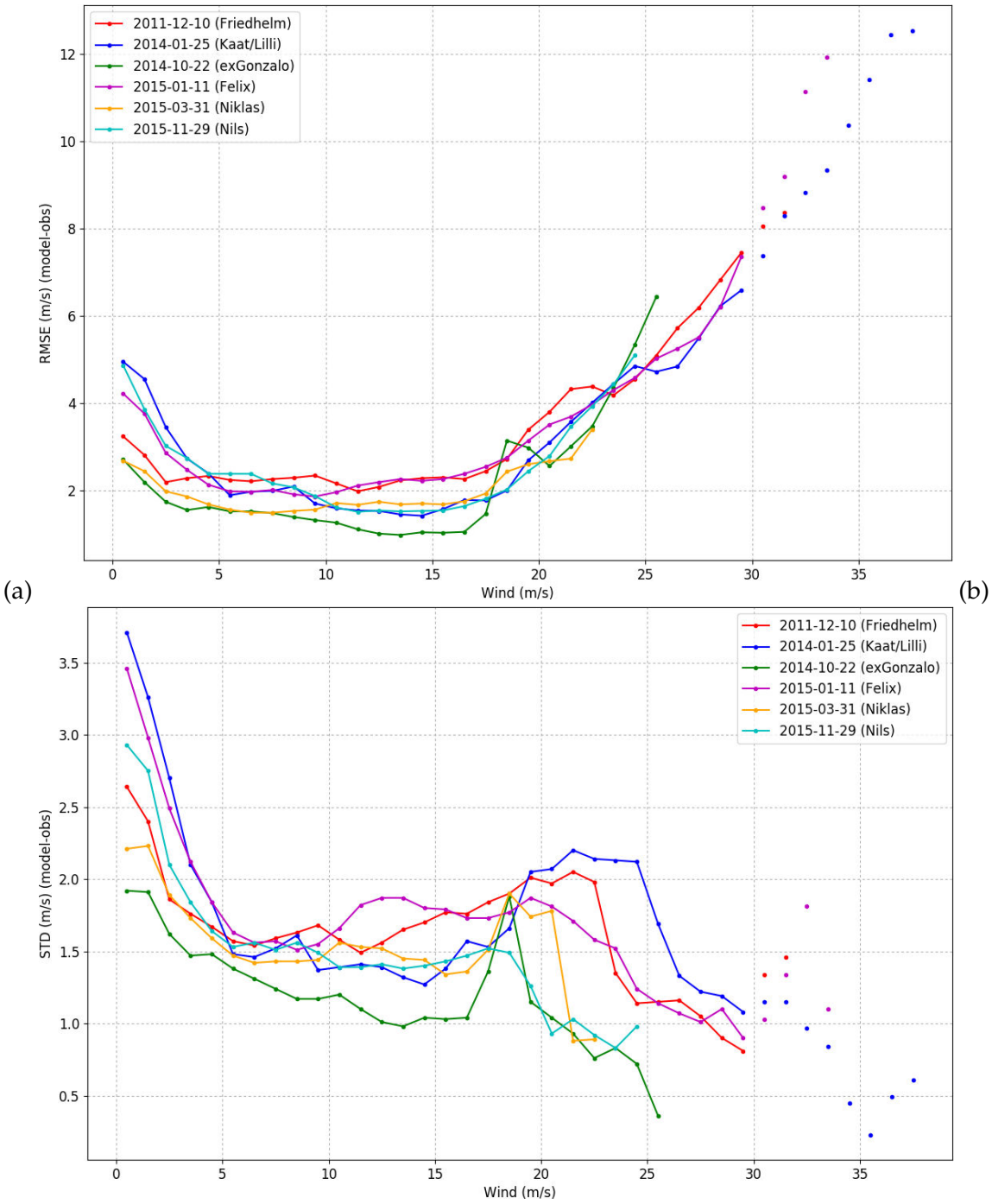

Figure C.1 – Wind RMS Error (a) and Standard Deviation (b) between ECMWF (CY41R1) model and WindSat, computed over a 5-day simulation for each storm. The date in the legend corresponds to the first of the five days. Beyond 30 m/s, values are plotted as points, due to large uncertainties in observations.

Appendix D

Impact of the method to compute the surges

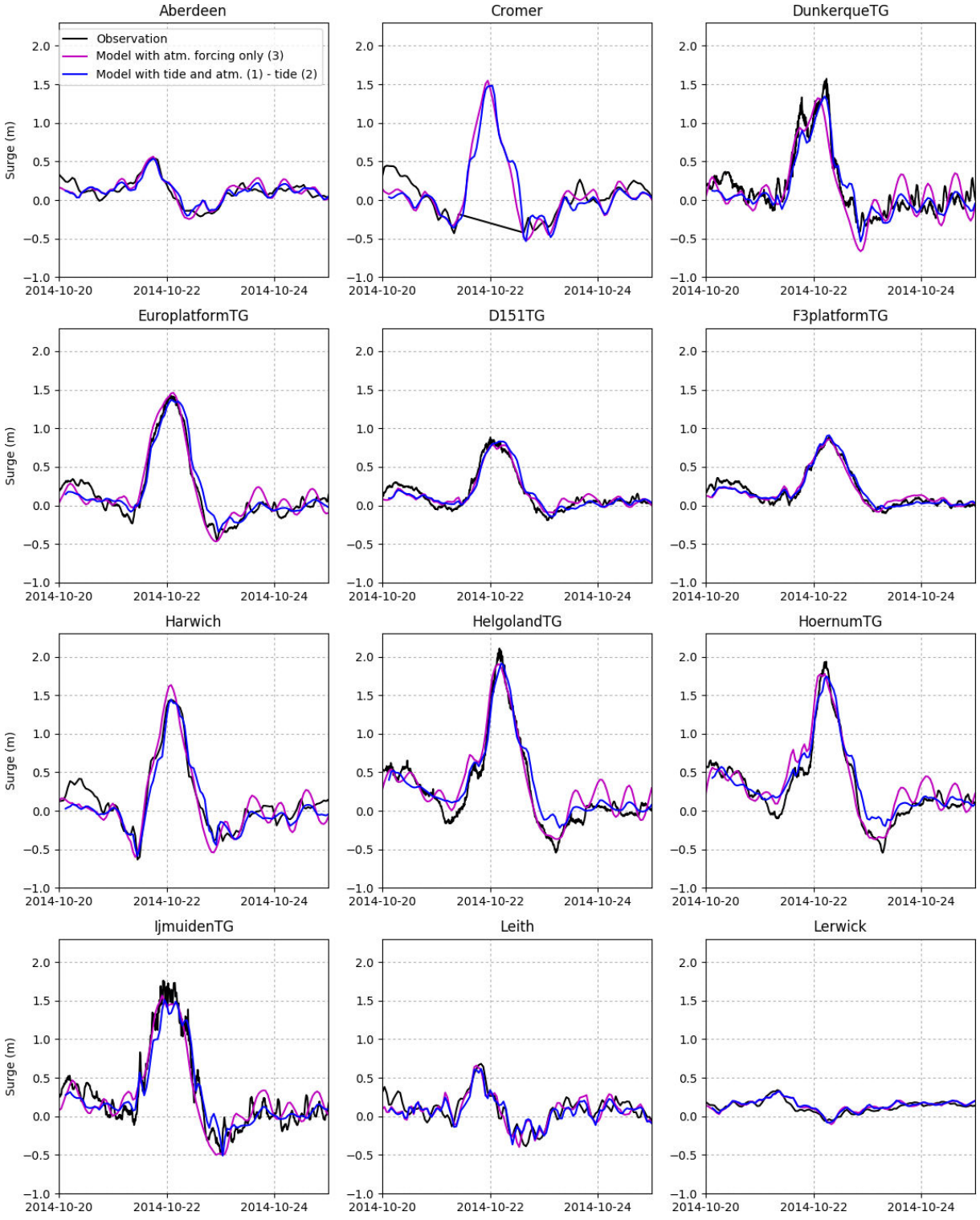

Figure D.1 – Impact of the method to compute the surge at tide gauges (Aberdeen to Lerwick)

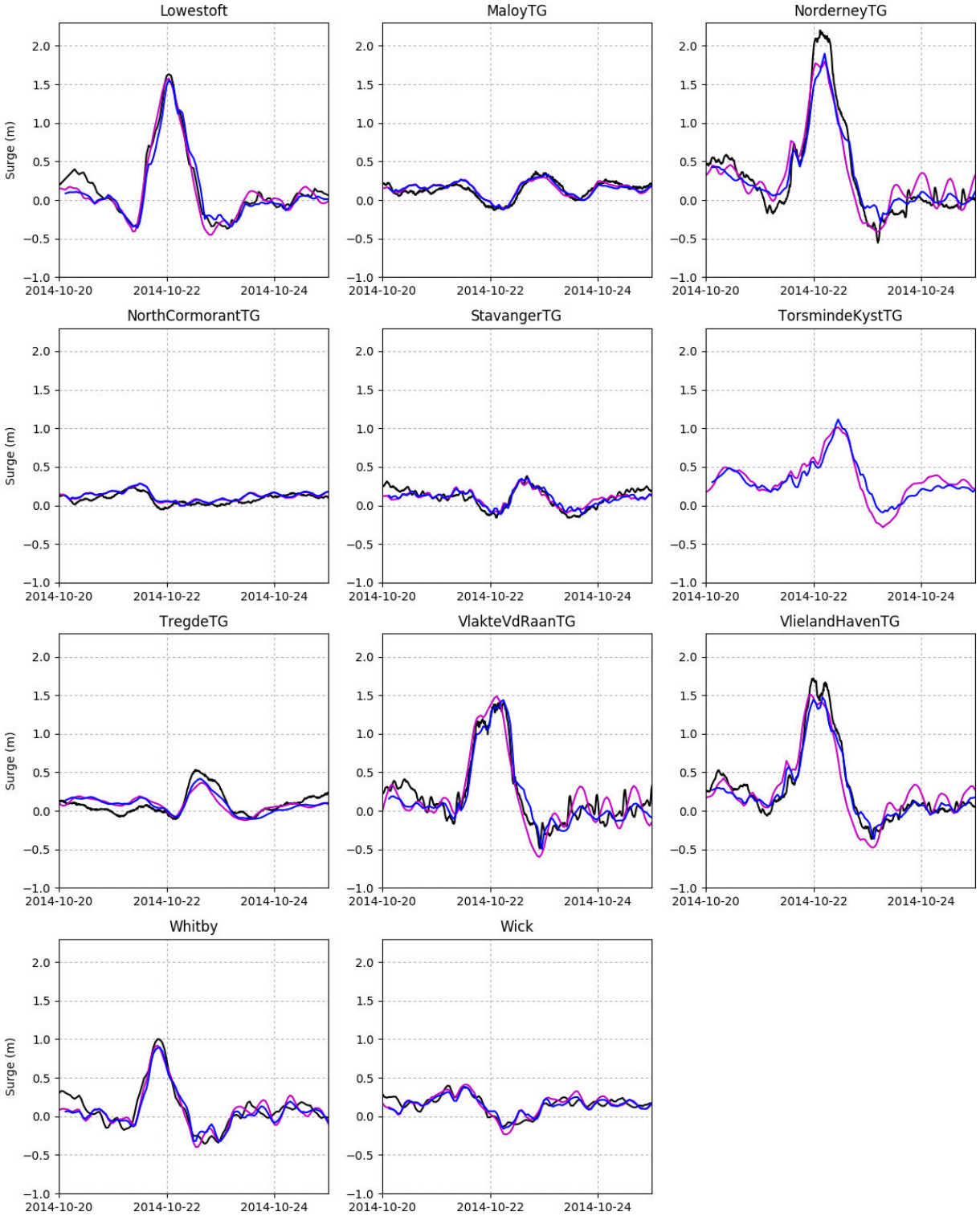

Figure D.2 – Impact of the method to compute the surge at tide gauges (Lowestoft to Wick)

Appendix E

Modelled surges at 23 tide gauges location

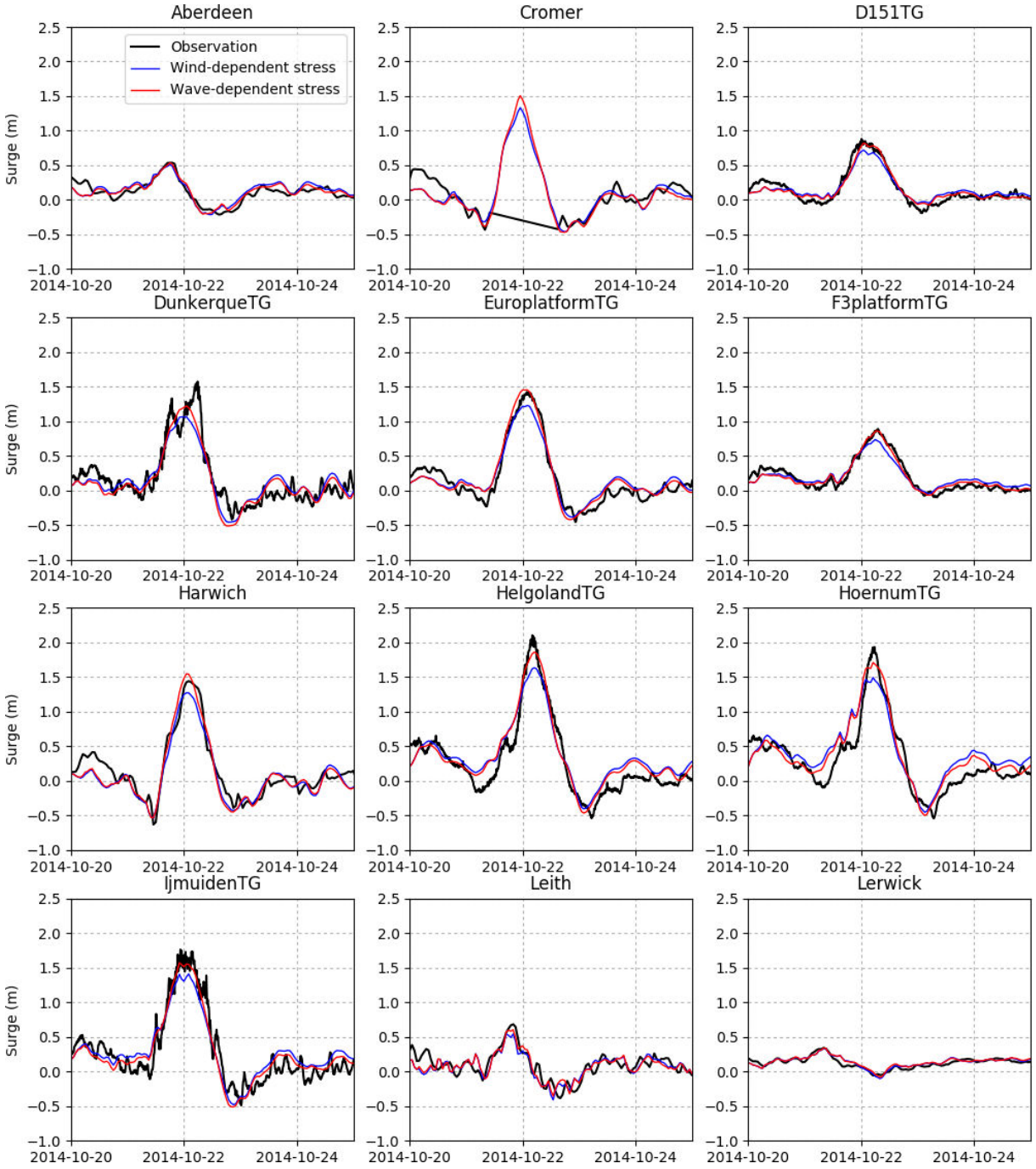

Figure E.1 – Observed and modelled surges with two parameterizations (wind- and wave-dependent) at tide gauges (Aberdeen to Lerwick) during ex-Gonzalo storm

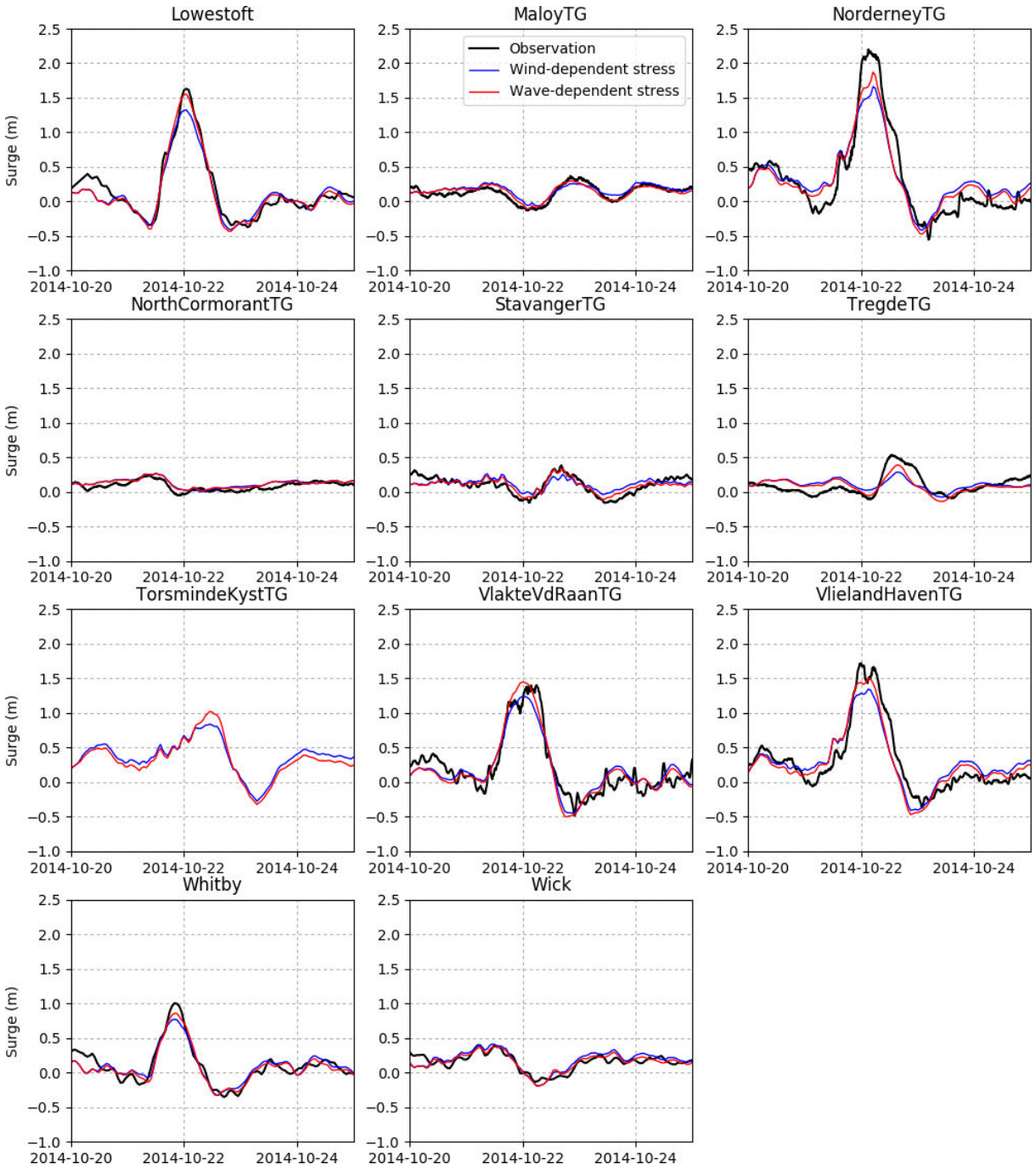

Figure E.2 – Observed and modelled surges with two parameterizations (wind- and wave-dependent) at tide gauges (Lowestoft to Wick) during ex-Gonzalo storm

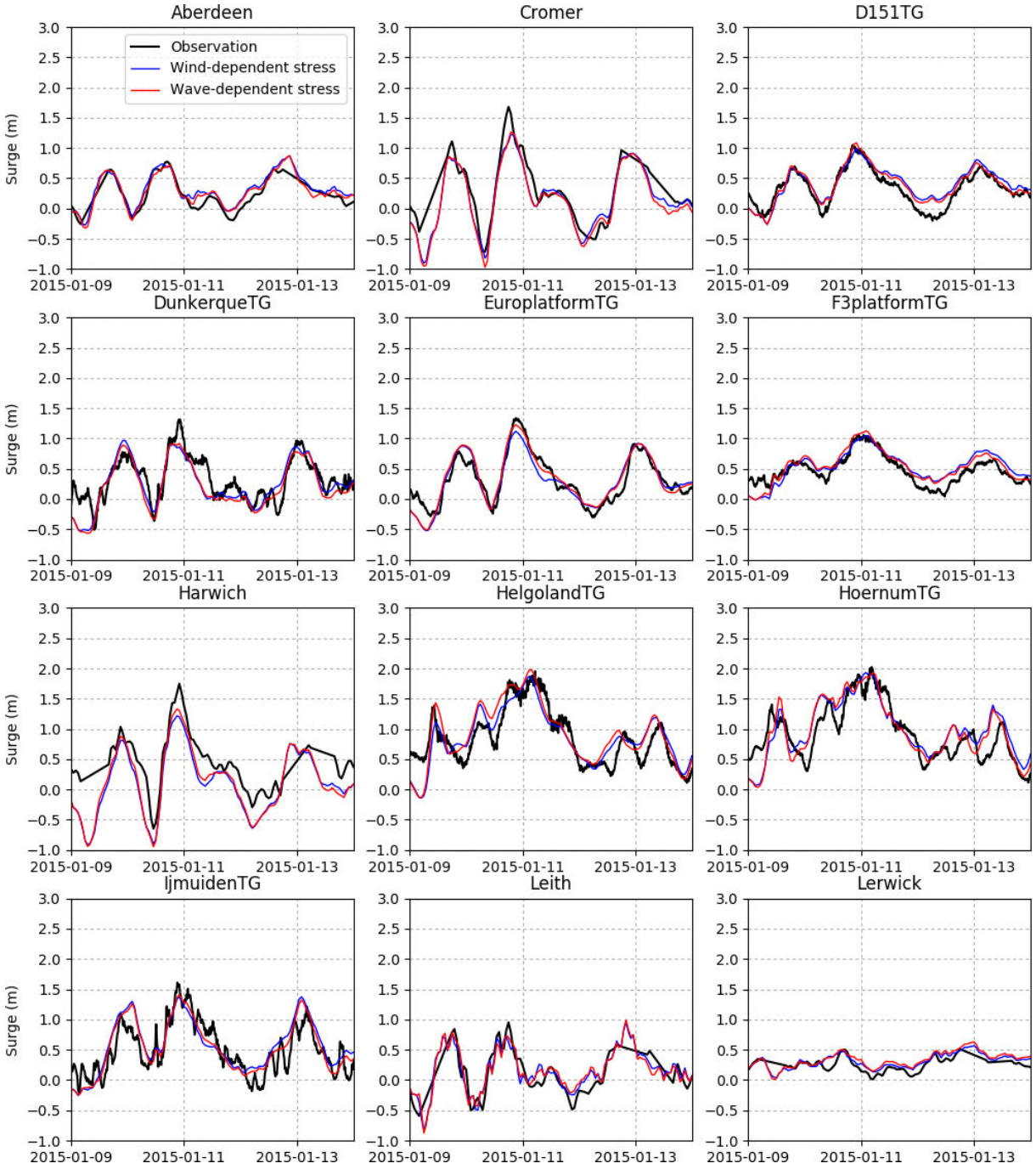

Figure E.3 – Observed and modelled surges with two parameterizations (wind- and wave-dependent) at tide gauges (Aberdeen to Lerwick) during Felix storm

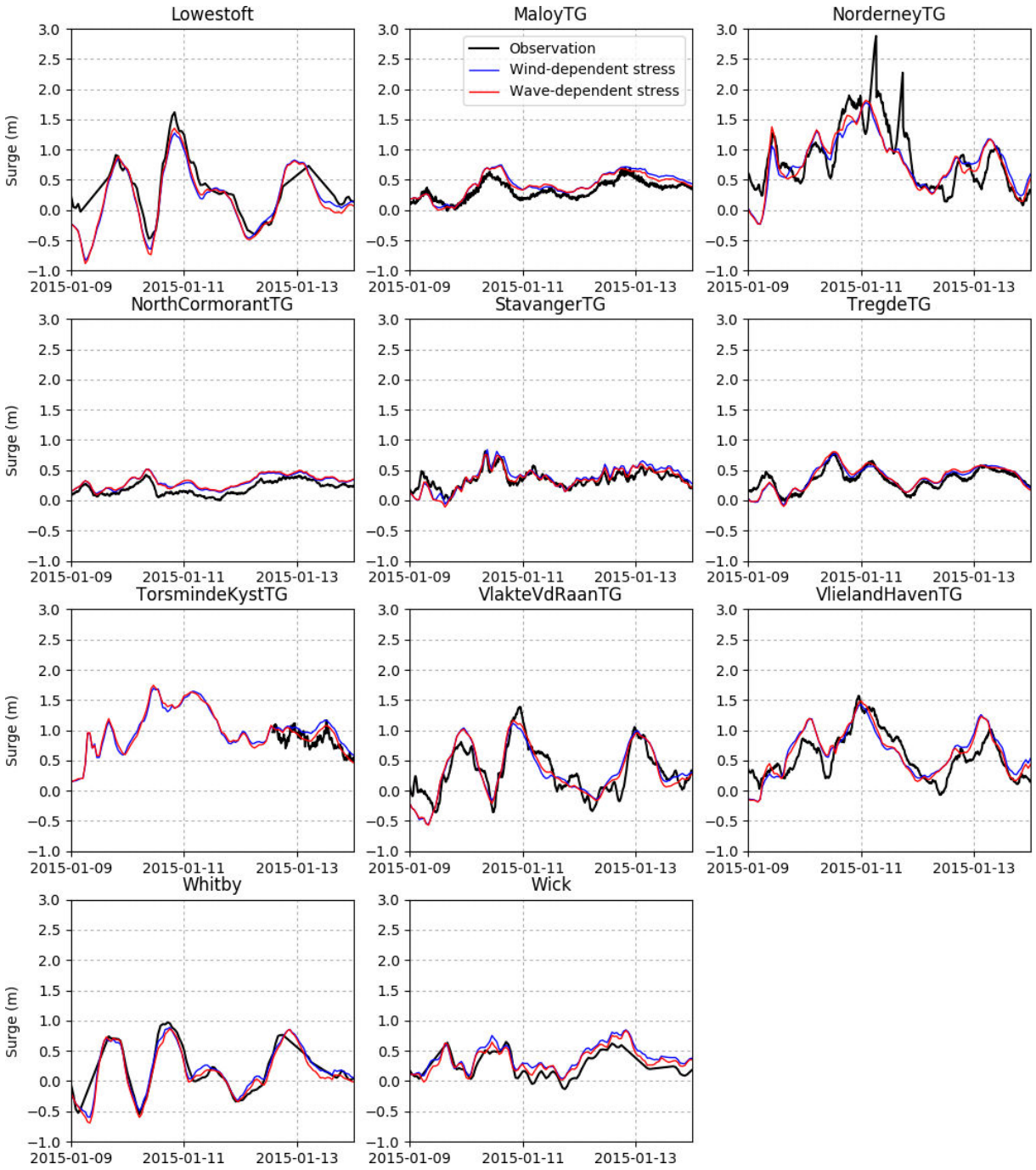

Figure E.4 – Observed and modelled surges with two parameterizations (wind- and wave-dependent) at tide gauges (Lowestoft to Wick) during Felix storm

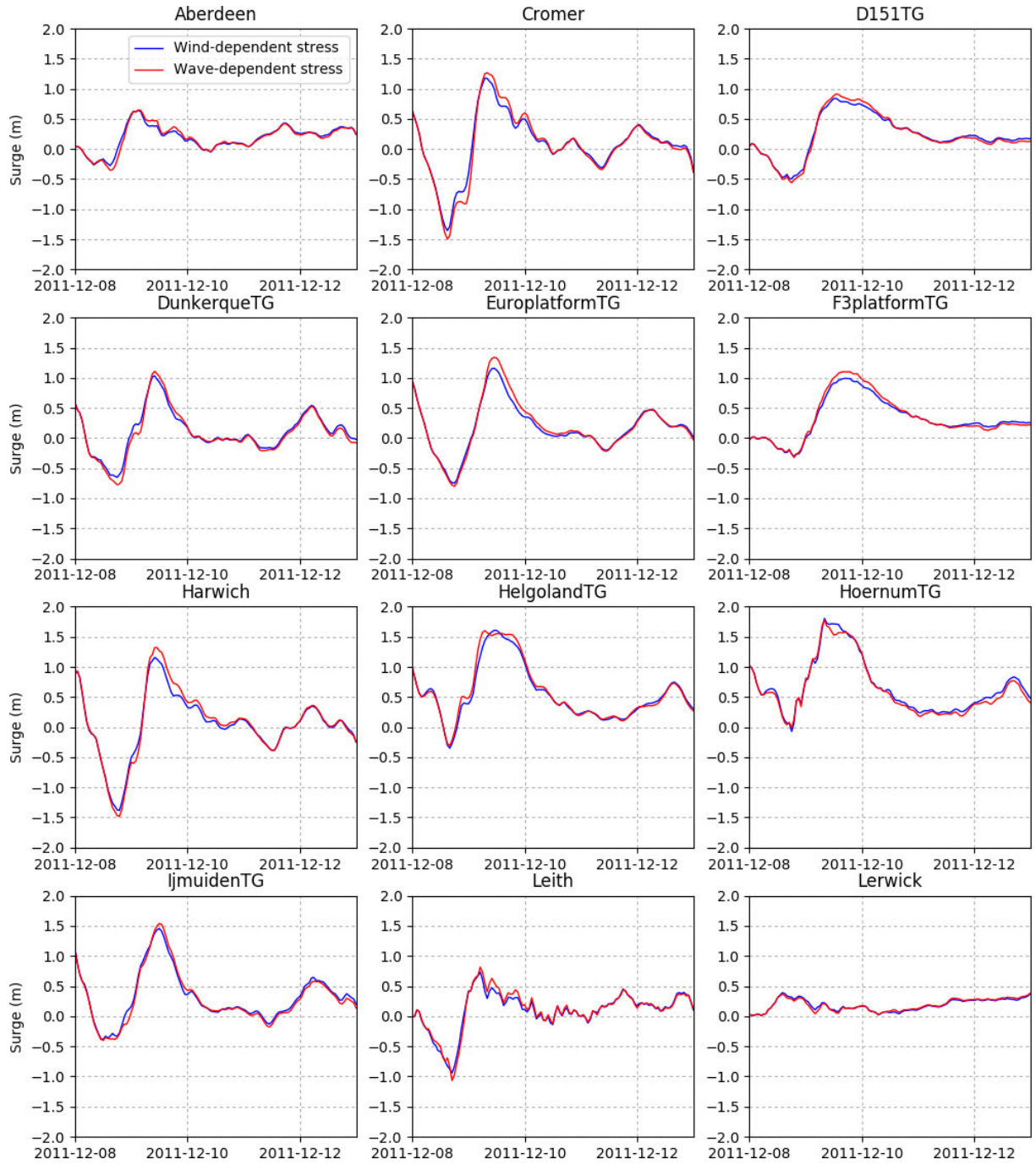

Figure E.5 – Modelled surges with two parameterizations (wind- and wave-dependent) at tide gauges (Aberdeen to Lerwick) during Friedhelm storm

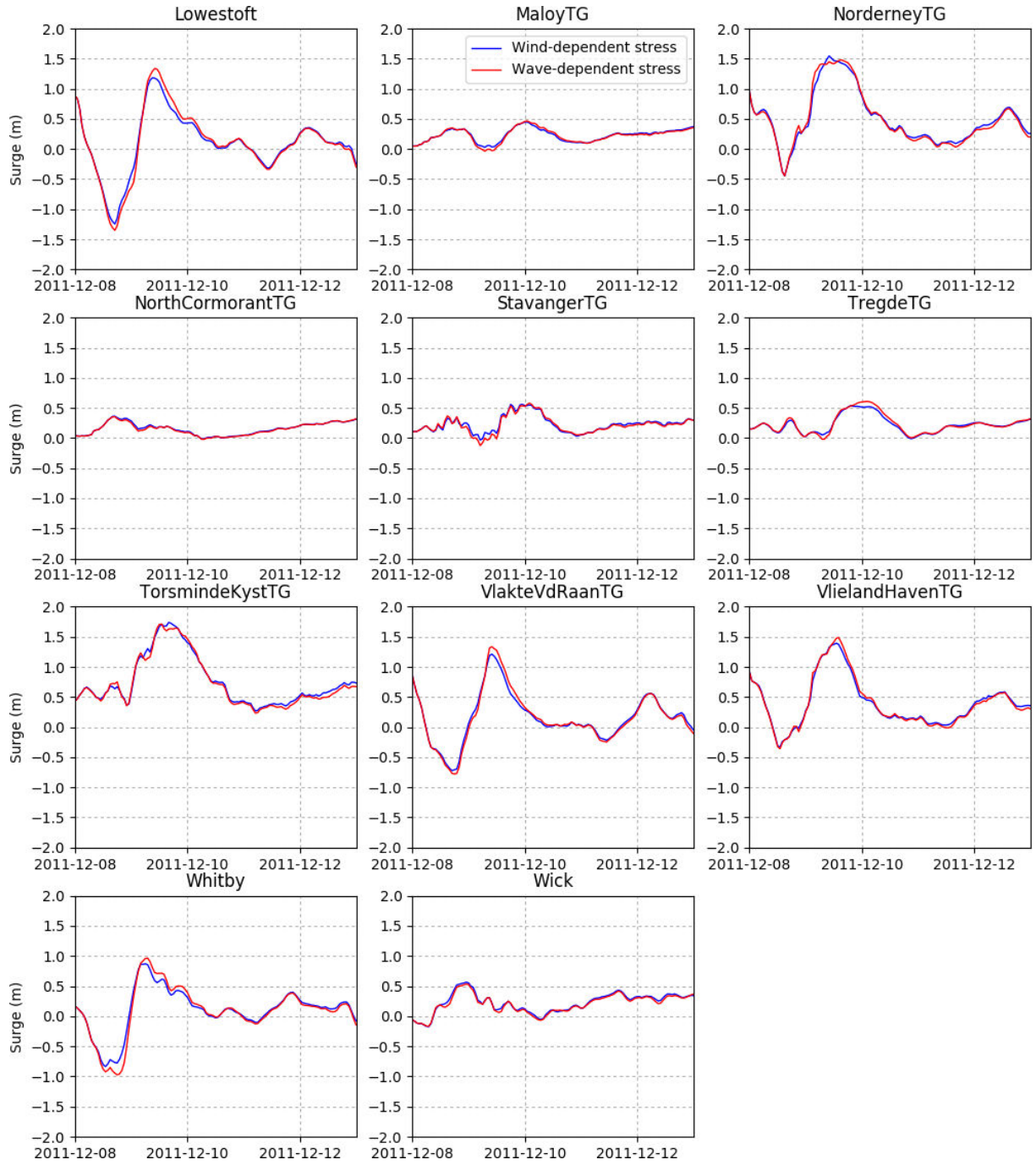

Figure E.6 – Modelled surges with two parameterizations (wind- and wave-dependent) at tide gauges (Lowestoft to Wick) during Friedhelm storm

Appendix F

Modelled surges along JASON-2 tracks

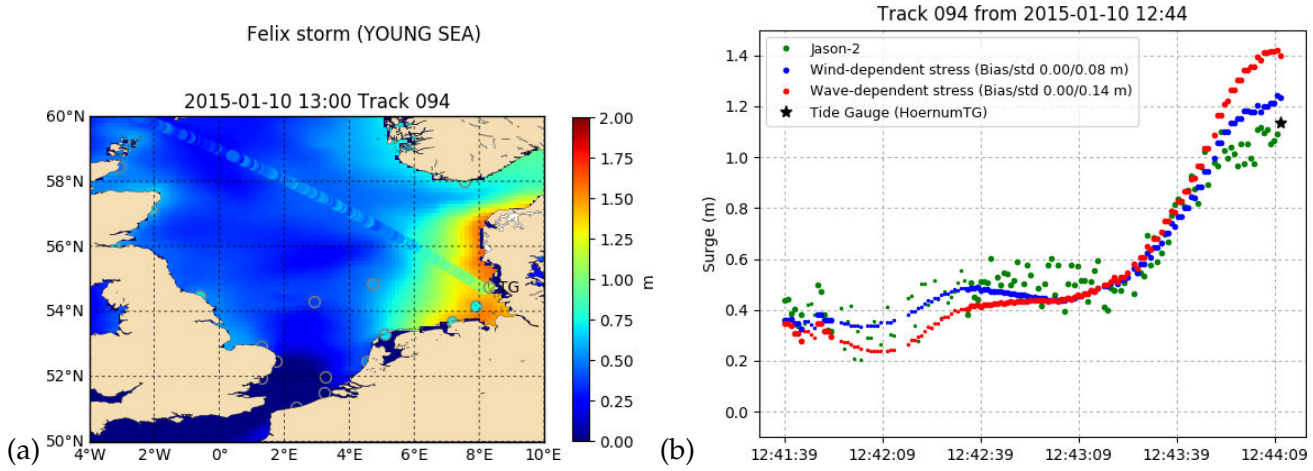

Figure F.1 – Surges from TUGO model, JASON-2 altimeter and tide gauges during Felix. The markersize is smaller on (b) when the bathymetry is lower than 100 m.

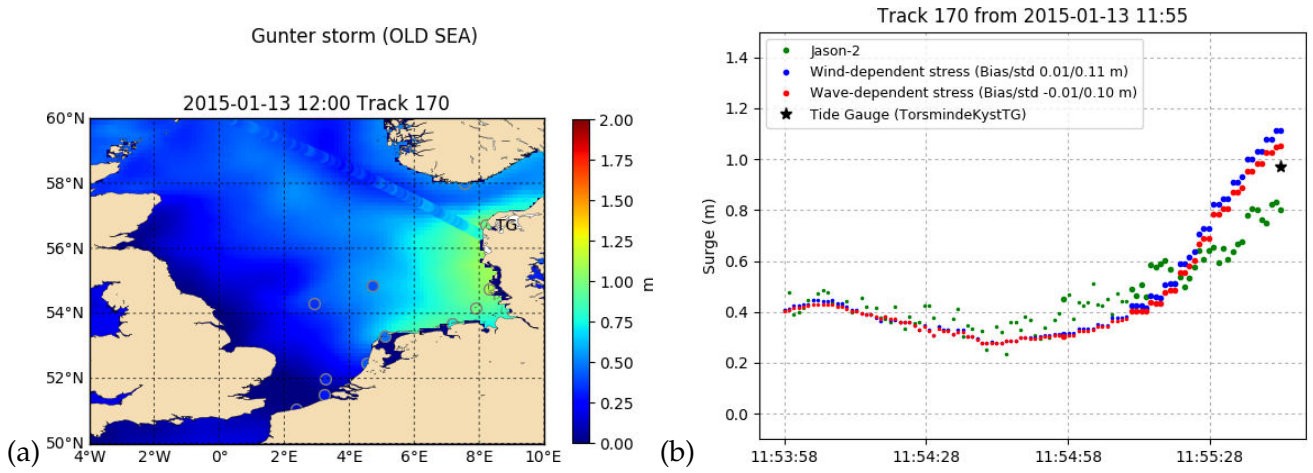

Figure F.2 – Surges from TUGO model, JASON-2 altimeter and tide gauges during Gunter. The markersize is smaller on (b) when the bathymetry is lower than 100 m.

Bibliography

Allain, D. J. (2013). TUGOm tidal toolbox. Technical report. LEGOS Documentation.

Amorocho, J. and DeVries, J. J. (1980). A new evaluation of the wind stress coefficient over water surfaces. *J. Geophys. Res.*, 85(C1):433–442.

Andreas, E. L. (2004). Spray stress revised. *J. Phys. Oceanogr.*, 34:1429–1440.

Andreas, E. L. (2009). Relating the drag coefficient and the roughness length over the sea to the wavelength of the peak waves. *J. Phys. Oceanogr.*, 39:3011–3020.

Andreas, E. L. and Emanuel, K. (2001). Effect of sea spray on tropical cyclone intensity. *J. Atmos. Sci.*, 58:3741–3751.

Antony, C., Testut, L., and Unnikrishnan, A. (2014). Observing storm surges in the Bay of Bengal from satellite altimetry. *Estuarine, Coastal and Shelf Science*, 151:131–140.

Ardhuin, F., Rogers, E., Babanin, A., Filipot, J.-F., Magne, R., Roland, A., van der Westhuysen, A., Queffeulou, P., Lefevre, J.-M., Aouf, L., and Collard, F. (2010). Semi-empirical dissipation source functions for wind-wave models: part I, definition, calibration and validation. *J. Phys. Oceanogr.*, 40(9):1917–1941.

Aucan, J. and Ardhuin, F. (2013). Infragravity waves in the deep ocean: An upward revision. *Geophys. Res. Lett.*, 40:3435–3439.

Beljaars, A. C. M. (1995). The parameterization of surface fluxes in large-scale models under free convection. *Quart. Journ. Roy. Meteorol. Soc.*, 121:255–270.

Benoit, R. (1977). On the integral of the surface layer profile-gradient functions. *J. Appl. Meteor.*, 16:859–860.

Bertin, X., Bruneau, N., Breilh, J.-F., Fortunato, A. B., and Karpytchev, M. (2012). Importance of wave age and resonance in storm surges: The case Xynthia, Bay of Biscay. *Ocean Modelling*, 42:16–30.

Bertin, X., Li, K., Roland, A., and Bidlot, J.-R. (2015). The contribution of short-waves in storm surges: Two case studies in the Bay of Biscay. *Continental Shelf Research*, 96:1–15.

Birol, F., Fuller, N., Lyard, F., Cancet, M., Niño, F., Delebecque, C., Fleury, S., Toublanc, F., Melet, A., Saraceno, M., and Léger, F. (2016). Coastal applications from nadir altimetry: Example of the X-TRACK regional products. *Advances in Space Research*, 59(4):936–953.

Black, P. G., DAsaro, E. A., Drennan, W. M., French, J. R., Niller, P. P., Sanford, T. B., Terrill, E. J., Walsh, E. J., and Zhang, J. A. (2007). Airsea exchange in hurricanes: Synthesis of observations from the coupled boundary layer airsea transfer experiment. *Bull. Amer. Meterol. Soc.*, 88:359374.

Brown, J. M., Souza, A. J., and Wolf, J. (2010). An investigation of recent decadal-scale storm events in the eastern Irish Sea. *J. Geophys. Res.*, 115:C05018.

Businger, J. A., Wyngaard, J. C., Izumi, I., and Bradley, E. F. (1971). Flux-profile relationships in the atmospheric surface layer. *J. Atmos. Sci.*, 28:181–189.

Businger, J. A. and Yaglom, A. M. (1971). Introduction to Obukhovs paper "turbulence in an atmosphere with a non-uniform temperature". *Bound.-Layer Meteorol.*, 2:3–6.

Carrère, L. and Lyard, F. (2003). Modeling the barotropic response of the global ocean to atmospheric wind and pressure forcing - comparisons with observations. *Geophys. Res. Lett.*, 30(6):1275.

Carrère, L., Lyard, F., Cancet, M., and Guillot, A. (2015). FES 2014, a new tidal model on the global ocean with enhanced accuracy in shallow seas and in the Arctic region. In *EGU General Assembly Conference Abstracts*, volume 17 of *EGU General Assembly Conference Abstracts*, page 5481.

Chapron, B. (2017). A guideline to derive ocean surface currents from space: analysis and interpretation framework. Technical report. From GlobCurrent Consortium.

Chapron, B., Collard, F., and Ardhuin, F. (2005). Direct measurements of ocean surface velocity from space: interpretation and validation. *J. Geophys. Res.*, 110(C07008).

Charnock, H. (1955). Wind stress on a water surface. *Quart. Journ. Roy. Meteorol. Soc.*, 81:639–640.

Donelan, M. (1982). The dependence of the aerodynamic drag coefficient on wave parameters. In *Proceedings of the First Int. Conf. on Meteorology and Air-Sea Interaction of the Coastal Zone, The Hague*, pages 381–387. Amer. Meteor. Soc.

Donelan, M. A., Haus, B. K., Reul, N., Plant, W. J., Stiassnie, M., Graber, H. C., Brown, O. B., and Saltzman, E. S. (2004). On the limiting aerodynamic roughness of the ocean in very strong winds. *Geophys. Res. Lett.*, 31:L18306.

Doyle, J. D. (2002). Coupled atmosphere-ocean wave simulations under high wind conditions. *Mon. Weather Rev.*, 130:3087–3099.

Drennan, W. M., Graber, H. C., Hauser, D., and Quentin, C. (2003). On the wave age dependence of wind stress over pure wind seas. *J. Geophys. Res.*, 108(C3):8062.

Dyer, A. (1974). A review of flux-profile relationships. *Bound.-Layer Meteorol.*, 7:363–372.

ECMWF (2015a). *IFS Documentation CY41R1*. ECMWF Book.

ECMWF (2015b). *IFS Documentation CY41R1. Part VII: ECMWF Wave Model*. ECMWF Book Chapter.

Edson, J. B., Jampana, V., Weller, R. A., Bigorre, S. P., Plueddemann, A. J., Fairall, C. W., Miller, S. D., Mahrt, L., Vickers, D., and Hersbach, H. (2013). On the exchange of momentum over the open ocean. *J. Phys. Oceanogr.*, 43:1589–1610.

Emond, M. and Vandemark, D. (2018). Evaluation of potential buoy wind measurement biases under high sea states and gale force conditions. In prep. for J. Atm. Ocean. Tech.

Fabrikant, A. L. (1976). Quasilinear theory of wind-wave generation. *Izv. Atmos. Ocean. Phys.*, 12:524–526.

Fairall, C. W., Bradley, E. F., Hare, J. E., Grachev, A. A., and Edson, J. B. (2003). Bulk parameterization of air-sea fluxes: updates and verification for the COARE algorithm. *Journal of Climate*, 16:571–591.

Fairall, C. W., Bradley, E. F., Rogers, D. P., Edson, J. B., and Young, G. S. (1996). Bulk parameterization of airsea fluxes in TOGA COARE. *J. Geophys. Res.*, 101:3747–3767.

Furevik, B. R. and Haakenstad, H. (2012). Near-surface marine wind profiles from rawinsonde and NORA10 hindcast. *J. Geophys. Res.*, 117:D23106.

Garfinkel, C. I., Molod, A. M., Oman, L. D., and Song, I. (2011). Improvement of the GEOS-5 AGCM upon updating the air-sea roughness parameterization. *Geophys. Res. Lett.*, 38:L18702.

Gaspar, P. and Ponte, R. (1997). Relation between sea level and barometric pressure determined from altimeter data and model simulations. *J. Geophys. Res.*, 102(C1):961–971.

Geernaert, G. L., Katsaros, K. B., and Richter, K. (1986). Variation of the drag coefficient and its dependence on sea state. *J. Geophys. Res. Oceans*, 91(C6):7667–7679.

Geernaert, G. L., Larsen, S. E., and Hansen, F. (1987). Measurements of the wind stress, heat flux, and turbulence intensity during storm conditions over the North Sea. *J. Geophys. Res. Oceans*, 92(C12):13127–13139.

Haigh, I. D., Wadey, M. P., Wahl, T., Ozsoy, O., Nicholls, R. J., Brown, J. M., Horsburgh, K., and Gouldby, B. (2016). Spatial and temporal analysis of extreme sea level and storm surge events around the coastline of the UK. *Nature Scientific Data*, 3:160107.

Hanafin, J., Quilfen, Y., Ardhuin, F., Sienkiewicz, J., Queffeulou, P., Obrebski, M., Chapron, B., Reul, N., Collard, F., Corman, D., de Azevedo, E. B., Vandemark, D., and Stutzmann, E. (2012). Phenomenal sea states and swell radiation: a comprehensive analysis of the 12-16 February 2011 North Atlantic storms. *Bull. Amer. Meterol. Soc.*, 93:1825–1832.

Hasager, C. B., Stein, D., Courtney, M., Peña, A., Mikkelsen, T., Stickland, M., and Oldroyd, A. (2013). Hub Height Ocean Winds over the North Sea Observed by the NORSEWInD Lidar Array: Measuring Techniques, Quality Control and Data Management. *Remote Sens.*, 5:4280–4303.

Hellerman, S. and Rosenstein, M. (1983). Normal monthly wind stress over the world ocean with error estimates. *J. Phys. Oceanogr.*, 13(7):1093–1104.

Holthuijsen, L. H., Powell, M. D., and Pietrzak, J. D. (2012). Wind and waves in extreme hurricanes. *J. Geophys. Res.*, 117:C09003.

Holtslag, A. A. M., de Bruijn, E. I. F., and Pan, H.-L. (1990). A high-resolution air mass transformation model for short-range weather forecasting. *Mon. Wea. Rev.*, 118:1561–1575.

Idier, D., Dumas, F., and Muller, H. (2012a). Tide-surge interaction in the English Channel. *Nat. Hazards Earth Syst. Sci.*, 12:37093718.

Idier, D., Krien, Y., Pedreros, R., Desramaut, N., Pineau-Guillou, L., and Dumas, F. (2010). Système de prévision de surcotes en Manche/Atlantique et Méditerranée : Etude bibliographique [D1]. Technical report. BRGM/RP-58918-FR.

Idier, D., Muller, H., Pedreros, R., Thiebot, J., Yates, M., Creach, R., Voineson, G., Dumas, F., Lecornu, F., Pineau-Guillou, L., Ohl, P., and Paradis, D. (2012b). Système de prévision de surcotes en Manche/Atlantique et Méditerranée : Amélioration du système existant sur la façade Manche/Gascogne [D4]. Technical report. BRGM/RP-61019-FR.

Janssen, P. (2004). *The interaction of ocean waves and wind*. Cambridge University Press, Cambridge, UK.

Janssen, P. (2012). Ocean wave effects on the daily cycle in SST. *J. Geophys. Res.*, 117:C00J32.

Janssen, P. A., Breivik, O., Mogensen, K., Vitart, F., Balmaseda, M., Bidlot, J.-R., Keeley, S., Leutbecher, M., Magnusson, L., and Molteni., F. (2013). Air-sea interaction and surface waves. Technical report. ECMWF Technical Memorandum 712.

Janssen, P. A. E. M. (1986). On the effect of gustiness on wave growth. KNMI Afdeling Oceanografisch Onderzoek memo 00-86-18, De Bilt, The Netherlands.

Janssen, P. A. E. M. (1991). Quasi-linear theory of wind wave generation applied to wave forecasting. *J. Phys. Oceanogr.*, 21:1631–1642.

Jarosz, E., Mitchell, D. A., Wang, D. W., and Teague, W. J. (2007). Bottom-up determination of air-sea momentum exchange under a major tropical cyclone. *Science*, 315:1707–1709.

Keulegan, G. H. (1951). Wind tides in small closed channels. *J. Res. nat. Bur. Stand.*, 46(5):358–381.

Kitaigorodskii, S. (1973). *The physics of air-sea interaction*. Israel Program of Scientific Translations.

Komen, G., Janssen, P. A. E. M., Makin, V., and Oost, W. (1998). On the sea state dependence of the Charnock parameter. *Global Atmos. Ocean Syst.*, 5:367–388.

Kraus, E. B. and Businger, J. A. (1994). *Atmosphere-Ocean Interaction*. Oxford University Press.

Kudryavtsev, V., Chapron, B., and Makin, V. (2014). Impact of wind waves on the airsea fluxes: A coupled model. *J. Geophys. Res. Oceans*, 119:1217–1236.

Kudryavtsev, V. N. (2006). On the effect of sea drops on the atmospheric boundary layer. *J. Geophys. Res.*, 111:C07020.

Kudryavtsev, V. N. and Makin, V. K. (2006). Impact of ocean spray on the dynamics of the marine atmospheric boundary layer. *Bound.-Layer Meteorol.*, 140(3):383–410.

Large, W. G. and Pond, S. (1981). Open ocean momentum flux measurements in moderate to strong winds. *J. Phys. Oceanogr.*, 11:324–336.

Longuet-Higgins, M. S. and Stewart, R. W. (1964). Radiation stress in water waves, a physical discussion with applications. *Deep Sea Research*, 11:529–563.

Lyard, F., Lefevre, F., Letellier, T., and Francis, O. (2006). Modelling the global ocean tides: modern insights from FES2004. *Ocean Dynamics*, 56:394–415.

Magnusson, L., Bidlot, J.-R., Bonavita, M., Brown, A., Browne, P., Chiara, G. D., Dahoui, M., Lang, S. T. K., McNally, T., Mogensen, K. S., Pappenberger, F., Prates, F., Rabier, F., Richardson, D. S., Vitart, F., and Malardel, S. (2018). ECMWF activities for improved hurricane forecasts. *Accepted in Bull. Amer. Meterol. Soc.*

Makin, V. K. (2004). A note on drag of the sea surface at hurricane winds. *Bound.-Layer Meteorol.*, 115:1.

Marié, L. and Ardhuin, F. (2018). DRIFT4SKIM experiment plan. Technical report. IFREMER.

Mastenbroek, C., Burgers, G., and Janssen, P. A. E. M. (1993). The dynamical coupling of a wave model and a storm surge model through the atmospheric boundary layer. *J. Phys. Oceanogr.*, 23:1856–1867.

Meissner, T., Ricciardulli, L., and Wentz, F. (2017). Capability of the SMAP mission to measure ocean surface winds in storms. *Bull. Amer. Meterol. Soc.*, 98:1660–1677.

Monin, A. S. and Obukhov, A. (1954). Basic laws of turbulent mixing in the surface layer of the atmosphere. *Geophys. Inst. Acad. Sci. USSR*, 151:163–187.

Moon, I.-J., Ginis, I., Hara, T., and Thomas, B. (2007). A physics-based parameterization of airsea momentum flux at high wind speeds and its impact on hurricane intensity predictions. *Mon. Weather Rev.*, 135(8):2869–2878.

Moon, I.-J., Kwon, J.-I., Lee, J.-C., Shim, J.-S., Kang, S. K., Oh, I. S., and Kwon, S. J. (2009). Effect of the surface wind stress parameterization on the storm surge modeling. *Ocean Modelling*, 29:115127.

Muller, H., Pineau-Guillou, L., Idier, D., and Ardhuin, F. (2014). Atmospheric storm surge modeling methodology along the French (Atlantic and English Channel) coast. *Ocean Dynamics*, 64(11):1671–1692.

Munk, W. (1950). Origin and generation of waves. *Coastal Engineering Proceedings*, 1(1):1.

Nicolle, A., Karpytchev, M., and Benoit, M. (2009). Amplification of the storm surges in shallow waters of the Pertuis Charentais (Bay of Biscay, France). *Ocean Dynamics*, 59:921–935.

Nordeng, T. E. (1991). On the wave age dependent drag coefficient and roughness length at sea. *J. Geophys. Res. Oceans*, 96(C4):7167–7174.

Obukhov, A. (1946). Turbulence in an atmosphere with inhomogeneous temperature. *Tr. Inst. Geofiz. Akad. Nauk SSSR*, 1:95–115.

Oost, W. A., Komen, G. J., Jacobs, C. M. J., and van Oort, C. (2002). New evidence for a relation between wind stress and wave age during ASGAMAGE. *Bound.-Layer Meteorol.*, 103:409–438.

Passaro, M., Cipollini, P., Vignudelli, S., Quartly, G. D., and M.Snaith, H. (2014). ALES: a multi-mission adaptive sub-waveform retracker for coastal and open ocean altimetry. *Remote Sens. Environ.*, 145:173–189.

Pedreros, R., Idier, D., Muller, H., Lecacheux, S., Paris, F., Yates-Michelin, M., Dumas, F., Pineau-Guillou, L., and Sénéchal, N. (2018). Relative contribution of wave setup to the storm surge: Observations and modeling based analysis in open and protected environments (Truc Vert beach and Tubuai island). *Journal of Coastal Research*, 85:1046–1050.

Peña, A. and Gryning, A. (2008). Charnocks roughness length model and non-dimensional wind profiles over the sea. *Bound.-Layer Meteorol.*, 128:191–203.

Peng, S. and Li, Y. (2015). A parabolic model of drag coefficient for storm surge simulation in the south china sea. *Nature Scentific Reports*, 5:15496.

Peureux, C. and Ardhuin, F. (2016). Ocean bottom pressure records from the Cascadia array and short surface gravity waves. *J. Geophys. Res.*, 121:28622873.

Peureux, C., Veras-Guimaraes, P., and Ardhuin, F. (2018). A modulation source term for short ocean waves numerical modelling. Oral Presentation at EGU, 8-13 April 2018, Vienna, Austria.

Pineau-Guillou, L., Ardhuin, F., Bouin, M.-N., Redelsperger, J.-L., Chapron, B., Bidlot, J.-R., and Quilfen, Y. (2018). Strong winds in a coupled wave-atmosphere model during a north atlantic storm event: evaluation against observations. *Quart. Journ. Roy. Meteorol. Soc.*, 144:317–332.

Pineau-Guillou, L., Lathuiliere, C., Magne, R., Louazel, S., Corman, D., and Perherin, C. (2012). Sea levels analysis and surge modelling during storm Xynthia. *European Journal of Environmental and Civil Engineering*, 16(8):943–952.

Powell, M. D., Vickery, P. J., and Reinhold, T. A. (2003). Reduced drag coefficient for high wind speeds in tropical cyclones. *Nature*, 422:279–283.

Rascle, N. and Ardhuin, F. (2013). A global wave parameter database for geophysical applications. Part 2: model validation with improved source term parameterization. *Ocean Modelling*, 70:174–188.

Reul, N., Branger, H., and Giovanangeli, J. (1999). Air flow separation over unsteady breaking waves. *Phys. Fluids*, 11:1959–1961.

Reul, N., Branger, H., and Giovanangeli, J.-P. (2008). Air flow structure over short-gravity breaking water waves. *Bound.-Layer Meteorol.*, 126:477–705.

Rio, M.-H., Mulet, S., and Picot, N. (2014). Beyond GOCE for the ocean circulation estimate: Synergetic use of altimetry, gravimetry, and in situ data provides new insight into geostrophic and Ekman currents. *Geophys. Res. Lett.*, 41(24):8918–8925.

Shen, J. and Gong, W. (2009). Influence of model domain size, wind directions and Ekman transport on storm surge development inside the Chesapeake Bay: A case study of extratropical cyclone Ernesto, 2006. *J. Mar. Sys.*, 275:198215.

Sheremet, A., Staples, T., Ardhuin, F., Suanez, S., and Fichaut, B. (2014). Observations of large infragravity wave runup at Banneg Island, France. *Geophys. Res. Lett.*, 41(3):976–982.

Shimura, T., Mori, N., Takemi, T., and Mizuta, R. (2017). Long-term impacts of ocean wave-dependent roughness on global climate systems. *J. Geophys. Res. Oceans*, 122:1995–2011.

Simon, B. (2007). *La marée océanique côtière*. Institut Océanographique Editeur, Paris, France.

Smith, S. D. (1980a). Comment on A new evaluation of the wind stress coefficient over water surfaces. *J. Geophys. Res.*, 86(C5):4307.

Smith, S. D. (1980b). Wind stress and heat flux over the ocean in gale force winds. *J. Phys. Oceanogr.*, 10:709–726.

Smith, S. D., Anderson, R. J., Oost, W. A., Kraan, C., Maat, N., De Cosmo, J., Katsaros, K. B., Davidson, K. L., Bumke, K., Hasse, L., and Chadwick, H. M. (1992). Sea surface wind stress and drag coefficients: the HEXOS results. *Bound.-Layer Meteorol.*, 60:109–142.

Smith, S. D. and Banke, E. (1975). Variation of the sea surface drag coefficient with wind speed. *Quart. Journ. Roy. Meteorol. Soc.*, 101:665–673.

Soloviev, A., Lukas, R., Donelan, M. A., Haus, B. K., and Ginis, I. (2014). The air-sea interface and surface stress under tropical cyclones. *Nature Scentific Reports*, 4:5306.

Stammer, D., Wunsch, C., and Ponte, R. (2000). De-aliasing of global high frequency barotropic motions in altimeter observations. *Geophys. Res. Lett.*, 27(8):1175–1178.

Stoffelen, A. (2018). CHEFS C-band High and Extreme-force Speeds - WP2: State of the art and user requirements. Technical report. From KNMI and CHEFS Consortium.

Stopa, J. E. and Cheung, K. F. (2014). Intercomparison of wind and wave data from the ECMWF Reanalysis Interim and the NCEP Climate Forecast System Reanalysis. *Ocean Modelling*, 75:65–83.

Takagaki, N., Komori, S., Suzuki, N., Iwano, K., Kuramoto, T., Shimada, S., Kurose, R., and Takahashi, K. (2012). Strong correlation between the drag coefficient and the shape of the wind sea spectrum over a broad range of wind speeds. *Geophys. Res. Lett.*, 39:L23604.

Taylor, P. K. (2002). *AIR-SEA INTERACTION Momentum, Heat, and Vapor Fluxes*. In Encyclopedia of Atmospheric Sciences, First Edition.

Taylor, P. K., Kent, E. C., Yelland, M. J., and Moat, B. I. (1999). The accuracy of marine surface winds from ships and buoys. *CLIMAR 99, WMO Workshop on Advances in Marine Climatology*, pages 59–68.

Van Dorn, W. G. (1953). Wind stress on a artificial pond. *J. Mar. Res.*, 12:249–276.

van Nieuwkoop, J., Baas, P., Caires, S., and Groeneweg, J. (2015). On the consistency of the drag between air and water in meteorological, hydrodynamic and wave models. *Ocean Dynamics*, 65(7):989–1000.

Verspeek, J., Stoffelen, A., Verhoef, A., and Portabella, M. (2012). Improved ASCAT wind retrieval using NWP ocean calibration. *IEEE Trans. on Geosci. and Remote Sensing*, 50:2488–2494.

Wei, Y. and Wu, J. (1992). In situ measurements of surface tension, wave damping, and wind properties modified by natural films. *J. Geophys. Res. Oceans*, 97(C4):5307–5313.

Wu, J. (1982). Wind-stress coefficients over sea surface from breeze to hurricane. *J. Geophys. Res.*, 87:9704–9706.

Yelland, M. J. and Taylor, P. K. (1996). Wind stress measurements from the open ocean. *J. Phys. Oceanogr.*, 26:541–558.

Zabolotskikh, E., Mitnik, L., and Chapron, B. (2014). GCOM-W1 AMSR2 and MetOp-A ASCAT wind speeds for the extratropical cyclones over the North Atlantic. *Remote Sens. Environ.*, 147:89–98.

Zeng, L. and Brown, R. (1998). Scatterometer observations at high wind speeds. *J. Appl. Meteorol.*, 37:1412–1420.

UNIVERSITE SCIENCES BRETAGNE DE LA MER LOIRE ET DU LITTORAL

UBO Université de Bretagne Occidentale

Titre : Interaction Océan-Atmosphère : Amélioration de la tension de vent pour la modélisation physique côtière

Mots clés : interaction air-mer – tension de vent – vents – surcotes – état de mer

Résumé : Les surcotes de tempête sont souvent sous-estimées dans les modèles hydrodynamiques, ainsi que les grandes vagues dans les modèles de vagues. Les causes possibles sont une sous-estimation des vents dans les modèles atmosphériques et/ou une formulation incorrecte de la tension de vent. Les objectifs de cette thèse sont (1) d'estimer les biais par vents forts dans les modèles atmosphériques (2) de développer une nouvelle paramétrisation du coefficient de traînée permettant de réduire ce biais (3) d'étudier l'impact des vagues sur la tension de vent. La méthode consiste à étudier la réponse de l'atmosphère et de l'océan à la tension de vent. Dans une première partie, nous utilisons le modèle couplé vagues-atmosphère d'ECMWF. Nous montrons que les vents forts sont sous-estimés, avec un biais de l'ordre de -7 m/s à 30 m/s. Des écarts significatifs existent aussi entre les observations, les bouées et les vents issus de ASCAT-KNMI étant généralement inférieurs à ceux des plateformes et des autres données satellites utilisées dans cette étude (AMSR2, ASCAT-RSS, WindSat, SMOS et JASON-2). La nouvelle paramétrisation développée permet d'obtenir des vents plus forts qu'avec celle d'ECMWF par défaut. Dans une deuxième partie (réponse de l'océan), nous utilisons le modèle global océanique TUGO du LEGOS forcé par le modèle couplé vagues-atmosphère d'ECMWF. Nous montrons qu'une paramétrisation de la tension de vent dépendant des vagues plutôt que du vent est plus appropriée quand l'état de mer est jeune. Elle conduit à des surcotes plus proches des observations (marégraphes et traces altimétriques de JASON-2). L'impact des vagues sur la surcote est significatif, et peut atteindre 20 cm.

Title : Ocean-Atmosphere Interaction : Improvement of wind stress for coastal physical modelling

Keywords : air-sea interaction – wind stress – winds – surges – sea state

Abstract : Storm surges may be underestimated in hydrodynamic models, as well as large wave heights in wave models. This could come from an underestimation of strong winds in atmospheric models and/or an inappropriate wind stress formulation. The objectives of the present work are (1) to estimate how strong are the biases for high winds in atmospheric models (2) to develop a new drag parameterization that could reduce this bias (3) to investigate the impact of the waves on the wind stress. The method consists of studying the response of the atmosphere and the ocean to the wind stress. In a first part, we use the coupled wave-atmosphere model from ECMWF. We show that strong winds may be underestimated, as much as -7 m/s at 30 m/s. Significant differences also exist between observations, with buoys and ASCAT-KNMI generally showing lower wind speeds than the platforms and other remote-sensing data used in this study (AMSR2, ASCAT-RSS, WindSat, SMOS and JASON-2). The newly empirically adjusted Charnock parameterization leads to higher winds compared to the default ECMWF parameterization. In a second part, we use the global ocean model TUGO from LEGOS forced with ECMWF coupled wave-atmopshere model. We show that a wave-dependent rather than wind-dependent stress formulation is more appropriate, when the sea state is young and the sea rougher. It yields to simulated surges closer to observations (i.e. tide gauges and JASON-2 altimeter tracks). The wave impact on the surges is significant, and may reach 20 cm.